REACTION DYNAMICS
STUDIED BY PHOTOEMISSION
SPECTROSCOPY

by

Dan Imre

B.A. University of Oregon
(1979)

Submitted in Partial Fulfillment of
the Requirements for the Degree of

DOCTOR OF PHILOSOPHY

at the

MASSACHUSETTS INSTITUTE OF TECHNOLOGY

August 1984

c Massachusetts Institute of Technology 1984

Signature of Author ______________________
Department of Chemistry
August, 1984

Certified by ______________________
James L. Kinsey
Research Supervisor

Accepted by ______________________
Departmental Committee on Graduate Students

MASSACHUSETTS INSTITUTE
OF TECHNOLOGY

DEC 0 3 1984

LIBRARIES

ARCHIVES

This doctoral thesis has been examined by a committee of the Department of Chemistry as follows:

Professor Robert Field Robert Field
Professor James Kinsey
Professor Sylvia Ceyer Sylvia Ceyer

ACKNOWLEDGEMENTS

I would like to than Professor J.L. Kinsey my research advisor for giving me a free hand during my stay at M.I.T., for trusting my judgment in designing and carrying out the experiments, and at the same time for providing his guidance, support, and hours of very stimulating discussion. His way of approaching scientific questions has often been unconventional and therefore condusive to the development of new and exciting observations. I would also like to express my gratitude to him for guiding my search for a new career. His enormous support in and out of M.I.T., greatly enhanced the quality of career opportunities open to me. I am confident that our productive relationship will continue in the future.

I would like to express very special thanks to R. Coalson and R. Sundberg whose main interest lies in theoretical chemistry. Their interest in my project led to a unique collaborative relationship between theoretical and experimental chemists; by which this project was greatly enriched. Our frequent discussions were an essential to my development at M.I.T. R. Coalson even provided us with his wave packet routines and guided us in their use. R. Sandberg in the past few months has completely devoted himself to helping me complete this work. His calculations on the ground state potential surface of methyl iodide are presented in chapter 7 of this thesis.

Special thanks to E. Abramson with whom I spent the whole period of my graduate studies for his friendship which helped sustain my five years in the M.I.T. basement.

Thanks to professor R. Field for showing so much enthusiasm for my project. To John Annese the nicest man on campus. To the Spectroscopy Laboratory for providing the equipment used in some of the experiments.

Finally my parents and my wife's parents for supporting and allowing us to remain carefree for so long. I dedicate this work to them.

TO: Zolten and Zezilia Imre and Walter and Maria Sheri

REACTION DYNAMICS
STUDIED BY PHOTOEMISSION
SPECTROSCOPY

by

DAN IMRE

Submitted to the Department of Chemistry
on August 13, 1984 in partial fulfillment of the
requirements for the Degree of Doctor of Philosophy

ABSTRACT

Photoemission spectra from molecules in the process of falling apart are used to study photodissociation reaction dynamics. Photodissociation represents a unique class of reactions, where experimental control of initial conditions is possible to the limits of the uncertainty principle. These systems are therefore suitable for detailed studies of molecular interactions during reactive collisions.

A photodissociation reaction takes place on an electronically excited state surface, that is connected to the ground state by an electronically allowed transition, and so can be studied using spectroscopic techniques. The transitory nature of reactive species (10^{-14} - 10^{-13} seconds) when compared to typical radiative lifetimes (10^{-6} - 10^{-8} seconds), allows only for a very low emission yield. That small but finite yield, however, is extremely informative, as its spectral characteristics provide insight to the reactive process. This is especially true when absorption and emission process are viewed in a time dependent formalism.

As the molecule proceeds on the path from reactant to products molecular geometries change, developing in the Franck-Condon overlaps with ground state vibrational levels with amplitude along the dissociation path. The emission spectrum can be seen as a footprint left by the reacting molecule. The nature of the vibrational lines present in the spectrum and their intensities are indications as to the intricate dynamic process on the excited state surface. The emission spectrum also provides valuable information about the ground electronic surface. During the reaction one of the molecular bonds increases indefinitely. As a result long progressions containing very selective vibrational levels are present in the spectrum.

We used two systems in our studies: methyl iodide as a test case because of its relative simplicity, and ozone for its interesting and qualitatively different behavior.

We proposed and used potential energy surfaces for preliminary calculations of methyl iodide photodissociation reaction and its ground state vibrational structure.

TABLE OF CONTENTS

Acknowledgements 3

Abstract 5

Chapter 1: History 7

Chapter 2: Half Collision Systems, Photodissociating Systems 27

Chapter 3: From Spectrum to Reaction 43

Chapter 4: Experimental Detail 65

Chapter 5: Methyl Iodide Photodissociation 72

Chapter 6: Ozone Photodissociation Dynamics 102

Chapter 7: Preliminary Calculation: Methyl Iodide 127

Chapter 8: Conclusion 184

References 187

Appendixes 192

CHAPTER 1: HISTORY

I. Introduction

This thesis presents a new experimental approach for characterizing transition states of chemical reactions.

In every elementary chemical reaction the molecular system passes through a continuously evolving intermediate species that is neither reactant nor product but the former in the process of turning into the later. This species is termed the transition state. The more we learn about such intermediate species the better we will understand the transformation of reactants into products. Theoretical groundwork and techniques for treating dynamics of small polyatomics have advanced to a point where fairly accurate predictions can be made. What is still lacking is extensive experimental data in a form which can yield, in a straightforward manner, parameters to be used in these calculations.

A time dependent formulation of photon absorption and emission developed by E.J. Heller and coworkers has helped turn these spectroscopic techniques into powerful tools for the study of molecular dynamics. Our results from methyl iodide and ozone U.V. photodissociation studies illustrate the uses of absorption and emission spectroscopy to study reaction dynamics. Besides providing a theoretical framework for complete calculation, the time dependent point of view also makes an intuitive connection between features in experimental spectra and the reaction process. With these connections in mind, one can obtain highly instructive results even from a qualitative examination of the pertinent experimental data. Ozone and methyl iodide were selected for our initial studies in this field because they exhibit quite different nuclear motion on their path to unimolecular dissociation.

This chapter of the thesis will present a very brief and subjective overview of various experimental approaches and developments in the field of molecular dynamics to provide a context into which the present contributions can be placed. The overwhelming information generated in the past 25 years or so provides the foundation of our basic understanding of reaction dynamics today. Chapter two points out the advantages offered by photodissociating systems as compared to bimolecular reactions. Chapter 3 contains a short sketch of the theory connecting spectroscopic data obtained experimentally and the dynamics in question. Chapter 4 contains the experimental details. Chapters 5 and 6, respectively, discuss the experimental results for methyl iodide and ozone. Conclusions about these reactions are drawn from qualitative analysis of the data. A more complete calculation of methyl iodide photodissociation reaction is the subject of chapter 7.

II. History of Experimental Approaches in the Study of Chemical Reactions

A central theme in chemistry has always been the question of what is it that takes place in a chemical reaction. This question provides a basic link between all disciplines of chemistry, each addressing a subsection of this broad subject. The organic, or inorganic chemist might ask: What reactants lead to what products? With what yield? How do temperature, concentrations, pH, solvent, etc. affect these yields? The kineticist, on the other hand, addresses questions such as: How fast is the reaction? How do temperature, pH, solvent, etc. affect the rate?

The chemical dynamicist attempts to study the microscopic factors which determine the rate of production of various product molecules: What forces are at play? How do the nuclei react to these forces in such a way that a new distinct chemical species is formed? Answers to questions such as these require detailed understanding of events occuring on a very short time scale, typically less than a psec, during which atomic substances can change less than 10^{-10} meters and determine the fate of the reactions. At this juncture, it is inappropriate to aim such detailed questions at the enormous numbers of chemical reactions which are either of theoretical or of practical interest. Instead, one wishes to focus on key molecular systems likely to provide penetrating insight for these detailed studies. From those prototype systems, generalizations could then be drawn to other systems. The aim is to develop basic concepts which could then be used on a more-or-less intuitive basis to guide us in developing new chemistry or new understanding of old processes.

The field of experimental molecular dynamics has developed in the last 25 years at a very fast rate, tackling a great variety of elementary problems with new experimental techniques. The following overview of this prolific field makes no pretense of completeness, but is rather intended to provide a general context in which to put the work described in the thesis.

Many of the basic concepts that underlie what is currently known about chemical reactions had been already established by Arrhenius and Bodenstein in the early part of this century. These developments were summarized in Hinshelwood's famous 1926 monograph.[1] At that time, the gross behavior of reacting mixtures was well characterized experimentally, and the basic microscopic concept of collision-induced reactions was correctly interpreted. It was also known that the rate (R_0) for a reaction such as:

$$A + BC \longrightarrow AB + C$$

depends upon the product of the number densities of the reagents, nA and nBC:

I.1 $$R_o = k(T)\ nA\ nBC$$

Here k(T) is the "rate constant" at temperature T, which was shown to obey the following equation

I.2 $$k(T) = A(T)\ EXP\ (-Ea/RT)$$

The pre-exponential factor A(T) reflects dependence on the relative speeds of the reagents, their molecular shape, etc. Ea is the so-called activation energy. Eq. I.2 introduces the important idea of activation energy of a reaction, which led to the concept of energy path diagrams. In the early days it was felt that knowing Ea for a reaction is all one needed to know since that determines the rate of the reaction. Many research groups[2,3] were involved in determining activation energies by studying reaction rates as a function of temperature. Fig. 1-1. shows a typical energy path diagram for the A + BC reaction.

A close examination of this simple diagram reveals that, already at this level of representation, many problems arise. The critical quantity Ea which determines the rate of the reaction is actually not clearly defined in microscopic dynamic terms. The apparent activation energy in some way measures the the effectiveness of the vibrational (V_i) rotational (J_i) and translational energies of the reactants, but in what way?

With that question in mind, the natural next conceptual step is subdivision of the overall rate k(T) into constituent microscopic rates $k(T)\ i \to f$ for reagents in state i yielding products in state f. For a macroscopic sample at temperature T

I.3 $$k(T) = \sum_i \sum_f f_i(T) k(T)_{i \to f}$$

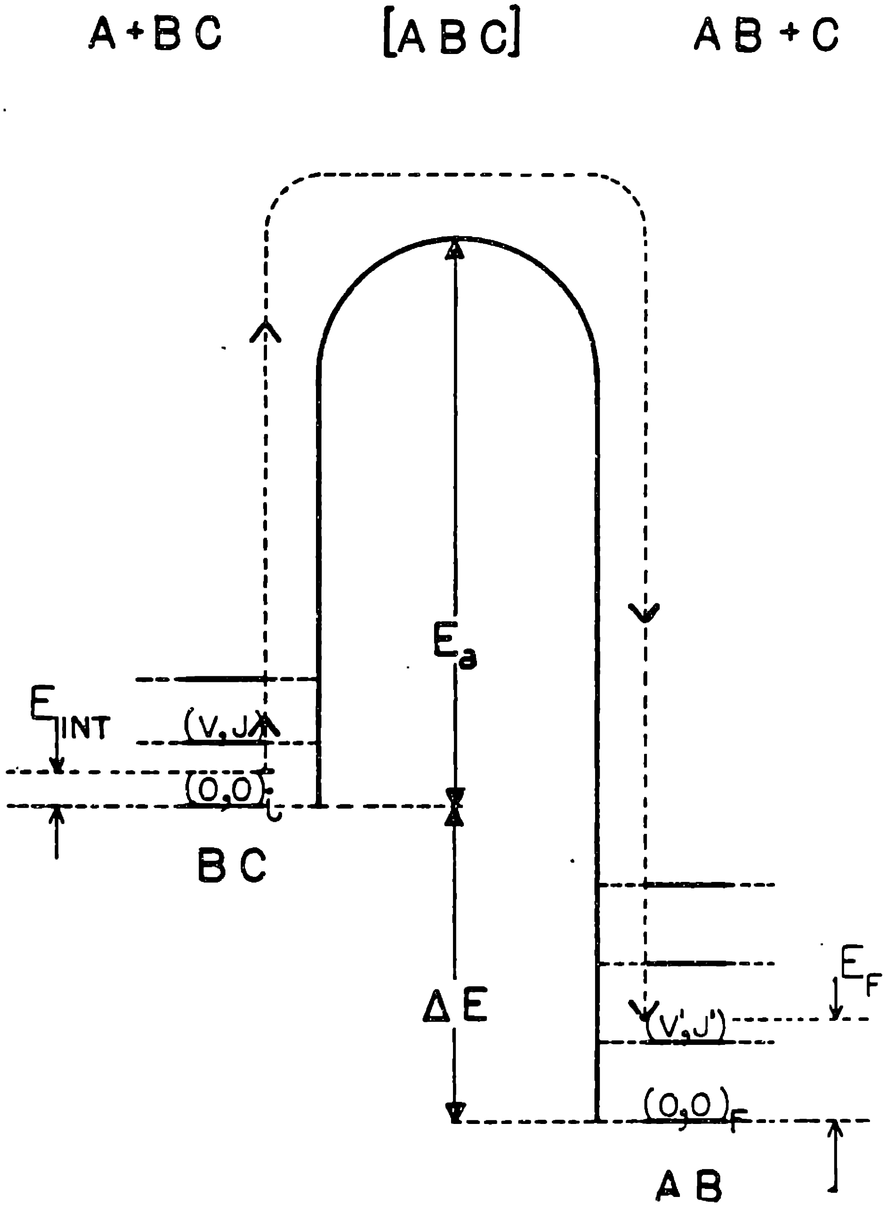
A+BC
[ABC]
AB+C
E_{INT}
(V,J)
$(0,0)_i$
BC
E_a
ΔE
E_F
(V',J')
$(0,0)_F$
AB

Fig 1-1 - Energy path diagram for the reaction A + BC ⟶ AB + C

where: $f_i(T)$ is the fraction of population of reagent molecules in initial state i. In bulk experiments, individual $k_{i \to f}$ cannot be determined. Moreover, the dependence of the reaction rate on initial vibrational energies is non-trivial and cannot be assessed merely by varying the temperature at which the reaction is carried out. In fact, the dependence on vibrational state turns out to be extremely informative as to the dynamics of the reaction. Hence workers in the field were strongly motivated to pursue a path towards state to state rates in order to understand reactive processes in detail.

To achieve such measurements special conditions are required. Reagents have to be prepared in a specific known initial state $(V,J)_i$, and the system has to be amenable to analysis of product states prior to the products suffering any collisional relaxation. The basic design for a system which fulfills such requirements is shown in Figure 1-2.

This type of apparatus is capable of producing reagents in a very narrow distribution of initial states (mostly the lowest $(V,J)_i$). Using various methods of product analysis such as laser induced fluorescence, multi-photon ionization, IR and visible chemiluminescence and time of flight, it is possible to obtain detailed product final state vibrational, rotational, and velocity distributions. To date such experiments have been performed on numerous systems. (A few examples can be found in references 4-10. These were selected to represent most of the techniques used in the field). A typical result for the HI + Cl reaction is shown in figure 1-3. Figure 1-4. shows an energy level diagram for this system.

A most significant observation in the HI + Cl experiment is that an increase in the total energy of the reaction (translational energy increased from 20 KJ/mol to 50 KJ/mol) leads to a decrease in total reaction cross section. I.e., though

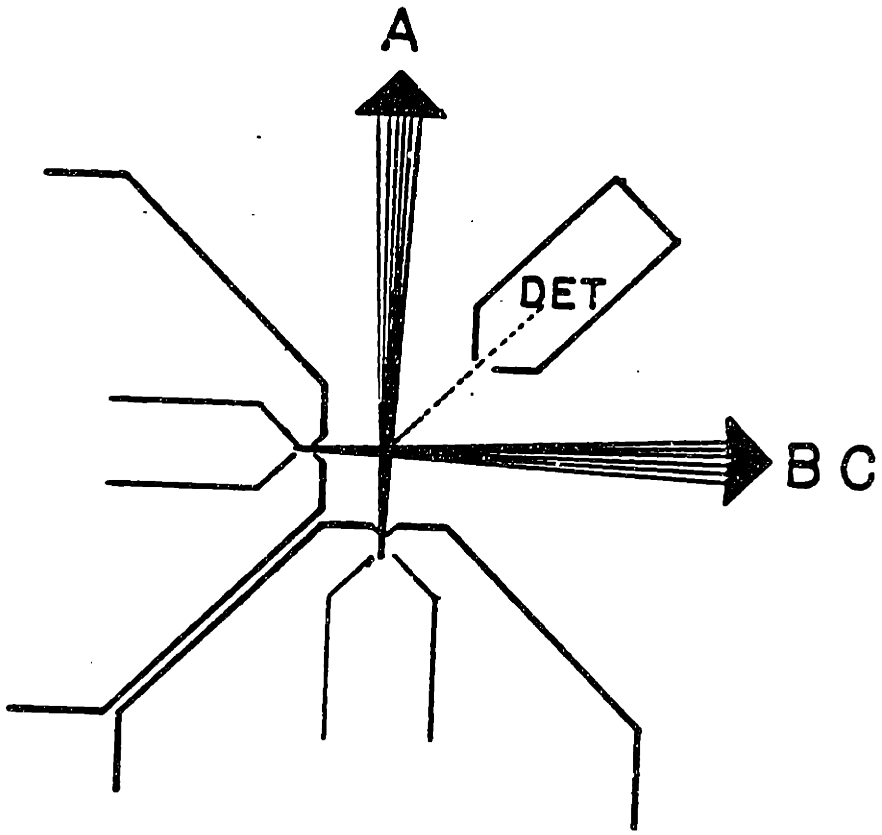

Fig 1-2 - Basic design for a crossed molecular beam apparatus. A well collimated beam of A is crossed by a beam of BC. The AB product is scattered into the low pressure region, and detected by a mass spectrometer (DET).

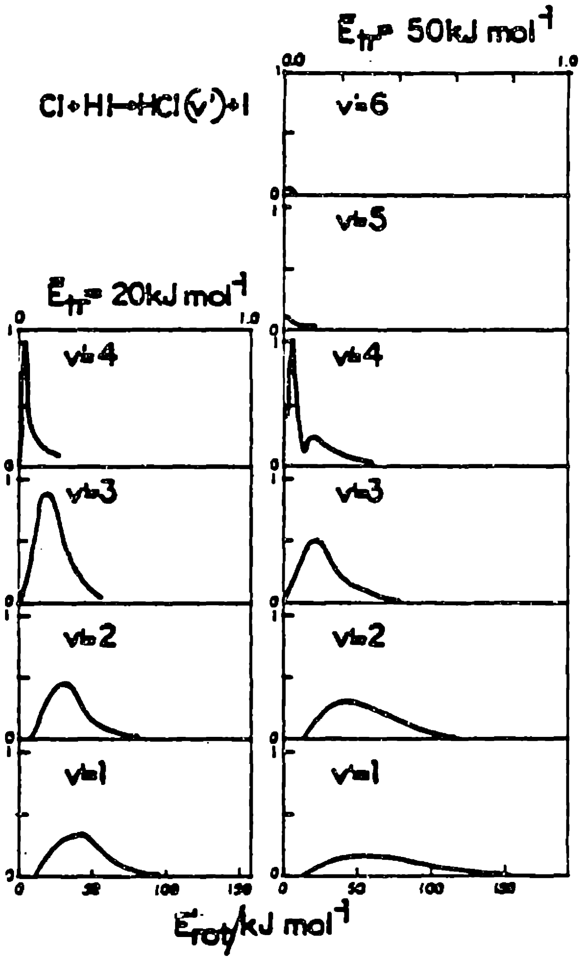

Fig 1-3 - Dependence of product nascent vibrational, and rotational state distributions upon reagents' relative translational energy, for the Cl + HI reaction. Plotted are relative rate constants for the formation of the indicated rotational and vibrational states, vs. rotational energy of HCl for two specific values of average collision energy. At the higher reaction energy (50 kj/mole), even though an increase in number of populated levels is observed, total reaction cross section is found to decrease.

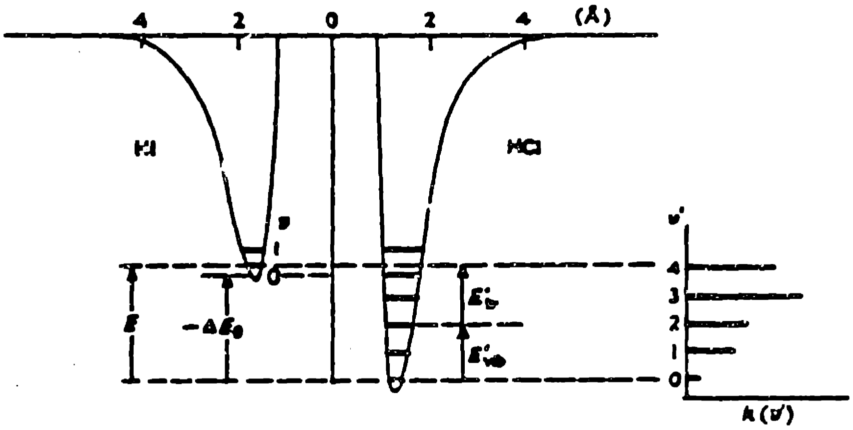
4
2
0
2
4
(Å)
HI
HCl
v
1
0
E
−ΔE₀
E'
E'
v'
4
3
2
1
0
k(v')

Fig 1-4 - Schematic energy level diagram for the Cl + HI reaction, showing the relative rates of formation for HCl (v') product vibrational states (from ref 11).

additional product vibrational and rotational states become accessible, total reaction probability decreases.

The energy level diagrams shown in figures 1-1. or 1-4 are too simplistic to account for the observed product energy partitioning, or the decrease in reaction rate with increase of total reaction energy. A different type of model is necessary in order to explain these phenomena.

Energy level diagrams attempt to represent reactions as one-dimensional systems. However, a three-dimensional method of representation is required to describe a reaction involving three atoms, and more dimensions are needed for larger systems. The simplified one-dimensional picture must be replaced by the use of potential energy surfaces (PES) in modeling reactive systems.

The groundwork for describing reactions as motion of particles on Potential Energy Surfaces (PES) was laid long ago by H. Eyring, M. Polanyi, G.E. Kimball, J.O. Hirschfelder and others.[12] The theoretical basis for these ideas relies on the Born-Openheimer separation of electronic and nuclear motion. Most of the qualitative general questions to be asked had been anticipated by these early pioneers, though it took a long while before experimental and theoretical techniques were developed that allowed pursuit of their ideas.

Fig. 1-5 is a two-dimensional representation of PES's for the collinear A + BC → AB + C reaction.[13] For the purpose of simplicity the figure shows two extreme possibilities i.e. the "early" (a) and the "late" (b), barrier. These two basic examples were thoroughly discussed by Polanyi et al. (1969)[14]. Briefly, in the case of an early barrier, translational energy is expected to be efficient in promoting the reaction and to be effectively converted to product BC vibrational energy. The reverse is true for the late barrier. Here, reagent vibrational energy is expected to

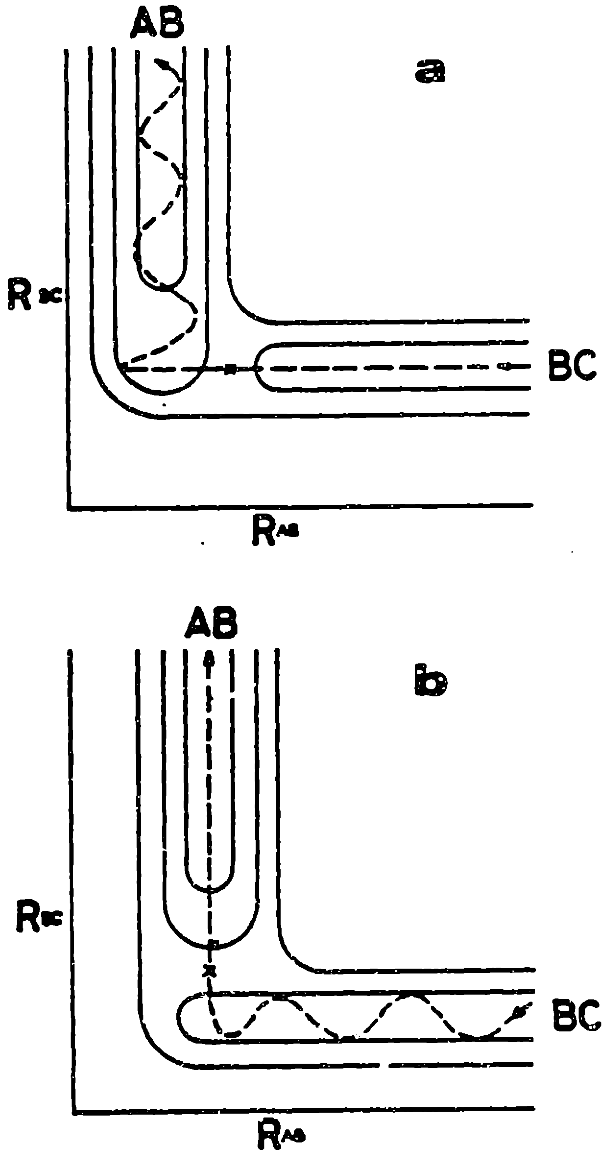

Fig 1-5 - Diagrammatic PES for co-linear A + BC reaction dynamics. (a) early barrier: reagents' translational energy is converted into products' vibrational energy. (b) late barrier: reagents' vibrational energy is converted into products' translational energy (from ref 14).

be more efficient in promoting the reaction and to be converted to product translational energy, yielding vibrationally cold products.

These examples illustrate how the complicated and intricate process of a chemical reaction can be represented by a motion of a simple particle on the PES. When the reagents are well separated, they do not affect each other. In this region, the PES is simply that of the BC molecule and the A atom. The PES along R_{A-B} is a straight line. Motion perpendicular to the A-B coordinate represents vibrational motion of the BC molecule. After the reaction, i.e., at large product separations, the surface corresponds to that of the product molecule AB and the C atom. The reaction occurs as the system rushes up the reagent side past a saddle point and then descends into the product canyon. What primarily governs the course of the reaction is the size, shape and location of this saddle point as illustrated by the two examples.

A typical reaction involves more complex situations, with addition of other degrees of freedom. As many saddle points and local valleys become available there even exist possibilities that the system will move among these for a considerable period of time before finding an exit. The importance of these intermediate states is recognized by identifying a quasimolecule called the transition state. The properties of this quasimolecule, its geometry and the rates at which it is formed and decomposed are the subject of many experimental and theoretical studies.

Molecular beam experiments choose to address such questions by controlling the preparation of the reagents and analyzing final products in great detail. This leads in principle to the most complete microscopic subdivision of the overall rate. Any measurable macroscopic rate can be synthesized from these building blocks.

However the experimental interaction with the system is deliberately remote from the central interaction region, i.e., reagents are prepared prior to their collision, and products are analyzed well after reaction is complete. The intermediate behavior is inferred from the behavior in these asymptotic regions.

Many of the theoretical approaches have concentrated on calculating PES's for reactive collisions, and developing techniques for solving equations of motion. Though great progress has been made in the past few years, the accuracy with which multi-dimensional potentials can be calculated from first principles is still limited. Techniques for calculating reactive processes using PES on the other hand seem to produce results with very good accuracy. A most promising approach appears to be the generation of semi-empirical PES's through the combination of experimental results with *ab-initio* calculations. One such attempt will be discussed in this thesis for the case of methyl iodide. To achieve a successful collaboration between theory and experiment requires experimental data which can be easily related to important features of the PES. To generate such data a new experimental approach is being developed, where the reactive system is interrogated *during* the interaction rather then at the two extremes, before and after the reaction.

Reaction complexes are usually quite transitory, and it has widely been assumed that their direct experimental observation would be impossible. The first indication that experiments of this type could actually be done was the observation by Harris and coworkers of laser induced atomic energy transfer.[15]

A schematic diagram of this process is shown in Fig. 1-6. An excited Sr atom in the $^1P_1$ level cannot transfer its electronic energy in collision to the $^1P_1$ level of Ca because there is an energy defect of 1954 cm^{-1}. When a second laser is

added and the system is irradiated at 497.7 nm, however, fluorescence at 551.3 nm is observed. This emission can only be produced in a simultaneous three body collision between Sr*, Ca and the 497.7 nm photon. A line shape is obtained by scanning the second laser. This line is found to peak at 497.7 nm with a line width of 14 cm^{-1}(FWHM). Similar results have been observed(16) for Eu + Sr + hv — Eu + Sr* (see figure 1-7). These results on inelastic energy transfer suggest that one might be able to photoexcite the transition state of a chemical reaction and thereby gain a basis for spectroscopic study of the transition region. Several experimental studies have now appeared in which reaction complexes have been directly probed:[17-20]

1. Laser induced Penning and associative ionization in crossed alkali metal beams have been observed by Weiner.[17] Two sodium beams are crossed in the field of two dye lasers. The first laser is tuned to the Na D line. The second laser is scanned in wavelength while Na_2 ions are monitored by a mass spectrometer. The reaction studied is

$$Na^* + Na + h\nu \rightarrow Na_2^+ + e^-$$

Na_2^+ ions are observed when the photon energy exceeds the threshold for the reaction. These persist up to 1000 cm^{-1} above threshold. The spectrum displays structure consistent with vibrational spacings in Na_2^+.

2. Emission from a reaction complex has been observed by Polanyi and coworkers.[18,19] In their experiment a beam of sodium dimers was crossed by a beam of F atoms. The reaction:

$$F + Na_2 \rightarrow [Na\ Na\ F]^\dagger \rightarrow NaF + Na^*$$

was studied by observing emission. A reproduction of this spectrum is shown in Fig. 1-8. The emission in the far wings of the Na D line was attributed to the

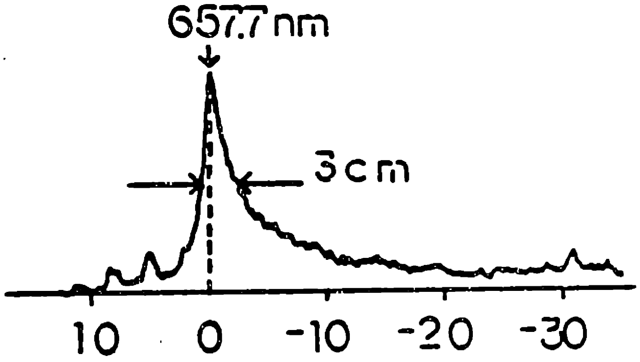

Fig. 1-7 - Experimental line shape from ref. 16 for laser induced energy transfer to Sr ($^1D_2$) level from Eu ($^8P_{9/2}$) level:

$$\mathrm{Eu}\ (^8P_{9/2}) + \mathrm{Sr} + h\nu\ (\lambda = 658\ \mathrm{nm}) \longrightarrow \mathrm{Eu}\ (^8S_{9/2}) + \mathrm{Sr}\ (^1D_2)$$

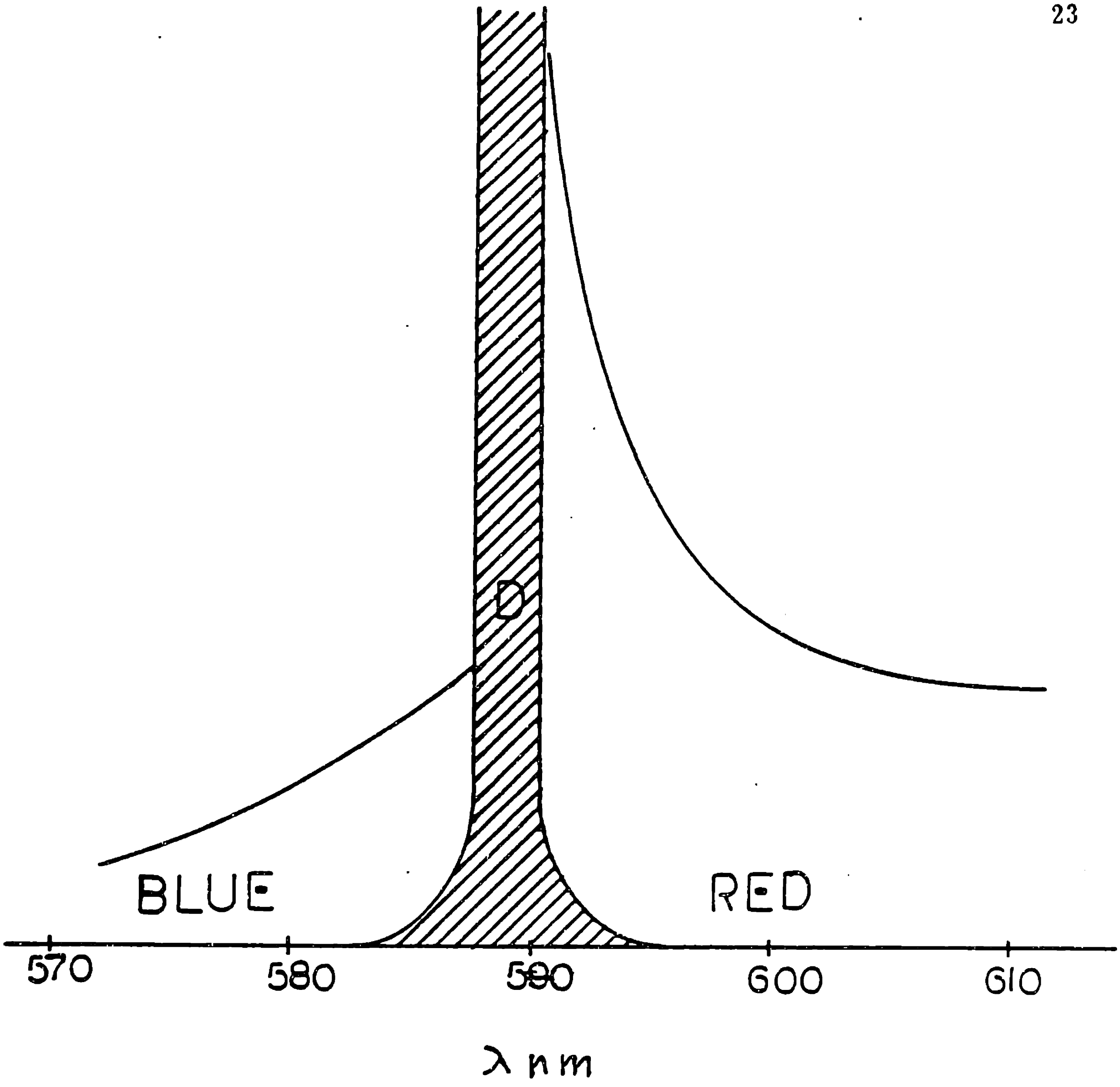

Fig 1-8 - Wing emission as observed by P. Arrowsmith et. al. from the reaction $F + Na_2 \longrightarrow FNa + Na^*$. (D corresponds to the sodium D line.)

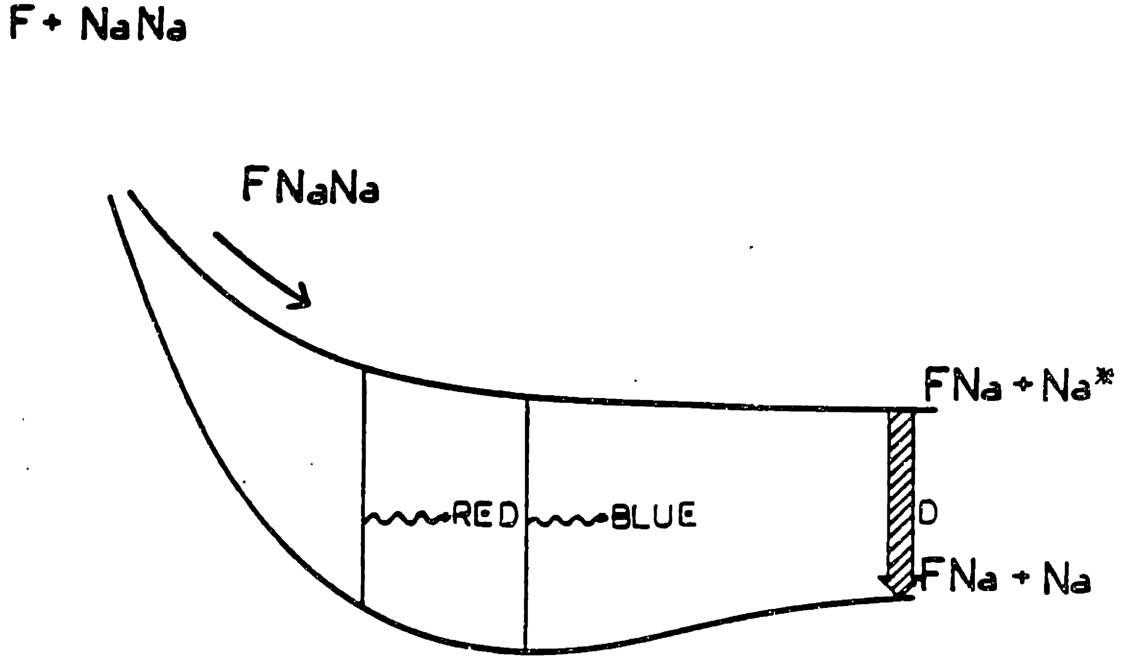
F + NaNa
FNaNa
FNa + Na*
RED
BLUE
D
FNa + Na

Fig 1-9 - Schematic one dimensional diagram showing the origin of the wing emission in Fig 1-8.

reaction complex FNaNa $^{++}$. Fig. 1-9. is a schematic one-dimensional representation of the experiment.

These results were used to extract qualitative information about the PES's involved.

3. Excitation of a reaction complex to open a new chemiluminescent reaction was studied by Brooks, Curl and coworkers[20] for the reaction

$$K + NaCl + h\nu \rightarrow KCl + Na^*$$

Fig. 1-10. gives a schematic representation for this experiment.

Here the reaction complex $[K\ NaCl]^{\ddagger}$ absorbs a laser photon which causes it to be transfered onto a new PES. On the new surface, the complex dissociates to yield KCl + Na*, and emission from Na* is detected. A spectrum is obtained by scanning the excitation laser while recording Na* emission VS. laser wavelength.

These pioneering experiments are very encouraging since they demonstrate the feasibility of direct observation of molecular species in a transitory state. At the same time many difficulties are involved in the interpretation of the observations.

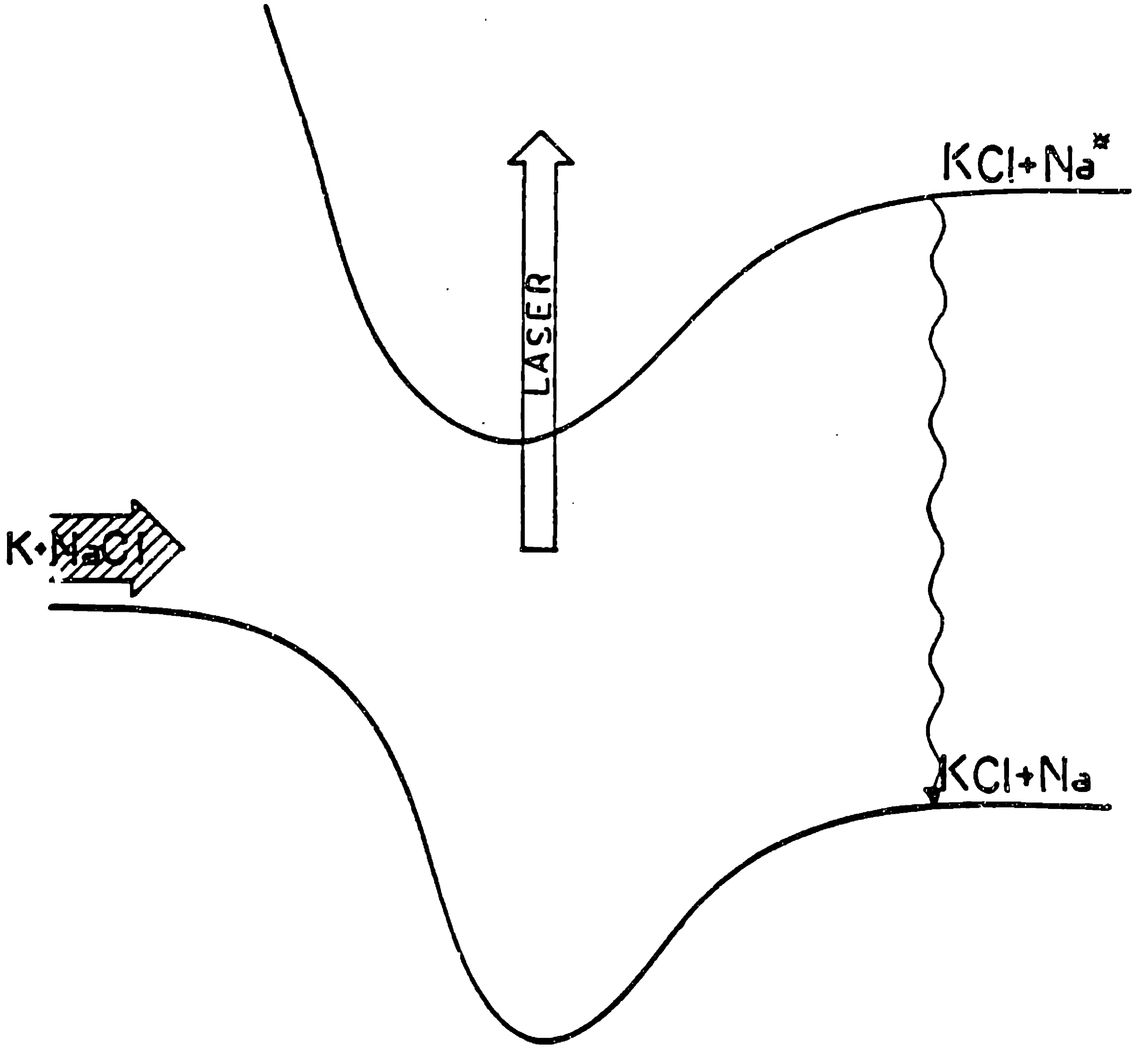
KCl+Na*
LASER
K+NaCl
KCl+Na

Fig 1-10 - Laser induced dissociation for the reaction K + NaCl + H ⟶ KCl + Na*. The triatomic KNaCl absorbs a photon. The subsequent reaction proceeds on the excited surface to yield an excited state sodium atom.

CHAPTER 2.

HALF COLLISION SYSTEMS, PHOTODISSOCIATING SYSTEMS

Spectroscopy of the transition state marks the beginning of a new experimental approach to the study of molecular dynamics. Attention is turned away from rate measurements, to focus instead on the properties of the reacting system itself for the purpose of gathering information on reactive trajectories (or their quantum analogs). Ideally, data obtained from such experiments describe bond lengths and their rate of change through the reaction process. (See Fig. 2-1.) The heavy line in figure 2-1 represents the most likely reactive trajectory at a given reaction energy. It describes the motion of the nuclei during the reaction. One must remember, however, that the whole process normally lasts less than a single psec. The variations in bond lengths and angles within the "reactive" region are extremely small. It would seem, therefore, that only by using spectroscopic methods could one hope to obtain a sufficient degree of detail. The spectroscopic experiments described in the previous section represent important steps toward the realization of this goal, but fall short of providing enough detail to allow complete analysis of the data. Typically, the spectra obtained in experiments such as described in references 17-20 exhibit very little if any resolvable structure, a fact which most experimentalists associate with the short lifetime of the reaction complex. In some cases the width of the described broad spectral features was even used to extract lifetimes of transition states.[21] The commonplace association of broad, structureless spectra with short lifetimes contains an element of truth but it also carries serious misconceptions which have seriously hampered

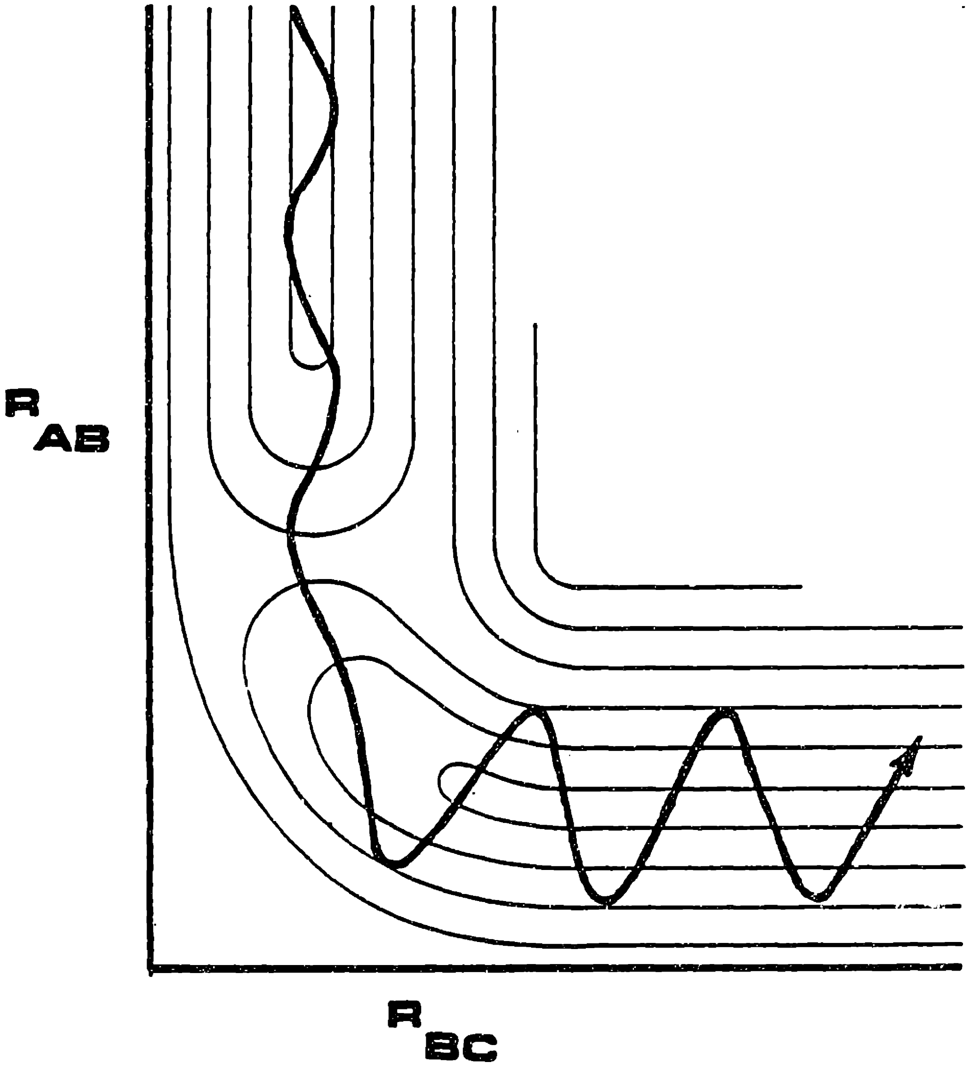

Fig 2-1 - Two dimensional representation for the reaction A + BC ⟶ AB + C. The heavy line indicates the most probable reactive trajectory.

experiments in this field. The connection led people to expect spectral line widths always to be lifetime dominated, and therefore in some cases no care was taken to minimize spreads. Most experiments were then conducted on samples at room temperatures.

A closer examination of these experiments reveals that by careful design it is possible to produce spectra with sharp and resolvable structure without violating the uncertainty principle even when the lifetimes are very short. This observation turns out to be extremely useful to the detailed understanding of the reactive process. Fig. 2.2. shows a possible schematic suitable for an experiment similar to the K + NaCl reaction. Two important changes have been made: 1) The initial energy spread of the reagents has been reduced to a minimum, and 2) The laser is tuned to induce free to bound rather than free to free transitions. The line width in such an experiment is determined by the energy spread of the incoming reagents regardless of the intrinsic time scale of the process.

The experimental set up for such a measurement might consist of two crossed molecular beams. As the A atom approaches the BC molecule the triatomic ABC is formed. It will exist for a few vibrational periods. A laser excites this molecule into another electronic state from which total fluorescence can be observed. A spectrum could be obtained as the detected fluoresence VS. laser wavelength. Whether this type of experiment could be used to obtain information about the reaction depends very much on the type of spectrum that can be obtained. If the excited state is bound it should be possible to obtain a discrete excitation spectrum, showing vibrational progressions, provided that the energy spread for the reagents is substantially smaller than the excited state vibrational spacings. This requirement can be satisfied through the use of supersonic molecular beams to cool

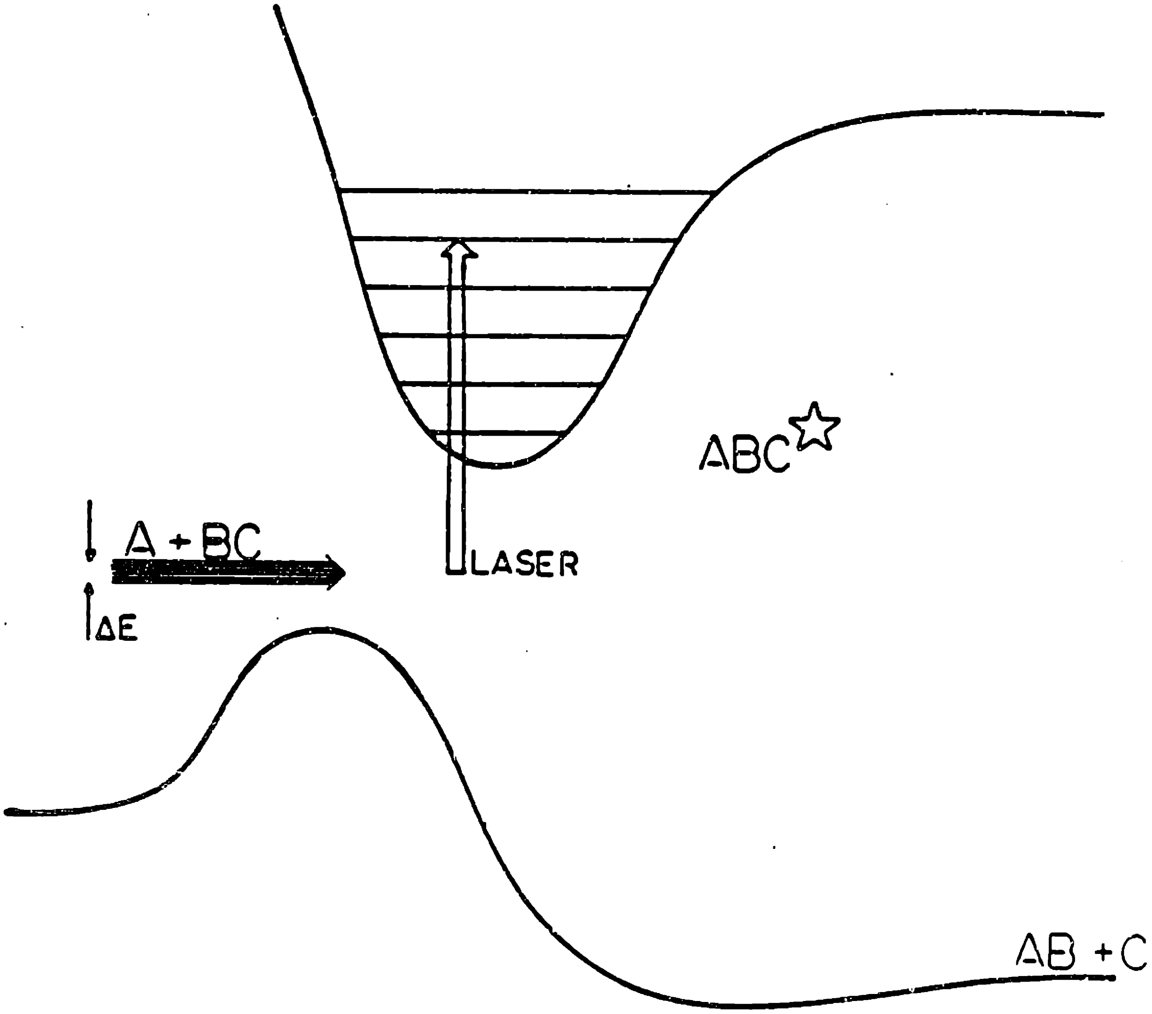

Fig 2-2 - Spectroscopic study of the transition state for the reaction A + BC ⟶ AB + C. The ABC ground state surface is repulsive, while the ABC* state is bound. The laser is tuned over ABC* vibrational levels to produce an excitation spectrum.

internal and translational degrees of freedom. A spectrum of this type has not yet been observed, but there is no fundamental barrier to such a measurement. Such a spectrum could be used to study the paths of reaction. Since the spectrum would consist of a Franck-Condon progression, its observed intensities reflect the geometry and momentum of the reaction complex in the sampled region. When the electronically excited state used to produce the emission is sufficiently well-understood spectroscopically, it provides a "picture" of the density of trajectories with excited state vibrational eigenstates serving as markers for coordinates and momenta.

The difficulty in interpreting such a spectrum stems from the fact that, under normal experimental conditions, it is impossible to select a productive sub-sample of all possible trajectories. This would amount to controlling impact parameters. The spectrum will thus contain features from a large distribution of trajectories, most of which are uninteresting because they are not reactive. This added complication makes the interpretation of spectra very difficult, but the idea of such a measurement deserves further exploration.

It is possible to by-pass the above problems by turning attention away from bimolecular reactions to focus on unimolecular ones, i.e. study only half collision processes. The simplest and most convenient half-collision systems are photodissociation reactions, for which information on the PES can be obtained. Once a PES has been characterized, it can be used to predict other reaction processes which could take place on it. For example, the $C^{18}O + {}^{16}O^* \longrightarrow C^{16}O + {}^{18}O^*$ exchange reaction occurring on the CO_2 excited state surface can be inferred by observing the photodissociation of CO_2 on that same surface. In this fashion information about the surface itself is obtained, this information then permits the prediction of the oxygen exchange process. Such an approach provides an alternative to the complex process of detailing the individual paths in a reactive system. It suggests, instead, a process by which only a small and well defined subset of trajectories is generated and studied. If chosen with care, the trajectories should sample those PES regions which provide the greatest insight into the detail of a given PES.

The study of half collisions offers a distinct advantage over that of bimolecular collisions, in that it allows great control over initial conditions. They can in fact be as well defined as the uncertainty principle allows and there are practical means for achieving such definition. The system can be prepared at an intermediate stage of the reaction and studied as the reaction fragments separate. Since the important interactions between molecular reagents take place when they are at close proximity, it is obviously desirable to initiate the reaction at such a point on the PES in order to derive the most relevant information concerning the surface under study.

In some cases, the half collision will not sample as much of the surface as a full bimolecular reaction. For example, the region where the A-B bond length in figure 2-3 is large would not be sampled by the half collision. What at first seems to be a disadvantage is in fact one of the advantages of the half collision systems. The fact that only certain regions of the surface can be sampled allows for the isolation of effects on the reaction from this part of the surface.

Photodissociation reactions are particularly attractive half collision systems, both from an experimental point of view and because of the simplicity with which the data can be analyzed. The following is a short description of the photodissociation process. A more complete treatment is given in the next chapter.

In photodissociation a molecule, typically in its electronic and vibrational

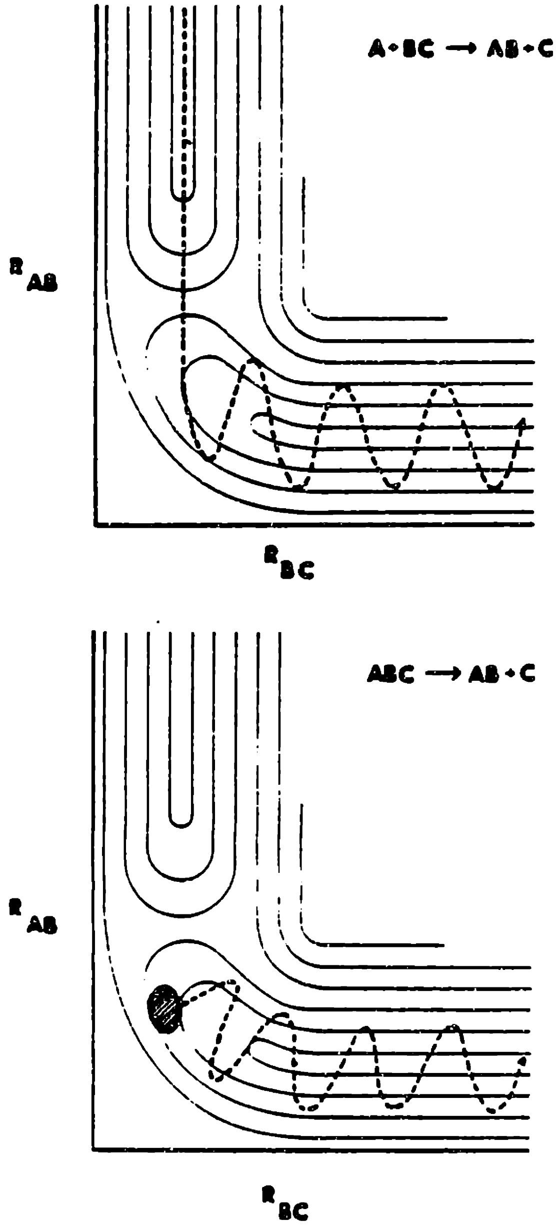
A+BC → AB+C
R_AB
R_BC
ABC → AB+C
R_AB
R_BC

Fig 2-3 - Trajectories for the bimolecular reaction A + BC ⟶ AB + C and the photodissociation reaction ABC + hν ⟶ AB + C.

ground states, absorbs a photon. As a result, a rapid change in the electronic structure takes place, while the more sluggish nuclei remain essentially frozen. If, as is commonly done, we neglect any variation of the transition moment with nuclear configuration, what has taken place in essence is a transfer of the ground state vibrational wave function to a new electronic surface (see Fig. 2-4). Since this wave function is not an eigenstate of the excited state Hamiltonian, it becomes a moving wave packet (a dephasing process). The motion of this wave packet on the excited state PES constitutes the reaction of interest. Thus the simple process of photon absorption can generate half collision systems with extremely convenient initial conditions. The reaction is initiated from a known and localized wave packet. When it is the vibrationless wave function that is being transferred to the excited state, reaction proceeds from a wave function that is initially gaussian in shape with average momentum, $\langle P \rangle$ equal to zero. The average bond lengths $\langle Q_n \rangle = Q_{n_{Re}}$ are short and well known. These conditions assure that the system will sample the strong interaction region. Spreads in momenta and coordinate are as small as possible ($\Delta Q \Delta P = h$) and the spread in energy is limited by the band width of the excitation source.

From an experimental point of view it is very easy to generate these conditions by using a simple experimental set up. High powered lasers can prepare large quantities (10^{14}) of reacting molecules for study within a short period of time (10 nsec). The simplicity with which these systems can be prepared allows experimental conditions to be reproduced by different research groups and different probes of the same system can be conducted. Fig. 2-5 summarizes some of the experimental probes commonly used. Every probe is most sensitive to a certain part of the reaction and can be used to learn about the corresponding parts of the PES.

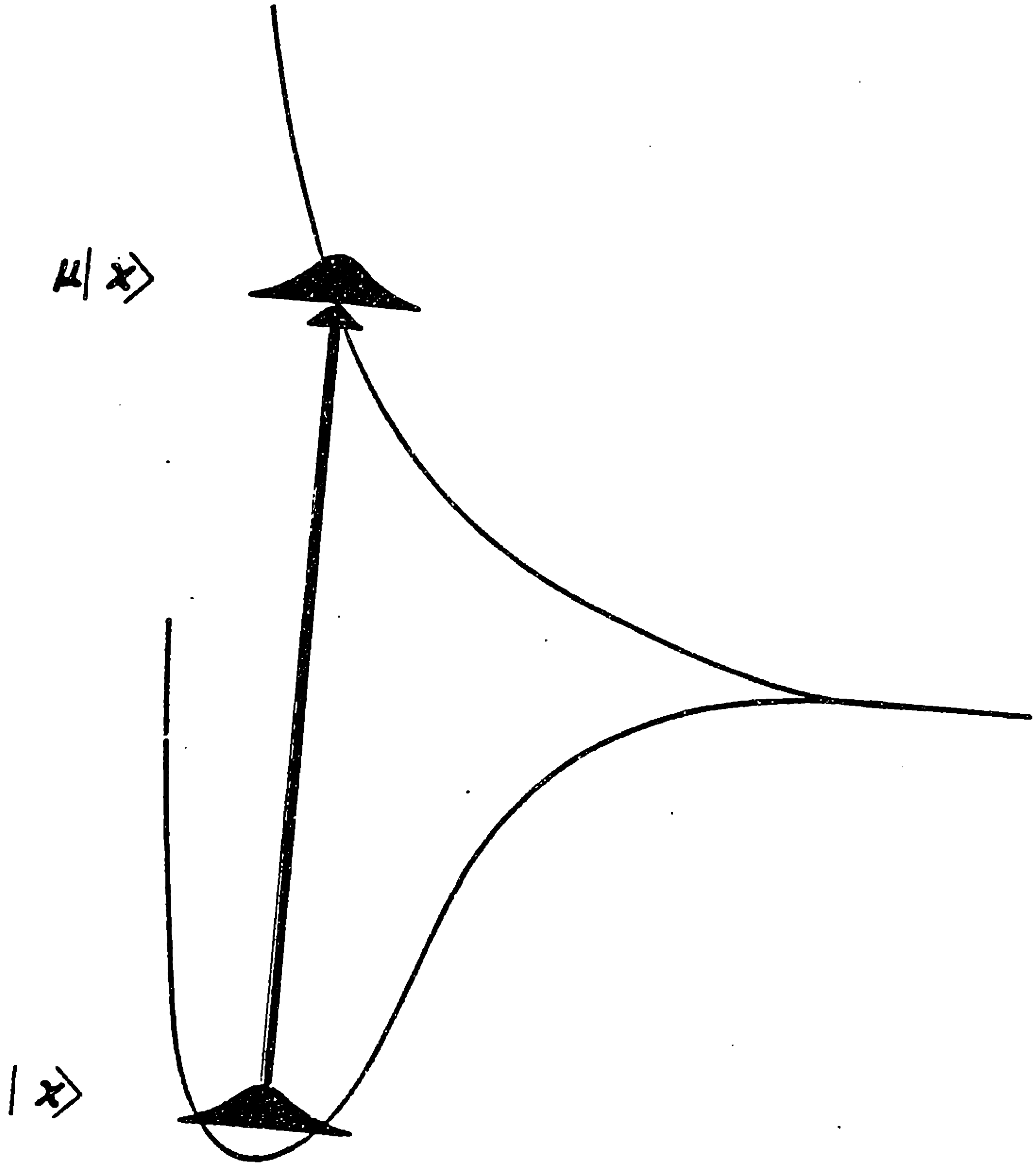
$\mu|\chi\rangle$
$|\chi\rangle$

Fig 2-4 - The photoabsorption process prepares the ground state vibrational wave function on the excited state surface.

1. Final Product Spectroscopic Information.

For most small photodissociating systems the final product spectroscopic properties are known. Vibrational and rotational constants of the final products can be used to construct the potential at large internulcear separations. Fig. 2-6 is a schematic representation of the photodissociation ABC + hν $\longrightarrow$AB + C or A + BC. Two sections through the potential are shown, one at large A-B bond length and one at large B-C bond length. The former is a potential curve for the BC diatomic molecule whereas the later corresponds to the AB diatomic potential curve. The equilibrium positions and shapes of these potentials are obtained from the spectroscopy of the AB and BC diatomic molecules.

2. Final Product Analysis

This method of investigation is widely used and has been applied to a variety of molecular systems (ref. 22 is a good review article on the subject). Many experimental techniques for probing final products have been developed. With the technological advances in intense light sources, the field of photofragment spectroscopy has been growing rapidly in the last few years.

The most commonly used method is one in which a uv light source, usually a pulsed laser, is used to photodissociate a molecule. The fragments are then probed by a second laser delayed a few nsec from the first. A laser-induced-fluorescence (LIF) spectrum of the nascent products is obtained by scanning the probe laser and detecting total fluorescence. This LIF spectrum is used to obtain the vibrational and rotational energy contents of the fragment. The LIF method is mostly limited

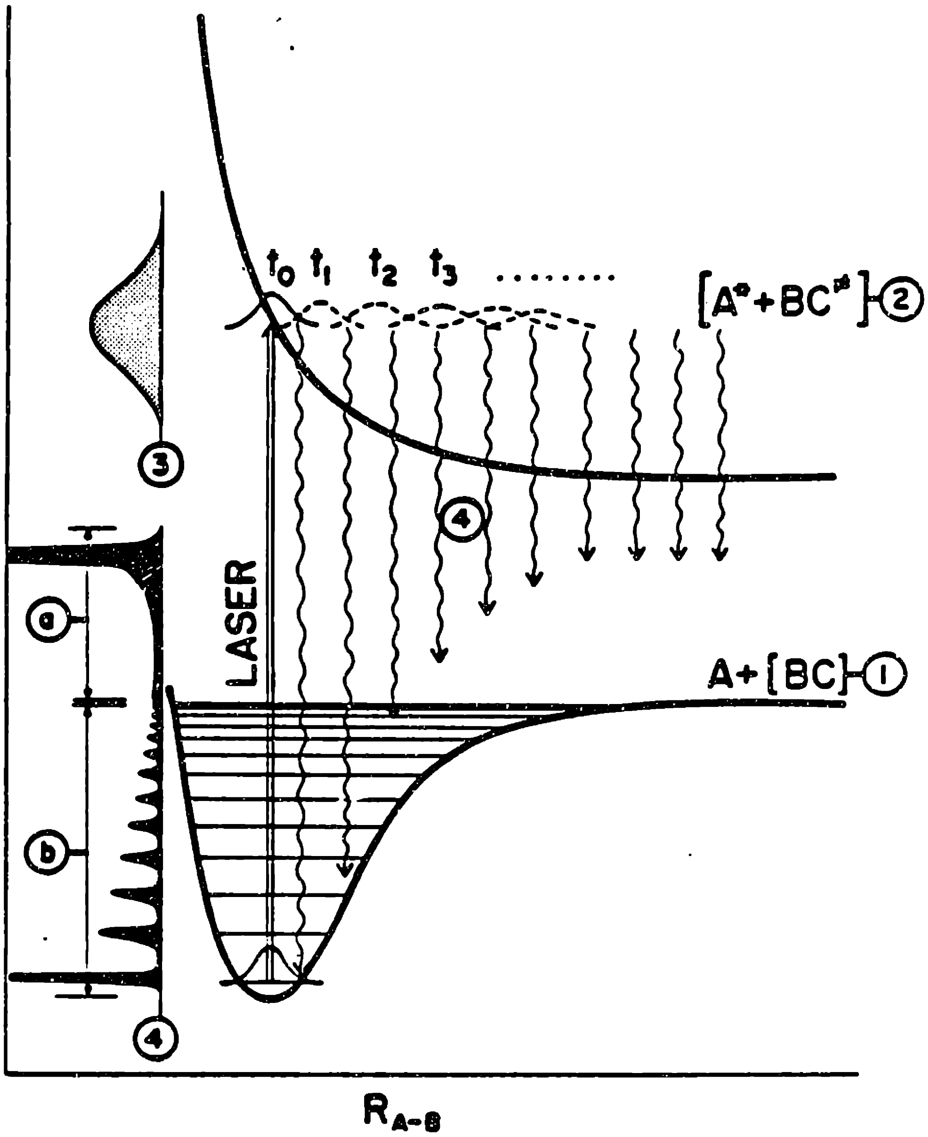

Fig 2-5 - A photodissociation experiment. The laser transfers the ground state wave function to the repulsive excited state where it evolves (dashed wave-packets t_1, t_2, t_3....) into A* + BC . Numbers indicate accessible experimental probes: (1) Equilibrium geometry and spectroscopic constants of the final BC product. (2) Internal state-angular-and velocity distributions of final products. (3) Absorption (photodissociation) spectrum. (4) Emission spectrum, (4a) wing emission, (4b) discrete emission.

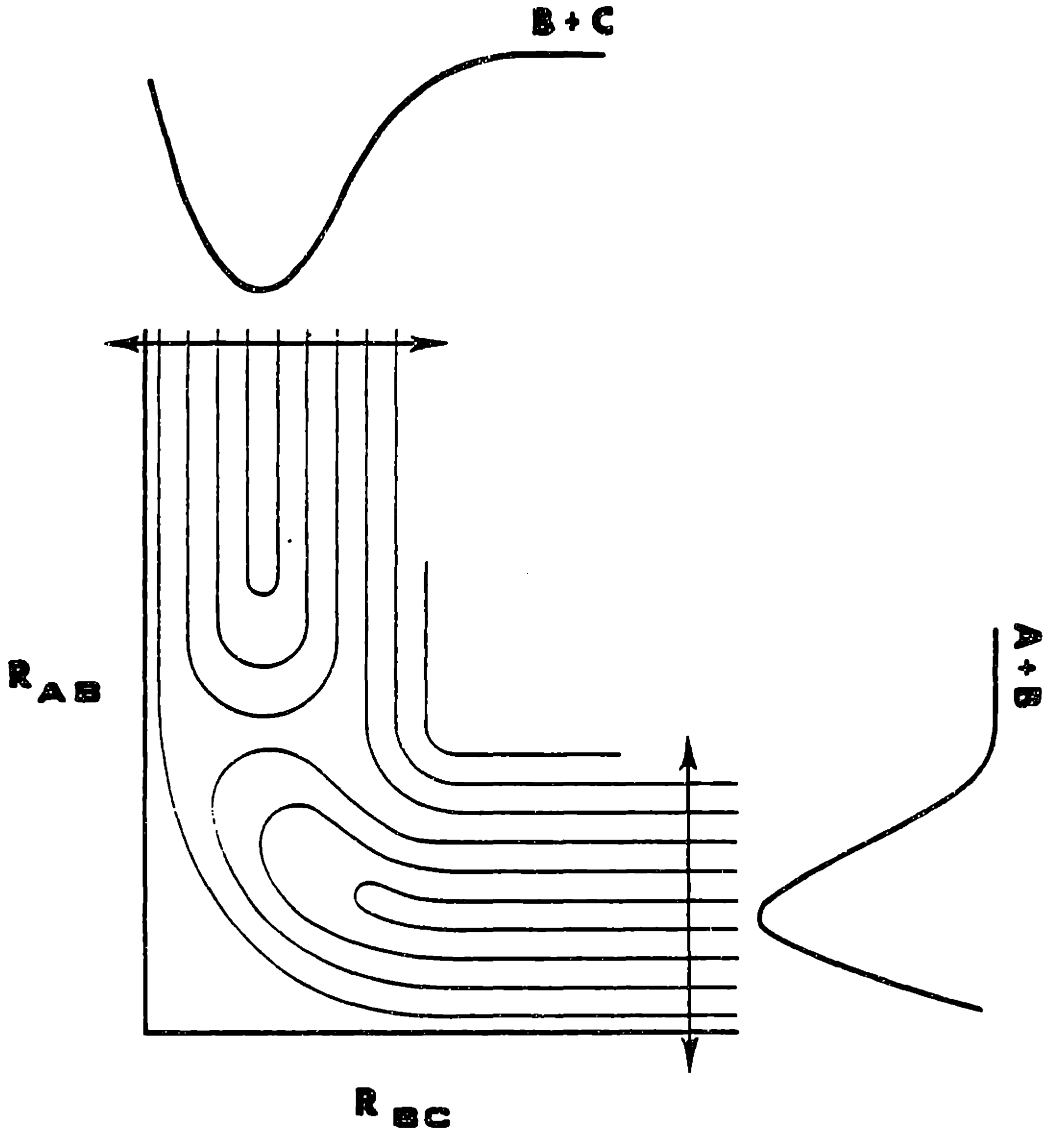
B + C
R_{AB}
A + B
R_{BC}

Fig 2-6 - Sections through the ABC PES at large R_{A-B} and R_{B-C} showing potential curves for the diatomics.

to small molecular fragments for which spectroscopic information is readily available. The ability to extract information about populations in a given level relies on a priori knowledge of transition moments, Franck-Condon factors, radiative lifetimes etc. These conditions have made a few fragments such as OH, CN, NO favorites with researchers in the field. Photofragmentation studies have provided information about the photodissociation of XCN, where X = H[23], Br[24], Cl[25], I[26], as well as C_2N_2[27], H_2O[28], H_2O_2[29], N_2O[30] etc.

Multiphoton ionization is currently becoming quite popular for studying internal-state distributions because of the added sensitivity gained through detecting ions rather than photons.

The study of product velocity and angular distributions requires somewhat more complicated instrumentation. A well collimated molecular beam is crossed by a pulsed polarized uv laser, which photodissociates the molecules in the beam. The product is scattered into the main chamber and can be detected with a mass spectrometer. Time of flight spectra of products provide information about their velocity distributions. For small products with large vibrational constants it may be possible to obtain the vibrational distribution from the same spectrum. To measure product angular distributions spectra of product flux at a given lab scattering angle VS. laser polarization angle are recorded. This type of information can be very useful for band assignment and for estimation of dissociation lifetimes, with rotation serving as an internal clock.

In general, final product distribution information is sensitive to the overall reaction path. No region of the PES can be identified a priori to be more important than another in determining final product distributions.

3. Absorption Spectrum.

Absorption spectra are available for most molecules. At first glance it is not obvious that the absorption spectrum contains information about the dynamic process. The next chapter reviews a theoretical formalism connecting the absorption spectrum with the dynamics of the reaction process. At this point it suffices to mention that, for most photodissociating molecules, the absorption spectrum is a probe for only a small part of the PES. This is particularly true for systems with broad and structureless spectra. The width of the spectrum in that case provides an indication of how fast the molecule leaves the initial Franck-Condon region. The broader the absorption spectrum, the faster the reaction. In some photodissociation cases, faint structure does appear in the spectrum. The analysis of such structure, when possible, can prove quite useful towards understanding the events taking place on the excited state surface. Structure in the frequency domain generally indicates periodic nuclear motion at that frequency during the reaction process.

Whenever absorption occurs into more than one surface in the same frequency region some spectroscopic techniques such as magnetic dichroism or polarization methods can be used to identify the surface involved and to separate overlapping bands, as well as to aid in band assignment.

4. Photo Emission (Raman) Spectrum.

Two general spectral regions can be distinguished in the emission spectrum marked 4a and 4b in figure 2-5. When one of the fragments is produced in an electronically excited state, capable of emitting at a fast rate, wing emission will be observed (4a in figure 2-5). For simplicity this fragment has been chosen to be an atom. Such a spectrum has been observed in the dissociation of NaI[19] where the excited atom is Na(^{3}P). This part of the spectrum is due to emission by the excited atom while the two fragments are still close enough for there to be appreciable interactions between them. If one assumes vertical Franck-Condon transitions, the emission will be blue- or red-shifted relative to the atomic transition, depending on whether the difference potential of the two surfaces is larger or smaller than their asymptotic separation. Wing emission develops at the latest stages of the dissociation, with transitions occuring mainly into the continuum of product translational states. This part of the spectrum is broad and relatively featureless. In many cases the spectral line shape is dominated by the change in transition moment with internuclear separation, rather than by Franck-Condon factors.

The higher energy end of the same spectrum (4b in Fig. 2-5) shows transitions into the bound part of the lower electronic surface, with distinct vibrational progressions. This region of the spectrum contains the most valuable information since it represents transitions into well characterized vibrational eigenstates. These provide the desired geometrical and temporal information.

Normally one does not think of a dissociating molecule as an emitter, because dissociation usually occurs orders of magnitude faster than emission. This means that photon yields are very low (10^{-5} - 10^{-8}). However, that small but finite photon yield and its spectral characteristics prove to be very informative about dynamic processes on both upper and lower energy surfaces. As the molecule comes apart, it sweeps through infinite displacements in molecular configuration, thus developing Franck-Condon overlap with highly excited vibrational levels of the ground state. This is reflected in long progressions in the emission spectrum. Moreover, the vibrational levels present in the spectrum are of special and interesting character. Because the reaction on the upper surface involves an extreme deformation of one of the bonds, the levels most likely to be observed in the spectrum will be those having a local mode character in the dissociation coordinate. These levels have been termed "vibrational hot spots".[31] The unique ability of a dissociating molecule to indicate the energies of ground state vibrational levels through its emission spectrum is matched by the opportunity it provides to probe dynamic processes on the excited state PES. The molecule leaves a "photograph" of its motion on the upper surface in the intensity pattern of the lines observed in the emission spectrum.

The following chapter provides the theoretical framework needed to convert the spectral information into information about the photodissociation reaction.

CHAPTER 3.

FROM SPECTRUM TO REACTION

The previous chapters dealt with a variety of experimental methods used to study molecular dynamics. Apart from technical detail, the choice of one experimental technique over another should take into account the relation between the data and the question at hand. Such considerations lead to the conclusions (drawn in the previous chapter) that half collision systems provide an excellent avenue to direct and detailed information about reactions and the forces involved in such processes.

The following is a brief outline indicating the relationship between spectroscopic observables and the dynamics. Most of the connections are made via an implicit time dependent formulation of the absorption and emission process as developed by E.J. Heller.[32-35]

Spectroscopy has been for many decades a powerful tool in the study of molecular structure. Detailed rotational and vibrational spectroscopic information has been used to infer geometries, force constants, etc. A very simple formalism has been developed to allow efficient extraction of such information from the spectroscopic data. Here, the word "structure" relates to static situations. Bond lengths and angles in this sense are meaningful only for stationary states. The molecular systems with which this thesis is concerned are those which undergo very rapid structural changes. I.e., a complete transformation of one molecular species into another is typically completed within a few psec or less. It seems clear therefore that the traditional spectroscopic approach, involving stationary states, would not be appropriate for such dynamic systems. A new formulation is necessary, one which relates spectra obtained in frequency space to dynamics occuring in the time domain. At the same time, the formulation should provide a simple and straightforward way to obtaining properties of the static PES. Heller's time dependent picture reveals a very intuitive connection between the spectrum and the dynamic process, such that simple inspection of the data often provides quite informative qualitative information.

It is usual in discussions of molecular electronic transitions brought about by absorption or emission of a photon to start with time dependent concepts embodied in the Born-Oppenheimer approximation. In that picture, the light electrons move extremely rapidly, while the sluggish nuclei are slow to adjust to new electronic configurations. For most molecular systems one finds that when the electrons have changed their configurations, the nuclei find themselves displaced from their new equilibrium configurations. Hence they experience forces. Most traditional discussions of electronic transitions start out with this kind of dynamic language. At this point, however, the time domain is forsaken. We (and the nuclei) are left in anticipation while the theoretical interpretation of the spectrum proceeds in terms of Franck-Condon overlaps between the initial stationary nuclear wave-function and the vibrational eigenstates of the new potential energy surface. Classical spectroscopists have always opted to obtain and interpret results in the frequency domain. The explicit motion of the nuclei in time is not discussed.

The Franck-Condon idea of vertical transitions implies a very important and potentially powerful consequence. At a naive level, it suggests that the electronic transition "prepares" the ground state vibrational wave-function on the excited state potential energy surface. One might then expect temporal development of that wave-function, since it is not an eigenstate of the excited state Hamiltonian. I.e., it would become a moving wave packet (see Fig. 3-1). The usual treatment of spectroscopic transitions does not pursue these time-dependent ideas, however. Instead, absorption strengths are expressed in terms of matrix elements between the initial and final stationary states of a transition moment.

Interpretation of a spectrum in the time independent formalism requires knowledge of all stationary states involved. These could be determined by solving the Schrodinger equation:

$$H\phi_n = E\phi_n$$

where H is the excited state or ground state nuclear Hamiltonian. The spectrum at infinite resolution is given by:

$$\text{III.1} \qquad \mathcal{E}'_{(\omega)} = C\omega \sum_n f_n \, \delta(\omega - \omega_n)$$

where c is a constant; f_n is the square of a transition moment matrix element:

$$f_n = |\langle \phi^g_{e\ell} \, \chi^g_o | \mu | \phi^e_{e\ell} \, \chi^e_n \rangle|^2$$

$|\chi^g_o\rangle$ is the initial nuclear wave-function, and $|\chi^e_n\rangle$ is one of the excited sate nuclear eigenstates. A true spectrum can than be obtained by convoluting the infinite resolution spectrum $\hat{\mathcal{E}}'_{(\omega)}$ with a finite width function $W_{(\omega-\omega')}$, which could be either instrument or life-time limited.

$$\text{III.2} \qquad \mathcal{E}_{(\omega)} = \int d\omega' \, W(\omega - \omega') \, \mathcal{E}'(\omega')$$

This method is most suitable for small systems with bound excited states where it is reasonable to calculate the required $|\chi^e_n\rangle$ ś. For systems with large state densities, calculation of enough $|\chi^e_n\rangle$ ś becomes overwhelming. Moreover, for most realistic systems individual eigenstates are not spectroscopically observable.

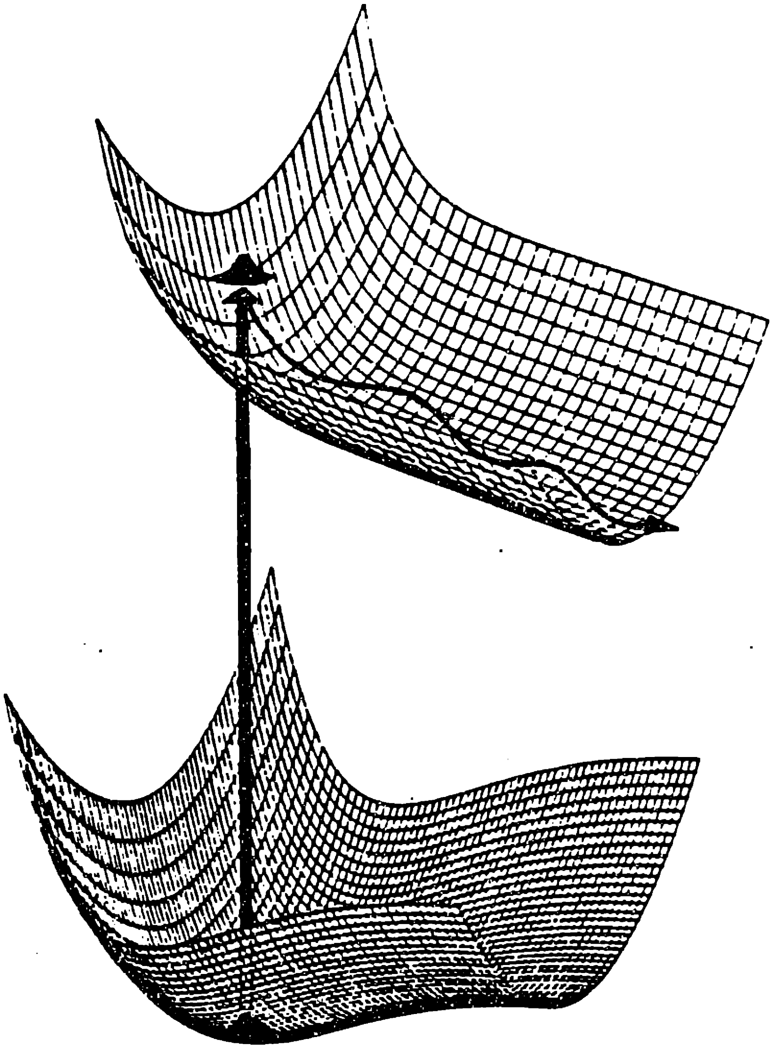

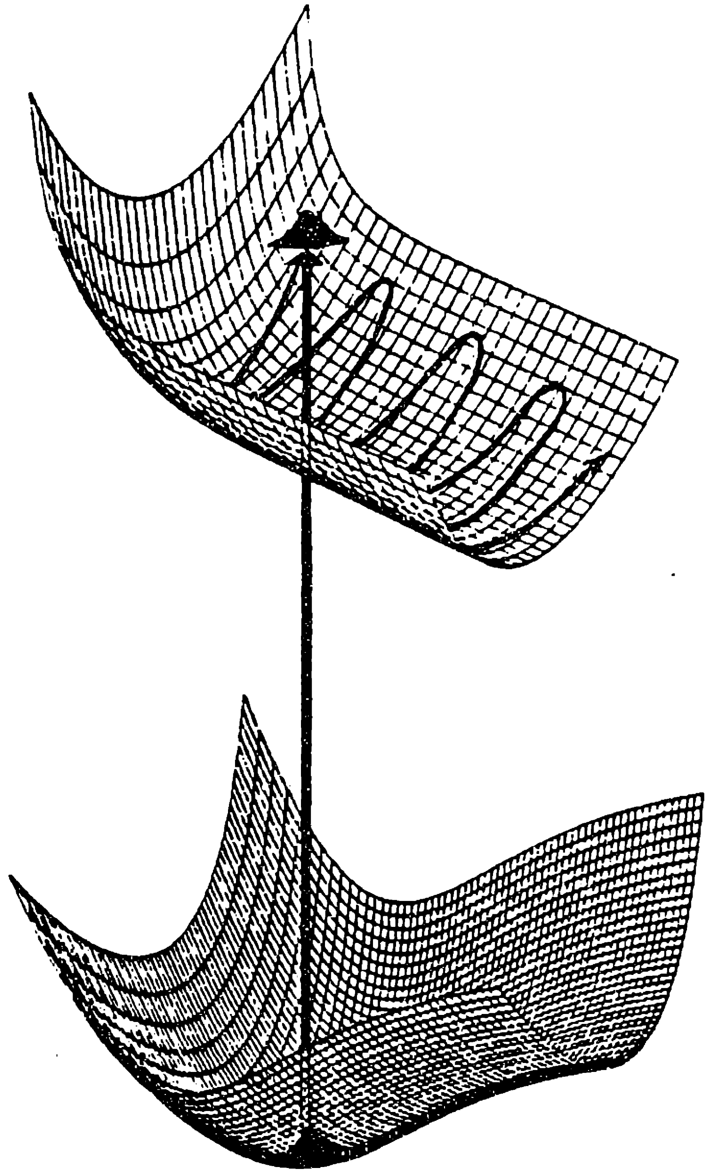

Fig. 3-1 - Absorption of a photon prepares a wave packet on the excited state surface. The wave-packet then proceeds to follow the path of steepest descent.

As a result, it is necessary to resort to drastic approximations which often lead to loss of valuable information. At the same time massive amounts of approximate information is generated in a form which can be quite difficult to use. This is all the more true for repulsive potentials where the vibrational states form a continuum. For these systems, the pertinent questions must be dynamic in nature. Because of the short times associated with dissociative systems they normally do not require a knowledge of the complete set of eigenfunctions to understand the reaction, or to extract the maximum possible information from the absorption spectrum. The fact that the system decays in a very short time requires that the absorption spectrum be broad. A sort of converse is also true: when a spectrum is structureless, it contains information only about short times, thus we expect an absorption spectrum for a photodissociating system to be intrinsically broad. $W(\omega)$ has a corresponding fourier transform:

III.3 $$W(t) = \frac{1}{2}\pi \int_{-\infty}^{\infty} e^{i\omega t}\, W(\omega)\, dt$$

For a $W(\omega)$ having a spread $\Delta\omega$ in frequency, there is a corresponding spread in time Δt, such that $\Delta\omega\Delta t > 1$, suggesting that for a spectrum with features resolvable to $\Delta\omega$, dynamics need to be followed for a period of time on the order of Δt only. In other words, the information in such a spectrum relates to dynamics on time scales on the order of Δt or less. Solving the time independent Schrodinger equation is equivalent to following dynamics for infinite time. Hence it corresponds to a serious "overkill" for intrinsically short-time systems.

To describe the photodissociation cross-section spectrum one may, therefore, return to the idea of vertical transitions, while maintaining a time-dependent picture, and follow the evolving wave packet for Δt.

The time independent expression for (eq. III.2) can be reformulated as the Fourier transform of a time correlation function:

III.4 $$\mathcal{E}_{(\omega)} = \omega \int_{-\infty}^{\infty} e^{i\omega t} \langle\phi|\phi_{(t)}\rangle \, dt$$

where c is a constant

$\phi = \mu|\chi\rangle$ the transition moment μ multiplying the initial vibrational eigenstate $|\chi\rangle$

$\phi(t) = e^{iH^{ex} t/\hbar} |\phi\rangle$ is a moving wave packet evolving out of $|\phi\rangle$ on the new potential by the excited state nuclear Hamiltonian, H^{ex}.

This equation is fully equivalent to Eq. III.2. It introduces no new approximations. The correlation function $\langle\phi|\phi(t)\rangle$ comes from the Franck-Condon part of the equation. In this case it has become an overlap of a stationary state $\langle\phi|$ with a time evolving wave packet $|\phi(t)\rangle$.

Figure 3-2. is a graphic illustration of the above process for the system ABC + hν $\longrightarrow$ AB + C.

A two dimensional contour plot of the excited state PES is shown in Fig. 3-2a. The wave packet at t = 0 is represented by the black area. Its center will follow the trajectory marked by a heavy line. The correlation function (Fig. 3-2b) starts at a maximum at t = 0 since $\langle\phi|\phi_{(t)}\rangle = 1$. As the wave packet leaves the Franck-Condon region on its way to products, $\langle\phi|\phi(t)\rangle$ decays. Should it revisit that region a recurrence in $\langle\phi|\phi_{(t)}\rangle$ would be observed (marked 4 in Fig. 3-2a, and b). The recurrence in this example is mainly due to the rapid spreading of the wave packet along the B-C coordinate. The absorption spectrum (Fig. 3-2c)

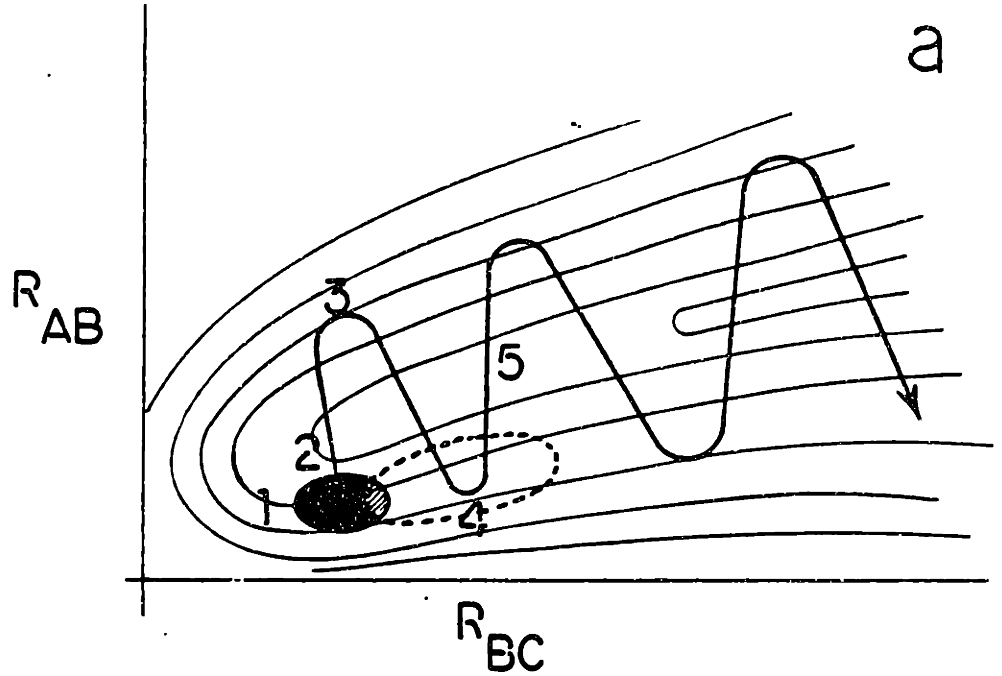
a
R_AB
R_BC
1
2
3
4
5

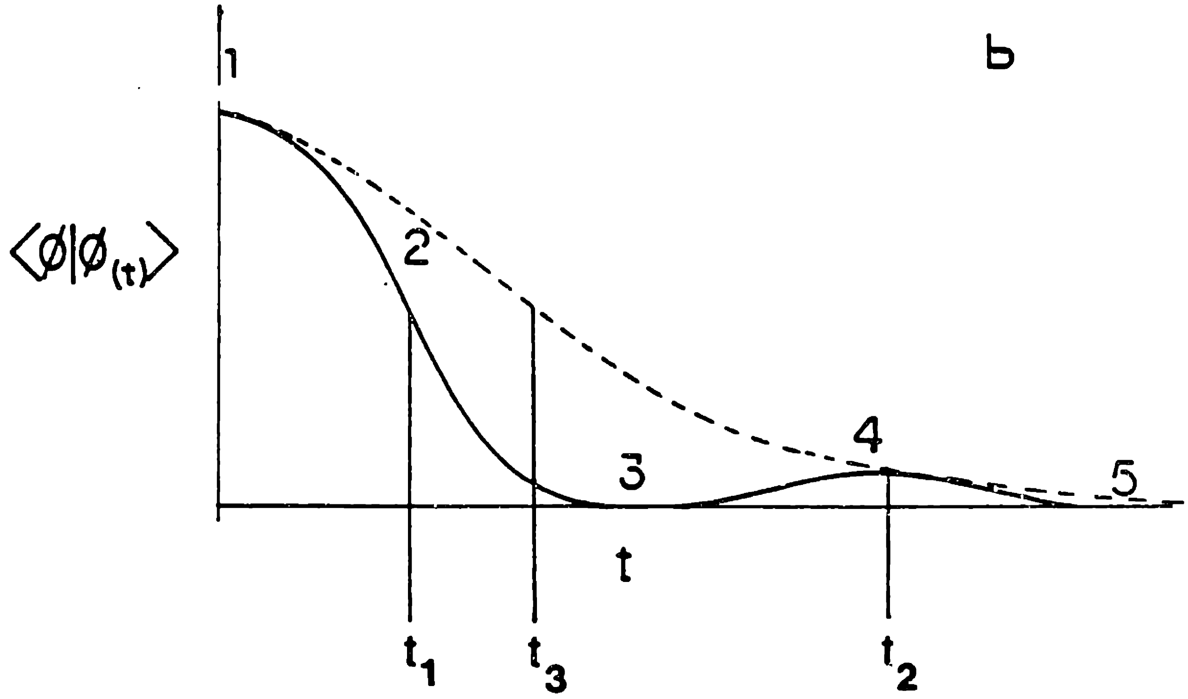
b
1
⟨Ø|Ø(t)⟩
2
3
4
5
t
t1
t3
t2

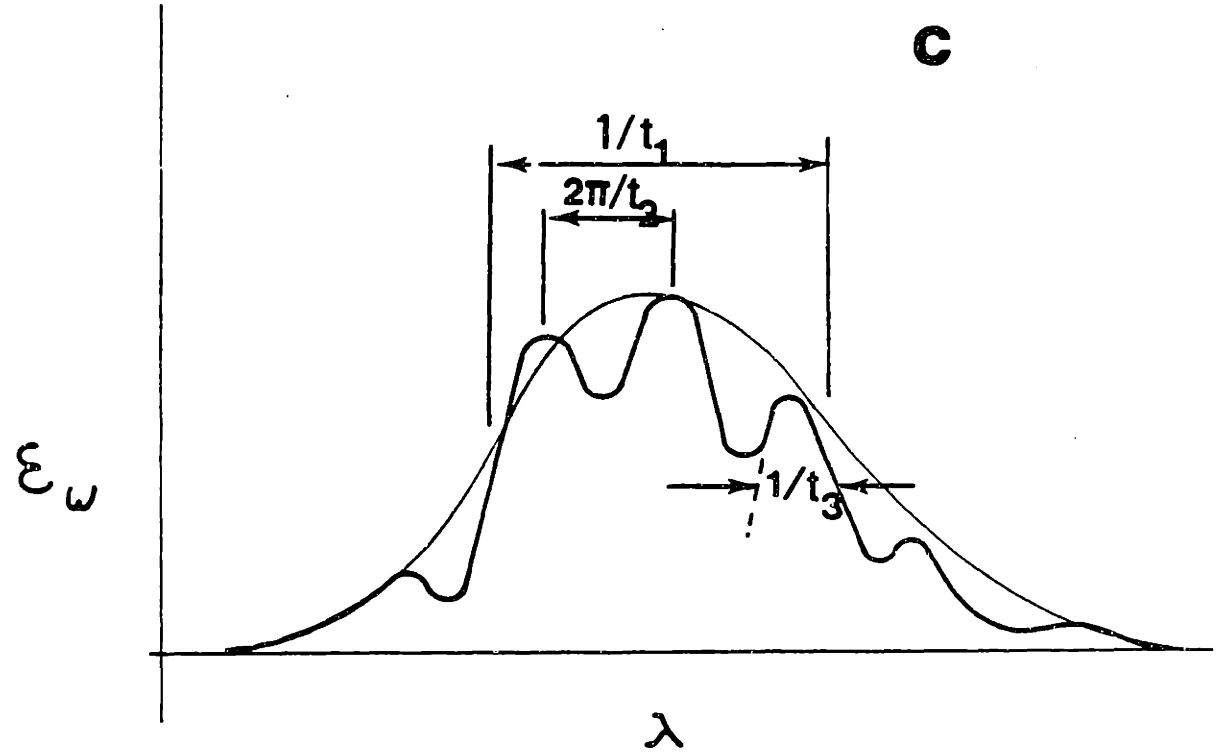

Fig 3-2 - (a) Photodissociation trajectory for $ABC + h\nu \longrightarrow AB + C$. Initial conditions were selected so that both coordinates will be active in the reaction. (b) The correlation function $\langle\phi|\phi(t)\rangle$ for the system plotted vs. time. (c) The absorption spectrum obtained by Fourier transforming $\langle\phi|\phi(t)\rangle$. Dashed line spectrum is obtained when only short times are included (less than 3). The structured spectrum is obtained when the full behavior of $\langle\phi|\phi(t)\rangle$ is included.

can be obtained by Fourier transforming $\langle\phi|\phi(t)\rangle$. Because of the partial recurrence, the corresponding spectrum exhibits some weak structure. The spacings between spectral features correspond to the periodic motion along the A-B coordinate. From a computational point of view the greatest advantage of the time dependent approach is for systems with inherent short time dynamics.

Fig. 3-3. shows a particularly simple example, which will be used following E.J. Heller's[33] treatment to illustrate time dependent methods for two dimensions. The absorption spectrum can be obtained by solving equation (III.4). The initial vibrationless wave-function can be taken to be a two dimensional gaussian, which is a good approximation for most molecules. If the reaction is rapid, as in this case, the wave packet will remain a gaussian for times on the order Δt and longer.

$$\phi(t) = \left(\frac{\omega_x\omega_y}{2}\right)^{1/2}\mathrm{Exp} - \left[\frac{\omega_x(t)}{2}(x - x_{(t)})^2 - \frac{\omega_y(t)}{2}(y - y_{(t)}) - iV_{x(t)}(x - x_{(t)}) - iV_{y(t)}(y - y_{(t)}) - i\gamma_{(t)}\right]$$

where: ω_x and ω_y are natural frequencies in x and y

$V_x = -\partial v/\partial x$ $\qquad$ $V_y = -\partial v/\partial y$

γ is a normalization factor

Equations of motion for x, y, p_x, p_y, and γ are:

III.5 $\dot{X}_{(t)} = P_x(t)$ $\qquad$ $\dot{Y}_{(t)} = P_y(t)$

III.6 $\dot{P}_x(t) = -\partial v/\partial x = V_x$ $\qquad$ $\dot{P}_y(t) = -\partial v/\partial y = V_y$

For short times, solutions of these equations can be written as

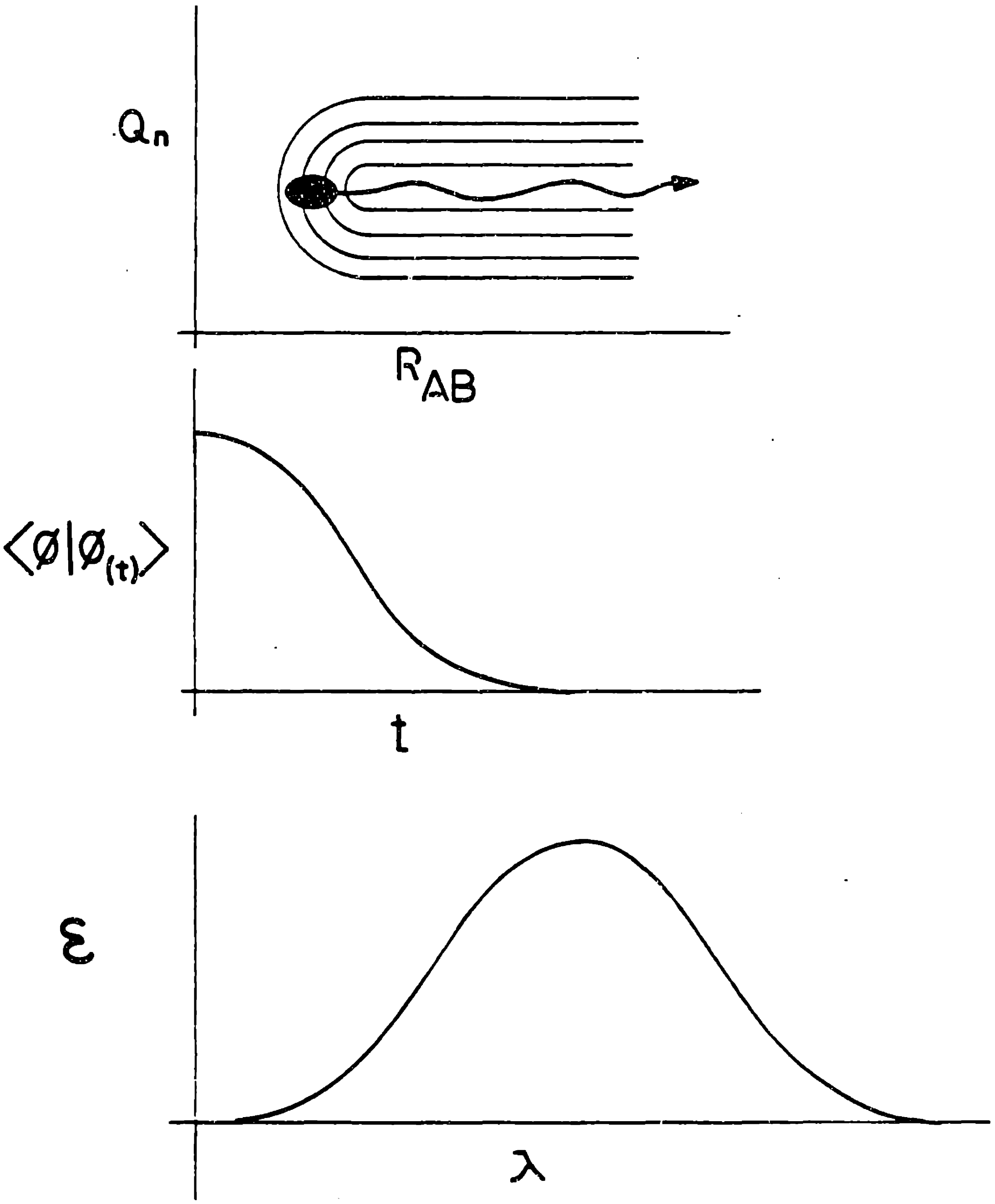
Q_n
R_{AB}
$\langle \phi | \phi_{(t)} \rangle$
t
ε
λ

Fig 3-3 - Same as Fig 3-2 except that initial conditions were selected so that the repulsive coordinate alone is active in the photodissociation.

III.7 $X(t) = X_0 + 0(t^2) \qquad y(t) = y_0 + 0(t^2)$

III.8 $P_x(t) = -V_x/t + 0(t^2) \qquad P_y(t) = -V_y/t + 0(t^2)$

III.9 $$\begin{aligned} \omega_x(t) &= \omega_{x_0} - i(\omega_{x_0}^2 - V_{xx}) + 0(t^2) \\ \omega_y(t) &= \omega_{y_0} - i(\omega_{y_0}^2 - V_{yy}) + 0(t^2) \end{aligned}$$

III.10 $V_{xx} = \partial^2 V/\partial x^2\Big|_{x = X(t)} \qquad V_{yy} = \partial^2 V/\partial y^2\Big|_{y = y(t)}$

III.11 $$\begin{aligned} \gamma_t &= \gamma_0 - Et + 0(t^2) \\ E &= \langle \phi_i | H^{ex} | \phi_i \rangle \end{aligned}$$

Neglecting terms of order t^2 or higher and replacing V by a locally quadratic potential yields:

III.12 $$\begin{aligned} \mathcal{E}(\omega) &= C\omega \, \mathrm{Exp}[-(\omega - \omega_0)^2/2\sigma^2] \\ 2\sigma^2 &= V_x{}^2/\omega_x + V_y{}^2/\omega_y \\ \omega &= E/\hbar \end{aligned}$$

This closed form expression for the absorption spectrum is approximate, but it is extraordinarily instructive. It shows the connection between the absorption spectrum and the shape of the excited state potential. For the simple system of this example, one can expect a smooth, gaussian-looking absorption spectrum. The width of this spectrum is directly related to the slope of the potential at the Franck-Condon region. Thus, even the broad and featureless spectra expected for such systems contain limited but valuable dynamic information. Only σ^2, which is related to the sum of all forces driving the wave packet out of the Franck-Condon region, can be determined from the spectrum. Hence, the spectrum tells "how fast" the wave packet is moving but provides no information as to the direction of motion. In contrast, the Raman (emission) spectrum is extremely informative as to the detailed nuclear motion during the reaction.

The usual energy form Kramers-Heisenberg-Dirac (KHD) expression used to describe the Raman amplitude α_{if} for a process starting at state i ending in state f is:

$$\text{III.13} \qquad \alpha_{if} = \sum_{n} \frac{\langle f|\mu_{ab}\cdot e_s|n\rangle\langle n|\mu_{ab}e_i|i\rangle}{E_i + \omega_I - \omega_n - i\Gamma} + \text{NRT}$$

where: μ_{ab} is the electronic transition moment between surfaces a and b.

e_i and e_s are unit vectors with polarization of the scattering and incident light respectively. $|i\rangle$ and $\langle f|$ are initial and final rovibranic levels.

NRT are non-resonant terms, these are small and usually neglected.

The sum is over excited state eigenfunctions and energies. For a polyatomic molecule it is practically impossible to implement this sum with any accuracy. A thorough knowledge of the complete PES is required in order to obtain $\langle n|s$. The KHD Raman expression presents similar limitations as those of the time-independent expression (eq. III-2) for the absorption spectrum. The complexity of the KHD expression can easily be avoided by using an alternative time dependent formula for the Raman amplitude:

$$\text{III.14} \qquad \alpha_{fi} = \int_0^\infty e^{i\Delta\omega t} \langle\phi_f|\phi(t)\rangle\, dt + \text{NRT}$$

where: $\Delta\omega = \omega_g - E_0$ is the detuning frequency from the center of the absorption band; ω_g is the laser frequency

$$|\phi_i\rangle = \mu_{ab} \cdot e_i |i\rangle$$

$$|\phi_f\rangle = \mu_{ab} \cdot e_s |f\rangle$$

$$|\phi(t)\rangle = e^{iH_{ex}t/\hbar} |\phi_i\rangle$$

H_{ex} is the excited state nuclear Hamiltonian. $|\phi_i\rangle$ is the ground state vibrational wave-function transferred to the excited state by the transition moment μ_{ab} where it is propagated by H_{ex}. As it evolves on a new potential it develops overlap with a final vibrational wave-function located on the ground electronic surface. A return to the ground state into $|f\rangle$ is accomplished by the scattering of a photon. Fig. 3-4. describes the process diagrammatically.

The overlap $\langle\phi_f|\phi(t)\rangle$ in Equation III-4 is a function of time alone. Its properties determine the Raman intensities. For μ constant over $|\phi_i\rangle$, at the instant of photon absorption (t = u in Figure 3-4) $\langle\phi_f|\phi(t)\rangle = \delta_{if}$. But $\langle\phi_i|\phi(t)\rangle$ decays as $|\phi(t)\rangle$ moves out of the Franck-Condon region. At the same time, overlaps with other vibrational states increase (See Fig. 3-5.). As a matter of fact, intensities into ground state levels develop in a simple and sequential manner, with higher vibrational levels gaining intensities later in time.

E.J. Heller[33] has shown that, for simple systems such as the one used to obtain equation III-12, it is possible to obtain the following approximate closed form expression relating Raman intensities to properties of the PES. Emission intensity into the K^th ground state normal mode fundamental is:

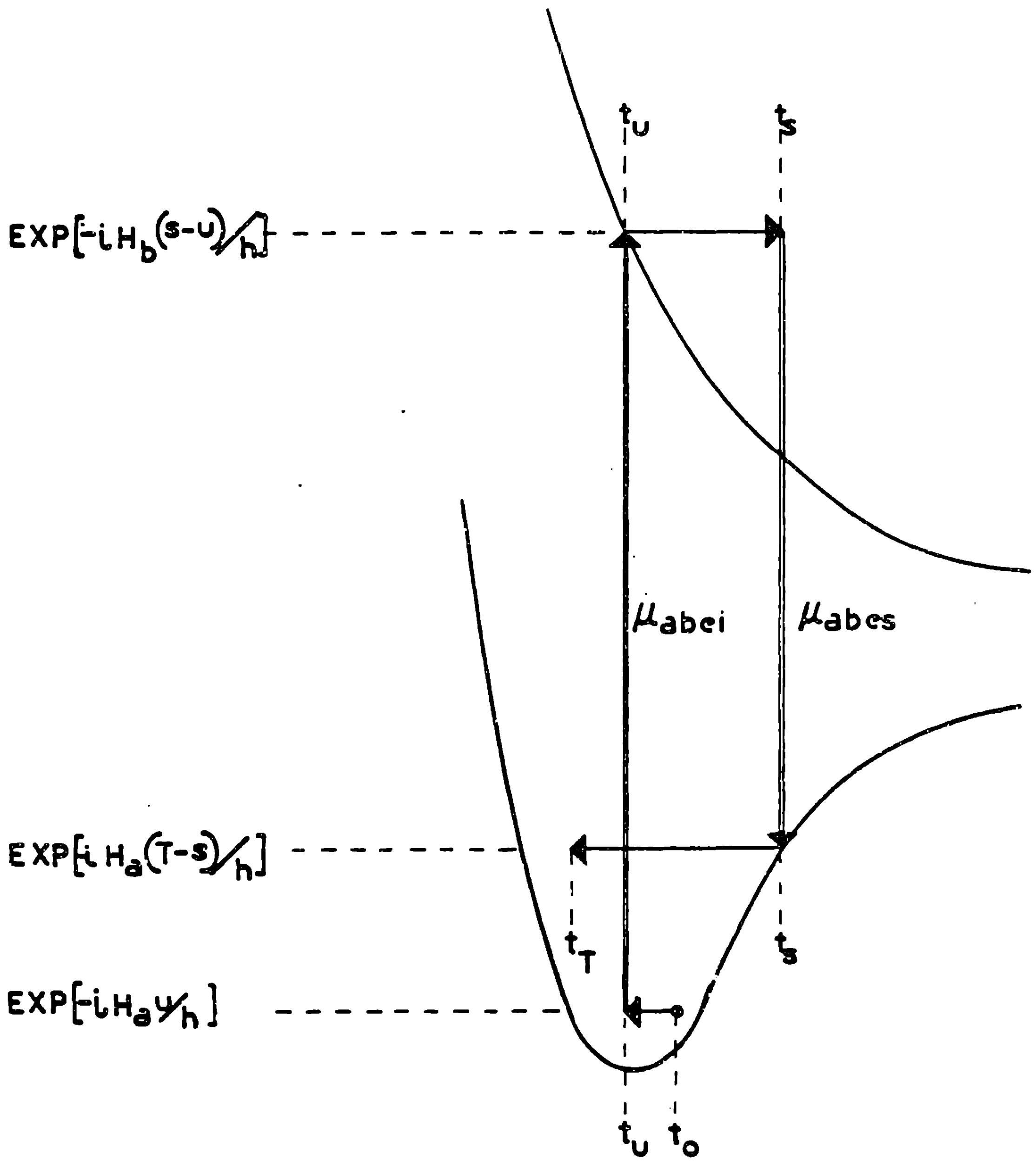
t_u
t_s
$EXP[-iH_b(s-u)/h]$
μ_{abei}
μ_{abes}
$EXP[iH_a(T-s)/h]$
t_T
t_s
$EXP[-iH_a u/h]$
t_u
t_o

Fig 3-4 - A two photon Raman process: At t = 0 the system is propagated by the ground state Hamiltonian (H_a) from t = 0 to t = u when it absorbs a photon. From t = u to t = s the system is proprogated on the excited state surface by H_b the excited state nuclear Hamiltonian. At t = s a photon is scattered and the system returns to the ground state surface where it is again propagated by H_a.

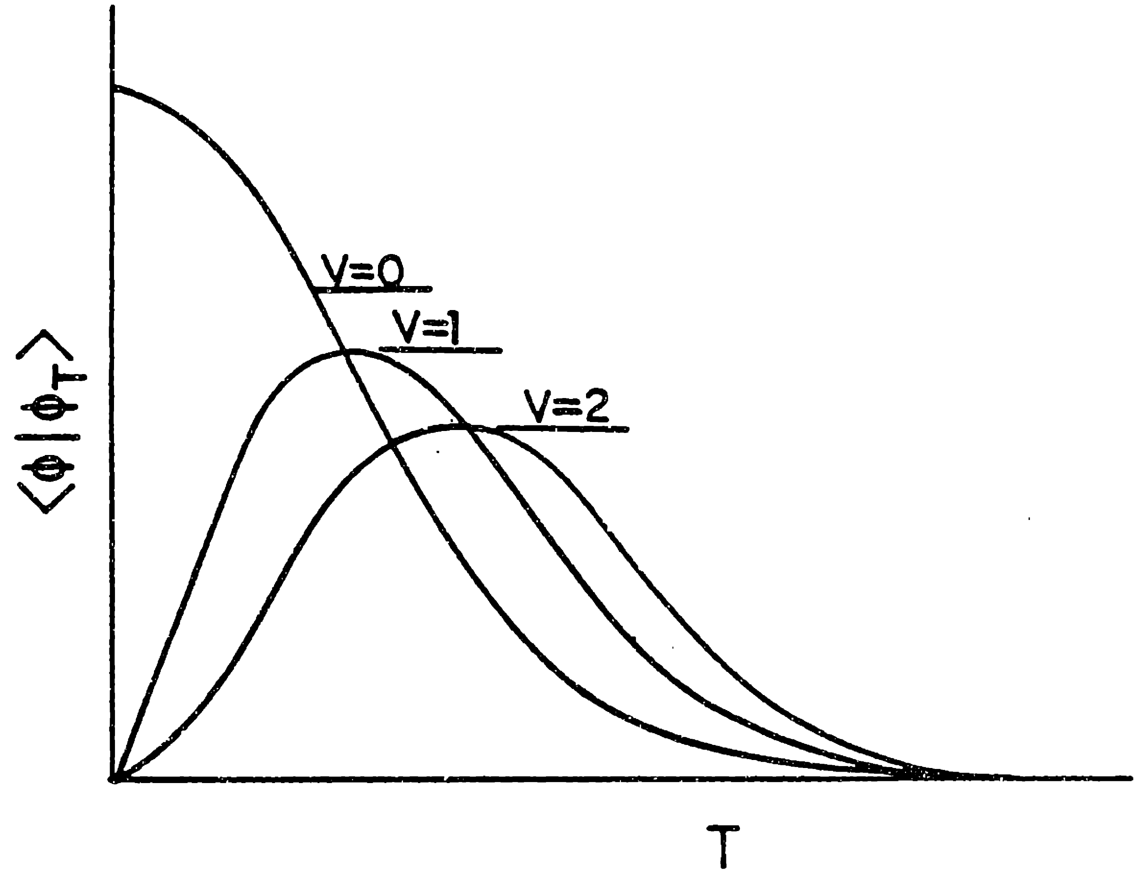

Fig 3-5 - Time evolution of emission into ground state levels

III.14 $$|\alpha^k_{10}\,(\omega_I)|^2 = \frac{V_k{}^2}{2\omega_{0k}\sigma^4}\,\varepsilon_1\left(\frac{\omega_{\wedge} - E}{\sigma}\right)$$

and into the first overtone when $\omega^2_{0k} \cong V_{kk}$

III.15 $$|\alpha^k_{20}\,(\omega_I)|^2 \propto \frac{V_k{}^4}{8\omega_{0k}\sigma^6}\,\varepsilon_2\left(\frac{\omega_{\wedge} - E}{\sigma}\right)$$

or, when $V_k = 0$ $$|\alpha^k_{10}|^2 = 0$$

III.16 $$|\alpha^k_{20}\,(\omega_I)|^2 = \frac{(\omega_{0k}{}^2 - V_{kk})^2}{8\omega_{0k}\sigma^4}\,\varepsilon_1\left(\frac{\omega_{\wedge} - E}{\sigma}\right)$$

where: $$\varepsilon_n(\omega) = \left|\int_0^\infty e^{i\omega t^2/2}\, t^n\, dt\right|^2$$

Since it is more common to obtain relative intensities than absolute ones, it is instructive to study ratios of various bands. The ratio of two fundamental intensities K and K' is given by

III.17 $$\frac{I^k_{10}}{I^{k'}_{10}} = \frac{V_k{}^2}{4\omega_{0k}\sigma^2}\,\frac{\varepsilon_2}{\varepsilon_1}$$

and the ratios of overtone to fundamental intensities are:

III.18 $$\frac{I^k_{20}}{I^k_{10}} = \frac{V_k{}^2}{4\omega_{0k}\sigma^2}\,\frac{\varepsilon_2}{\varepsilon_1} \qquad \text{for } \omega^2_{0k} \cong V_{kk}$$

or

III.19 $$\frac{I^k_{20}}{I^{k'}_{10}} = \frac{(\omega^2_{0k} - V_{kk})^2\omega_{0k}}{4\omega_{0k}V'_k} \qquad \text{for } V_k = 0 .$$

σ^2 can be determined from the absorption spectrum (eq. III.12). The Raman intensities and a pair-wise comparison yield potential slopes and curvatures in the

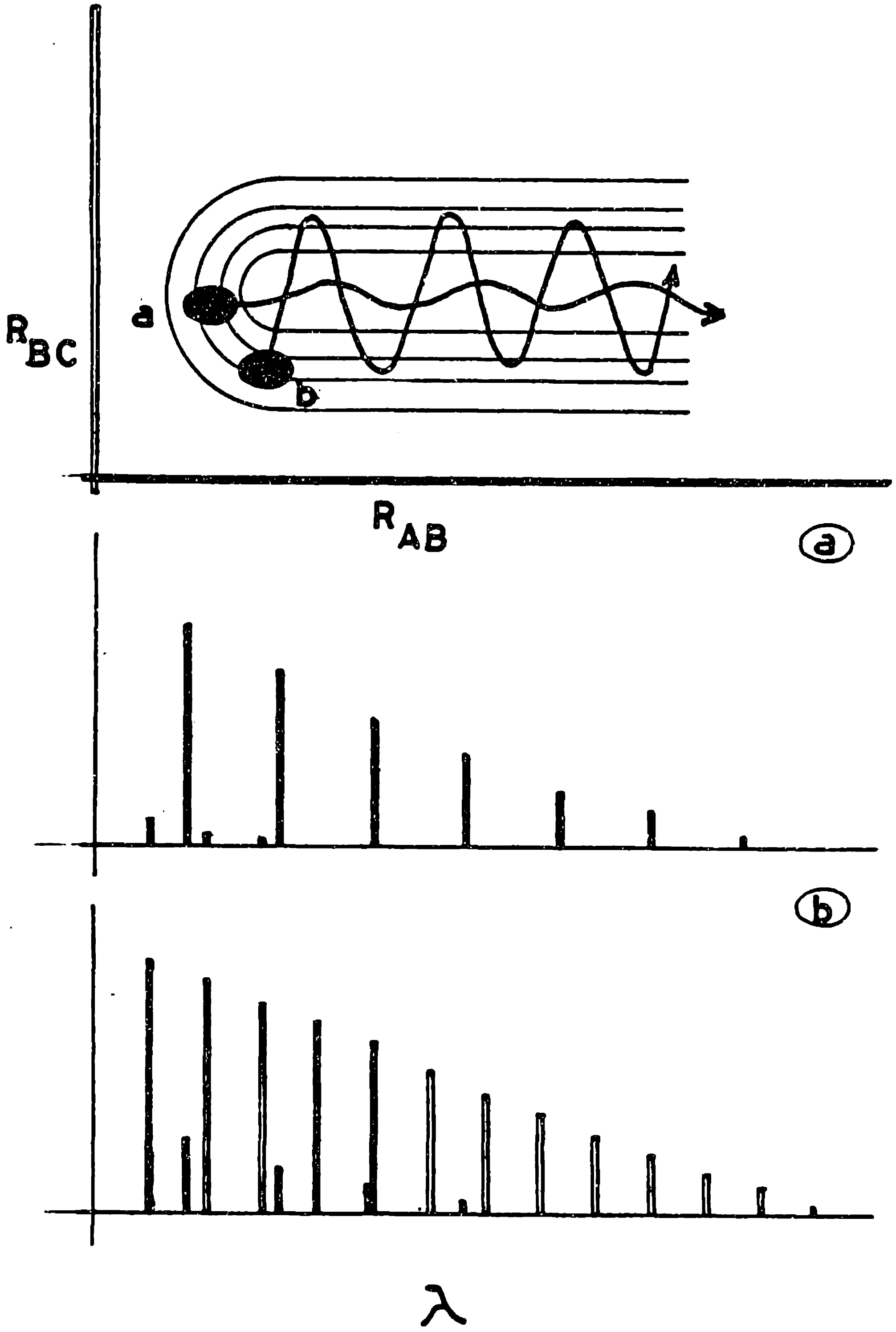

Fig 3-6 - Emission spectra generated by two wave packets. (a) Generates an AB progression (dark bars) while (b) generates predominantly BC stretching spectrum (open bars).

Franck-Condon region along each of the ground state normal modes. The fundamental picture that emerges from these simple equations is that the larger the force (not displacement) along a certain coordinate,the higher the intensity in the corresponding normal mode band. Fig. 3-6 illustrates how the Raman spectrum can be related to nuclear motion during the reaction.

Two wave packets are shown in the figure. (a) was prepared on the surface in a region where the initial force is almost exclusively along the A-B coordinate. In this case the motion of the wave packet generates a spectrum where AB stretches (dark bars) are predominantly observed. (b) The trajectory starts in a region where the main force acts along the BC coordinate. This wave packet generates spectrum b, which is dominated by bands corresponding to BC stretching modes (open bars). The time-evolving wave packet leaves a photograph of its motion on the excited state in the form of Raman intensities. At t = 0 the wave packet is still the initial vibrationless wave-function. It has no overlap with any other vibrational state at that time. As the wave packet starts to move, it develops overlap with higher vibrational states, especially those with significant amplitude in the direction of motion. For a given vibrational progression, overlaps will temporally develop in a very simple order, starting with the lowest level and continuing in a sequence of increasing energies. The difference in the configurations sampled by neighboring vibrational eigenstates (e.g. v = 0 and v = 1, or v = 1 and v = 2) are minute, yet the corresponding spectral features are at easily resolvable frequencies. In essence, the emission spectrometer acts as an extremely high resolution microscope, where a small change in bond length or momentum is transcribed into a change in emitted light frequency of hundreds of cm^{-1}.

At exact resonance, each α_{if} just contains the integral of the dynamic quantity $\langle \phi_f | \phi(t) \rangle$. This correlation function decays on a time scale which is intrinsic to the system. Since the dissociating molecule sweeps through infinite displacements in molecular configurations, developing Franck-Condon overlap with highly excited vibrational levels of the ground state, for bands along the dissociation coordinate one expects long progressions in the Raman spectrum. The decrease in band intensities (Fig. 3-6) is indicative of an accelerating and spreading wave packet. Such long progressions are expected only for excitation near band center (small $\Delta\omega$). As $\Delta\omega$ is increased, intensities in the higher vibrational levels decrease faster than those into lower ones. A qualitative explanation of this is related to the time-frequency relation $\Delta\omega \; \Delta t \; > \hbar$. As $\Delta\omega$ increases, the dynamic times contributing to the Raman amplitude decrease. Since emission into higher vibrational levels develops later in time, their intensities decrease faster with detuning. When $\Delta\omega \approx 0$, the time in which contributions to the Raman spectrum accumulate become of the order of τ_{diss} , which is an inherent molecular property. It is also easy to show that for large detuning frequencies ($\Delta\omega >> \sigma$) the integrand in equation III.14 oscillates very rapidly, resulting in self cancellation. As a result the Raman amplitude is dominated by short times $t_{obs} << \tau_{diss}$. Off resonance spectra show mainly fundamentals.

The relation between frequency and time could conceivably be experimentally exploited, to resolve a sequence of events occurring within a fraction of a psec. To successfully implement that notion, a scattering time for intermediate detunning frequency is required. One can borrow ideas from particle scattering theory, where a well defined scattering delay time was first proposed by Eisenbud[36] and later developed by Eisenbud and Wigner[37] and by F.T. Smith[38]. This time was defined as the delay, caused by the interaction, in the passage of a wave packet of particles across a large sphere. The formalism considered a wave packet synthesized from a small range of k vectors. The boundary conditions were set so that the packet entered a sphere of radius R at time -T. In the absence of scattering it left the sphere at time +T. The time difference between +T and exit time, with a scattering center present, was defined as the collision delay time (in the limit $R \longrightarrow \infty$).

In the Raman scattering process the particle wave packet is replaced by a packet of light. The outgoing flux in channel f is α_{if} for unit incoming flux in channel i at laser frequency ω_I . The corresponding delay time in the Eisenbud sense is:

III.20 $$t_{if} = I_m\{\alpha_{if}^{-1} \; \partial\alpha_{fi}/\partial\omega_i\}$$

I.e., t_{0f} is the delay time experienced by a photon leaving the molecule in the final state f, due to interaction with a molecule. The delay time t_{0f} is also the length of time during which the system's dynamics can be probed by that photon. Figure 3-7 shows curves of t_{0f} v.s. ω/σ for a gaussian wave packet $|\phi(t)\rangle$ emitting into various $|\phi_f\rangle$'s where $|\phi_f\rangle$'s are one dimensional harmonic oscillator wave-functions. On resonance, t_{0f} increases with increasing f, as expected from the fact the $\langle\phi_f|\phi(t)\rangle$ develop later in time the higher is $|\phi_f\rangle$. As $\Delta\omega$ becomes large, all t_{0f} decrease as expected, but they still preserve their order with increasing f. In the limit of $\Delta\omega \gg \sigma$

III.21 $$t_{0n} \approx \frac{n\Gamma}{\Delta\omega^2 + \Gamma^2}$$

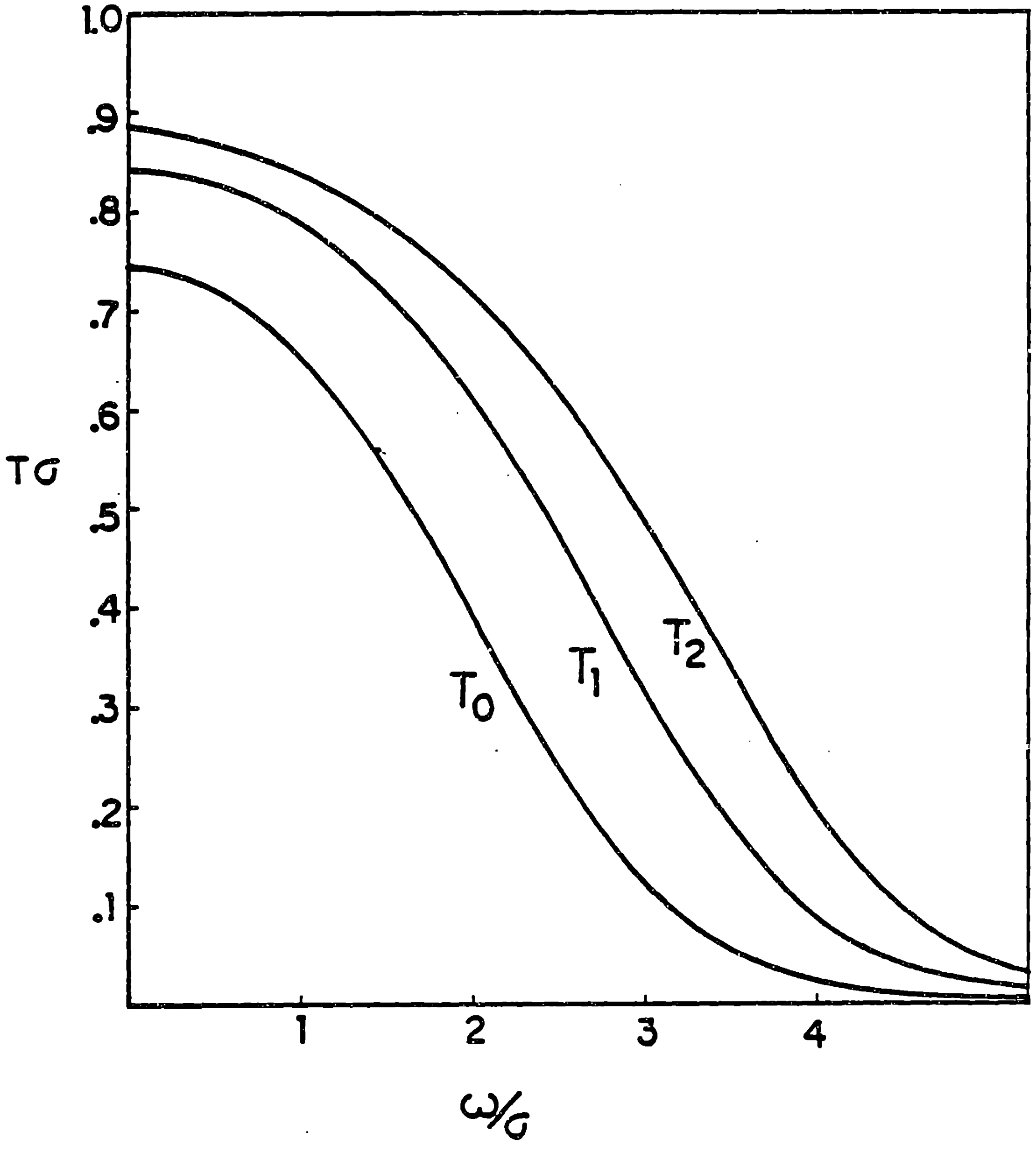

Fig 3-7 - Time delays (t_{of}) vs. detuning frequency in units of ω/σ, for a gaussian wave-packet emitting into harmonic oscillator final states.

CHAPTER 4.

EXPERIMENTAL DETAIL

A flow cell especially designed for this experiment was mounted vertically in front of a monochromator. Light from a pulsed laser was passed through the cell, where it photodissociated the tangent molecules. Emitted photons were collected by a set of optics and imaged onto the slit of a grating monochromator. The dispersed light was detected by a photomultiplier located at the exit slit. The resulting signal was amplified and recorded.

I. The Cell and Flow System.

A modular stainless steel cell was designed and built, Fig. 4-2 shows the basic cell design. The cell was constructed from tubing sections joined by threaded joints, which served to provide a vacuum seal, (using viton "O" rings) as well as to hold the light baffles in place. The baffles were made of brass and they were kept smooth, with their edges sharp. The size and location of baffles was chosen to minimize scattered light. Six baffles were used in all, three on each side of the cell. The entire interior of the cell was gold coated. High quality quartz windows were attached to the cell using Torr Seal. This arrangement allowed easy removal for cleaning or replacement. Four inlets served to flow the gas in and out of the cell.

During a run, fresh compound was injected into the cell, following degassing and purification over a cold trap. The injection region was directly adjacent to the

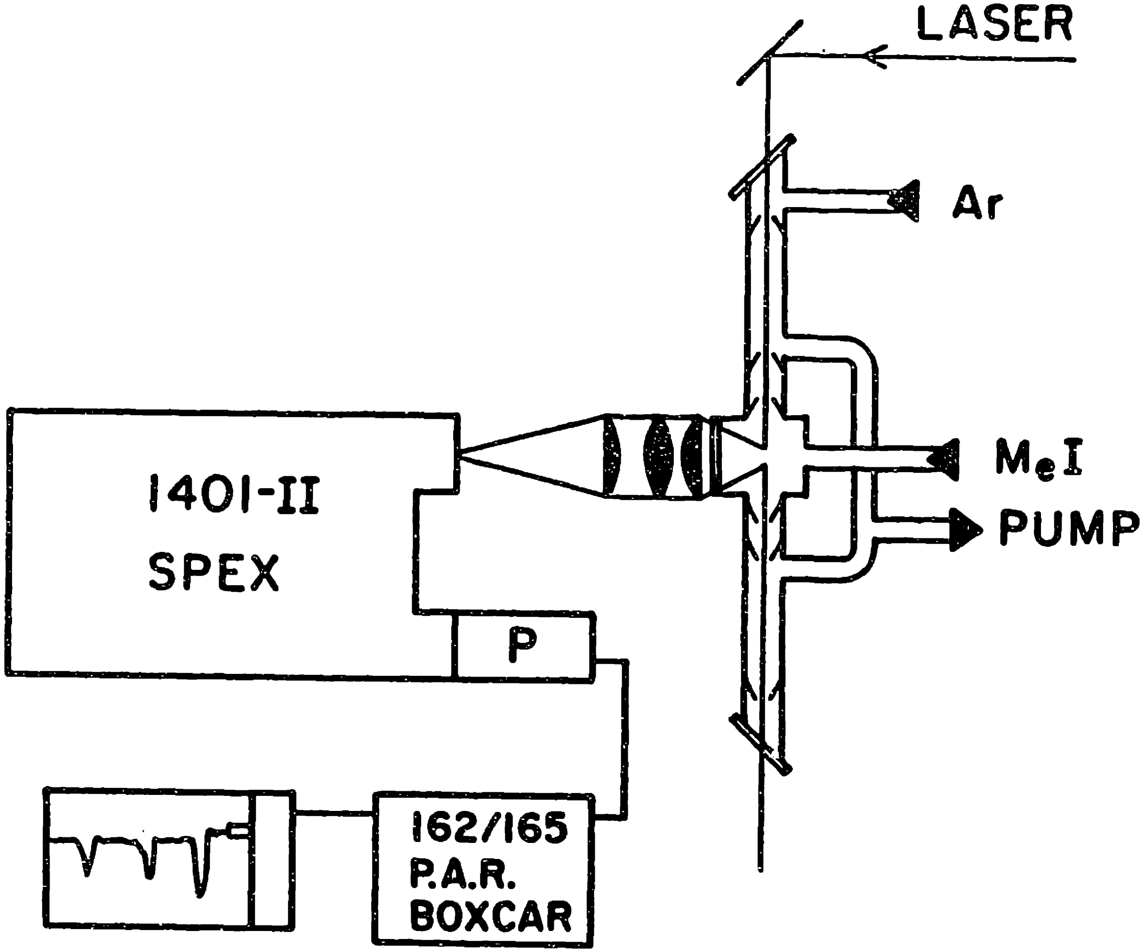
LASER
Ar
M_eI
PUMP
1401-II
SPEX
P
162/165
P.A.R.
BOXCAR

Fig 4-1 - General experimental layout, showing the flow cell collection optics, monochromator, and detection system.

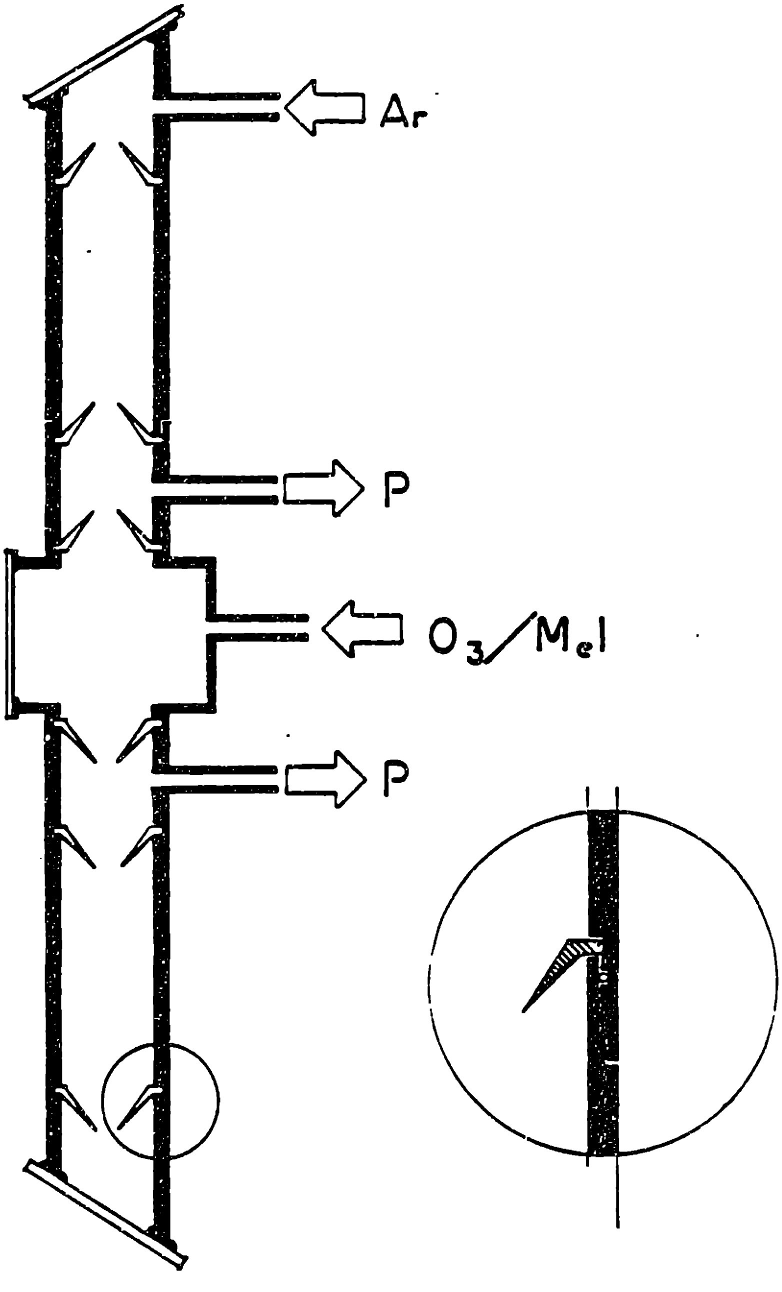

Fig. 4-2 - Flow cell, showing baffles and modular construction.

viewing region. Two pumping ports, located two inches from the viewing region on each end, served to remove photolysis products from the cell. An additional port, located approximately .5 inches away from the laser input window was used as an inlet for Argon gas. Argon served two purposes: it prevented the compound and its photolytic products from settling on the window, and helped reduce the partial pressure of the target compound on the laser entry side, in order to minimize light absorption in the side arm.

Fig. 4-3. shows the general gas flow system. The 550 liter/min mechanical pump, located as close as possible to the cell, was protected by two liquid nitrogen traps in the methyl iodide experiments, or by a copper trap kept at 100° C in the ozone experiments. The copper trap insured catalysis of O_3 decomposition for safety reasons. Despite the existence of these traps, the pump oil had to be changed frequently owing to decomposition and contamination.

Steady state pressure was kept at 10 torr for methyl iodide. In the case of ozone, pressures higher than 5 torr resulted in minor explosions. Methyl iodide (99.8% pure, Aldrich) was used after degasing by a sequence of five freeze-thaw cycles. The ozone was produced by discharge of pure O_2 using a commercial ozonizer. Discharge products were passed through a silica gel trap maintained at dry ice temperature. A sufficient quantity of ozone for a single run could be kept trapped on the gel. Most of the excess O_2 was pumped away before the samples were used. Mixtures of approximately 60% ozone and approximately 40% oxygen or mixtures richer in O_3 were routinely achieved, as determined by u.v. absorption. At the start of a run, excess O_2 was pumped off and the silica gel was allowed to warm to room temperature. The resulting O_3/O_2 mixture was allowed to expand into a reservoir bulb. The mixture was further purified on-line by

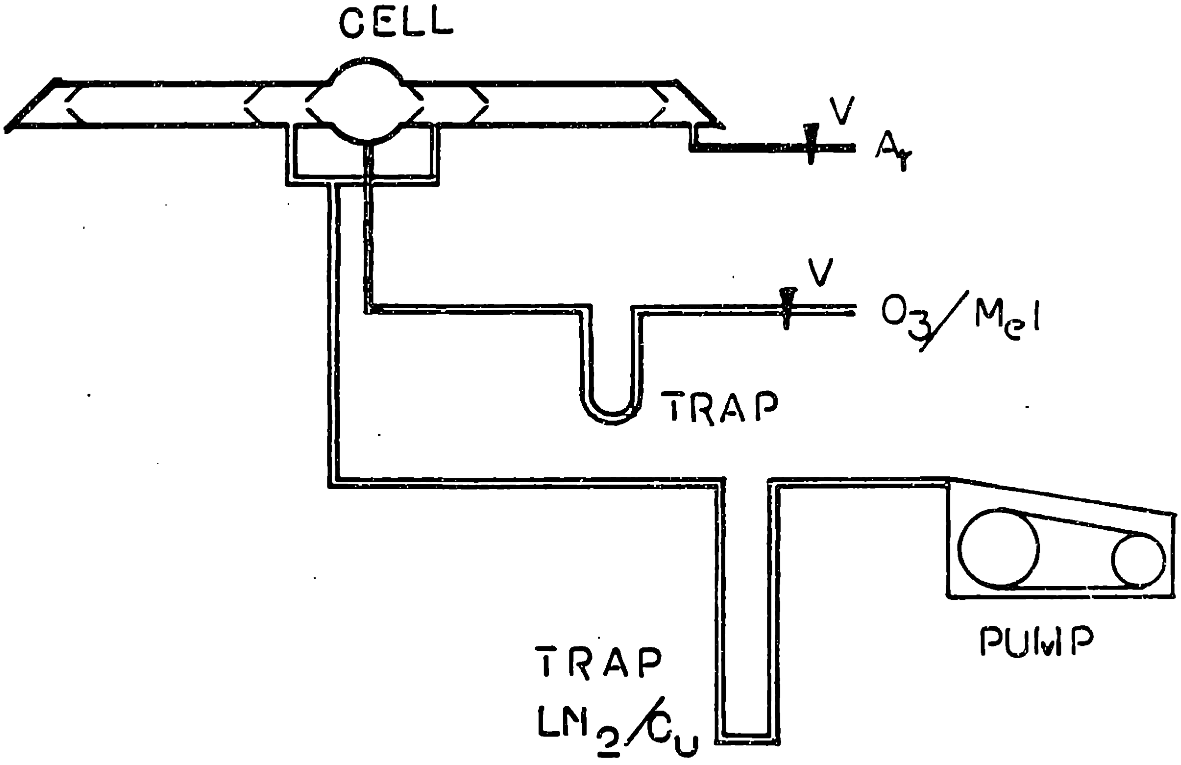
CELL
V
Ar
V
O3/MeI
TRAP
TRAP
LN2/Cu
PUMP

Fig. 4-3 - Gas flow system.

passage over a dry ice trap. This removed the H_2O_2, which was present in the mixture in small amounts.

II. Light Source and Optical System

Nd:YAG lasers were used in both phases of the work. For the methyl iodide experiment a Quanta Ray DCR1 laser was used. For the ozone experiment, it was a Molectron model MY 34. Both lasers were equipped with harmonic generators/separators. For most experiments frequency quadrupled output at 266 nm was used with 10-15 mj/pulse. The laser beam was focused down to 2.5 mm using long focal length (2.5 meter) lenses. The Molectron laser produced 15 nsec pulses at a repetition rate of 20 Hz. The Quanta Ray laser produced 7 nsec pulses at a 10 Hz rate.

The optics for collecting emitted photons consisted of high quality crystalline quartz lenses. A convex 2" diameter, 2" focal length lens placed in front of the cell window collected the signal photons. A second lens, biconvex 2" in diameter and of 12 cm focal length, was used to correct spherical abberations. The light passed through a final 5" focal length lens, which produced a line image on the monochromator slit. The system was designed to overflow the monochromator mirror to minimize effects of minor misalignments. The lens system was mounted on a two-way translator for fine adjustment.

Two different monochromators were used: (1) A 1704, 1 meter Spex monochromator equipped with a holographic grating, having 1800 grooves/mm. This provided a resolution of 8 Å/mm slit width FWHM in first order. (2) A 1401-II newly overhauled Spex .75 meter double monochromator equipped with a pair of gratings with 1200 grooves/mm, blazed at 1 . This system gave 1 Å/mm slit width FWHM when used at 4th order.

III. Detector and Electronics.

An RCA model 4501-V4 photomultiplier was used to detect the signal. A home made housing was used as an electronic shield. A LeCroy x 10 fast preamplifier was mounted directly in the housing. The maximum allowed voltage (2200 V) was applied to the photomultiplier to yield approximately .5 V/photon after amplification. This insured negligible contribution from electrical noise (approximately 2.5 mV). The amplified signal was fed into a P.A.R. 162/165 boxcar integrator. A gate of 10-15 nsec and a time constant 10-100 sec were used. A hundred to a thousand laser pulses were averaged at each monochromator setting. The boxcar output was fed directly into a chart recorder.

CHAPTER 5.

METHYL IODIDE PHOTODISSOCIATION

I. Criteria for Choice of System for Study.

The complexity of reactive systems (including photodissociation), together with the very few examples for which experimental and theoretical work have been combined to yield a consistent model to describe the reaction, led us to search for the simplest possible system. A good example for such a system is a linear triatomic molecule with dissociation occuring in a co-linear fashion. This makes the problem tractable by limiting the motion to two dimensions. Unfortunately, most triatomics that are linear in their ground states either have bent excited states (e.g. CS_2^{49}) or exhibit optical spectra with strongly overlapping bands (e.g. ICN, CdI_2^{49}). The only suitable triatomics free from either of these problems, CO_2 and N_2O,[49] have transitions at shorter wavelengths than are currently accessible with standard lasers. The linear triatomic is, however, not the only possible quasi-two dimensional system. A pyramidal ABC_3 molecule may also behave in an approximately two-dimensional fashion. Experimental evidence seems to indicate that methyl iodide is a molecule whose photodissociation involves essentially only two coordinates: the C-I stretch and symmetric umbrella bend. CH_3I is a particularly good choice because of the large number of reported experiments relating to its dissociation dynamics.

II. Background.

The CH_3I absorption spectrum shown in Fig. 5-1. has been investigated by Rowe and Gedanken.[50] They were able, using magnetic circular dichroism techniques, to resolve the absorption spectrum into three separate components $^3Q_1$ $^3Q_0$ and ^1Q (marked in the figure). Most of the intensity is carried by the $^3Q_0$, which is of A_1 symmetry. At 266nm, (where our results were obtained) nearly 96% of the absorption is in the $^3Q_0$ state. This state was predicted[51] to correlate to the $^2P_{\frac{1}{2}}$ state of iodine and the CH_3 ground electronic state. As one might expect in a rapidly dissociating molecule such as CH_3I, the absorption spectrum is featureless, and, as previously indicated, such an absorption spectrum provides minimal insight into the reaction detail, aside from the initial force at the Franck-Condon region.

The overlapping absorption bands of CH_3I indicate the close proximity of a number of excited state PES's. The Gedanken results provide information as to the relative absorption probabilities for each of the surfaces. However, this does not mean that the reaction is confined to a single surface. For many molecules it has been found that absorption can occur into one electronic surface (the spectroscopically active state) while subsequent dissociation takes place on a nearby surface which may be spectroscopically dark, (see Fig. 5-2). This phenomenon has been termed curve crossing.

In the case of CH_3I, curve crossing would be evident since it will result in production of ground state iodine atoms ($I^2P_{3/2}$). The initial evidence that curve crossing is not a major channel in the photolysis of CH_3I comes from the laser work by Kasper et al.[52] and Riley et al.[53] These groups succeeded in constructing the

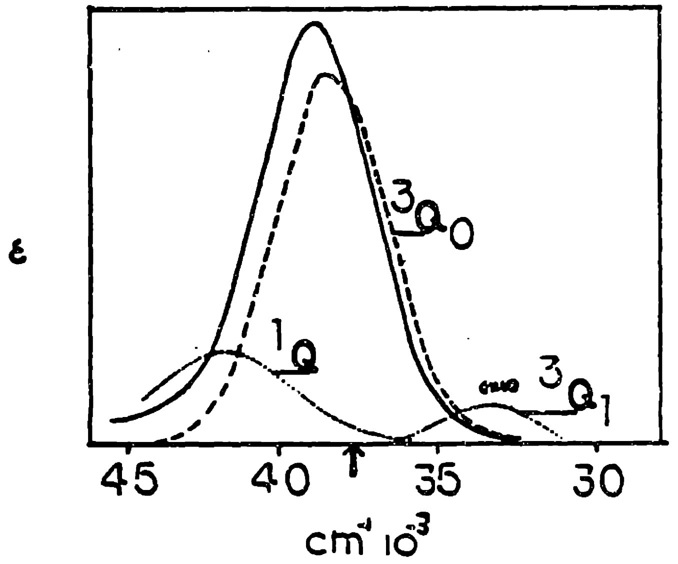

Fig 5-1 - U.V. absorption spectrum of methyl iodide decomposed into three components, $^3Q_0$, $^3Q_1$, and ^1Q.

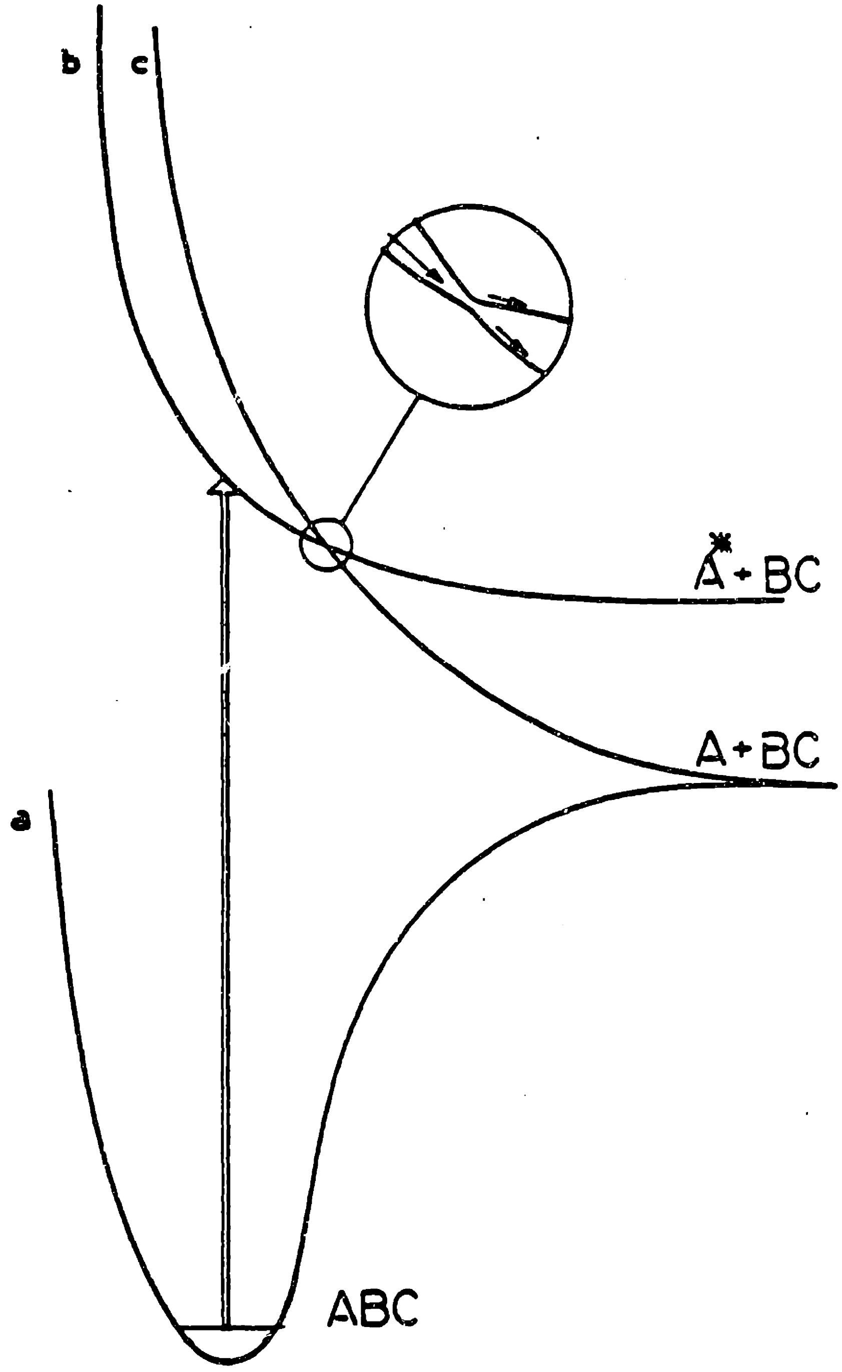
b
c
A* + BC
A + BC
a
ABC

Fig 5-2 - Schematic illustration of curve crossing during photodissociation.

first photodissociation laser. Following photodissociation of CH_3I by a u.v. flash lamp, intense lasing at 1.315μ, corresponding to the I ($^2P_{3/2}$ — $^2P_{1/2}$) transition was observed. This indicates that more than 50% of the dissociation occurs on the $^3Q_0$ surface. In photofragment studies by Sparks and Lee,[54] both reaction channels I $^2P_{3/2}$ and I $^2P_{1/2}$ were observed in the time of flight spectrum. Their results indicate that excitation at 266 nm yields only about 10% ground state products. In that experiment, a supersonically cooled CH_3I molecular beam was flash photolysed by a Nd:Yag laser, and time-of-flight spectra of the photo-fragments were recorded. Two peaks were observed, one attributed to the I($^2P_{1/2}$) channel, the other to I ($^2P_{3/2}$). Most of the available energy (84%) was found to be released in the form of translational energy. Analysis of the line shape of the time-of-flight spectrum suggested that the only vibration excited in the CH_3 product is the out of plane umbrella bend. Sparks proceeded to fit the data with a vibrational distribution based on the above assumption. Their results are shown in Figure 5-3. Subsequently, another experiment supporting the assumption of umbrella-mode excitation has been carried out by Baughcum and Leone.[55] Here, CH_3I at room temperature was flash photolysed with an excimer laser at 248 nm. Products were observed by frequency and time resolved infra-red emission detection. The only observed emission that was prompt with the dissociation laser was in the 500-700 cm^{-1} region. No IR emission was observed on the 3000 cm^{-1} region where the symmetric C-H stretch mode would emit. Their conclusion was that CH_3 was produced vibrationally excited in the umbrella mode only. In another molecular beam experiment, Dzvonik and Yang[56] found that the I atoms emerged preferentially along the direction of the electric vector of the laser. This strong anisotropy showed that the transition moment is along the three-fold axis,

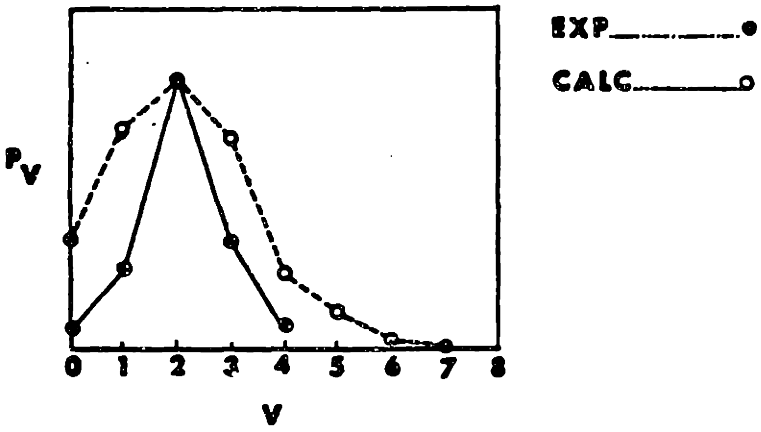

Fig 5-3 - Comparison between experimental results (ref 54) and theoretical predictions (ref. 60) for the vibrational distribution of the CH_3 product. v designates vibrational levels in v_2.

Experimental..... ●

Theory............. o

consistent with an excited state of A_1 symmetry. Strong anisotropy also indicates that dissociation is immediate, i.e. the excited state is strongly repulsive with no long lived intermediate being formed.

A very interesting experiment on the cage effects in the photodissociation of CH_3I in an inert matrix was reported by L.E. Brus and V.E. Bandybey.[57] In this experiment a cold matrix of CH_3I in Ne at 4.2° K was flash photolysed by a frequency-doubled dye laser. Time and frequency resolved emission was observed. Results are shown in Figure 5-4. The spectrum consists of a progression from 700-1000 nm, with bands spaced by an average of 305 cm^{-1}. Further studies using CD_3I showed similar results. The observed isotope shifts are consistent with bands belonging to C-I stretching vibrations. In the Ne matrix, the purely repulsive gas phase CH_3I potential is modified at long range due to the presence of the Ne atoms. A shallow minimum is formed at large H_3C-I separation. The estimated minimum is found at approximately 3 Å. When the molecule absorbs a uv photon, the C-I bond length increases until the repulsive cage forces on the alkyl radical and the I* atom equal the repulsive chemical forces between the two fragments. Rapid vibrational relaxation produces a vibrationally relaxed electronically excited "stationary state" with a new equilibrium C-I bond length. The new molecule is detected through its fluorescence into the chemically bonded ground electronic state.

The ground electronic state of CH_3I has been investigated by infrared absorption spectroscopy. Recent results provide accurate information as to the low lying vibrational states.[58] The infrared spectrum of CH_3 has been investigated by Yanada et al.,[59] who found that the equilibrium geometry is in the planar configuration and that the out of plane bend has a vibrational frequency of approximately 600 cm^{-1}.

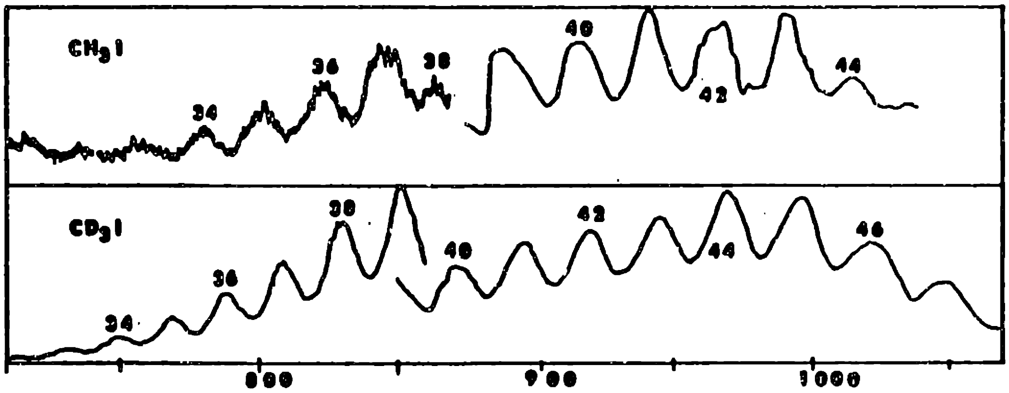

Fig 5-4 - Emission from photolized CH3I and CD3I in a cold Ne matrix (from ref 57). Bands are numbered according to our assignments, referring to v_3 quanta of energy.

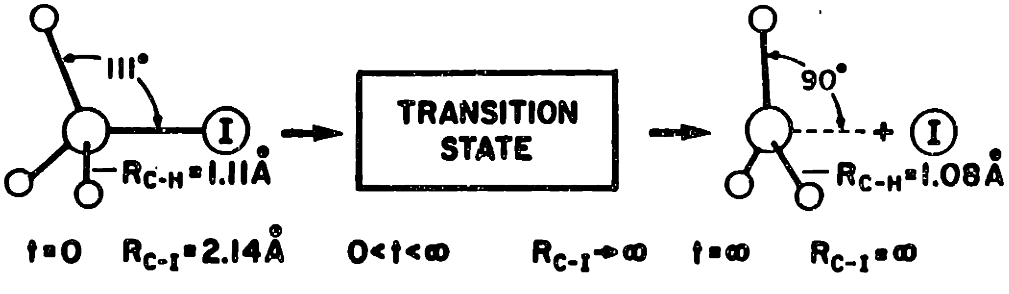
111°
$R_{C-H}=1.11Å$
TRANSITION STATE
90°
$R_{C-H}=1.08Å$
I
I
$t=0$ $R_{C-I}=2.14Å$
$0<t<\infty$
$R_{C-I}\to\infty$
$t=\infty$
$R_{C-I}=\infty$

Fig 5-5 - Transformation of CH3I into CH3 + I* during photolysis.

Thus a simple picture for dissociation of CH_3I emerges. Fig. 5-5 shows the transformation from CH_3I to CH_3 + I^*. Both ground and excited states are of non-degenerate A_1 symmetry. Therefore the center of the three hydrogens, the carbon atom and the iodine atom lie on a common straight line in the ground state equilibrium geometry as well as that of the excited state. The only vibration active in the dissociation, other than the C-I stretch, is the symmetric umbrella bend.

This unique simplicity of CH_3I photodissociation has made it attractive to theoreticians as well. In a recent report by Shapiro and Bersohn,[60] analytic two-dimensional potentials have been proposed for the ground and excited states. These potentials were then used in a quantum mechanical calculation of the dissociation process to predict the vibrational distribution in the final CH_3 product. The results were not in good agreement with experimental observations by Sparks et al.[54] (see Fig. 5-3). Later, the same surfaces were tested by Heller et al.,[61] using a sophisticated semi-classical approach. Heller, et al. were able to reproduce the results obtained by Shapiro and Bersohn, suggesting that the difficulty lay in the surfaces rather than the dynamic calculations. This situation exemplifies one of the major problems in the field: theoretical methods have advanced to a point where multi-dimensional dynamical calculations are possible with good accuracy. However, it is often the case that no adequate PES exists. We have used our data, as well as results from ab-initio calculations on CH_3I, to generate new potentials for the $^3Q_0$ state as well as for the ground state. These results will be discussed in chapter 7.

III. The Photoemission Studies.

Emission spectra for three different excitation wave lengths (514, 355 and 266 nm) are shown in figures 5-6,7, and 8. The marked changes in the spectra with exciting frequency illustrate one of the points discussed in chapter 3, namely, the time-frequency reciprocal relationship. As has been mentioned, increasing $\Delta\omega$, the detuning frequency, corresponds to decreasing the effective observation time. The first spectrum (Fig. 5-6. from ref. 62) was obtained by excitation with 514 nm light ($\Delta\omega$ = 18500 cm^{-1}). Such a large detuning corresponds to a very short observation time. Accordingly, no overtones appear in the emission spectrum. The most intense band observed with 514 nm excitation was the C-I stretch fundamental (ν_3) with weaker intensities in the umbrella mode ν_2 and the C-H symmetric stretching mode (ν_1). At such large detuning from resonance, possible "contamination" of the spectrum by effects from other electronic states has to be suspected. This is especially true for the ν_1 (C-H stretch). Since the $^3Q_0$ is an n —— σ^*, with the excitation involving the promotion of an electron localized primarily on the I atom, one would not expect a large change in the equilibrium geometry of the alkyl part of the molecule in the Franck-Condon region. Moreover, in the vuv region there are some quite intense absorption bands[49] that do correspond to excitation of electrons localized mainly on the CH_3 group.

To test for the possibility that ν_1 band emission may contain contributions from more than one excited state surface, we examined the dependence of the relative intensity in this band on excitation wavelength. The simple equations from chapter 3 predict a wavelength independent ratio of fundamental intensities for

Fig 5-6 - Methyl iodide Raman spectrum from ref 62, obtained with excitation at 514 nm.

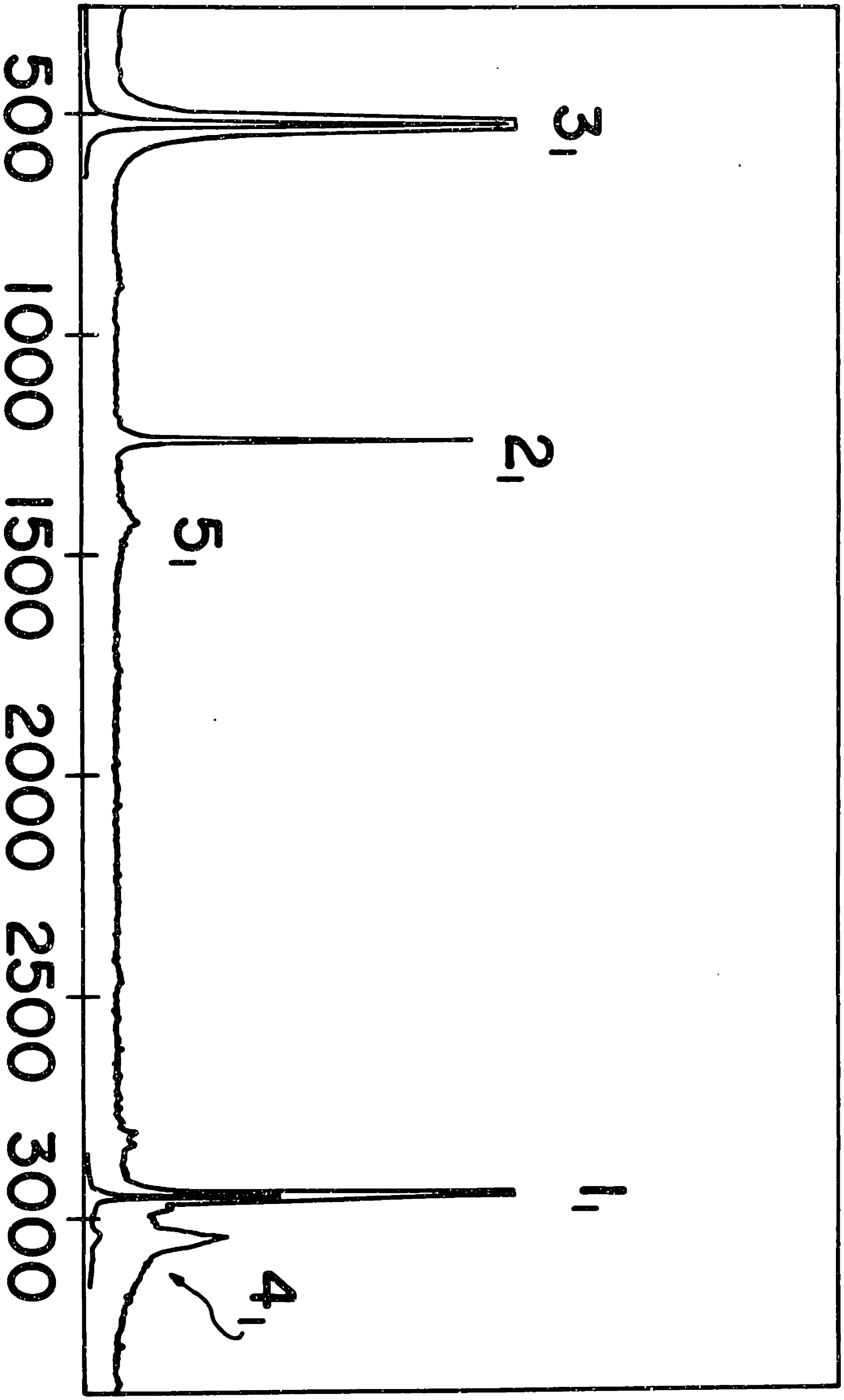
500
1000
1500
2000
2500
3000
3
2
5
1
4

Fig 5-7 - Methyl Iodide Raman spectrum obtained with excitation at 355 nm, note the weak ν_3 overtone (3_2).

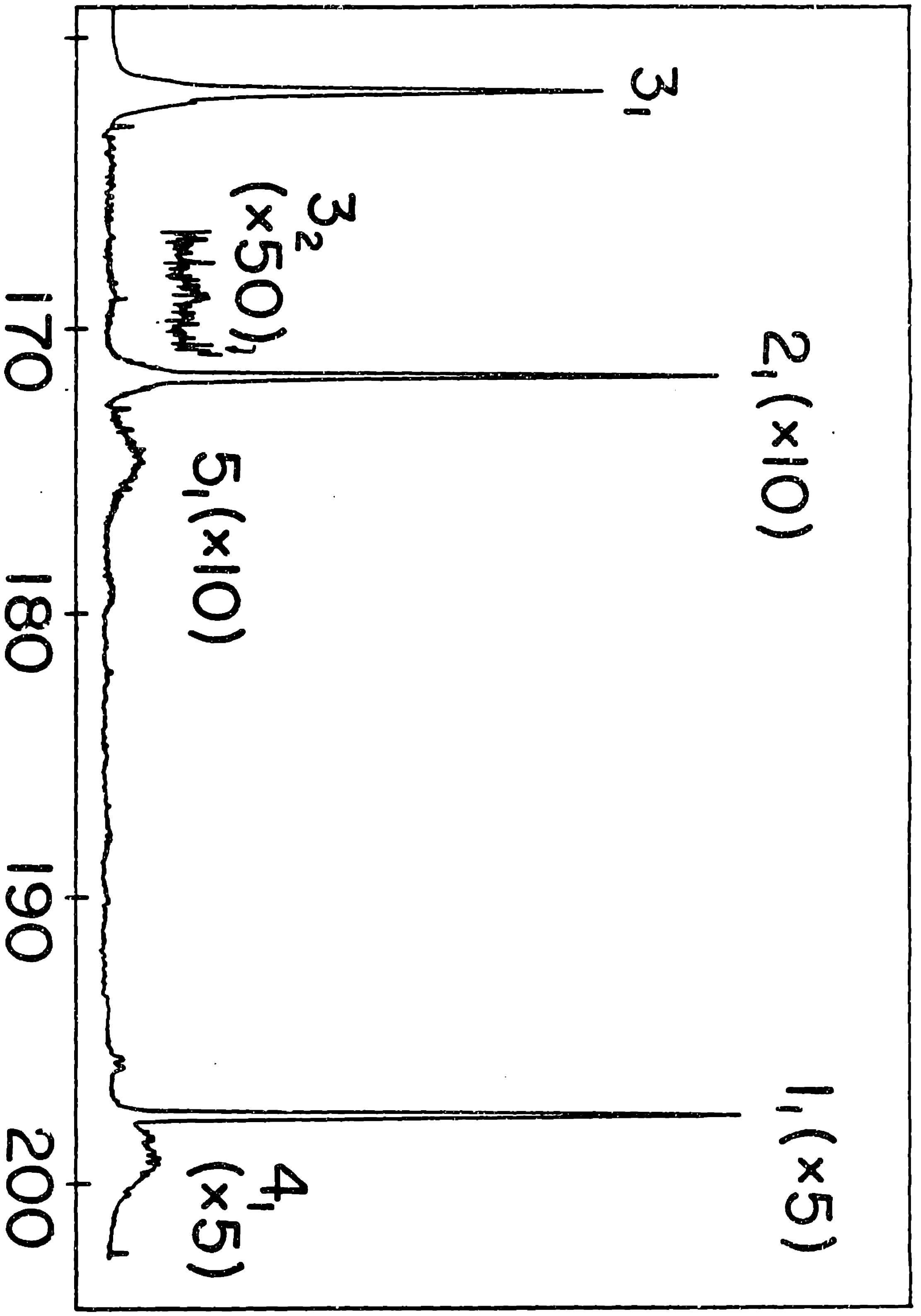
3₁
3₂ (×50)
2₁(×10)
5₁(×10)
1₁(×5)
4₁ (×5)
170
180
190
200

Fig 5-8 - Methyl iodide Raman spectrum obtained with excitation at 266 nm, note the long ν_3 progression. Orders refer to grating orders.

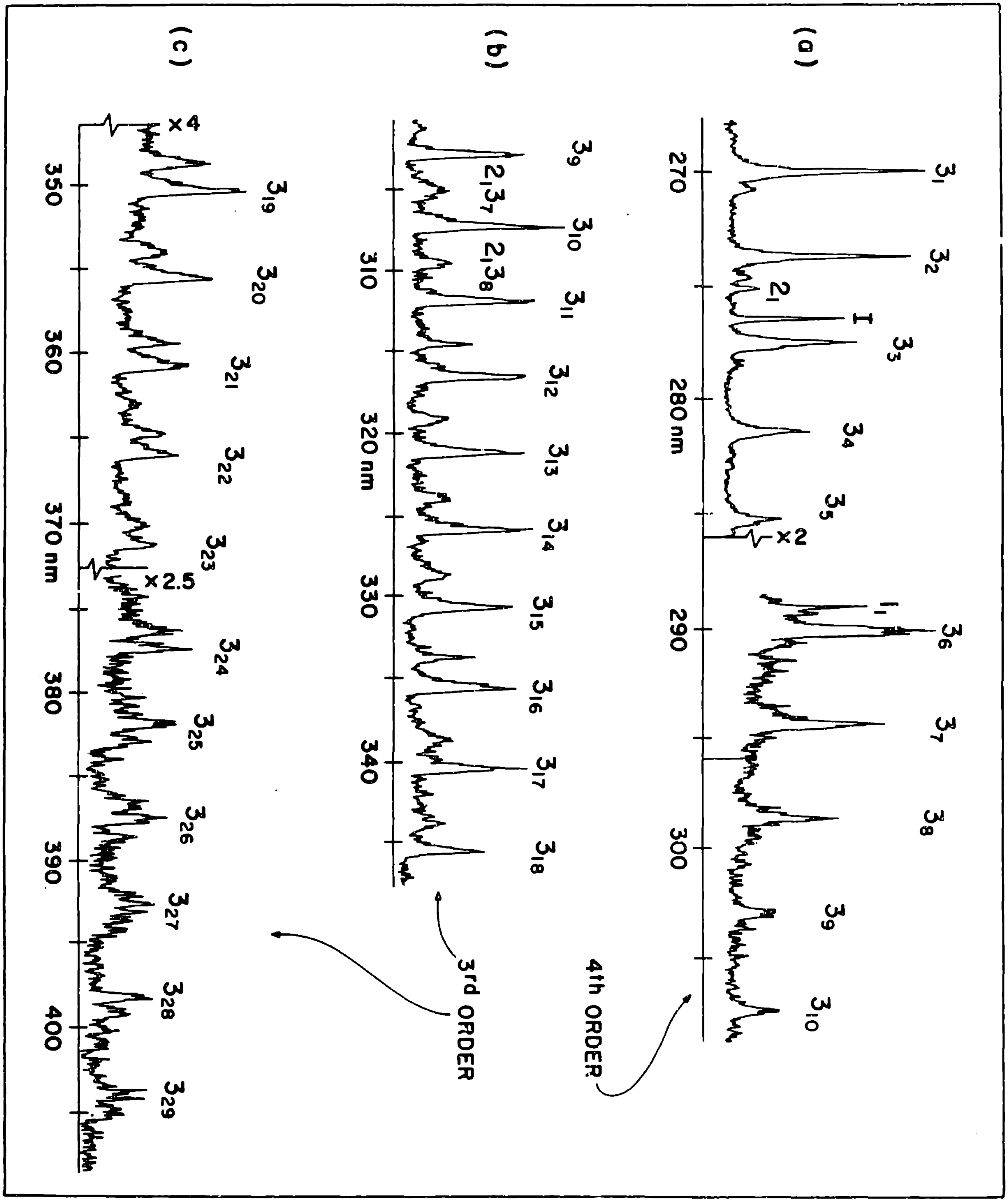
(a)
(b)
(c)
270
280 nm
290
300
310
320 nm
330
340
350
360
370 nm
380
390
400
3_1
3_2
2_1
I
3_3
3_4
3_5
×2
1_1
3_6
3_7
3_8
3_9
3_{10}
4th ORDER
3_9
2_13_7
3_{10}
2_13_8
3_{11}
3_{12}
3_{13}
3_{14}
3_{15}
3_{16}
3_{17}
3_{18}
3rd ORDER
×4
3_{19}
3_{20}
3_{21}
3_{22}
3_{23}
×2.5
3_{24}
3_{25}
3_{26}
3_{27}
3_{28}
3_{29}

bands originating from a single electronic state. Our results show that I_{ν_1}/I_{ν_3} decreases from approximately .45 to .18 as resonance is approached. This indicates that the off-resonance ν_1 intensity contains substantial contributions from another surface. I_{ν_2}/I_{ν_3}, on the other hand, remains constant, indicating that the two bands originate from a single surface (the ^3Q_o). Likewise observation of weak intensity in the asymmetric e modes in the 514 nm spectrum is not necessarily an indication of dynamics associated with these modes. The net forces at the Franck-Condon region along these coordinates must vanish by symmetry. A large intensity due to fast spreading, the result of a drastic change of the local second derivative upon excitation, is also unexpected for the e-modes. Hence, these bands do not seem to be dynamic in origin. However, variation of the transition moment function with the corresponding normal coordinate can produce intensity in asymmetric fundamental bands. So far, we have treated the transition moment as a constant over the initial ground state vibrational wave function. The transition moment, μ, can be expanded in a Taylor series around the equilibrium geometry

$$\mu = \mu_0 + q \cdot \frac{\partial\mu}{\partial q}\bigg|_{q_0}$$

The second term, assumed to be small, has been neglected in our treatment. This is valid in most cases. However, the wave packet which is prepared on the excited state surface is: $\mu|\chi_0\rangle$ where $|\chi_0\rangle$ is the initial vibrational wave-function, thus:

$$|\phi\rangle = \mu_0|\chi_0\rangle + q\frac{\partial\mu}{\partial q}\bigg|_{q_0}|\chi_0\rangle$$

the first term just transfers $|\chi_0\rangle$ into a new PES without change. The second term, being linear with respect to q_n, prepares a wave packet which looks more like the first excited state in the normal coordinate q_n.

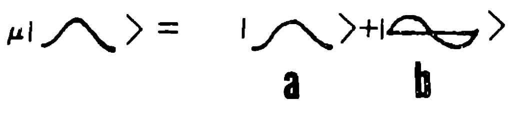

Wave packet (a) needs to evolve on the excited state to develop overlap with $v_n = 1$ while (b) can already at $t = 0$ emit back into $v_n = 1$. It is in this sense that we believe the e-mode intensities are "non-dynamic" in origin. There will, of course also be "dynamic" intensity in the modes from evolution of a or b, although in this case one would expect very small dynamic contributions to the intensity.

This short discussion should provide a cautionary note regarding off-resonance Raman spectra. In general, when only fundamentals are present in a spectrum it is advisable to be extremely cautious in drawing conclusions about dynamics.

In order to increase the effective observation time for molecular dynamics, the laser was tuned closer to resonance, producing the spectrum shown in figure 5-7 (at $\lambda = 355$ nm excitation, $\Delta\omega = 10{,}000$ cm^{-1}). This spectrum is not strikingly different from the previous one, except for a slight decrease in ν_1 relative to ν_3. A significant difference, however, is the appearance of a barely visible new band corresponding to two quanta in the C-I stretch. The intensity in this new band shows that within less than .5 femtoseconds following absorption the wave packet has evolved (mainly in momentum space) enough to develop a small but observable overlap with $v_3 = 2$. This observation substantiates the original expectation that the earliest motion of the wave packet would be predominantly along the C-I coordinate.

Fig. 5-8 is a spectrum for near-resonant excitation, obtained with $\lambda = 266$ nm ($\Delta\omega = 600$ cm^{-1}). This spectrum is dominated by an astonishingly long progression in the/ C-I stretch. Up to 29 quanta in v_3 are observed, corresponding to a ground state vibrational energy equal to 75% of the dissociation energy. This pattern is consistent with a wave packet that is initially at rest at $t = 0$ ($\langle P_0 \rangle = 0$), and then accelerates essentially along the C-I coordinate. Some fundamental activity in ν_1 and ν_2 is also noticeable. The long intense ν_3 progression, is an unmistakable signature of wave packet dynamics on a resonantly excited surface.

The first several features in the observed progression are pure $_3$ overtones. Farther along in the progression, and hence also later in time, new types of bands appear. These are combination bands between ν_3 and ν_2, indicating that the initial motion which is almost exclusively along q_3 subsequently develops components of motion in the q_2 direction as well. At even higher vibrational energies the spectrum broadens so that only envelopes of bands containing several vibrational eigenstates can be seen with our current resolution.

Figure 5-9 shows a qualitative two dimensional contour diagram, kindly provided by R. Coalson of Harvard University, of the excited state surface as a function of q_2 and q_3. The surface is repulsive along q_3 with contour lines almost parallel to the q_3 coordinate for small C-I displacements. The minimum along q_2 in this region is at about $\Theta_{HCH} = 108^o$ (i.e. the ground-state equilibrium bond angle). This is consistent with an $n \rightarrow \sigma^*$ excitation where the CH_3 part of the molecule is not expected to feel any significant new forces at its ground state C-I configuration. For large q_3, however, the potential along q_2 correlates to the q_2 potential of the free CH_3 radical. This potential has its minimum at a value of q_2 corresponding to a planar configuration ($\Theta_{HCH} = 120^o$). Thus, as the wavepacket moves almost directly along q_3, it comes to feel new forces in the q_2 direction, causing it to "turn", increasing the HCH bond angle in the process. Not only does the potential minimum in q_2 shift to a larger equilibrium angle as q_3 increases, but its shape changes as well. Since the q_2 vibrational frequency decreases during the dissociation from 1200 cm^{-1} in CH_3I to 600 cm^{-1} in the free CH_3 product, the

Fig 5-9 - Schematic illustration of the CH_3I excited state potential surface for q_2 and q_3. (a) Equipotential contour diagram with a photodissociation trajectory. (b) Sections of the potential along q_2 at the ground state geometry (1), and at large q_3(2).

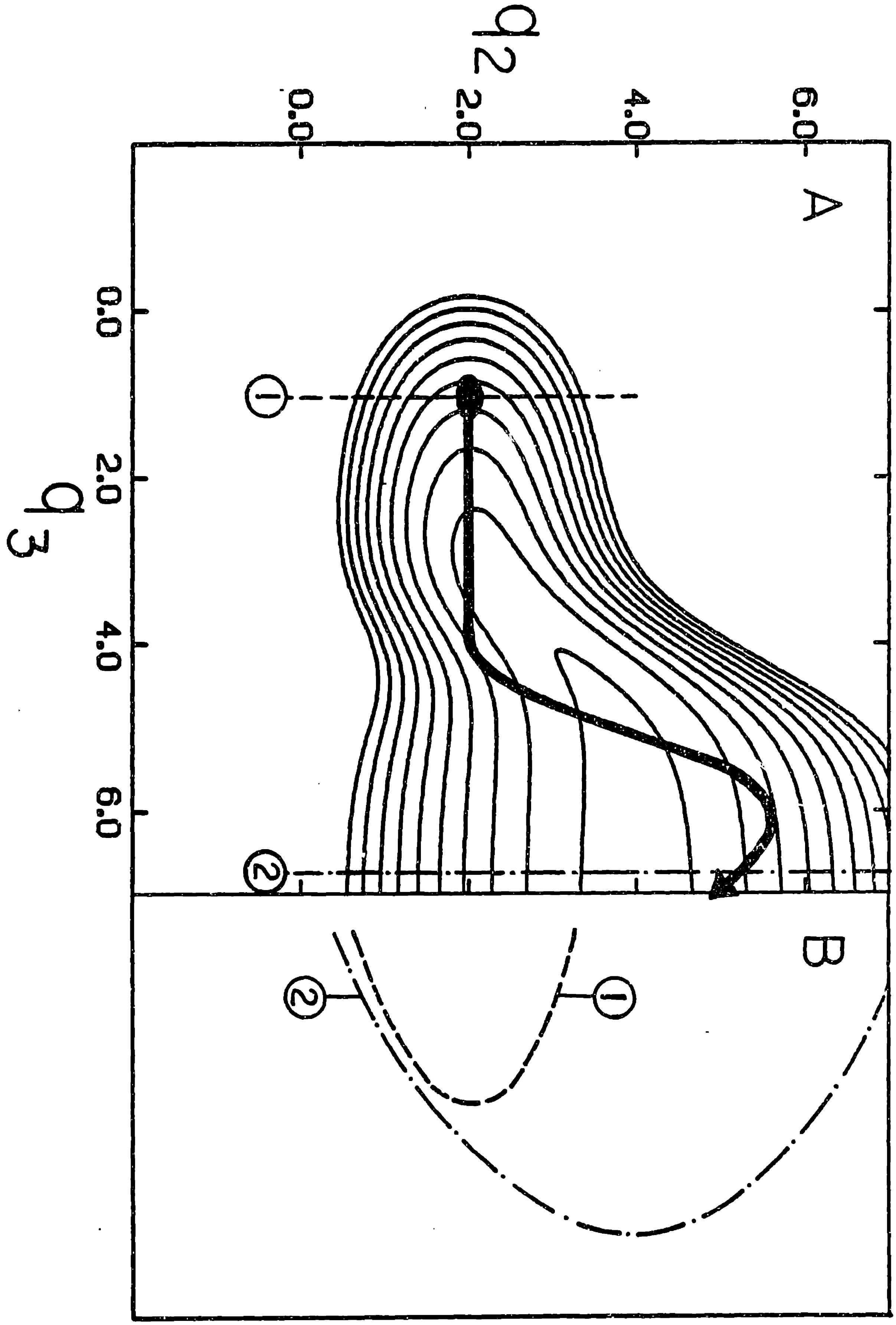
A
B
q_2
q_3
0.0
2.0
4.0
6.0
0.0
2.0
4.0
6.0
①
②
①
②

contour lines have to "open up" as q_3 increases. A schematic photodissociation trajectory illustrating this is shown as the heavy line in figure 5-10.

At t = 0 the wavepacket is only slightly displaced from the minimum along q_2. The only strong force it feels is along q_3. The trajectory proceeds along this coordinate developing overlaps with higher vibrational levels in q_3. This leads to a spectrum dominated by ν_3 overtones. The intensities decrease with increasing V_3, due to acceleration and rapid spreading of the wavepacket in its transition from a localized version towards one corresponding to a free particle in q_3. As the C-I bond length increases, new forces in q_2 cause an increase in bond angles and a trade of vibrational energy from q_3 to q_2, resulting in the appearance of new ν_2, ν_3 combination modes. The dissociation eventually leads to a CH_3 product vibrationally excited in the q_2 coordinate as observed in the molecular beam[54] and infra red emission studies.[55]

As has been discussed earlier, besides pinpointing the reactive process on the excited state surface, the spectrum contains information about the ground state electronic surface as well. In this case the information is quite selective and pertains mainly to the two normal coordinates q_2 and q_3. Tables 5-1 and 5-2 list the band positions and the spectroscopic constants derived from the spectra. The fact that only two types of bands appear in the spectrum illustrates a distinct advantage of Raman spectroscopy with dissociative intermediate states over conventional fluorescence techniques for the study of ground state dynamics. Out of an enormous density of states the Raman spectrum isolates a few for observation. This makes the task of assignment and analysis easy to accomplish.

Fig. 5-10 shows a plot of the vibrational energy differences $(G_{V_3+1} - G_{V_3})$ as a function of V_3. The figure includes levels observed by us (open circles with

TABLE 5-1

v_3	v_2	Energy cm^{-1}
1	-	532.8
2	-	1060
-	1	1254
3	-	1579
4	-	2092
5	-	2594.5
3	1	2814
6	-	3093.5
4	1	3306
7	-	3589.5
8	-	4079
9	-	4565
7	1	4781
10	-	5044
8	-	5277
11	-	5516
9	1	5788
12	-	5982
10	1	6248
13	-	6446
11	1	6702
14	-	6896
12	1	7159
15	-	7347
13	1	7604
16	-	7784
17	-	8049
18	-	8634
19	-	9060
20	-	9476
21	-	9886
22	-	10293
23	-	10697
24	-	11091

TABLE 5-2

	cm^{-1}
ω_2	1252.4
ω_3	533.8
ω_{33}	2.98
ω_{23}	4.5

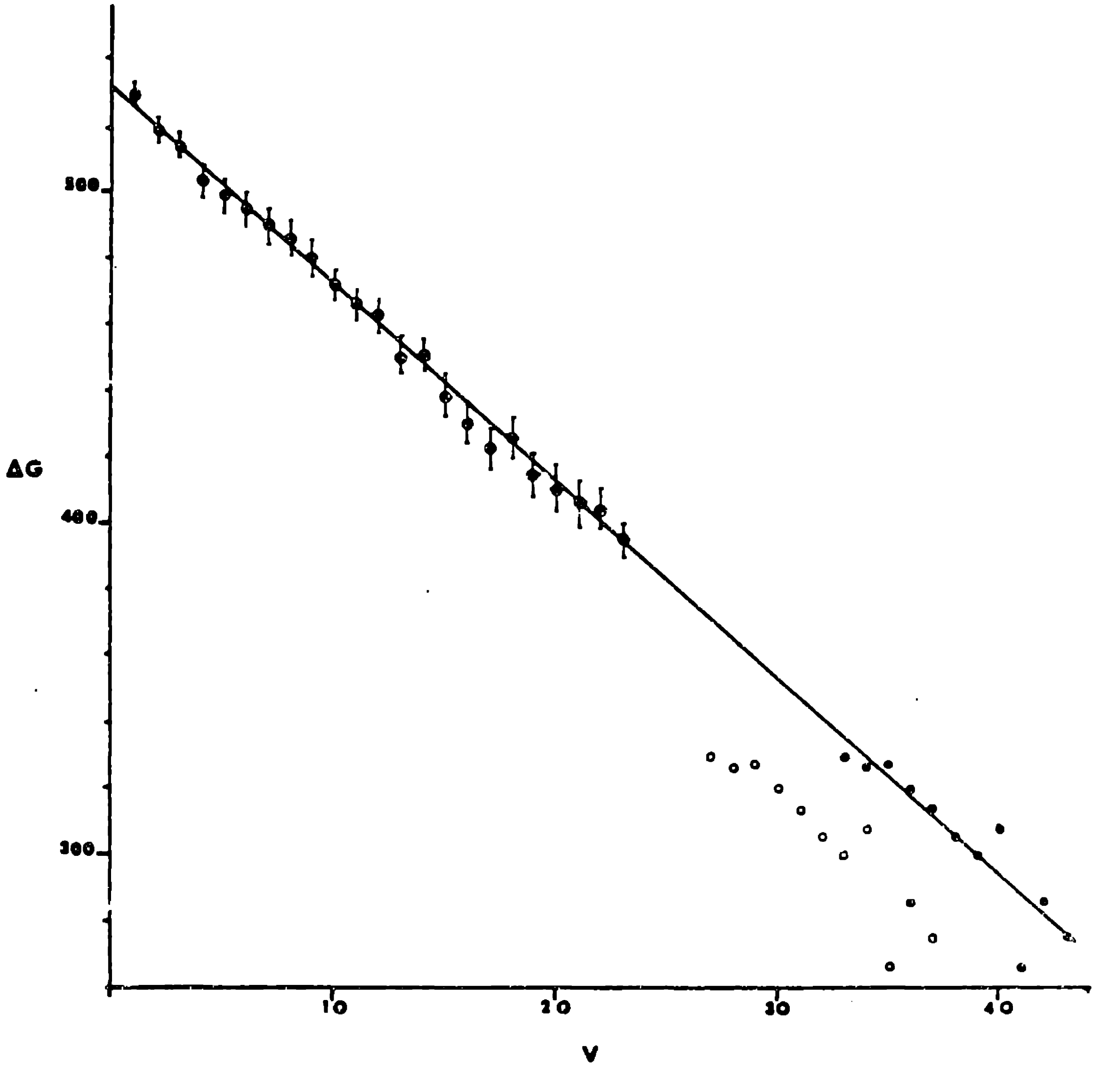

Fig 5-10 - Birge-Sponer plot for v_3 levels observed in Fig 5-8 (open circles with error bars), and v_3 levels observed in the matrix isolation study (ref 57). Open circles refer to Bondybey's assignment and filled ones to our reassignment of that same data.

error bars) as well as those observed by Bondybey in the matrix isolation study. (Open circles refer to Bondybey's assignment and dark ones mark our reassignment of his data). The data are consistent with a straight line Birge-Sponer plot, indicating that the C-I mode is well described by a local Morse oscillator up to V_3 42.

A qualitative two dimensional contour diagram for the ground state potential along q_3 and q_2 is shown in Figure 5-11. For fixed q_3, the q_2 dependence is harmonic. For fixed q_2, the q_3 dependence is that of a Morse oscillator. For low energies q_2 and q_3 are only slightly coupled. This is consistent with known infra red data and our observation of a clear progression in the C-I stretch. As with the excited state potential, this surface correlates asymptotically to a q_2 dependence characteristic of a free CH_3 radical. Its minimum for large R_{C-I} therefore must also move towards a value of q_2 corresponding to $\Theta_{HCH} = 120^o$, and the curvature must open from one giving ω_2 approximately 1200 cm^{-1} to one with approximately 600 cm^{-1}.

If a local C-I oscillator were prepared on this surface with energies less than 10,000 cm^{-1} the resulting wave packet motion would be almost periodic. The "energy stored in the C-I bond" would not spread significantly to other degrees of freedom. At higher energies, however, a C-I oscillator can only be prepared as a superposition of ν_3 and ν_2 eigenstates, which will evolve in time, executing complicated motion involving both q_2 and q_3. This phenomenon will manifest itself in the broadening of bands in this energy region. The band widths are a measure of the time scale of energy flow from C-I stretch into umbrella bend, a dephasing process.

Our Birge-Sponer plot of the ν_3 overtones can be used to calculate an

Fig 5-11 - Methyl iodide ground state potential surface along q_2 and q_3: (a) equipotential contour diagram illustrating schematically the coupling between q_2 and q_3. A trajectory for a local q_3 oscillator at high energies is shown in heavy line. (b) Sections of the potential along the thermodynamic dissociation path (2) and along a local q_3 oscillator (1). These illustrate why the Morse oscillator extrapolation over-estimates the dissociation limit.

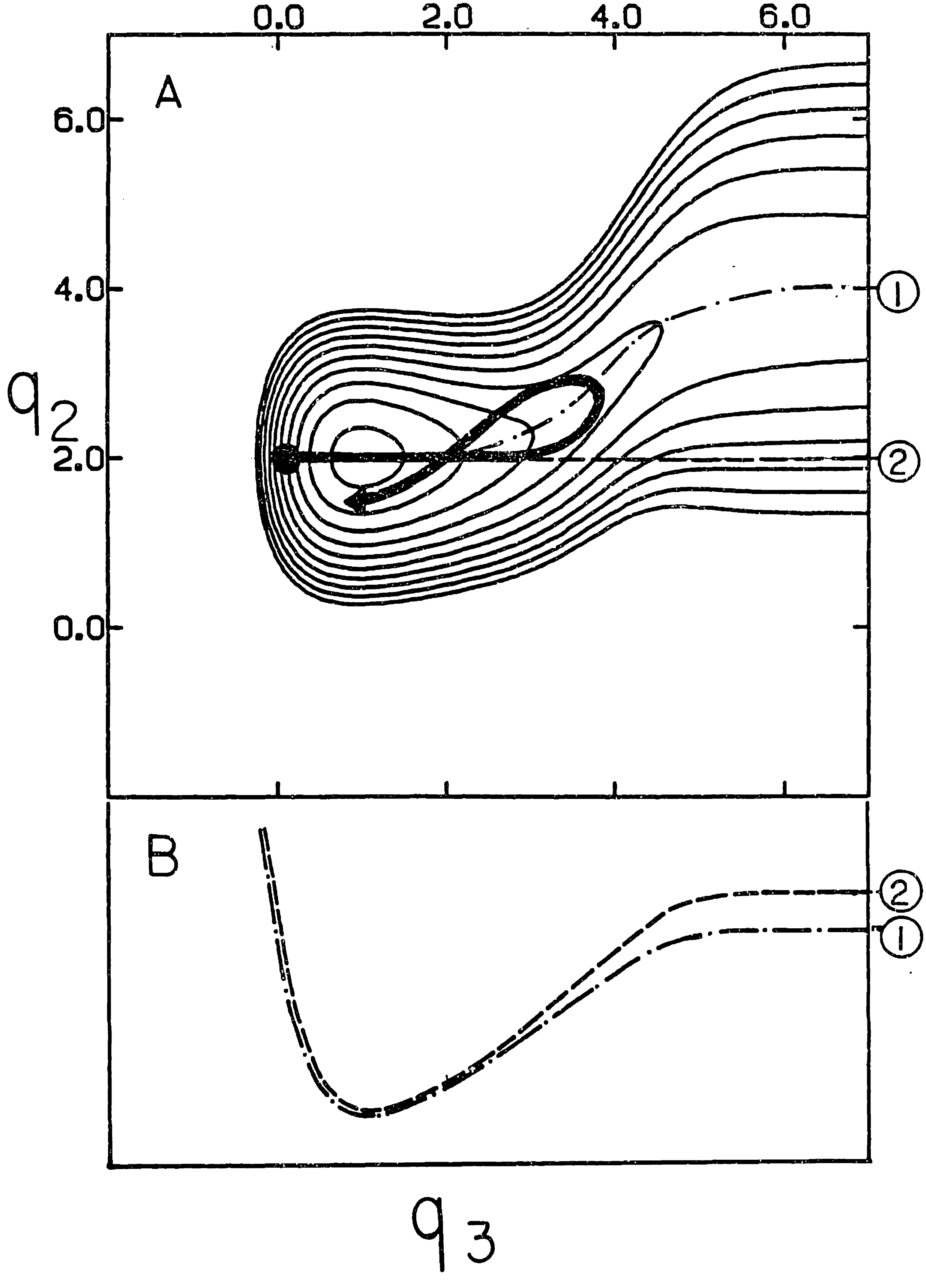
0.0
2.0
4.0
6.0
A
6.0
4.0
q_2
2.0
0.0
①
②
B
②
①
q_3

approximate dissociation limit for the ground stae surface. We obtain De = 2.9 eV using the Morse formula and our constants. This value over-estimates the true De by .6 to .4 ev when compared to the reported dissociation energy obtained from thermodynamic studies.[63] Fig. 5-11 gives a qualitative explanation for this discrepancy. The Morse extrapolation "forces" the molecule to dissociate purely along q_3 keeping $\Theta_{HCH} = 108^o$. When the difference in energy between planar CH_3 and CH_3 at $\Theta_{HCH} = 108^o$ (.33 eV) is taken into account using the potential for q_2 in CH_3 as suggested in ref. 59, the Morse prediction is in surprisingly good agreement with the thermodynamic value. The large uncertainty in De (2.3 - 2.5 eV) as reported by the thermodynamic studies can be narrowed somewhat, by using results from Bondybey's matrix isolation experiment. Fig. 5-12 illustrates how these data can be used to estimate the ground state dissociation energy.

In this experiment emission was observed at 965 nm (10363 cm^{-1}) into V_3 = 36, according to our assignment. The energy of V_3 = 36 is 15,514 cm^{-1}. If we assume a Ne induced C-I* well depth approximately 2000 cm^{-1}, as suggested by these authors, and adding the known I* -I energy difference (7604 cm^{-1}) yields De = 2.5 eV.

All conclusions drawn from the data to this point are based on rather qualitative arguments. Even at this level of analysis however, quite instructive conclusions have been drawn about the two PES's, demonstrating the power of the technique and the time dependent point of view. In order to refine the picture, a more quantitative analysis is required. In chapter 7 a summary of our dynamical calculations is given.

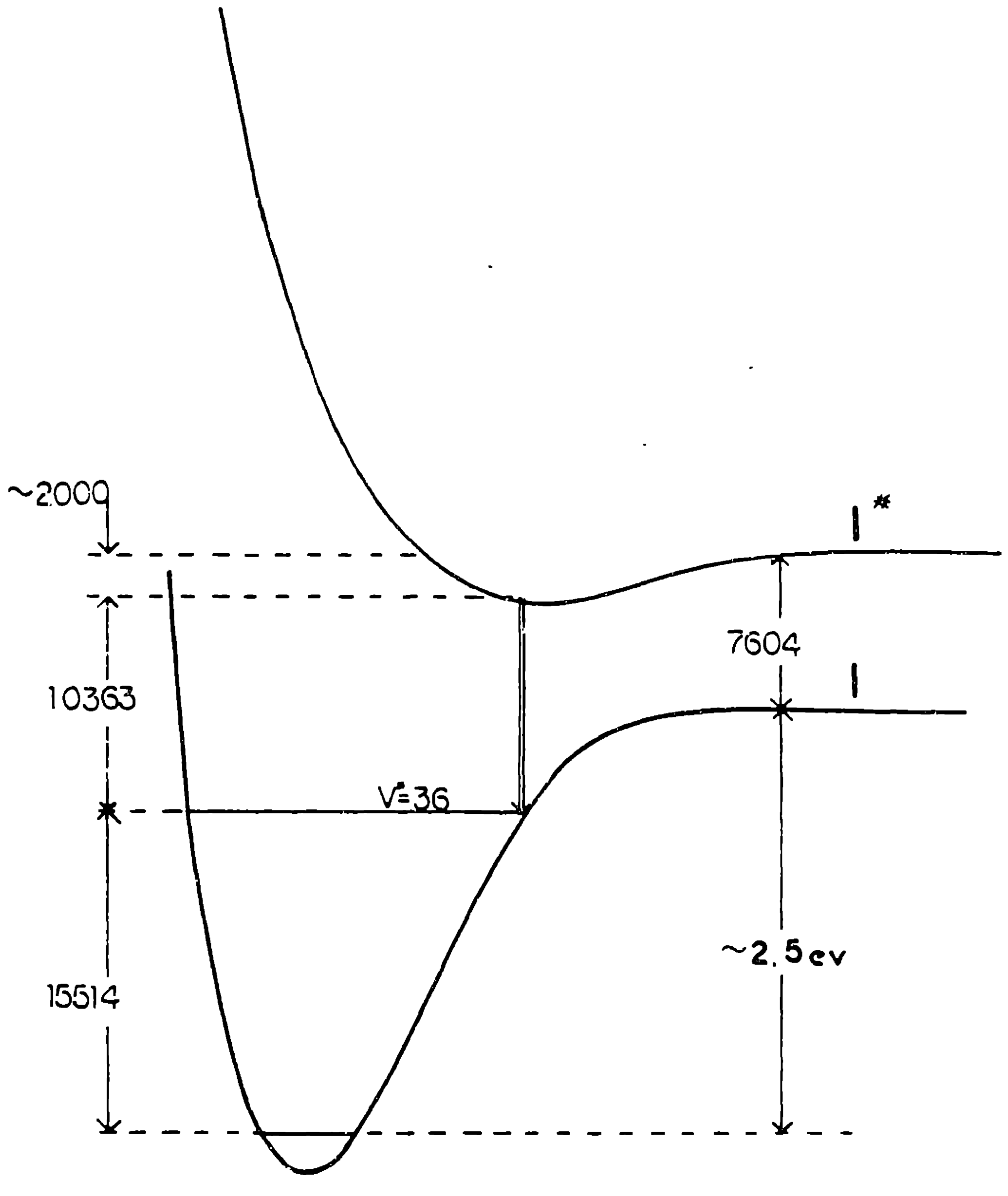
~2000
10363
15514
V"=36
7604
I*
I
~2.5ev

Fig 5-12 - Estimation of ground state dissociation energy.

CHAPTER 6.

OZONE PHOTODISSOCIATION DYNAMICS

I. Background.

The photodissociation of ozone presents a very different case from that of methyl iodide. Though ozone appears to be simpler than methyl iodide because of its symmetry and the smaller number of atoms, that very symmetry contributes to its dynamic complexity. The initial equivalence of the two O-O bonds requires that dissociation proceed by wave packet spreading, rather than by a simple motion of the packet's center (which would be dominated by forces). A detailed study of the photodissociation mechanism should provide some insight into the effects of symmetry constraints on that type of reaction.

The U.V. photolysis of ozone is important not only from a theoretical point of view but also from a practical one. The U.V. absorption band (Hartley Band) provides the most important atmospheric U.V. shield in the 300-200 nm region. When ozone absorbs a U.V. photon it dissociates to yield mostly $O_2\ {}^1\Delta$ and $O\ {}^1D$, both of which are important constituents in atmospheric reactions. $O\ {}^1D$ is especially reactive. Once produced, it goes on to react with hydrogen-containing compounds to yield OH. In the atmosphere, the predominant reaction involves H_2O. Because of its importance to atmospheric chemistry, ozone has been a subject of numerous investigations, theoretical as well as experimental.

The U.V. absorption spectrum (Fig. 6-1.) has been studied by many groups.[64,65,66] The most recent report deals with the effects of temperature on

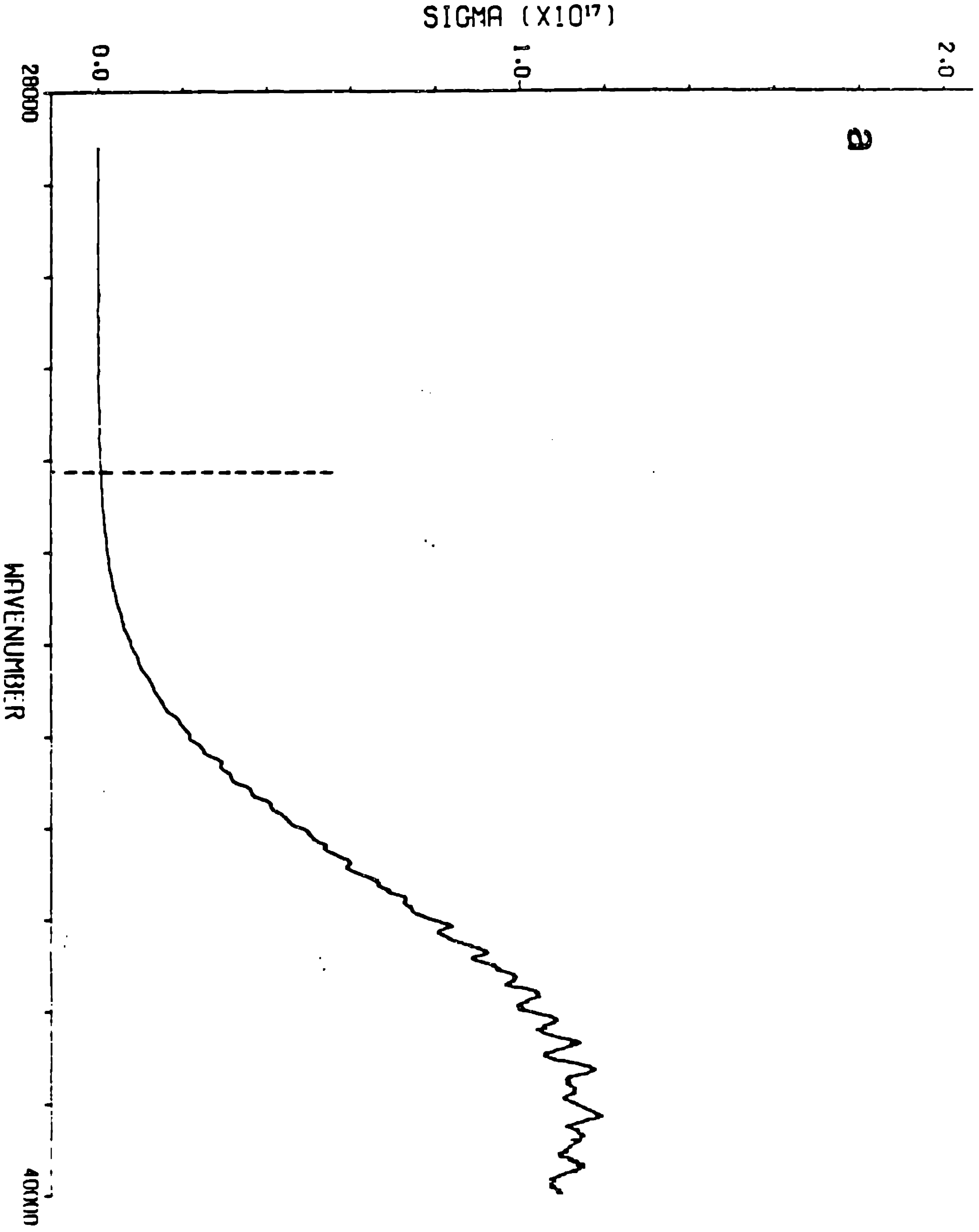
SIGMA (X10^17)
0.0
1.0
2.0
28000
40000
WAVENUMBER
a

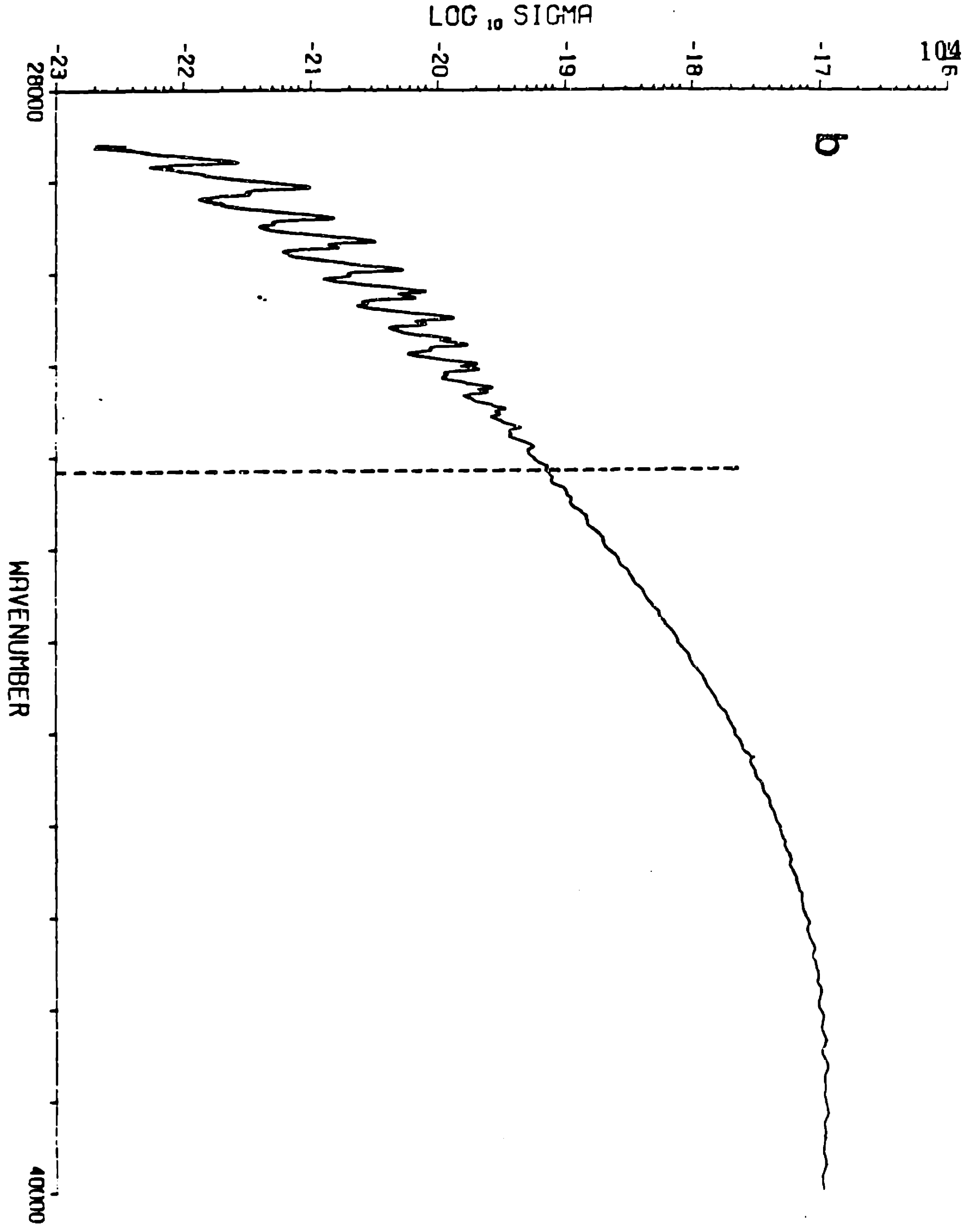

Fig 6-1 - Ozone U.V. absorption spectrum taken at dry ice temperature. (a) the Hartley band continuum, note the faint structure in the middle of the band. The dashed line marks the threshold for O_2 ^{1} and O ^1D production. (b) Logarithmic plot of the same spectrum showing vibrational progressions at the red end (Huggins bands). Both spectra were kindly provided by Yoshino.

the spectrum.[67] Unlike methyl iodide which has a smooth absorption spectrum, the ozone spectrum exhibits faint structure, which becomes more pronounced when the spectrum is taken at dry ice temperatures. In contrast, to this weak structure in the Hartley region, the red end of the spectrum (Fig. 6-1(b)) (the Huggins bands 350-308 nm) shows distinct vibrational band structure even at room temperature. This region has been recently investigated by D. Katayama. Using both, $^{16}O_3$ and $^{18}O_3$, he was able to pin down vibrational assignments for most of the observed bands. The spectrum consists of long progressions in one of the stretching modes (ν_1 according to Katayama). Also visible in the spectrum are hot bands originating from V_1'' and $V_3'' = 1$. There has been a long-standing controversy concerning the origin of the Huggins bands. Some suggested the $^1A_1$ electronic state[69] while others[70,71] maintained that the Huggins band is actually part of the Hartley continuum, i.e., the two bands constitute a continuous absorption into a single electronic surface ($^1B_2$). Recent experiments in our laboratory indicate that the Huggins band is indeed a $^1B_2$ —— X $^1A_1$ transition. The Hartley band is unambigiously assigned to the $^1B_2$ state. This assignment is supported by many theoretical studies,[69,71] as well as product angular distribution measurements by Fairchild.[72]

Studies of the absorption spectrum of vibrationally excited O_3 were done by S.G. Adler.[73] Vibrationally excited O_3 (one quantum in the antisymmetric stretch) was prepared by a pulsed CO_2 laser. Subsequent collisions produce molecules with one quantum of symmetric stretch or bend. Adler was able to produce absorption profiles for each of the "hot bands".

Absorption profiles of vibrationally excited molecules provide important information about the shape of the excited state potential in the vicinity of the

Franck-Condon region. Fig. 6-2. shows a diagram of the effect of vibrational excitation on the absorption spectrum, for strongly displaced oscillators (a) and for a transition between two similar surfaces (b). Parts a and b of Figure 6-2. can also be viewed as different coordinates within the same molecule. When the two potentials are strongly displaced, as shown in figure 6-2(a), the absorption profiles reflect the shape of the initial wave-function. The $V'' = 0$ spectrum is gaussian in shape and the $V'' = 1$ spectrum exhibits a "node" where the cold spectrum has its maximum. When the two potentials are similar, as shown in figure 6-2(b), the spectra are similar as well. Hence hot band absorption profiles provide a sensitive probe for the difference between ground and excited state potentials. The mode along which the difference between the two potentials is greatest, shows the largest difference between $V'' = 0$ and $V'' = 1$ spectra. That same mode is also expected to dominate the short dynamics. The vibrationally excited wave packet also probes slightly larger regions of the surface than does $V'' = 0$, and therefore provides information about the surface in a wider vicinity of the Franck-Condon region. The results obtained by Adler on ozone demonstrate that displacement in the symmetric stretch dominates the breadth of the Franck-Condon progression in the Hartley band.

The quantum yield for production of O ^1D has been a subject of many investigations.[74-79] Fig. 6-3 is a level diagram showing all accessible photolysis products. The $^1B_2$ state correlates to O_2 $^1\Delta$ and O^1D_1, and the production threshold for these products is 308 nm. Experimental results show that above this threshold only two channels are open to the reaction:

$$O_3 + h\nu \rightarrow O_2{}^1\Delta + O^1D_1$$

$$\rightarrow O_2{}^3\Sigma_g^- + O^3P$$

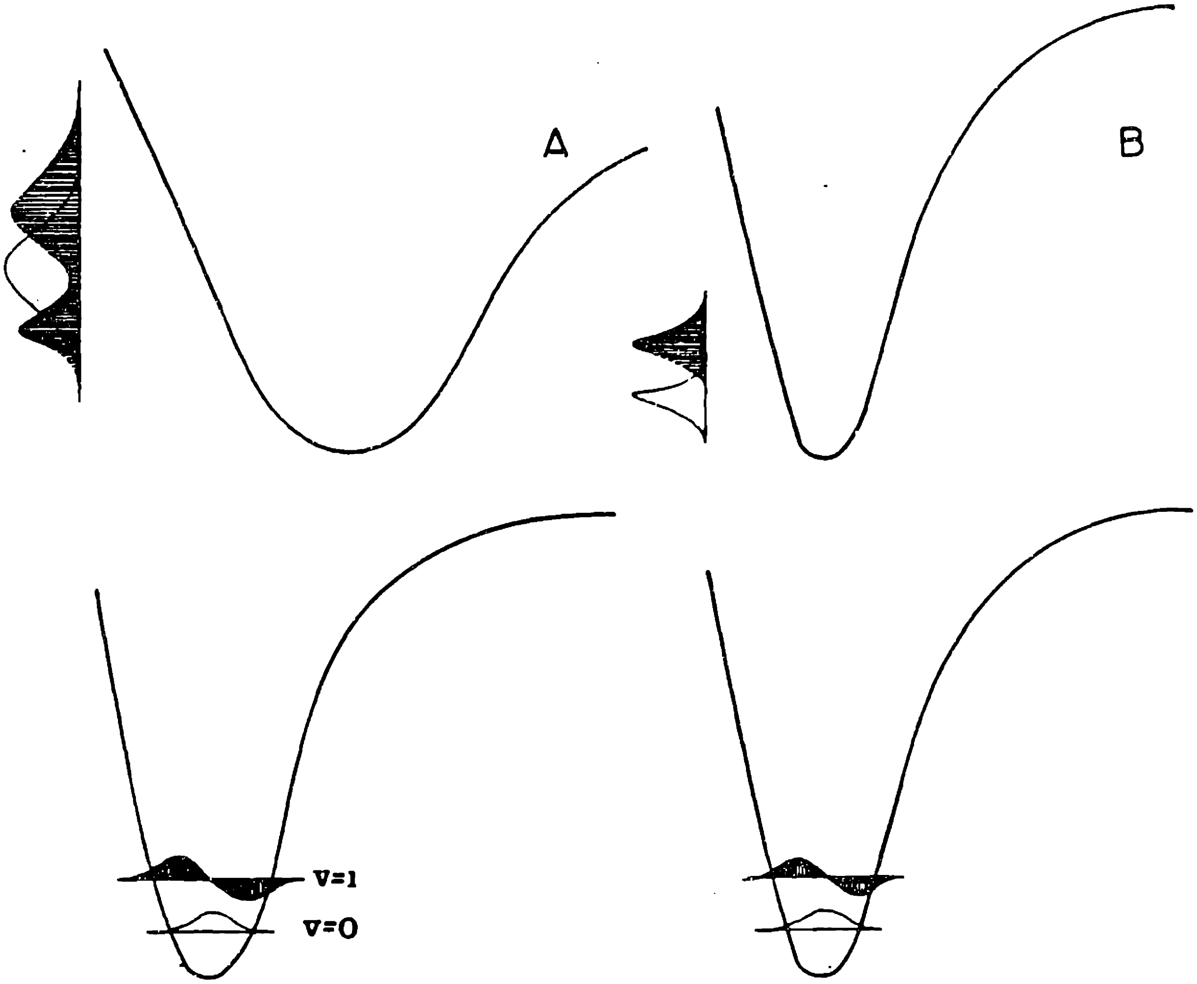

Fig 6-2 - Absorption spectra of vibrationally excited molecules. (a) Strongly displaced potentials. (b) Transition involving two similar surfaces.

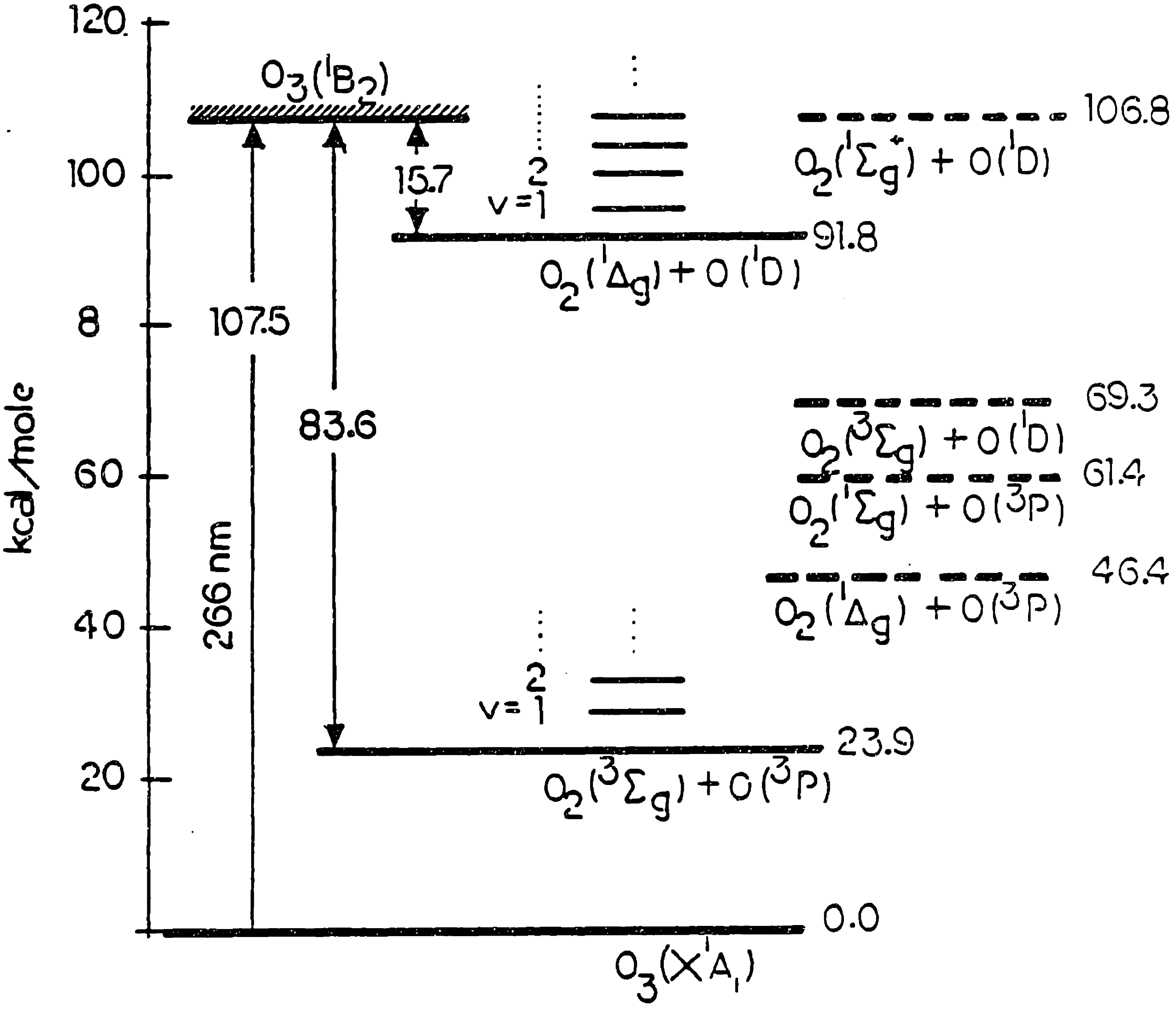
120
100
8
60
40
20
kcal/mole
O3(1B2)
107.5
266 nm
83.6
15.7
v=1
2
v=1
2
106.8
O2(1Σg+) + O(1D)
91.8
O2(1Δg) + O(1D)
69.3
O2(3Σg) + O(1D)
61.4
O2(1Σg) + O(3P)
46.4
O2(1Δg) + O(3P)
23.9
O2(3Σg) + O(3P)
0.0
O3(X1A1)

Fig 6-3 - Energy level diagram for possible O_2 and O products accessible in the u.v. photolysis of ozone. Dashed lines indicate spin forbidden products.

Below threshold, the only detected products are O_2 $^3\Sigma_g^-$ and O ^3P. The relatively small yield of ground state products ($\lambda < 308$) assures that curve crossing plays only a minor role in the dissociation at 266 nm.

Vibrational and velocity distributions were obtained (at 266nn) using photofragment spectroscopy by Sparks et al.[80] These results are shown in Fig. 6-4 along with results obtained by J. Valentini[81] for comparison. The Valentini results were obtained by probing the products by Coherent Antistokes Raman Spectroscopy (CARS), a technique providing sufficient resolution to obtain information on the rotational distributions of the O_2 $^1\Delta$. The CARS results show interesting alterations in the populations of even and odd rotational levels. Whether this is an indication of a dynamic process or an experimental artifact remains to be resolved.

The ground electronic surface of O_3 has been investigated by Barbe et al.[82-87] using high resolution infra red and microwave absorption. Their results indicate that the ground state surface is highly anharmonic, as expected for a molecule bound by only 1 eV. Barbe has proposed a three dimensional surface in analytic form based on polynomial expansions.[82] Though this surface does not predict the proper dissociation limit, it gives indications as to band positions with moderate accuracy. The shallow potential and near degeneracy of the symmetric (ω_1= 1103 cm^{-1}) and antisymmetric (ω_3 = 1041 cm^{-1}) stretching modes make the ground state of ozone very difficult to deduce from spectroscopic data.

Numerous theoretical calculations have been done on the O_3 molecule and its electronic structure. The latest ab initio results predict a ground state binding energy of approximately .5 eV (50% accuracy). These calculations do reproduce the fundamental vibrational frequencies quite accurately. The $^1B_2$ surface was

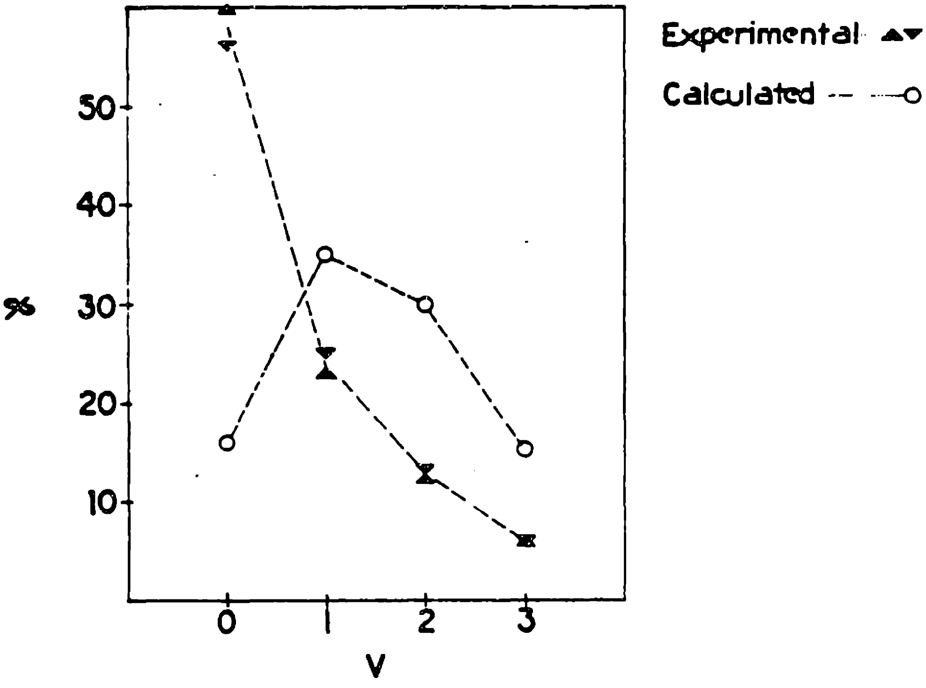

Fig 6-4 - Vibrational distribution of $O_2\,{}^1\Delta$. Comparison of experimental results (▲ ref 80; ▼ ref 81) and theoretical prediction (o ref 8a).

predicted by the *ab initio* calculations[71] to be of C_S symmetry with a saddle point along the C_{2V} axis. On each side of the saddle ($R_{O\text{-}O}$ = 3.4 a_o), a shallow minimum (bound by approximately .2 eV with respect to the O_2 $^1\Delta$ and $O^1 D_1$ dissociation limit) is predicted. The authors used their *ab initio* surfaces to reproduce the Hartley absorption spectrum with moderate success. Most of the discrepancy occurred on the red end of the spectrum. An attempt to reproduce the vibrational distribution yielded results that were significantly different from experimental observations.[88] Semi-empirical surfaces based on the *ab initio* ones were later proposed by M. Shepperd.[89] Fig. 6-5. shows a contour plot of these surfaces. Shepperd used these surfaces to calculate absorption profiles for vibrationally excited molecules. His absorption profiles are in qualitative agreement with the experiment. However, product vibrational distributions were still in very poor agreement with experimental results. (See Fig. 6-4.)

II. Photoemission Studies.

We have obtained the emission spectrum shown in Fig. 6-6. The excitation wavelength (λ=266 nm) was chosen so that $\Delta\omega$ = 1700 cm^{-1}. Bands are labeled V_1, V_2, V_3, with assignments referring to basis functions which carry oscillator strength, and not to eigenstates. The spectrum is dominated by symmetric stretch (ν_1) progressions. Bands up to 500 cm^{-1} below the dissociation limit are observed. Table 6-1 summarizes all our observed bands and energies. The calculated band positions are based on the Barbe surface (from ref. 82). Fig. 6-7. shows higher resolution scans of the features assigned as 004 and 500. The higher resolution scans indicate that strong mixing between the fundamental normal modes occurs at

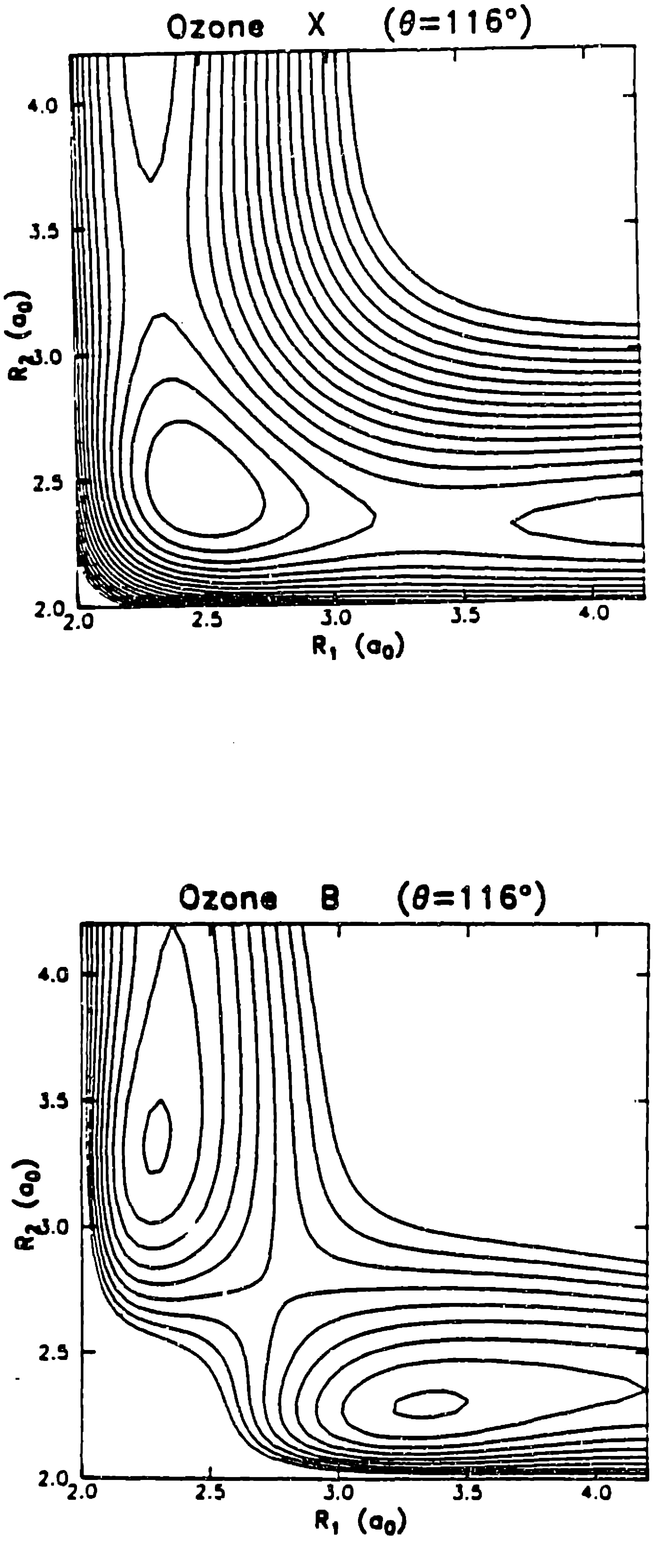

Fig 6-5 - Semiempirical potential energy surface for the X $^1A_1$ and the $^1B_2$ states of ozone (from ref 89).

Fig 6-6 - Ozone Raman spectrum obtained by exciting at 266 nm. Bands are labled v_1, v_2, v_3. Referring to basis functions. The insert is a higher resolution scan of the first band (100).

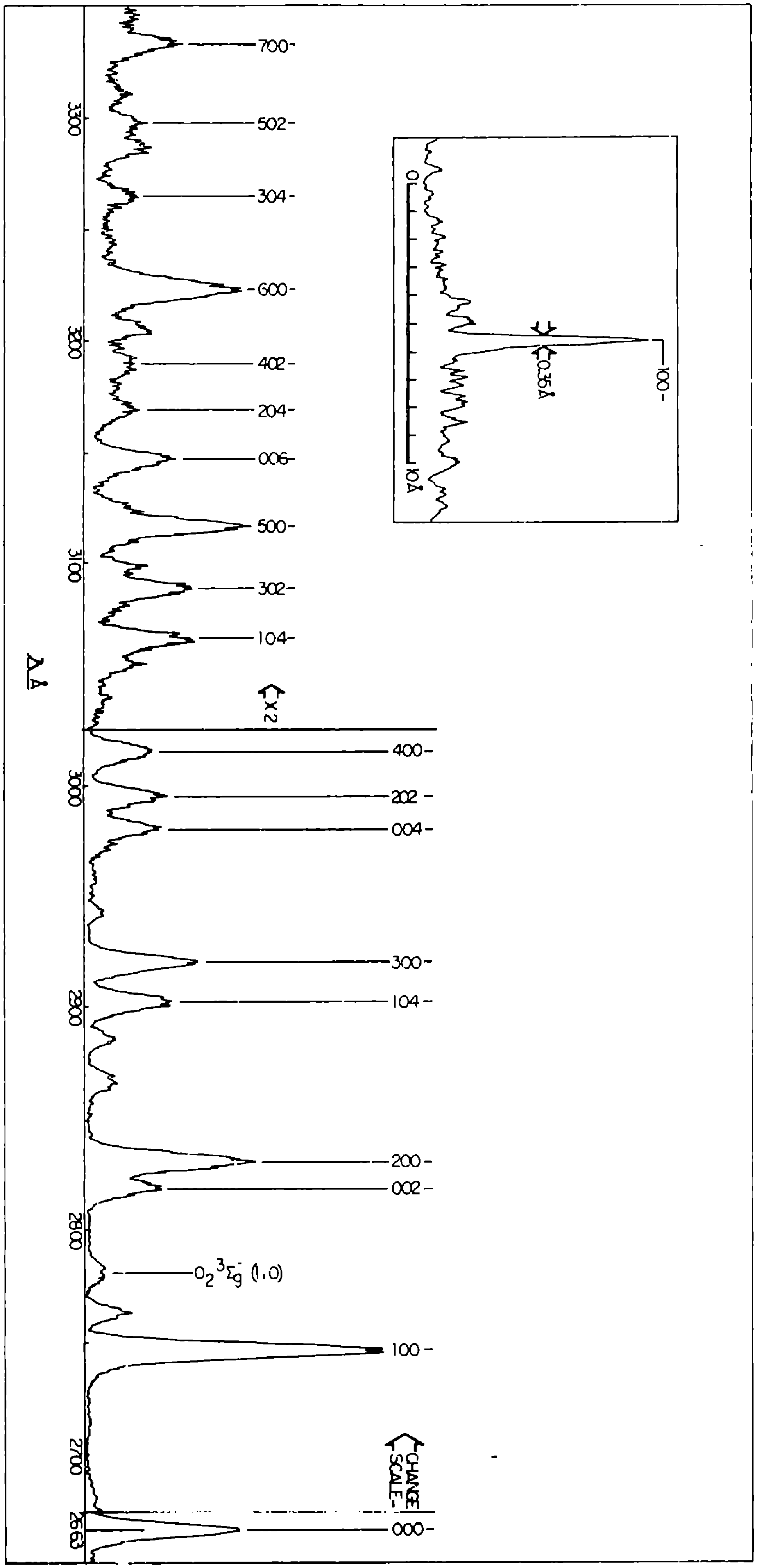
700-
502-
304-
600-
402-
204-
006-
500-
302-
104-
x2
400-
202-
004-
300-
104-
200-
002-
O2 3Σg- (1,0)
100-
CHANGE SCALE-
000-
3300
3200
3100
3000
2900
2800
2700
2663
λ Å
0
10Å
0.36Å
100-

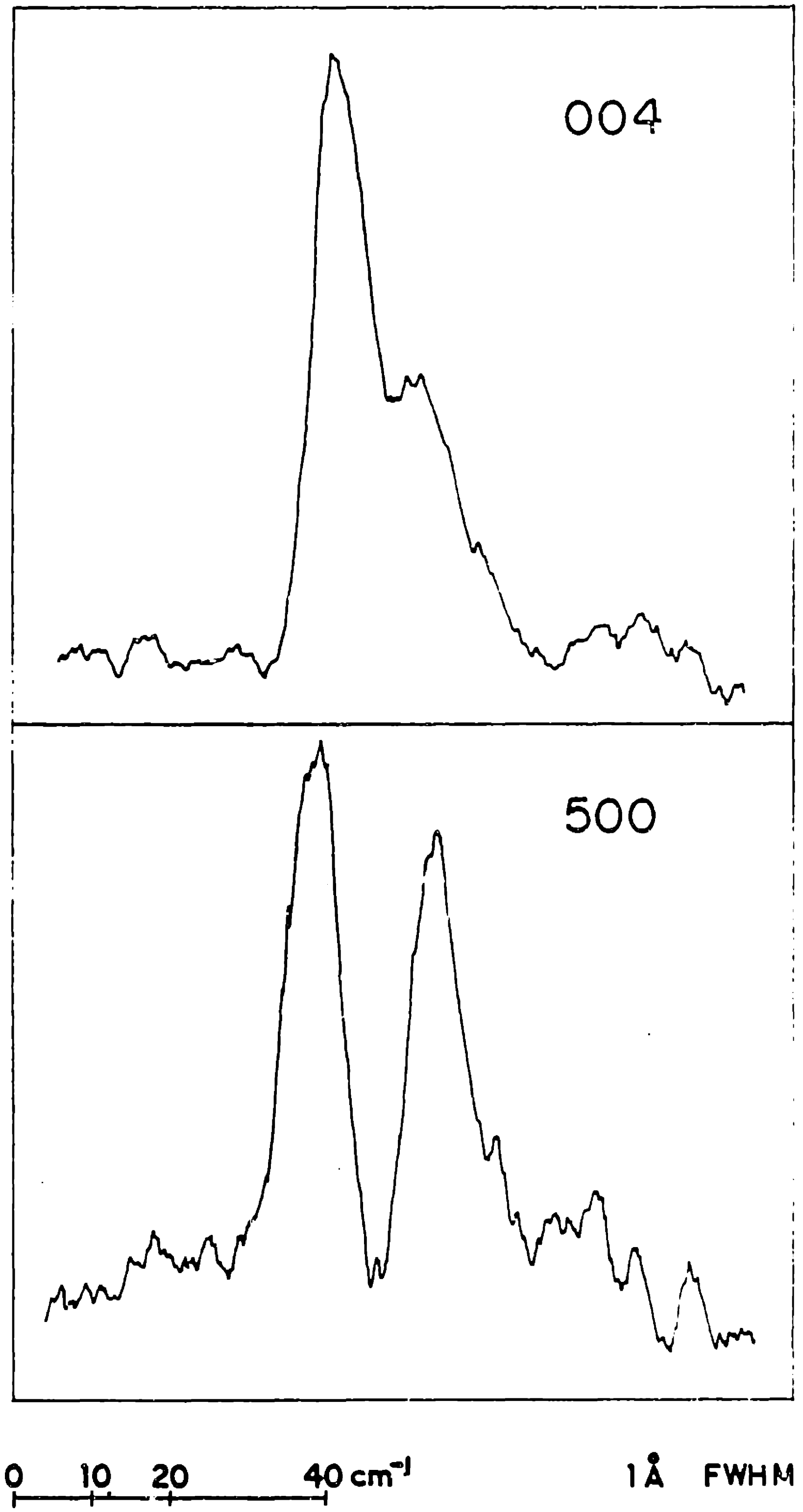

Fig 6-7 - High resolution scans for 004 and 500 bands showing that these bands are composed of more than one eigenstate.

TABLE 6-1

	relative intensities	this work ± 10 cm^{-1}	calculated
100		1103	
002		2058	
102		2201	
300		3294	3291
004	1	4010	4000
	.45	4021	
202	.5	4165	4142
	1	4203	
400		4357	4372
212	.5	4740	
	1	4766	
	1	4850	
104	.6	4883	4934
	.4	4921	
	.2	5094	
302*	1	5125	
	1	5146	5179
	1	5177	
024		5246	-
500	1	5420	
	.7	5437	5444
006*	.2	5680	
	1	5734	5797
	.6	5761	
204		5963	5984
402		6187	6219

TABLE 6-1 (continued)

	relative intensities	this work $\pm$ 10 cm^{-1}	calculated
600*	1	6479	
	.3	6507	6506
	.2	6530	
304		6897	6939
502		7207	7244
700		7523	7560

*Poor signal to noise

higher energies. No sign of activity in the bending mode (ν_2) has been observed, in marked contrast to the Raman spectrum obtained with visible excitation[90] (λ = 638 nm), where appreciable intensity in the bend was observed. In the 266 spectrum all levels containing odd quanta of the antisymmetric stetch (ν_3) are missing. Even numbered levels in ν_3 as well as combination bands of ν_1 with even quanta of ν_3 can be observed with appreciable intensity. The spectrum suggests an immediate conclusion: the bending mode is not significantly involved in the early stages of the reaction. That is in accord with ab initio calculations, which predict similar equilibrium bond angles for the ground and excited surfaces. It is also consistent with observations made by S.G. Adler, of very minor changes in the absorption profile due to vibrational excitation in the bending mode.

The most striking feature in the Raman spectrum at λ=266 nm excitation is the relatively large intensity in the antisymmetric stretch. The Raman intensity as discussed in the case of CH_3I was shown to be dominated by forces. Since the force along the antisymmetric stretch coordinate vanishes by symmetry at the initial wave packet configuration, the center of the wave packet remains forever at $q_3 = 0$. As a result, very low intensity would normally be expected in the ν_3 mode. What actually gives rise to the (002) band is a rapid spreading of the wave packet along q_3, which is largely governed by the difference in curvature $\partial^2 v/\partial q^2$ between the upper and lower surfaces. Because the square of the curvature difference appears in the dynamic expression (Equation III.19), there is a sign ambiguity. This leads to two possible values for the upper-state curvature that would produce agreement with observed relative intensities in 100 fundamental and 002. Fortunately, one of the two values is a positive curvature which corresponds to an implausibly large ν_3 vibrational frequency in the excited state.

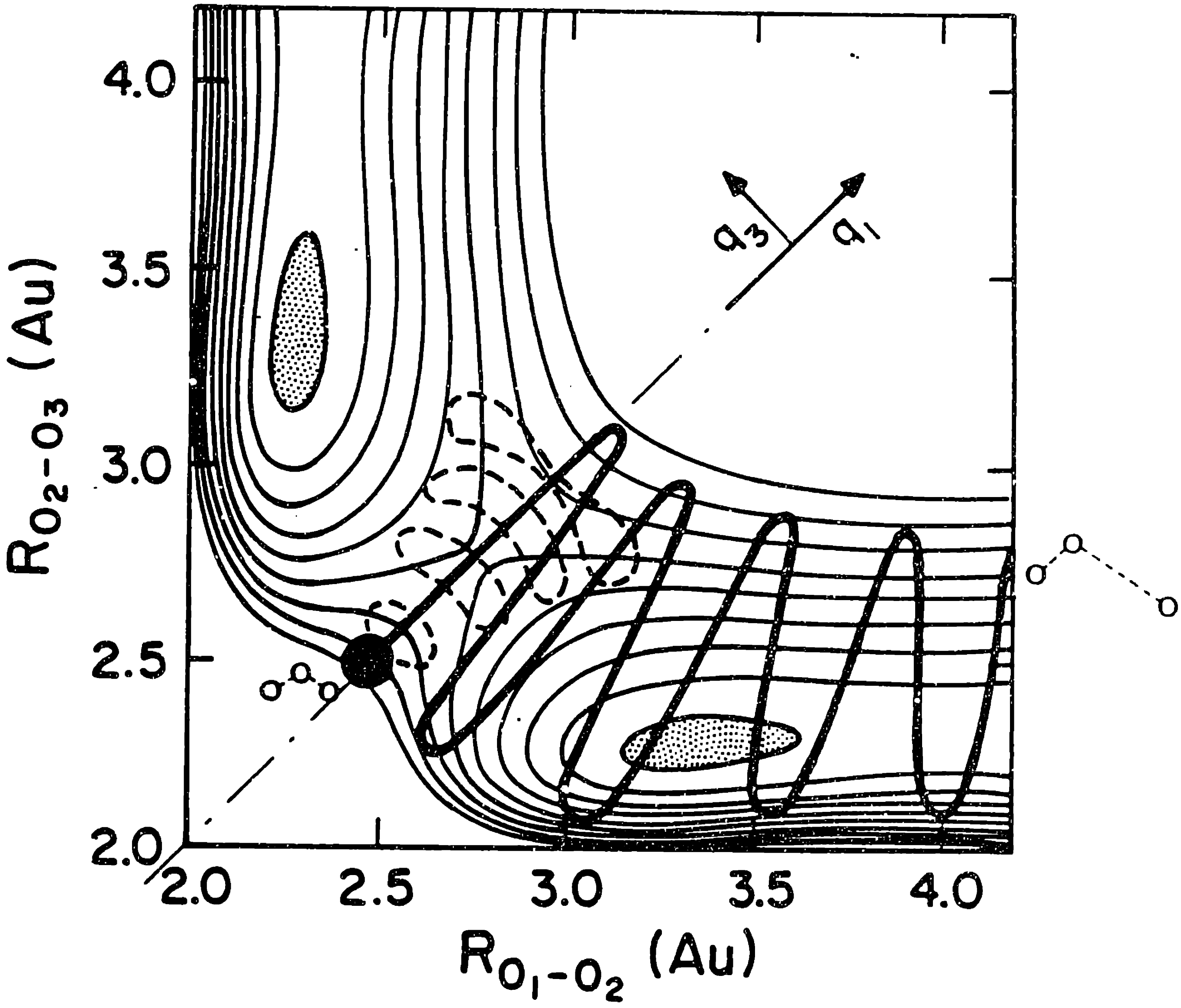

Fig 6-8 - The ozone $^1B_2$ excited state surface along the stretching coordinates (reproduced from ref 21). A photodissociation trajectory is shown by a heavy line. The grey areas indicate the quasi bound regions in the exit channels.

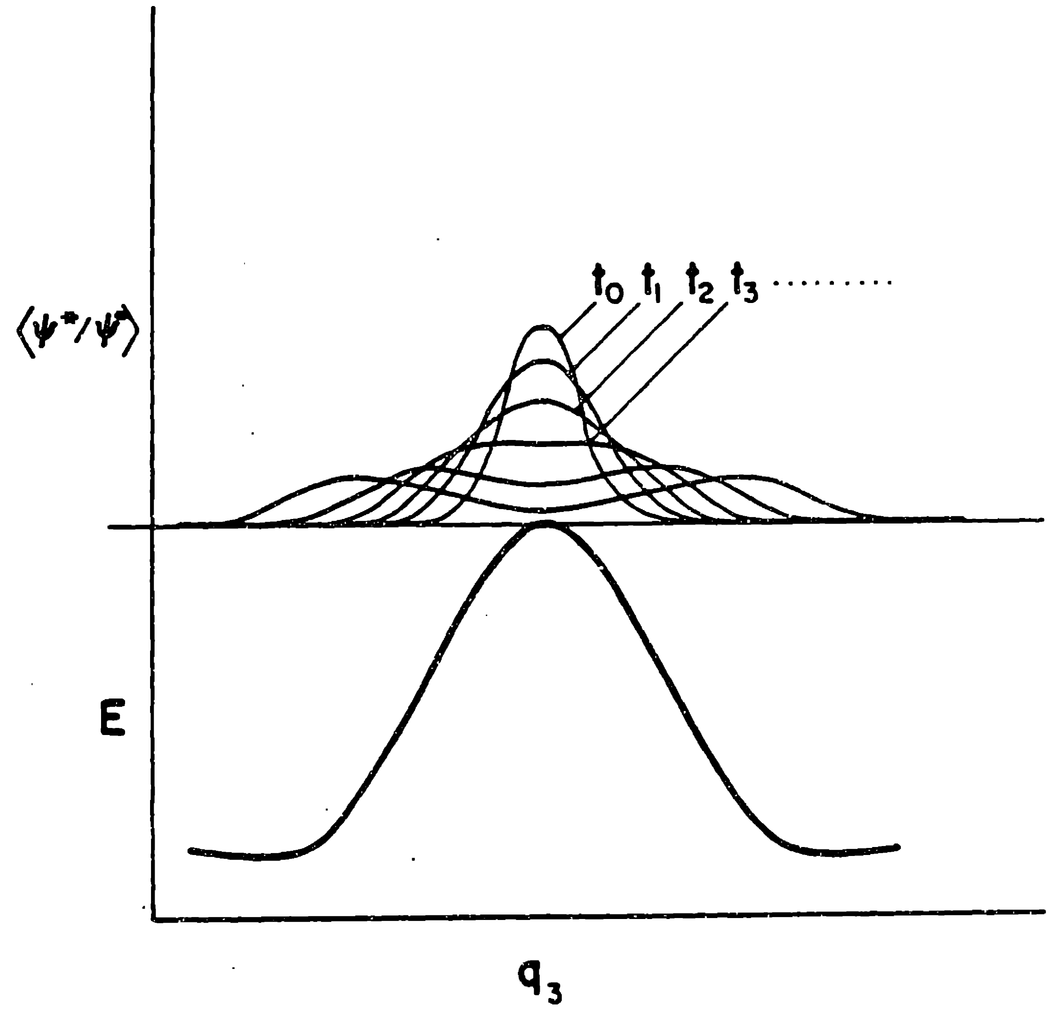
t_0 t_1 t_2 t_3 ·········
$\langle\psi^*/\psi\rangle$
E
q_3

Fig 6-9 - Section along q_3 of the surface shown in Fig 6-8, showing the saddle point. The spreading wave packet is shown above.

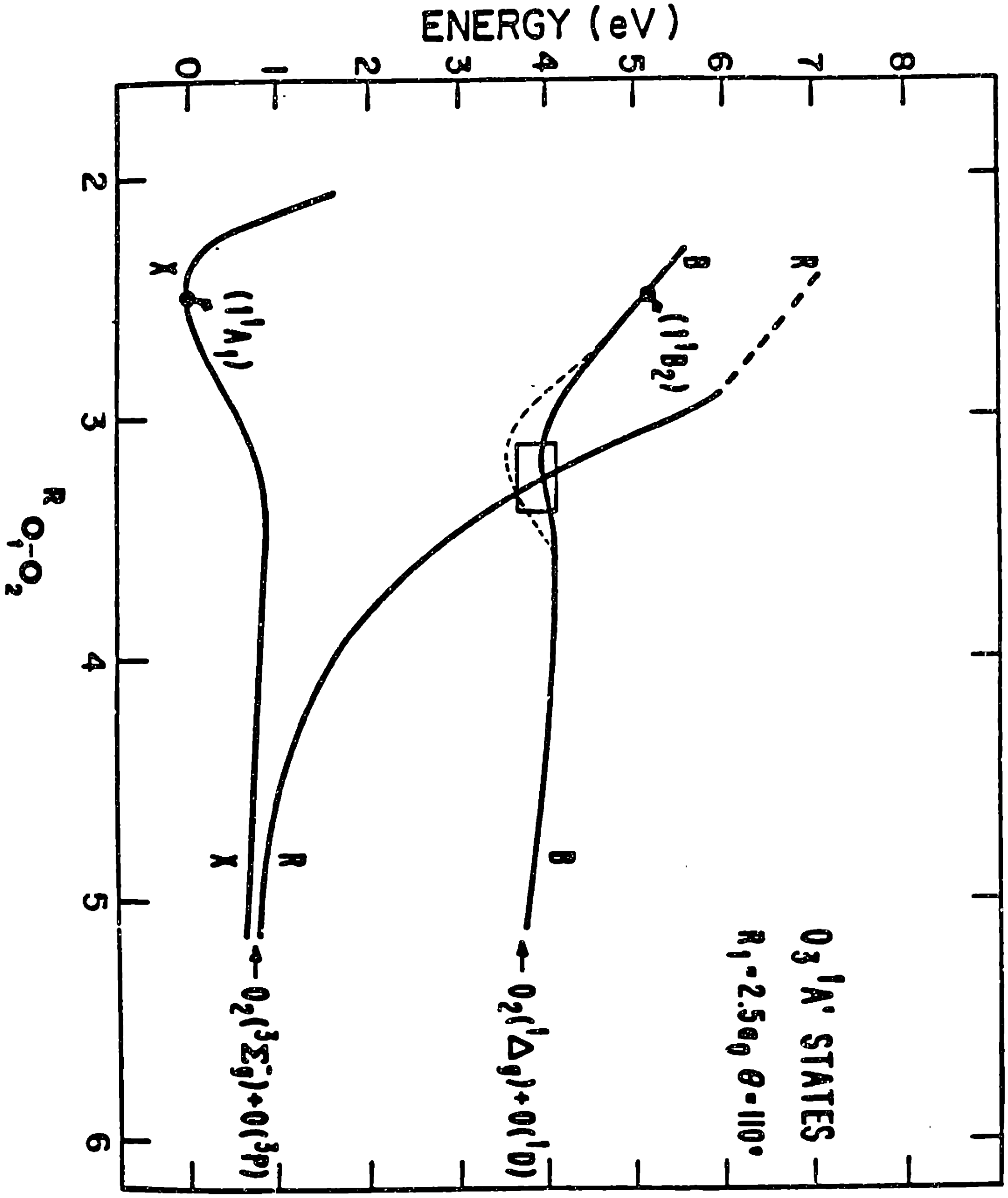

Fig 6-10 - Section along the minimum path "reaction coordinate" of the $^1B_2$ surface shown in Fig 6-7. Also shown is the R state predicted in ref 71. The dashed line indicates the depth of the "pools" as deduced from experimental results.

This possibility can therefore be rejected. The other value gives a negative curvature for the upper state potential and a corresponding imaginary antisymmetric stretch vibrational frequency: ω_3 = i1650 ± 250 cm^{-1} (this value was obtained using Equation III.19). The large error bars reflect the inherent approximate nature of the theoretical expression, rather than that of the accuracy of the measurements. The value we obtain for ω_3 is in extremely good agreement with that predicted from the ab-initio surface (i1850 cm^{-1}). The negative value for the curvature indicates that the upper state PES has a maximum rather than a minimum at $q_3 = 0$. The ab-initio equipotential contour plot reproduced from ref. 71 is shown in Fig. 6-8. with the time evolution of the wave packet schematically diagrammed on it. To show the spreading along q_3 a section along q_3 is shown in Fig. 6-9. The spreading wave packet is depicted at various points in time at the top of the diagram.

In the O_3 photodissociation process, the ground state vibrationless wave packet is transferred to the excited state and placed on top of the saddle point along the C_{2v} axis. It is initially displaced significantly from the excited state minimum along the q_1 coordinate. The force in the q_1 direction drives the wave packet, causing it to accelerate rapidly along the q_1 coordinate. As it executes this motion, it generates a long V_1 progression in the emission spectrum. At the same time, the packet spreads along q_3. Eventually, the spreading results in a bifurcation of the wave packet, with the two pieces proceeding in phase towards products. The spreading motion maintains symmetry about the C_{2V} axis. Hence, overlaps with odd vibrational quanta in q_3 (which are antisymmetric) vanish at all times so that only even values of ν_3 are observed.

Since the spreading process is relatively slow as compared with the acceleration along q_1, the wave packet can revisit the Franck-Condon region before it "leaks" irreversibly into q_3. Such recurrences in the correlation function $\langle\phi|\phi(t)\rangle$ are manifested as weak structure in the absorption spectrum (i.e. the kind actually observed). This phenomenon is more prominent in the CO_2 photodissociation spectrum.[92] For that molecule, R. Pack has shown that the vibrational progression in the absorption spectrum could be attributed to symmetric stretch motion on the excited surface. What distinguishes between the two cases is mainly the rate of spread in q_3 relative to the rate of symmetric stretch (q_1) motion. The fact that the fine detail in O_3 is very weak and poorly resolved indicates that wavepacket spreading in O_3 is more rapid than in CO_2, and therefore recurrences in $\langle\phi|\phi(t)\rangle$ decay more rapidly.

The resolved vibrational bands to the red end of the absorption spectrum (Huggins band) are manifestations of quasibound states in the pools indicated by the gray areas in Fig. 6-7. Preliminary results by A. Sinha in our laboratory have shown that absorption in this spectral region is dominated by non Franck-Condon transitions. These observations, together with the vibrational analysis by D. Katayama, indicate that the so-called shallow pools are actually bound by approximately .6 eV with respect to the $O_2\ {}^1\Delta$ and $O\ {}^1D$ dissociation limit rather than the theoretically predicted .2 eV. A discrepancy of this magnitude from the ab-initio prediction is not surprising in the light of the known inaccuracy of the ground state surface. Fig. 6-10 shows a section along the minimum path "reaction coordinate", also shown in the figure is the "R" state from ref. 71. When O_3 is excited in the 350-308 nm region, it dissociates into ground state fragments. Dissociation in this spectral region is probably a result of curve crossing by the R state. Since this process is relatively slow, the molecule survives for approximately 1 psec. This estimate is based on the line width observed by A. Sinha.

Comparison of the experimental results with the ab-initio predictions suggests that the shapes of the calculated surfaces are fairly accurate in the Franck-Condon region, as is evident from the good reproducibility of absorption spectra and the curvature along q_3. However, at larger internuclear separations it appears that the depth of quasi bound region has been underestimated by approximately .4 eV. This may account for the poor agreement between theoretical and experimental internal state distributions but this has not yet been confirmed by calculations on a surface with deeper "pools". As the wave packet proceeds to products it encounters the wells where, depending on its momentum and the shape of the wells, "inelastic processes" can take place that affect final product distributions.

Ozone provides a unique opportunity to study dynamics of a single wave packet prepared on two different surfaces. When O_3 absorbs a visible photon (λ = 700-450 nm), ($^1B_1$ —— X $^1A_1$), it dissociates with a quantum yield of unity into ground electronic state products. An emission spectrum obtained by Selig and Clausen[90] with excitation in this spectral region is shown in Fig. 6-11 The spectrum indicates that the dynamics on the $^1B_1$ surface is quite different from that on the $^1B_2$ surface. Bending-mode activity appears to be prominent on the $^1B_1$ surface, in accord with ab-initio predictions. We have also attempted to study the emission spectrum in this region. Unfortunately, dissociation in this region seems to be dominated by curve crossing into an optically dark state (probably $^1A_2$). This appears in the spectrum in the form of an abrupt decrease in intensity for bands with more than one quantum. The ab-initio[70] calculations predict a

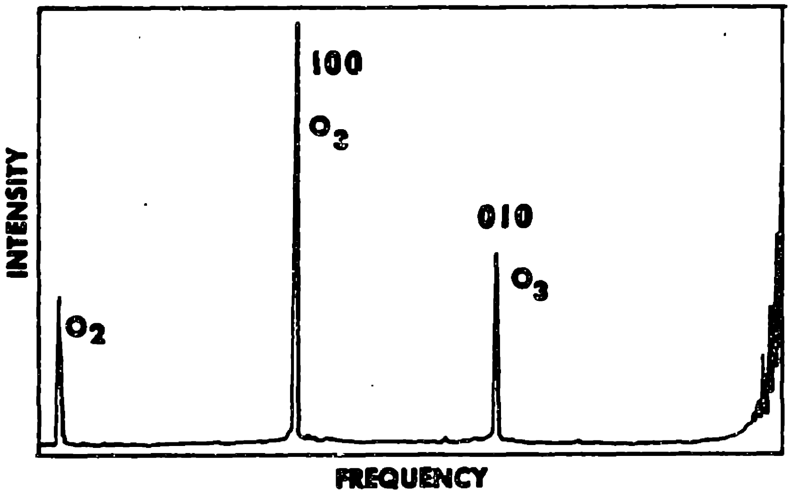

Fig 6-11 - Ozone Raman spectrum obtained by excitation at 638 nm. (from ref 90). Note the relatively high intensity in the 010 band and the absence of overtones.

bound $^1B_1$ state with respect to its dissociation limit, (O_2 $^1\Delta$ and O^1 D). They also predict a crossing near the Franck-Condon region of this state by the repulsive $^1A_2$ state. These predictions are consistent with our observations.

CHAPTER 7.

PRELIMINARY CALCULATION: METHYL IODIDE

I. Excited State Dynamics

Dynamic calculations require potential energy surfaces. For initial estimates regarding the shapes of the two surfaces involved in our experiment, we used ab initio data which had been kindly supplied to us by W. Wadt of the Los Alamos National Laboratory. These data contain information on twelve adiabatic surfaces at the energy region of the ${}^3Q_0$ state. Fig. 7-1 shows a one-dimensional cut of these surfaces along the C-I bond coordinate at a fixed value of the umbrella-mode bending coordinate.

A total of 58 points on a two-dimensional grid (R_{C-I} and θ HCI) were used in our analysis. From among the 12 surfaces, the ${}^3Q_0$ state was identified by the large value of transition moment along the z axis. The ground state was easily identified as the lowest in energy. Figures 7-2 and 7-3 show contour plots in the R_1, R_2 coordinate system for the ground and the ${}^3Q_0$ excited ab initio surfaces respectively. R_1, R_2 are reduced mass coordinates chosen so that the kinetic energy would be diagonal in the limit of separated fragments. Methyl iodide is treated as a linear triatomic molecule:

$$X \xleftrightarrow{r_{c-x}} C \xleftrightarrow{r_{c-I}} I$$

$$X=H_3$$

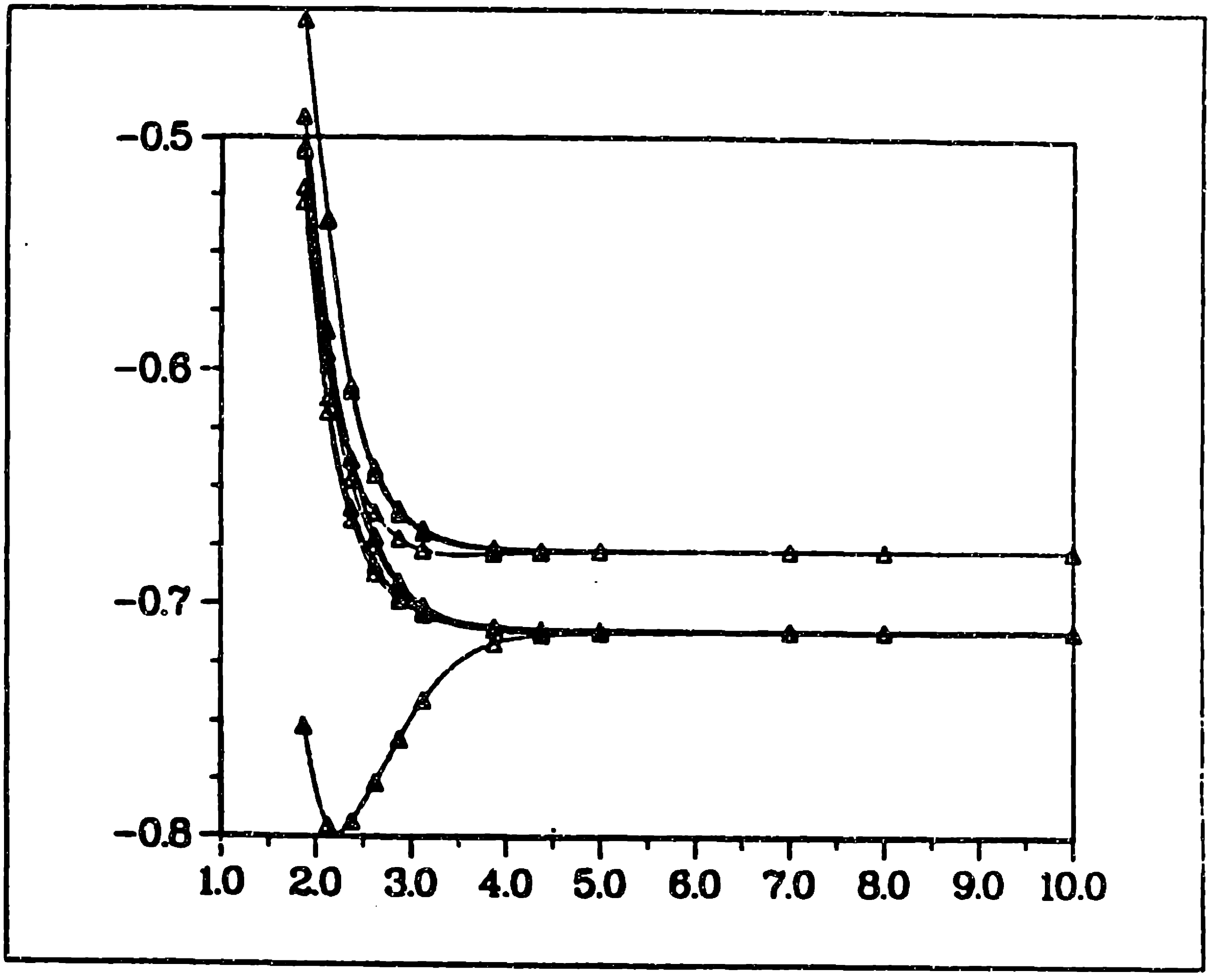

Fig 7-1 - One dimensional cut along r_{C-I} with the bending coordinate held at 72.5°. Showing all 12 surfaces given by the ab initio data.

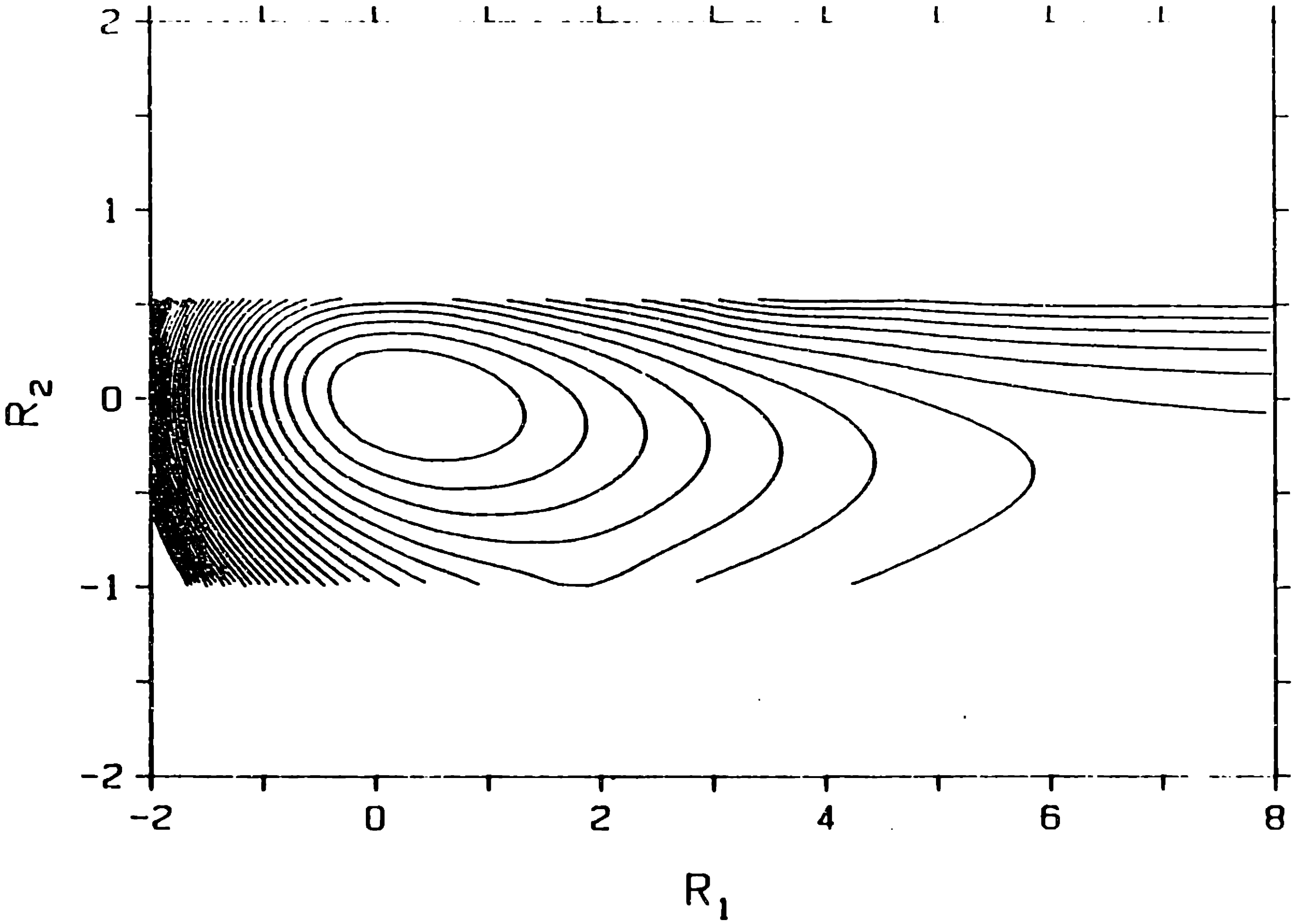

Fig 7-2 - Contour plot of the ab initio ground state surface.

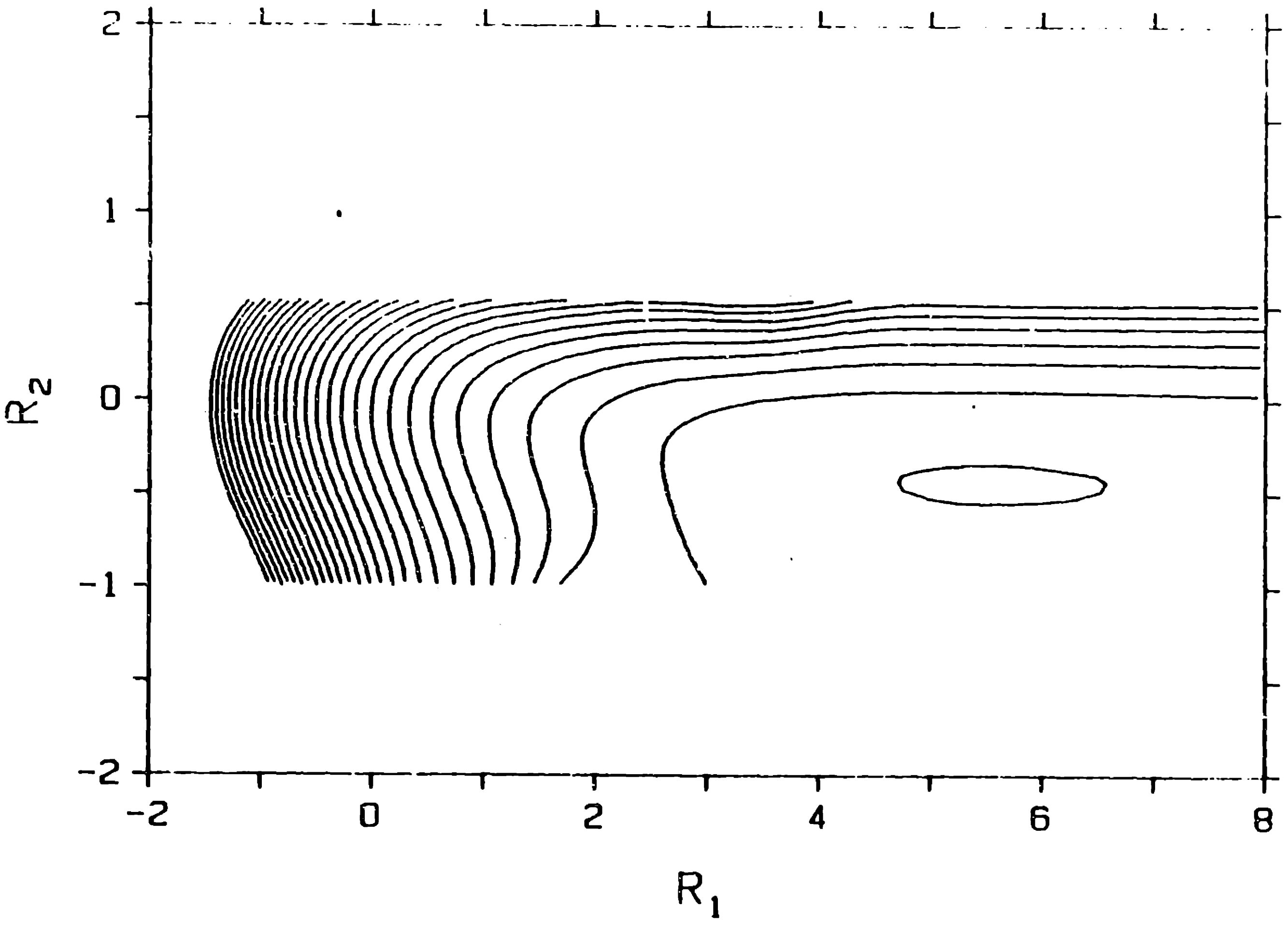

Fig 7-3 - Contour plot of the ab initio $^3Q_0$ state.

VII.1 $$R_1 = \left(\frac{m_I m_{CX}}{M}\right)^{1/2} \left[R - r^{\circ}_{(C-I)} - \frac{m_X}{m_{CX}} r^{\circ}_{(C-X)}\right]$$

VII.2 $$R_2 = \left(\frac{m_C m_X}{M_{CX}}\right)^{1/2} \left[r_{(C-X)} - r^{\circ}_{(C-X)}\right]$$

where: $R = r_{(C-I)} + \frac{m_X}{m_{CX}} r_{(C-X)}$ and designates equilibrium geometry.

In these coordinates, the quantum mechanical kinetic energy operator is:

VII.3 $$T = -\frac{\hbar^2}{2}\left[\partial^2/\partial R_1^2 + \partial^2/\partial R_2^2\right]$$

units were chosen such that R would be expressed in Å(amu)$^{\frac{1}{2}}$ R_1 is the dissociation coordinate, and R_2 represents the umbrella bending motion.

The ab initio data were fitted with analytic expressions, using the following procedure: points along the C-I coordinate with the HCI angle held fixed at 72.29; were plotted for the two surfaces. The curve obtained from the ground state (Fig. 7-4) was fitted with a Morse function. The corresponding excited state curve (Fig. 7-5) was fitted with an exponential function. To fit the potential along the bending coordinate, sections taken at ten different R_{C-I} were least square fitted with quadratic functions. This gave the location and value of the potential minimum and a bending frequency at each R_{C-I}. Figures 7-6 and 7-7 show the points used, as well as the analytical fits obtained in the above procedure. The functional form chosen to represent the R_{C-I} dependence of the bending-coordinate minimum and curvature was a hyperbolic tangent in R_{C-I}. Tanh is a particularly convenient function, since it is well behaved and has well defined limits. The potential functions derived from these fits were of the forms.

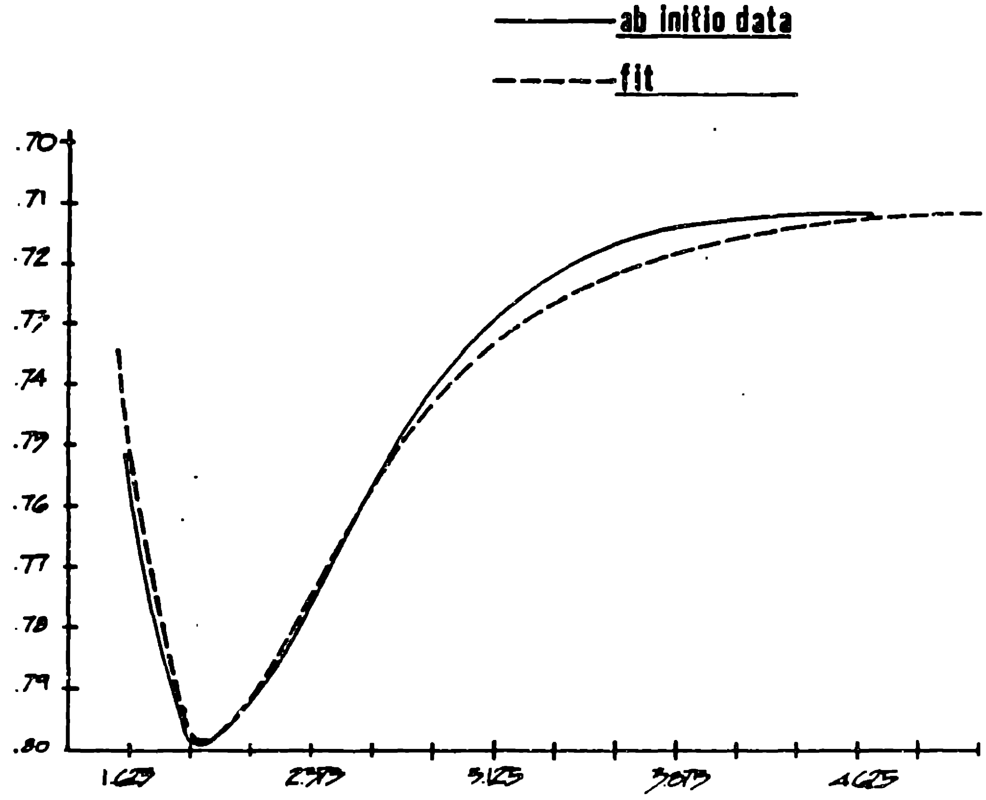

Fig 7-4 - Cut through the *ab initio* data for the ground state along r_{C-I} with the bend held at 72.29°, and the Morse fit to this data.

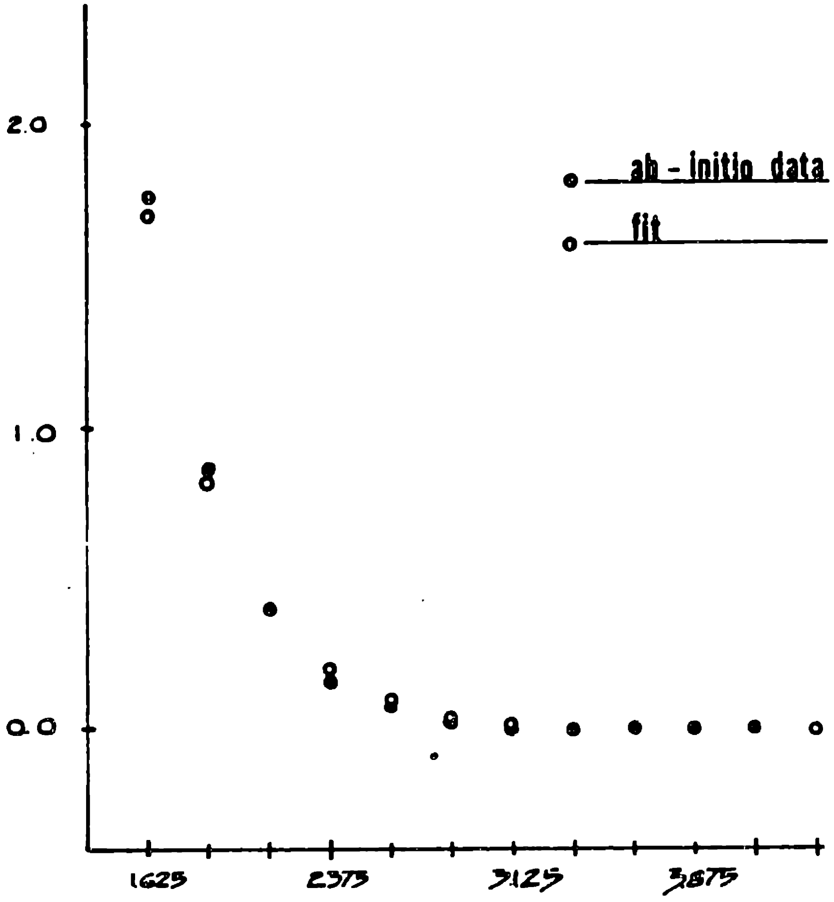

Fig 7-5 - Cut through the ab initio data for the $^3Q_0$ state along r_{C-I} with the bend held at 72.29°, and the fit using an exponential function.

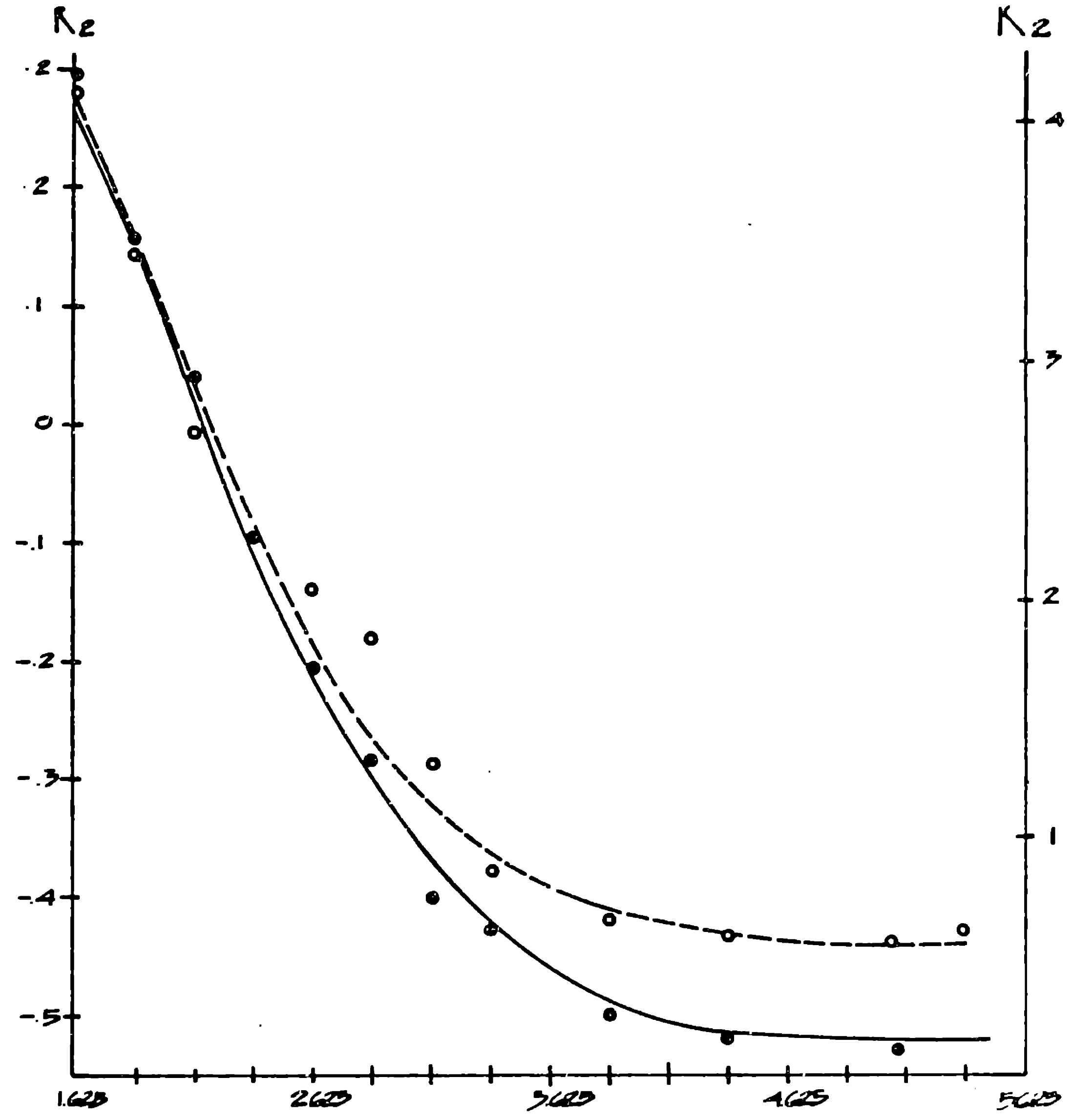

Fig 7-6 - Dependence of the force constant (K_2) and potential minimum R_{2mm} on r_{C-I}, in the ground state as obtained by the least square fit to the ab initio data (K_2 - o, R_{2min} - ●). The tanh fit to the ab initio data (k_2 ----, R_{2min} ——).

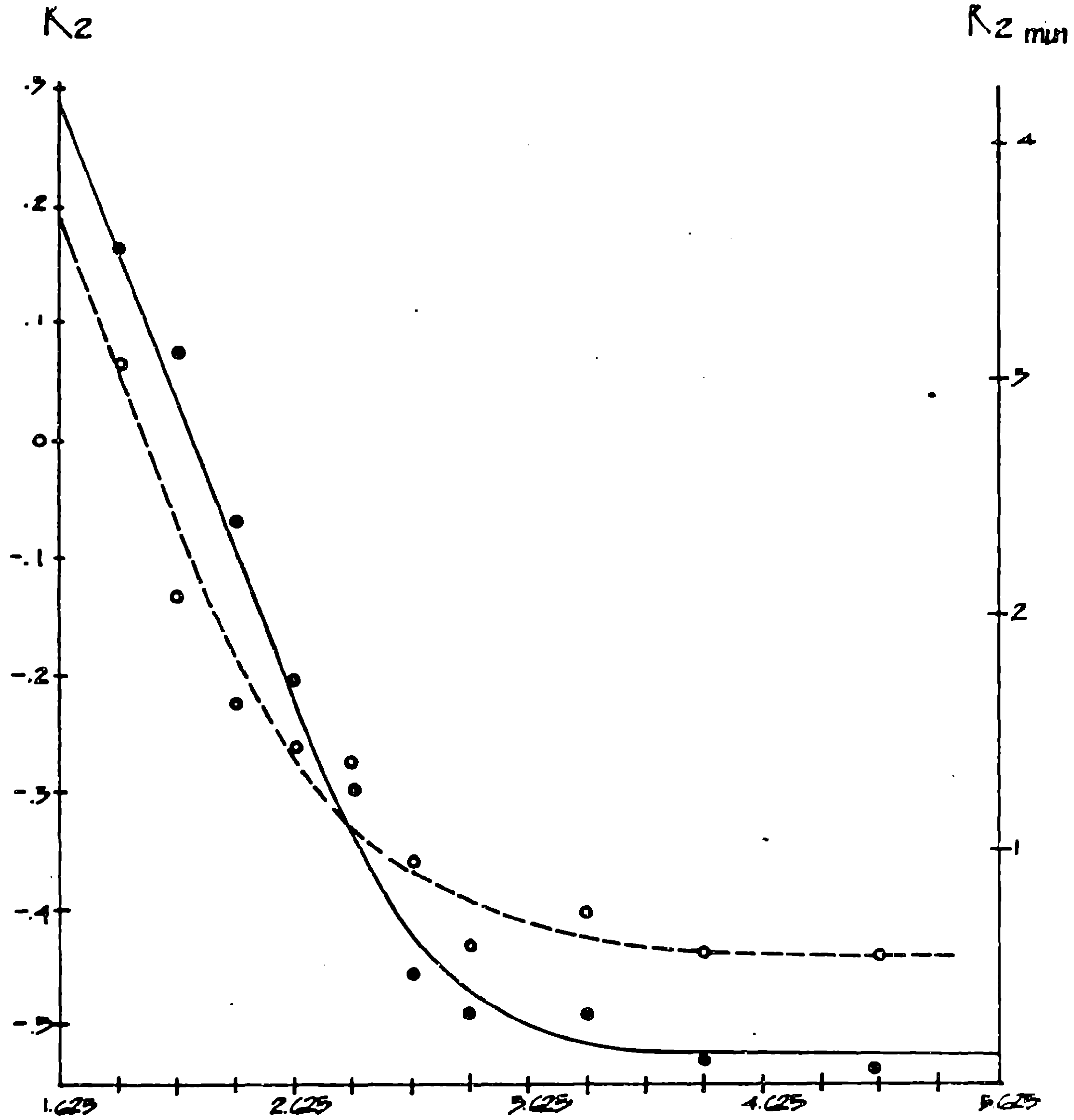

Fig 7-7 - Same as Figure 7-6 for the $^3Q_0$ state.

VII.4 $$V_x = D_e(1 - e^{-\beta(r_{c-I})})^2 + k_{(r_{c-I})}(r_{bend} - r_{min(r_{c-I})})^2$$

for the ground state and;

VII.5 $$V_{^3Q_0} = A \cdot e^{-a r_{c-I}} + k_{(r_{c-I})}(r_{bend} - r_{min(r_{c-I})})^2$$

for the $^3Q_0$ state.

Appendix A gives the potentials (G (A) and Ex (A)) in FORTRAN form and their derivatives in units of Hartrees: 10, in the R_1, R_2 coordinate system (R_1 = X, R_2 = Y). Figures 7-8 and 7-9 show contour plots for the ground (G (A)) and Excited (Ex (A)) state surfaces respectively.

These fitted surfaces yield the following calculated experimental observables:

calculated	**experimental**
D_o = 2.1 ev	2.5 ev
ω_2 = 1830 cm^{-1}	1254 cm^{-1}
ω_3 = 485 cm^{-1}	534 cm^{-1}
ω_2 (CH_3) = 666 cm^{-1}	611 cm^{-1}
$V^{excited}$ = 44500 cm^{-1} (R_1 = R_2 = 0)	38300 cm^{-1}
$\omega^*{}_{2CH_3}$ = 669 cm^{-1}	611 cm^{-1}

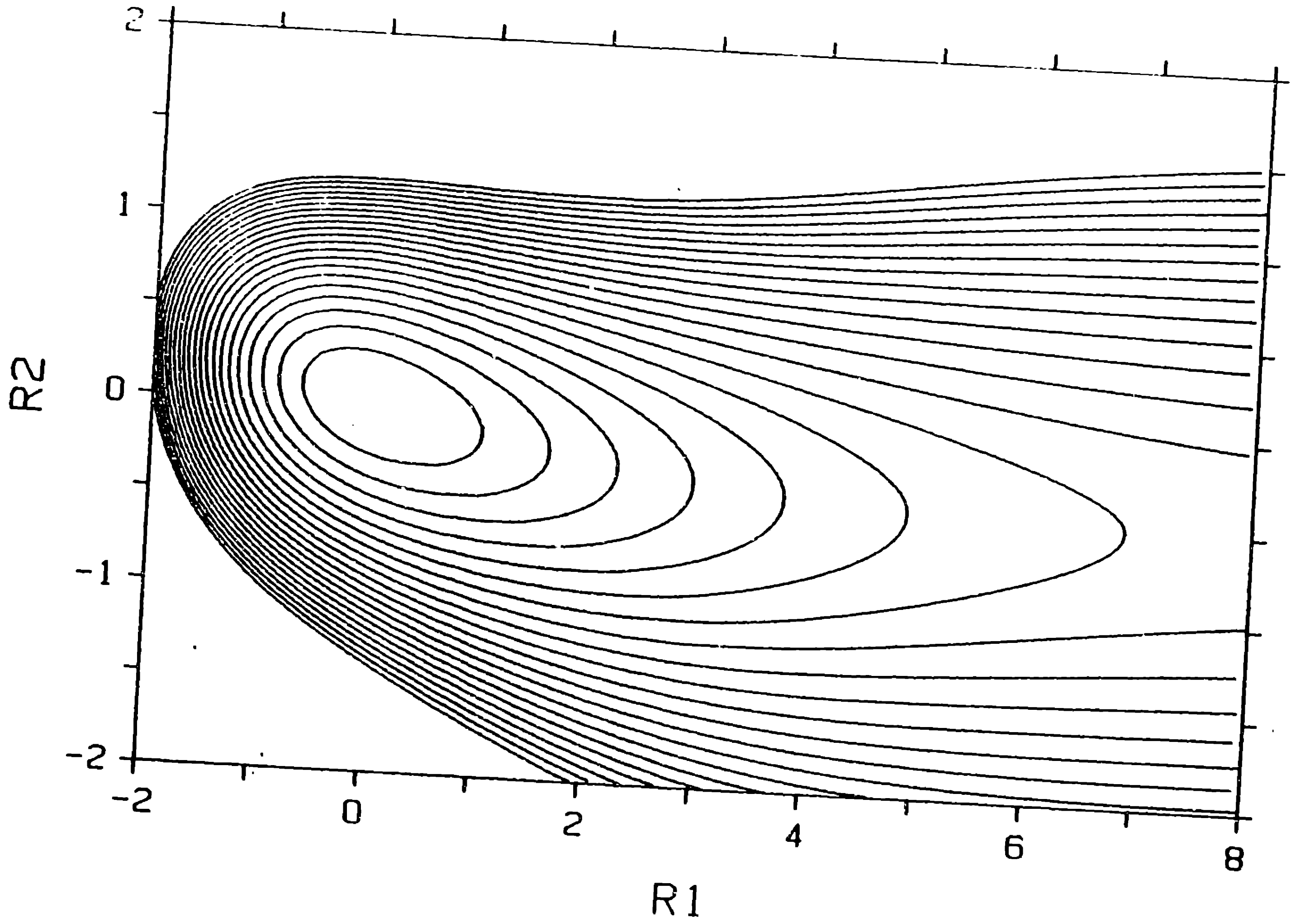

Fig 7-8 - Contour plot for the analytic ground state potential G (A).

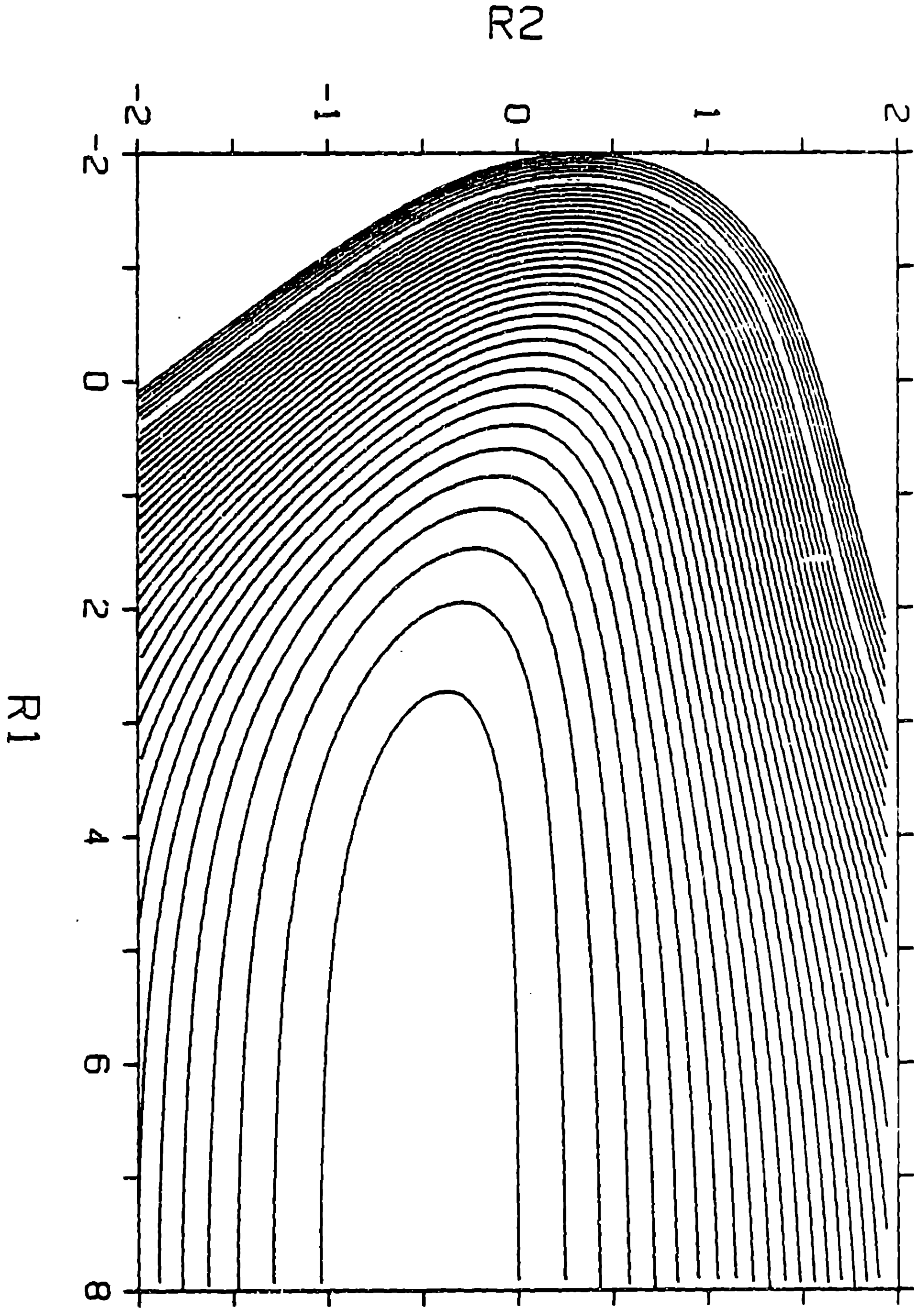

Fig 7-9 - Contour plot for the analytic $^3Q_0$ state potential Ex (A)

where ω_2 and ω_3 are the ground-state harmonic frequencies in the umbrella bend and the C-I stretch respectively and ω_2 CH_3 and $\omega^*2_{CH_3}$ are harmonic frequencies corresponding to the out of plane bend in the limit of the separated fragments as determined by the ground and excited state potentials, respectively in their asymptotic limits.

Because of the poor agreement between calculated and experimental observables, the ground state PES was modified to yield the surface given in the form of a FORTRAN subroutine appendix B, (G (B)) and shown in figure 7-10. This surface yields the following observables:

calculated for G (B)	**experimental**
D_o = 2.54 ev	2.5 ev
ω_2 = 1249 cm^{-1}	1254 cm^{-1}
ω_3 = 530 cm^{-1}	534 cm^{-1}
ω_2 (CH_3) = 603 cm^{-1}	611 cm^{-1}

The harmonic vibrationless wave function corresponding to the G (B) potential has been used as the initial wave packet for subsequent dynamic calculations of the photodissociation process on the ^3Q_o surface. All the wavepacket propagation routines were kindly provided by R. Coalson.

Using a thawed gaussian wave packet propagation method[93], the trajectory of the above wave packet was calculated on EX (A). The overlap between evolving wave packet and the ground-state vibrational wave function, $\langle\phi|\phi(t)\rangle$, was calculated and Fourier transformed to yield the absorption spectrum shown in figure 7-11. The calculated spectrum differs significantly from the experimental

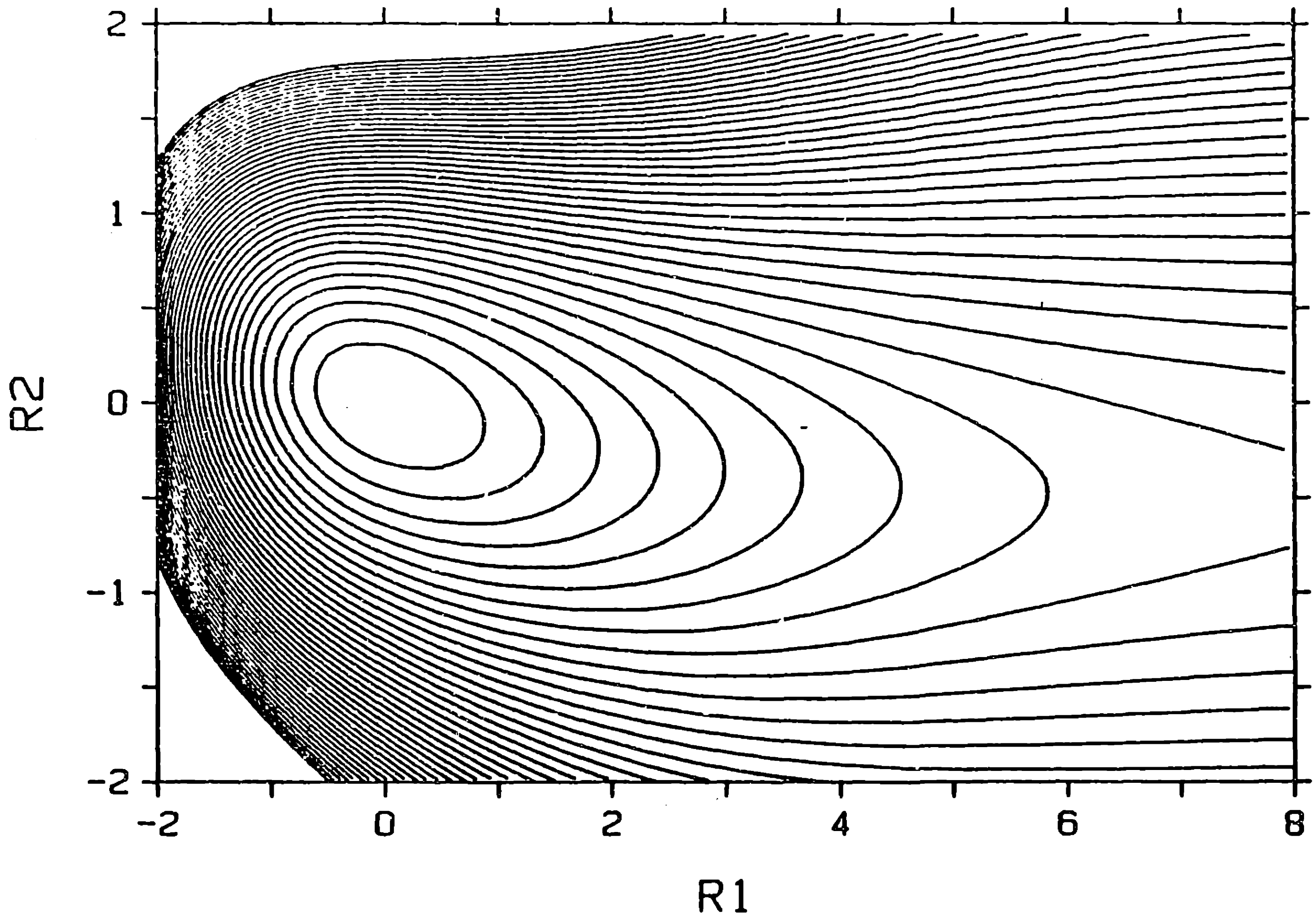

Fig 7-10 - Contour plot for G (B).

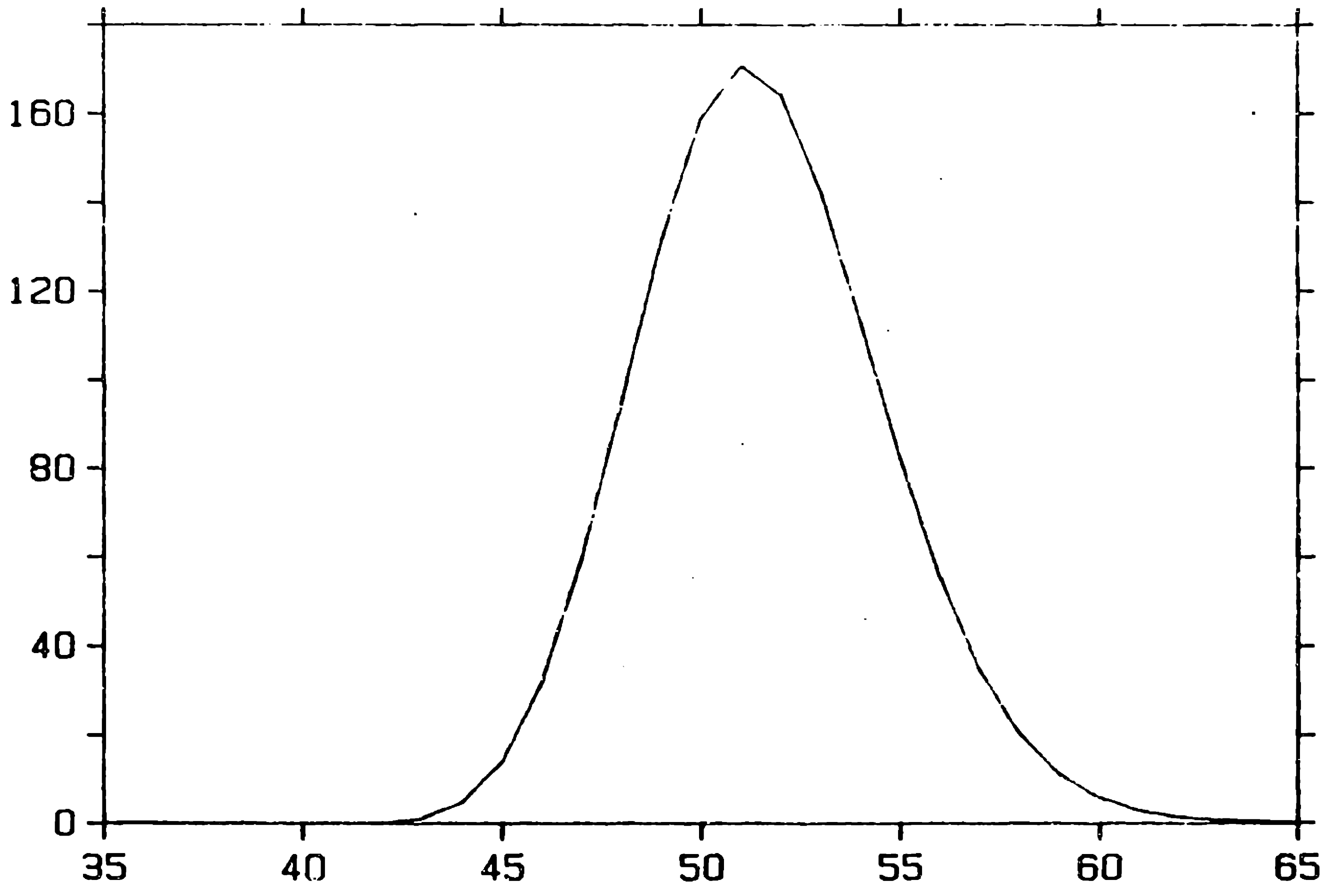

Fig 7-11 - Absorption spectrum for the transition Ex (A) - G (B).

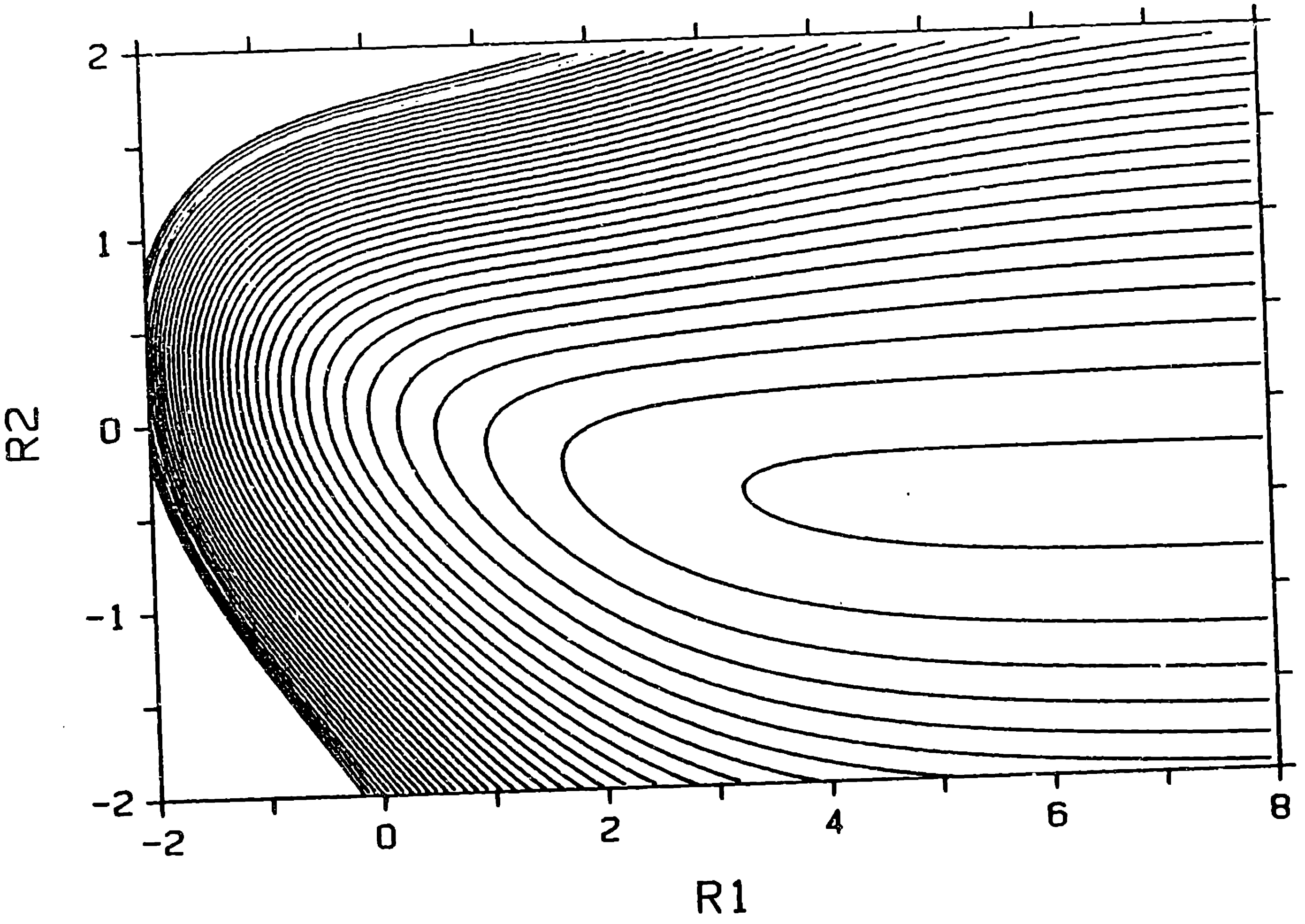

Fig 7-12 - Contour plot for Ex (B)

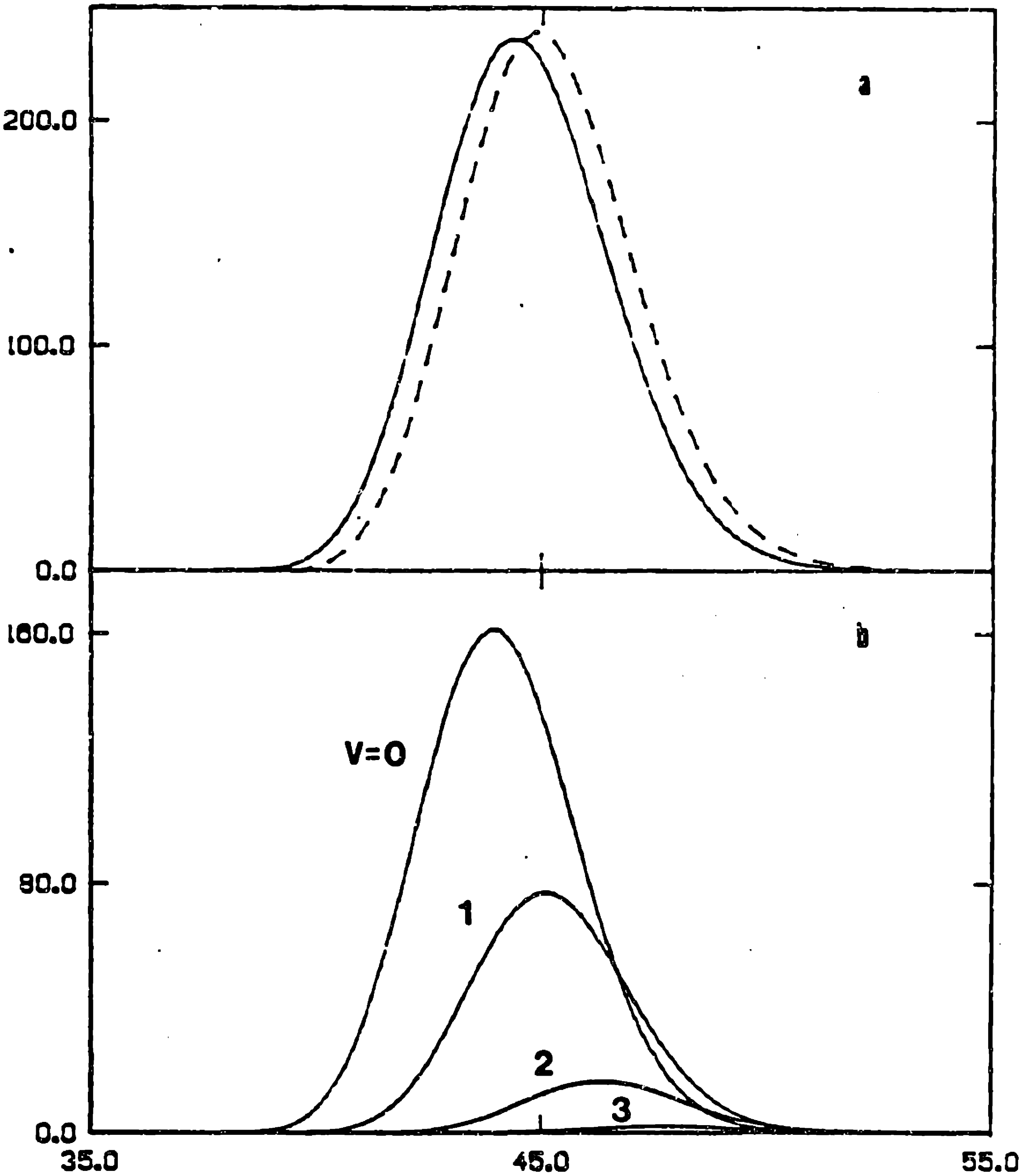

Fig 7-13 - (a) Absorption spectrum for the transition Ex (B) - G (B), calculated by Fourier transform ---, or by summing over the partial cross sections——. (b) Partial cross sections for the final CH_3 vibrational states.

both in position and width, indicating that the ab initio excited state surface does not adequately represent the true potential. Since the absorption spectrum is mainly dominated by the C-I coordinate, a modified potential with change only in the exponential part was generated. This surface is shown in Figure 7-12 (Ex (B)) and given in FORTRAN form in Appendix C. Ex (B) gave rise to the calculated spectrum shown in Figure 7-13a (dashed line), which fits the experimental absorption spectrum quite well. The main discrepancies occur in the wings of the spectrum, and are probably due to variation of the transition moment with nuclear coordinates. In our dynamic calculation the transition moment was assumed to be constant over the ground state wave function. In fact, the ab initio results suggest an appreciable variation with C-I internuclear separation. Neglect of this dependence is expected to affect mainly the wings of the absorption spectrum.

To test the rest of the surface, final product vibration state distributions were calculated. This calculation employed methods developed by E.J. Heller[94] and R. Coalson[95]. The CH_3 bending vibrational states were assumed to be harmonic. Overlaps between the CH_3 wave functions and the asymptotic wave-packet were calculated at two separate times. The two times were used to assure convergence. Results from these calculations are shown in Figure 7-13b. For comparison with experimental results: The time of flight spectrum was obtained by excitation at 266 nm (43.2 in our units). The relatively unstructured time of flight spectrum was decomposed by a fitting procedure into separate peaks for the various vibrational states. The distribution obtained was found to peak at $V_2 = 2$. The calculated distribution, on the other hand, predicted a distribution with maximum population $V_2 = 0$ for excitation at this wavelength. The solid line spectrum shown in Figure 7-13a was obtained by summing over all final product states. This spectrum is slightly red-shifted relative to the one obtained by the Fourier transform method. The degree of discrepancy reflects the inaccuracy of the calculation of the final-state distribution. In that computation, the wave packet was assumed to remain gaussian throughout the reaction. However, since the potential is not quadratic, the wave packet cannot remain truly gaussian for a long time. Therefore, the wave packet propagation is more reliable for short times than for long times. Thus, the dashed-line spectrum in Fig 7-13a is definitely the more accurate of the two.

In order to better reproduce the experimental vibrational distributions the excited-state PES (Ex (B)) was further modified by increasing the rate with which the minimum in R_2 varies with R_1. The slope along R_2 in the Franck-Condon region was also increased by shifting the minimum slightly. The relative slopes in R_1 and R_2 are consistent with the relative Raman intensities we have observed. The modified potential (Ex (C) is shown in Figure 7-14 and is given in Appendix D in FORTRAN form. Figures 7-15 and 7-16 show the calculated absorption spectra and the final product vibrational distributions respectively for Ex (C). The discrepancy between the two calculated absorption spectra shown in Figure 7-15 is of the same origin as that observed in Figure 7-13. As before, the solid curve is the more reliable.

The vibrational distribution has undergone a marked change because of the PES modification. V = 2 is now the most probable vibrational level for excitation at 266 nm. Figures 7-17 through 7-22 summarize the results of several semi-classical and classical studies on this surface.

Surface Ex (C) yields results which are closer to experiment than those obtained from the previous surfaces. Even so, the shape of the vibrational

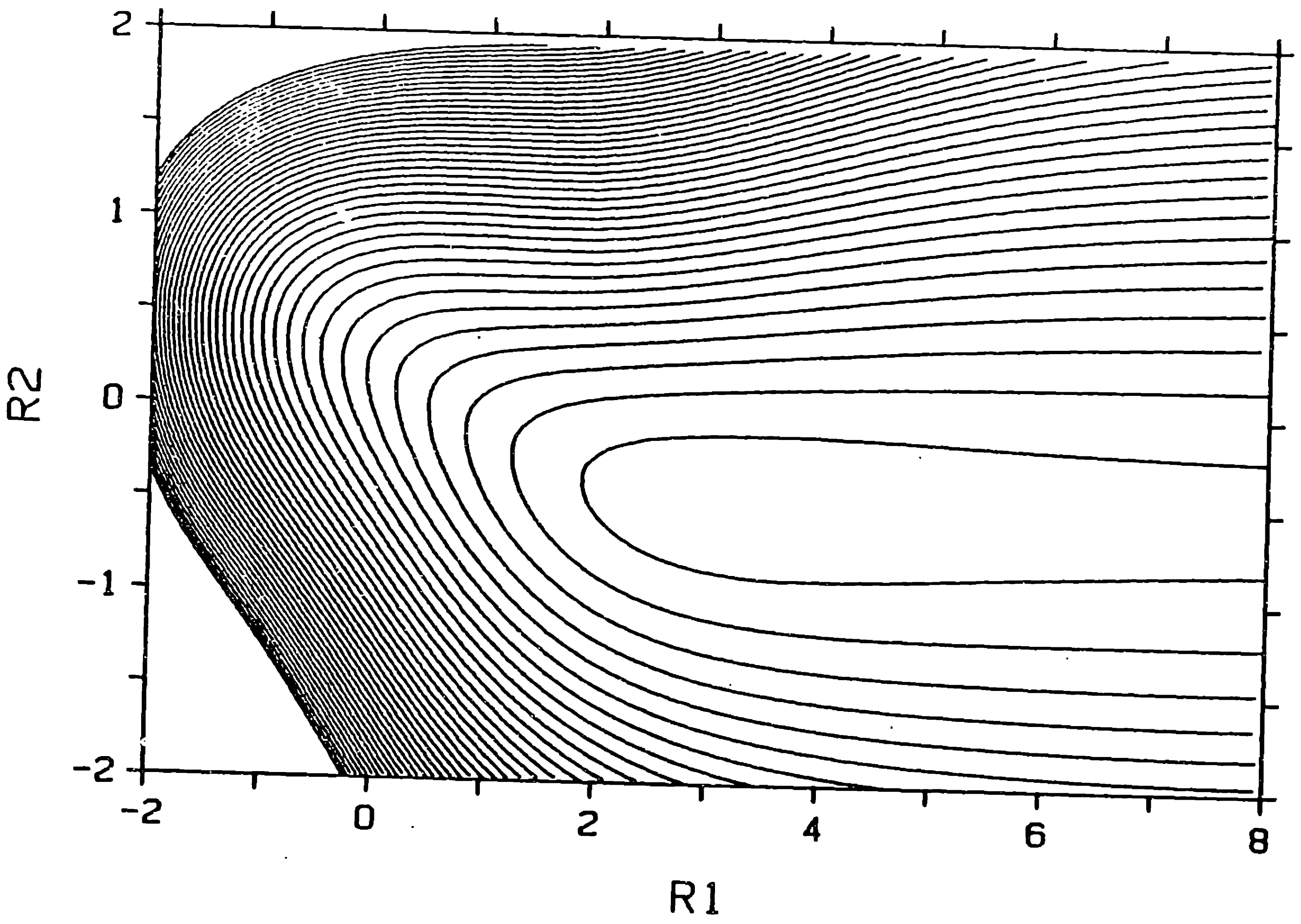

Fig 7-14 - Contour plot for Ex (C).

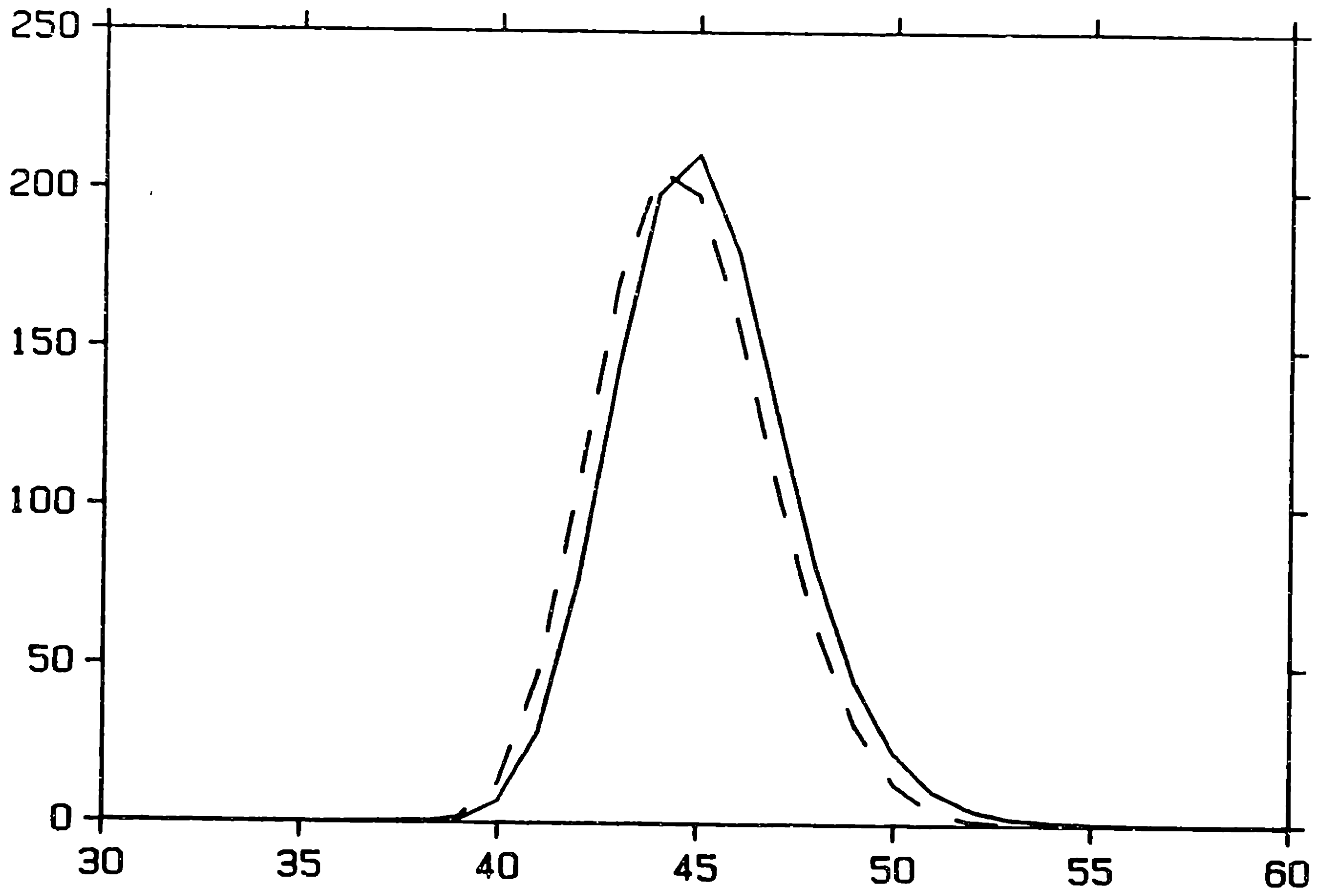

Fig 7-15 - Absorption spectra for the transition Ex (C) - G (B). —— Fourier transform method, --- sum of partial cross sections.

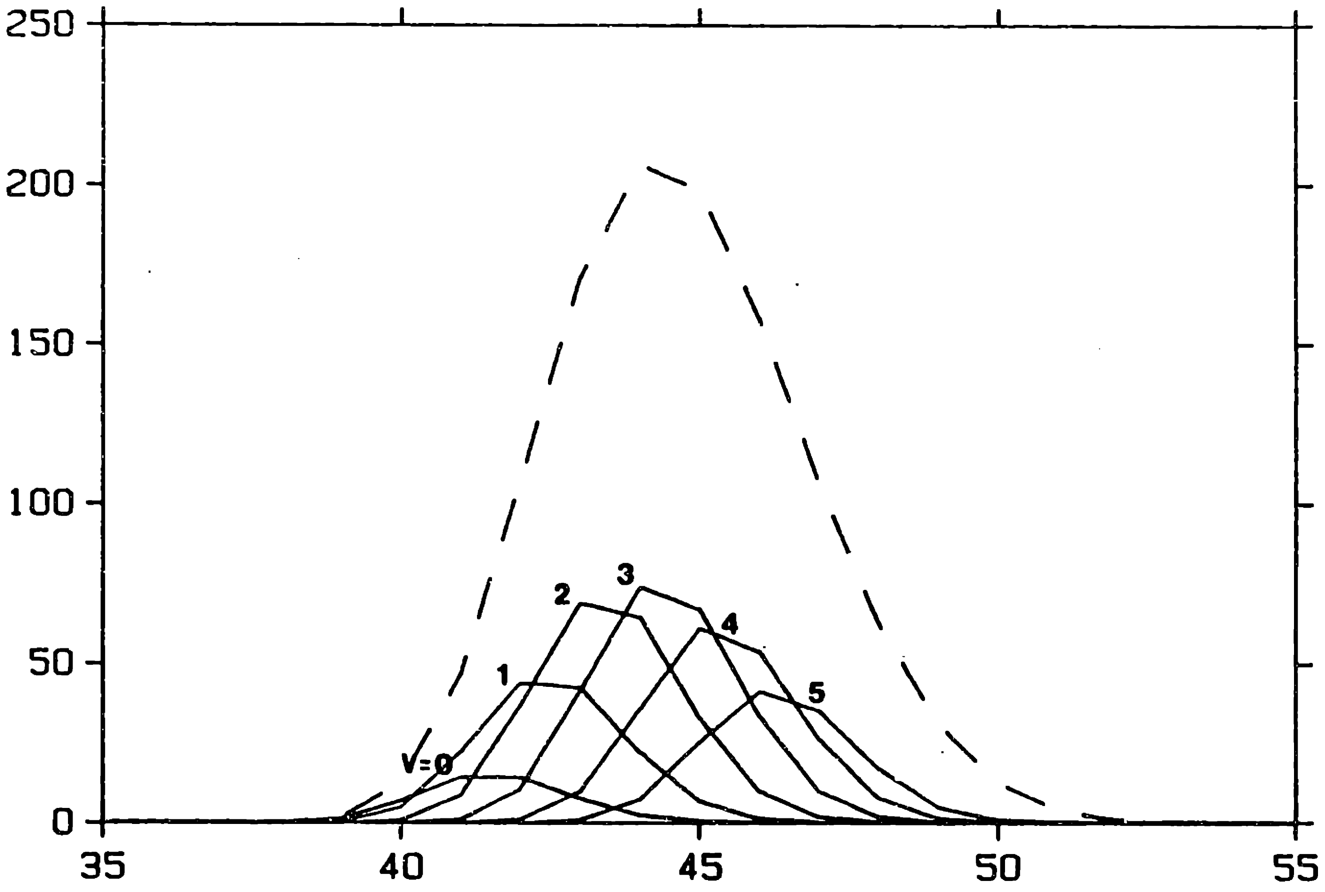

Fig 7-16 - CH_3 vibrational level partial cross sections, from the reaction on Ex (C).

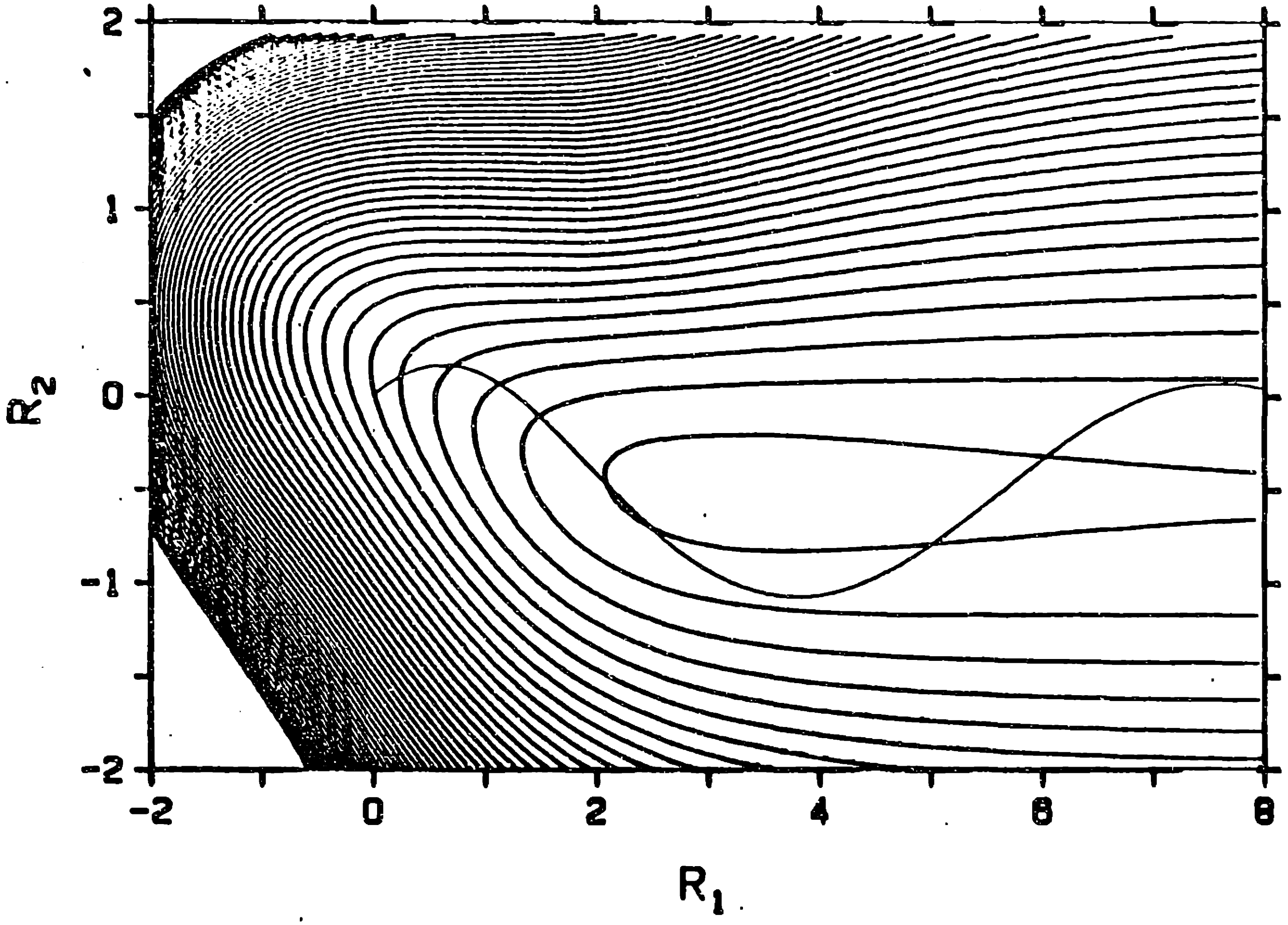

Fig 7-17 - Photodissociation classical trajectory on Ex (C).

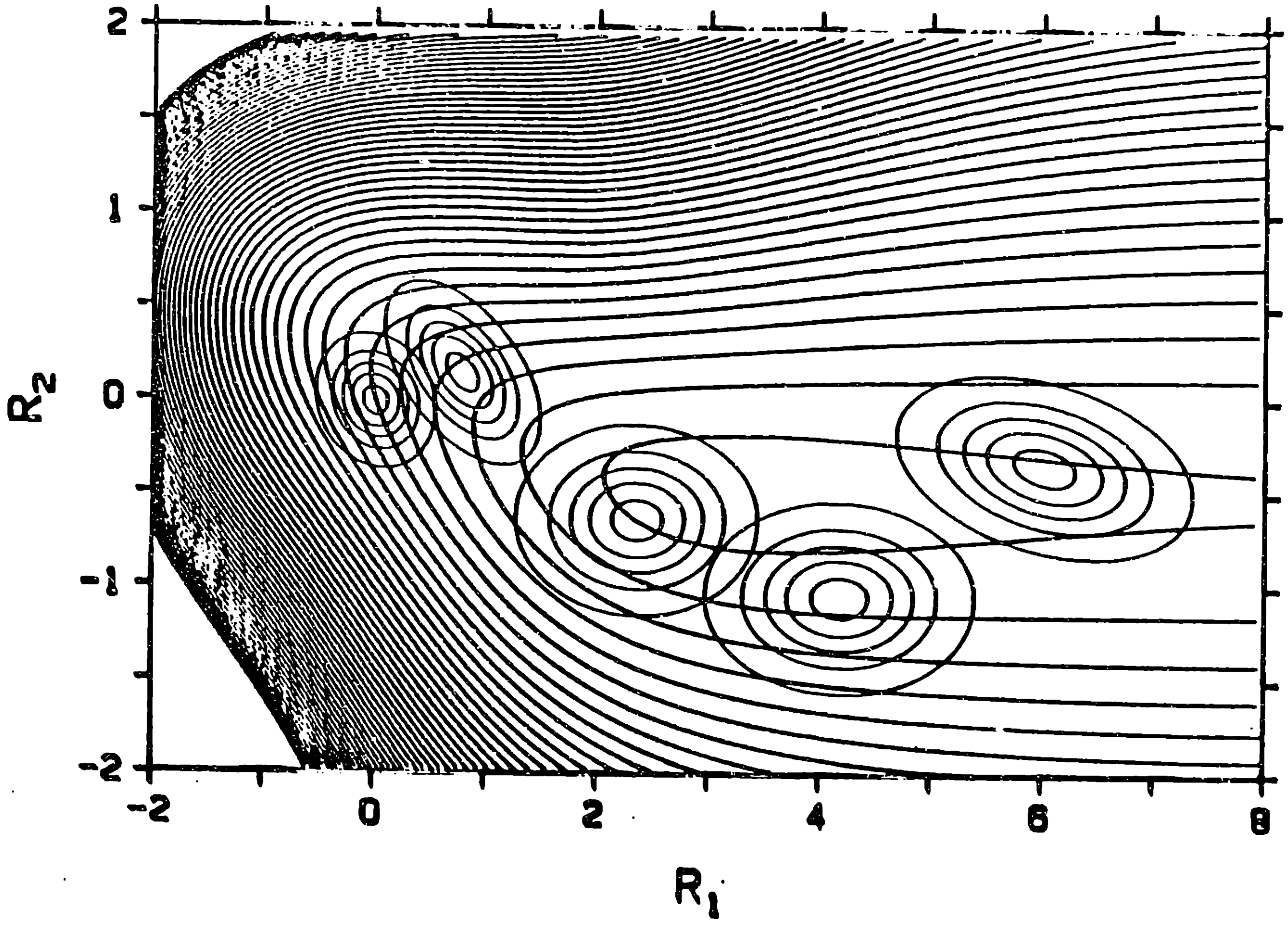

Fig 7-18 - $|\psi_1|^2$ at various times (~2 femto seconds apart), during the reaction on Ex (C).

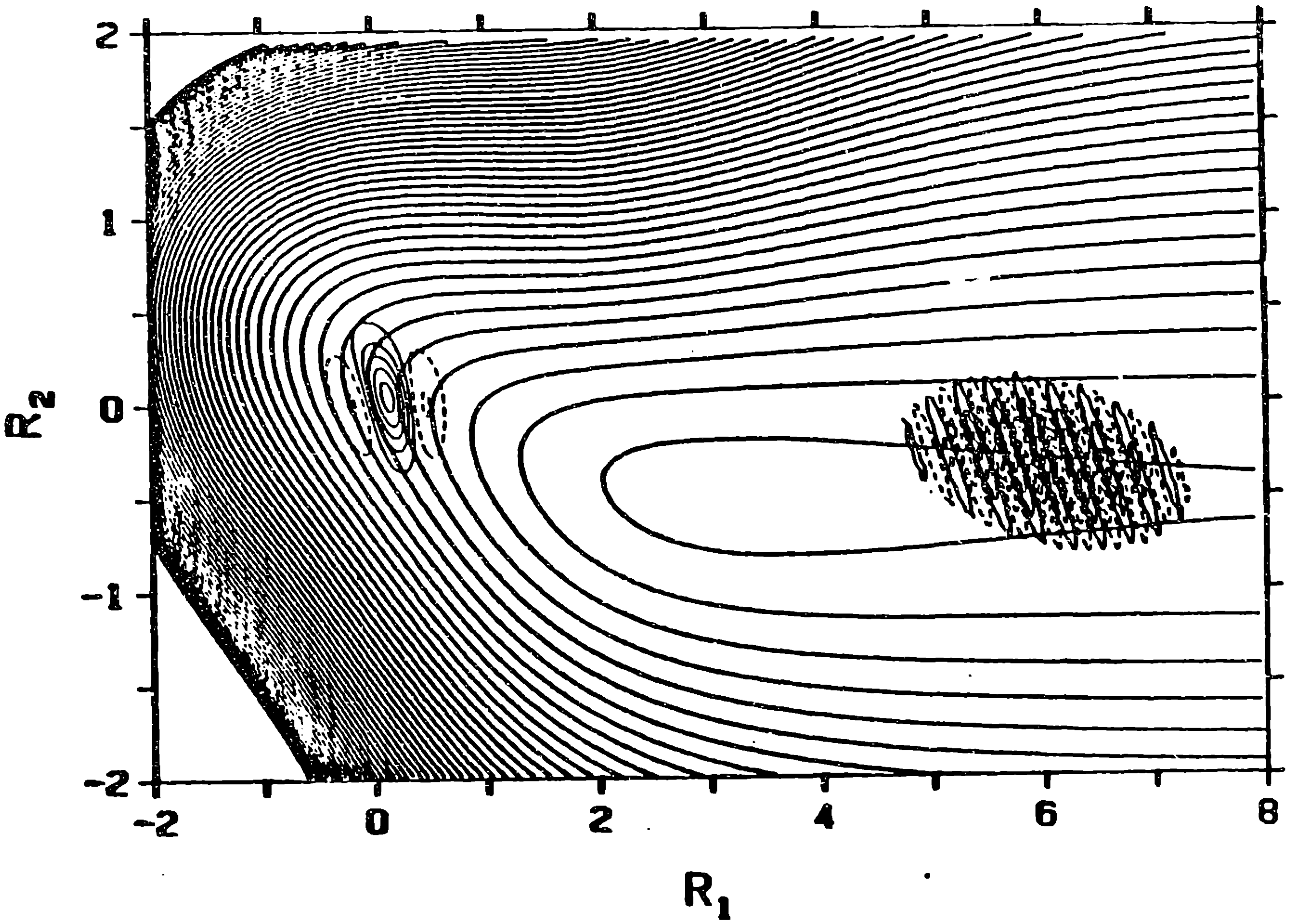

Fig 7-19 - $I_m \psi$ at 4 and 49 femto seconds. Note the rapid node development.

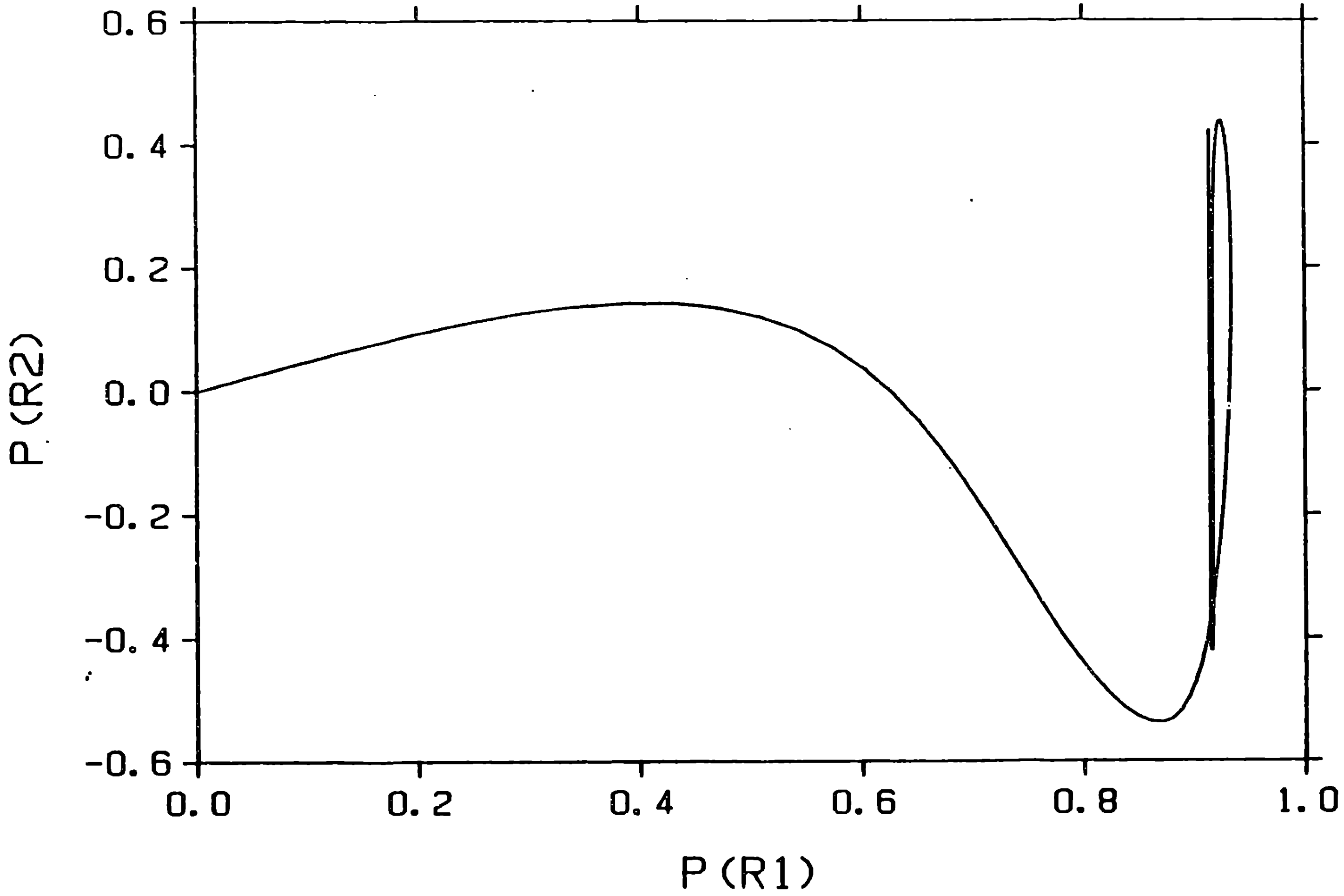

Fig 7-20 - **Classical trajectory in momentum space. Note the rapid increase in P_{R_1} in comparison to P_{R_2}.**

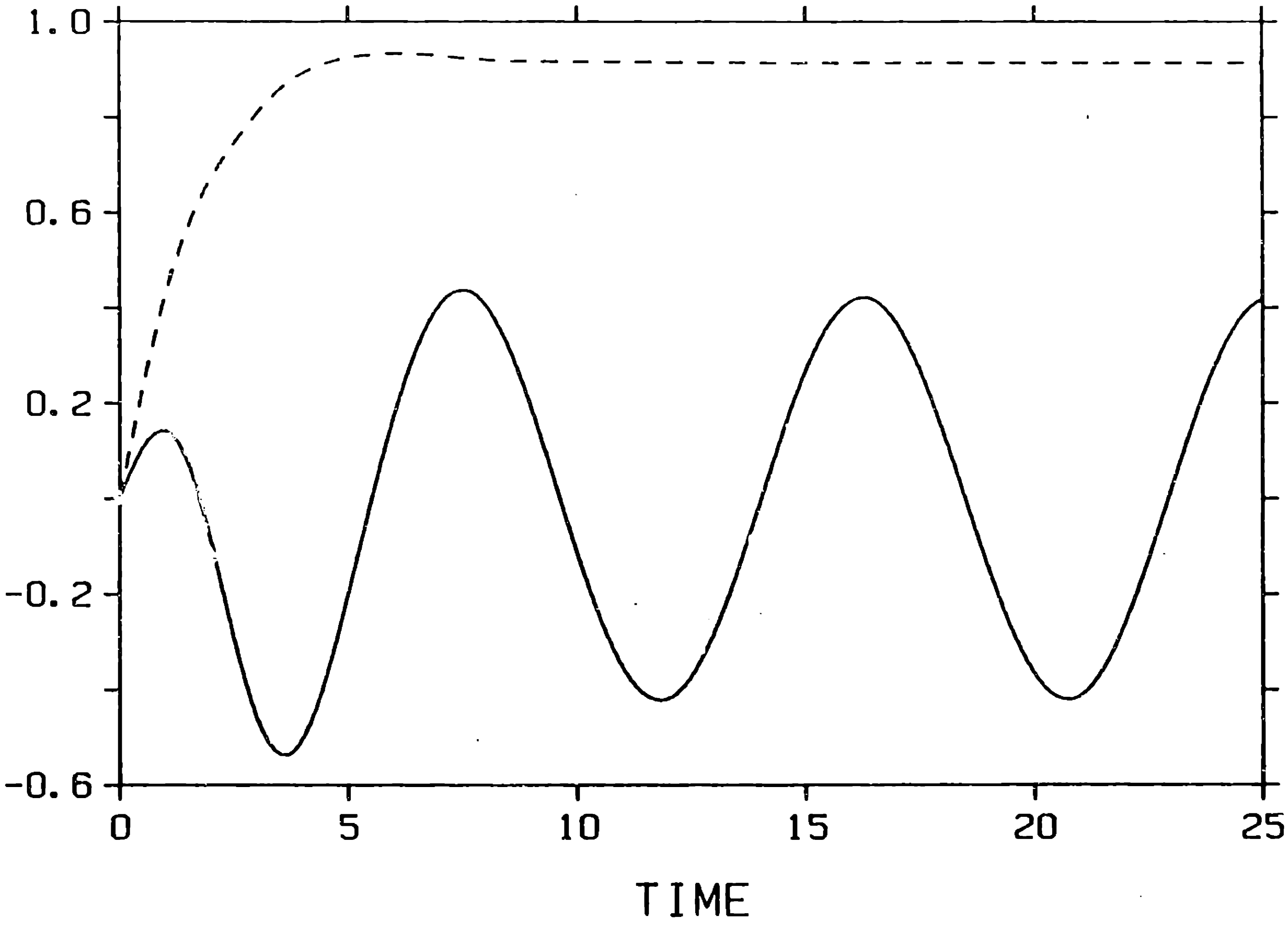

Fig 7-21 - Time evolution of P_{R_1} ---, and P_{R_2} ——. Note the linear rise in P_{R_1} for short times.

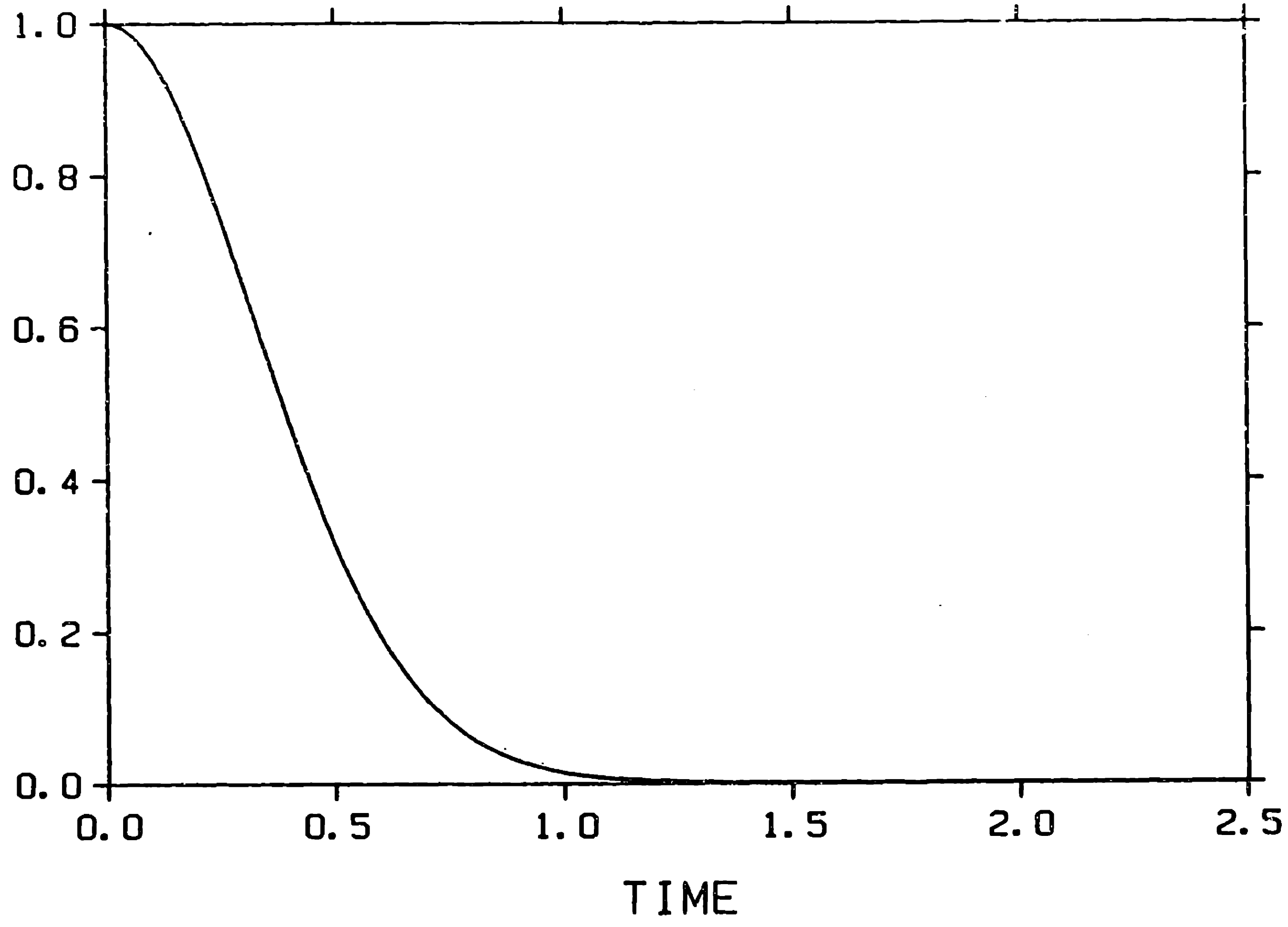

Fig 7-22 - $\langle\phi|\phi(t)\rangle$ for the reaction on Ex (C)

distribution (at the experimental wavelength) and its wavelength dependence are in relatively poor detailed agreement with experiment. Recent experiments[96] found product time of flight spectra at 248 nm to be almost identical to spectra obtained by excitation at 266 nm, i.e., final state distributions seem to be wavelength insensitive. Our calculations do not show this.

A further modification of surface Ex (C) was undertaken in an attempt to reproduce the observed absence of wavelength dependence of the final state distributions. The new surface Ex (D), shown in Figure 7-23 and given in Appendix E in FORTRAN form, is very similar to the qualitative one we proposed in chapter 5, in that the minimum in R_2 changes only very slightly in the initial stages of the reaction. The transformation from bent to planar CH_3 occurs only at large R_1. Figures 7-24 and 7-25 show the calculated absorption spectra and final state distributions. Note that there is a greater difference between the two calculated absorption spectra than we found with the other surfaces. This implies that here the gaussian approximation is rather poor. If the qualitative features of the predicted distributions can be trusted, they suggest that the modifications leading to Ex (D) do produce the desired effect. I.e., the distribution has become largely wavelength insensitive. Figures 7-26 through 7-31 give a summary of semi-classical and classical studies on surface Ex (D).

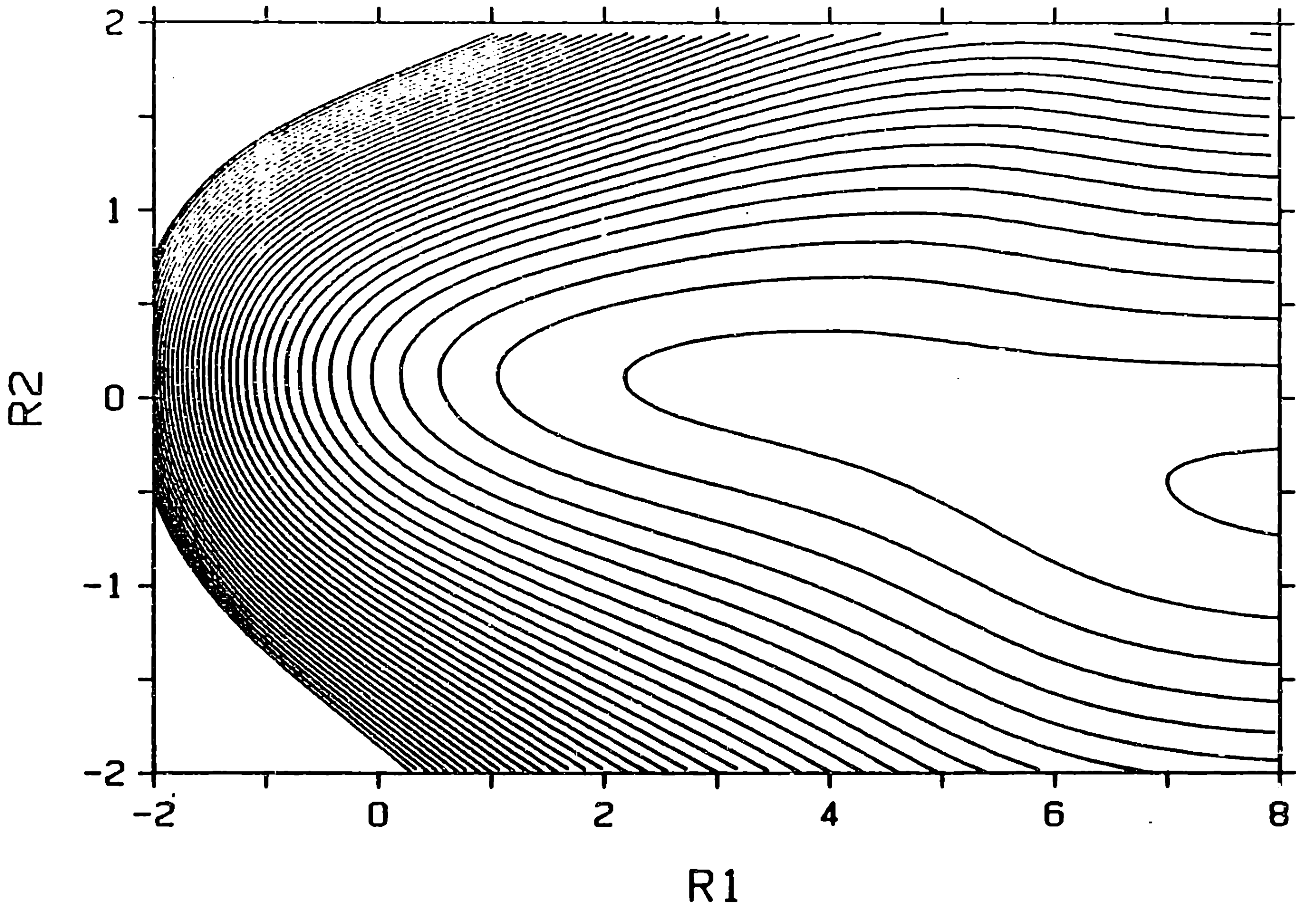

Fig 7-23 - Contour plot for Ex (D)

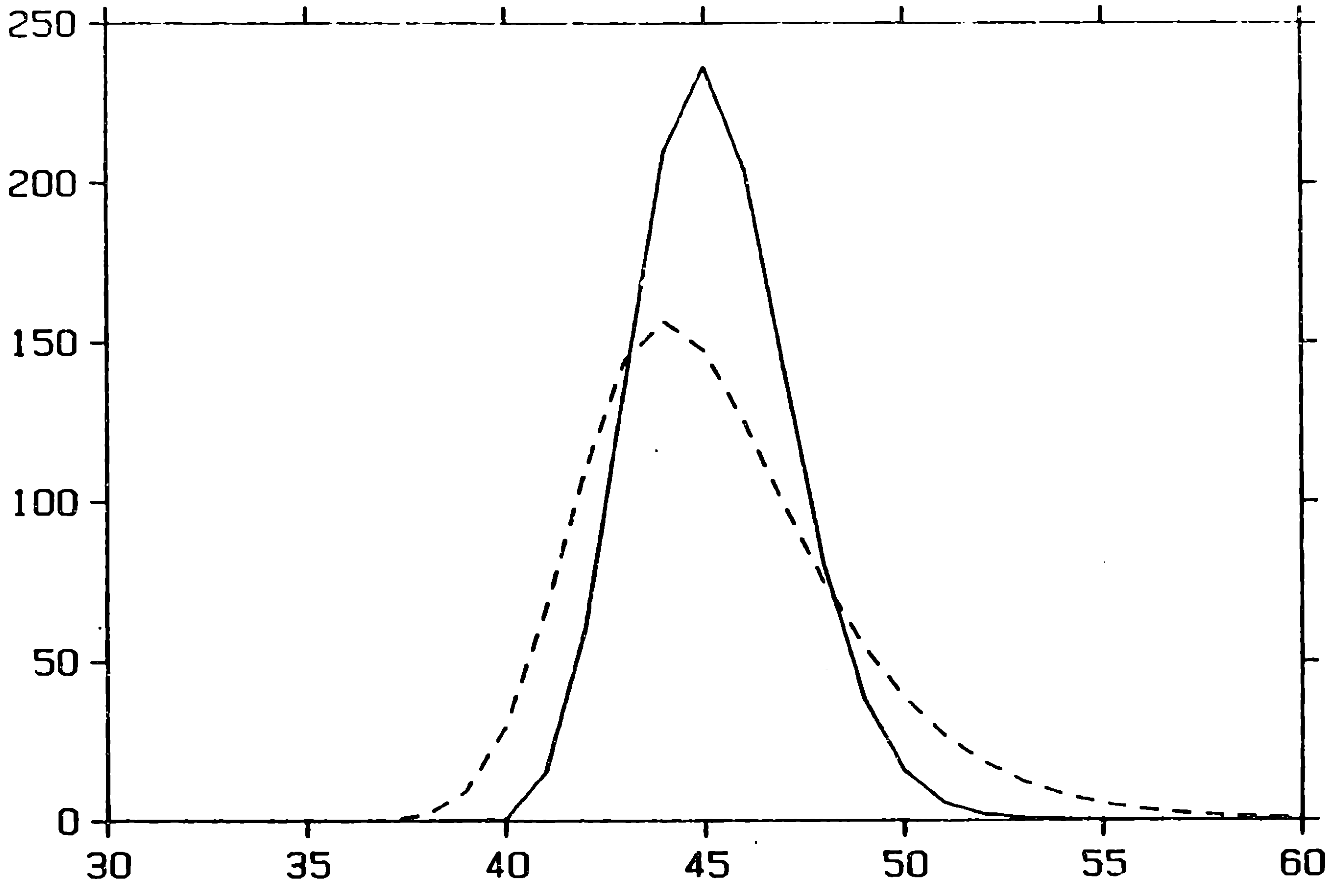

Fig 7-24 - **Absorption spectra for the transition Ex (D) - G (B).** —— **Fourier** transform method, --- sum of partial cross sections.

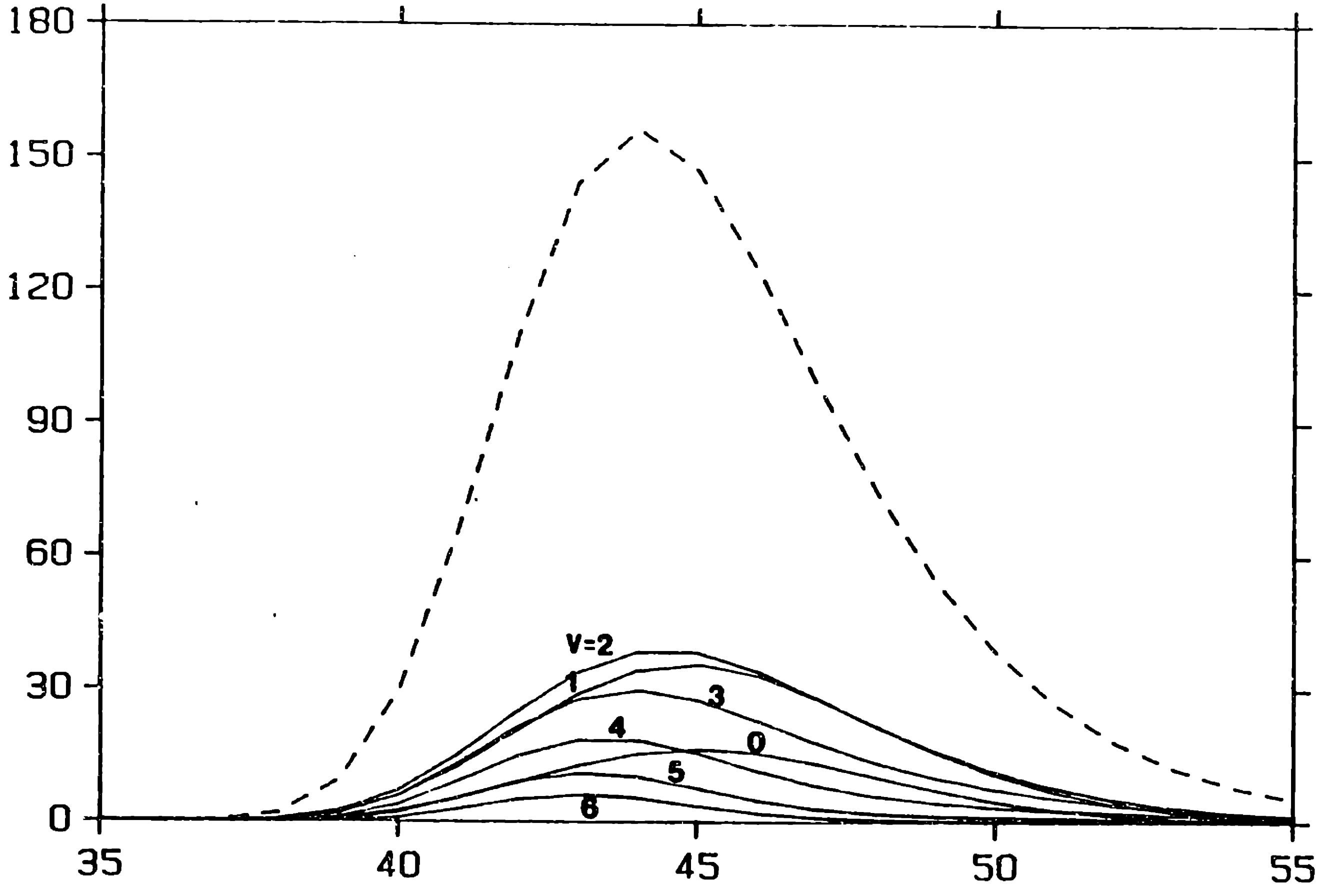

Fig 7-25 - CH_3 vibrational level partial cross section from the reaction on Er (D).

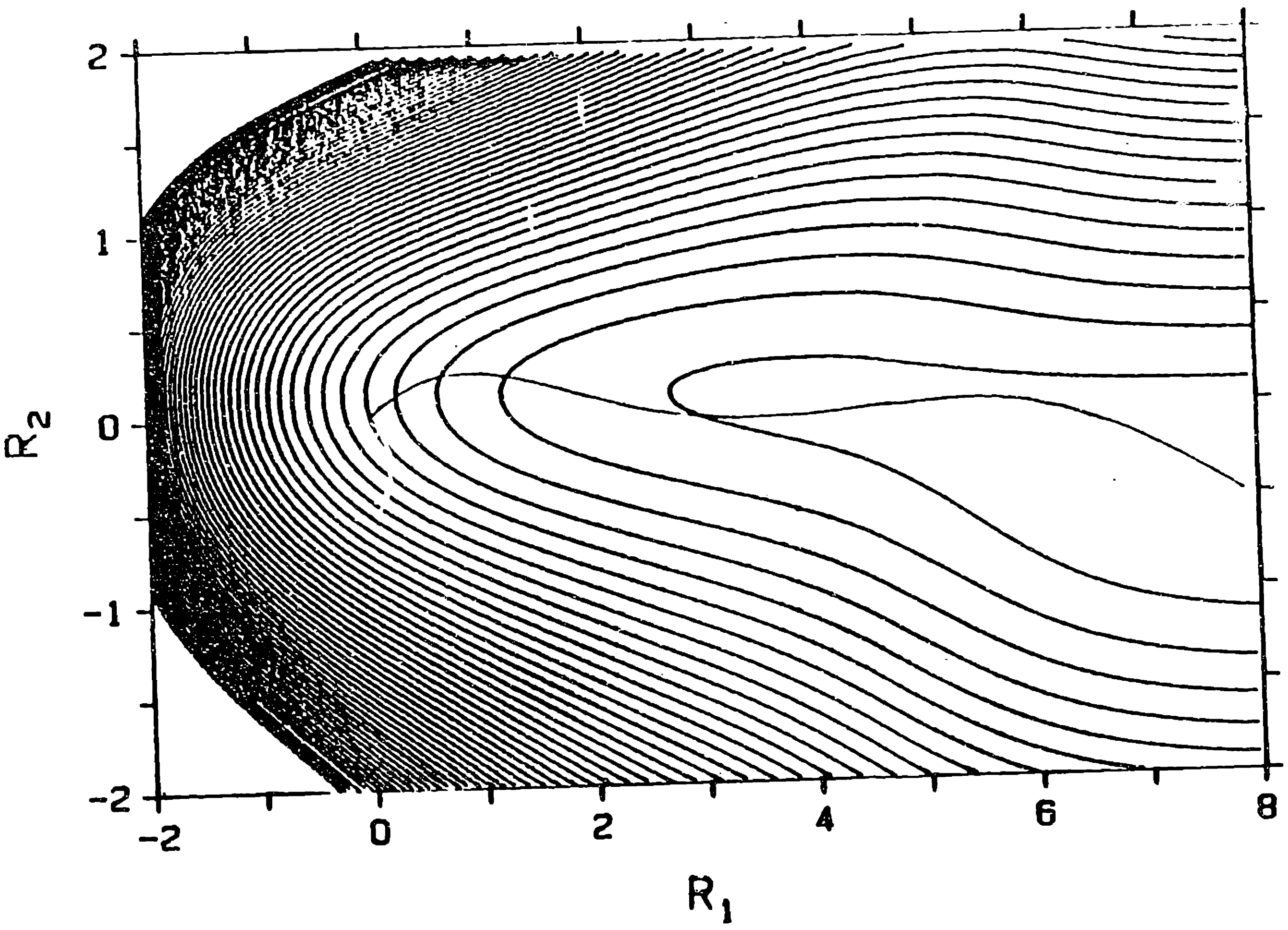

Fig 7-26 - Photodissociation classical trajectory on Ex (D).

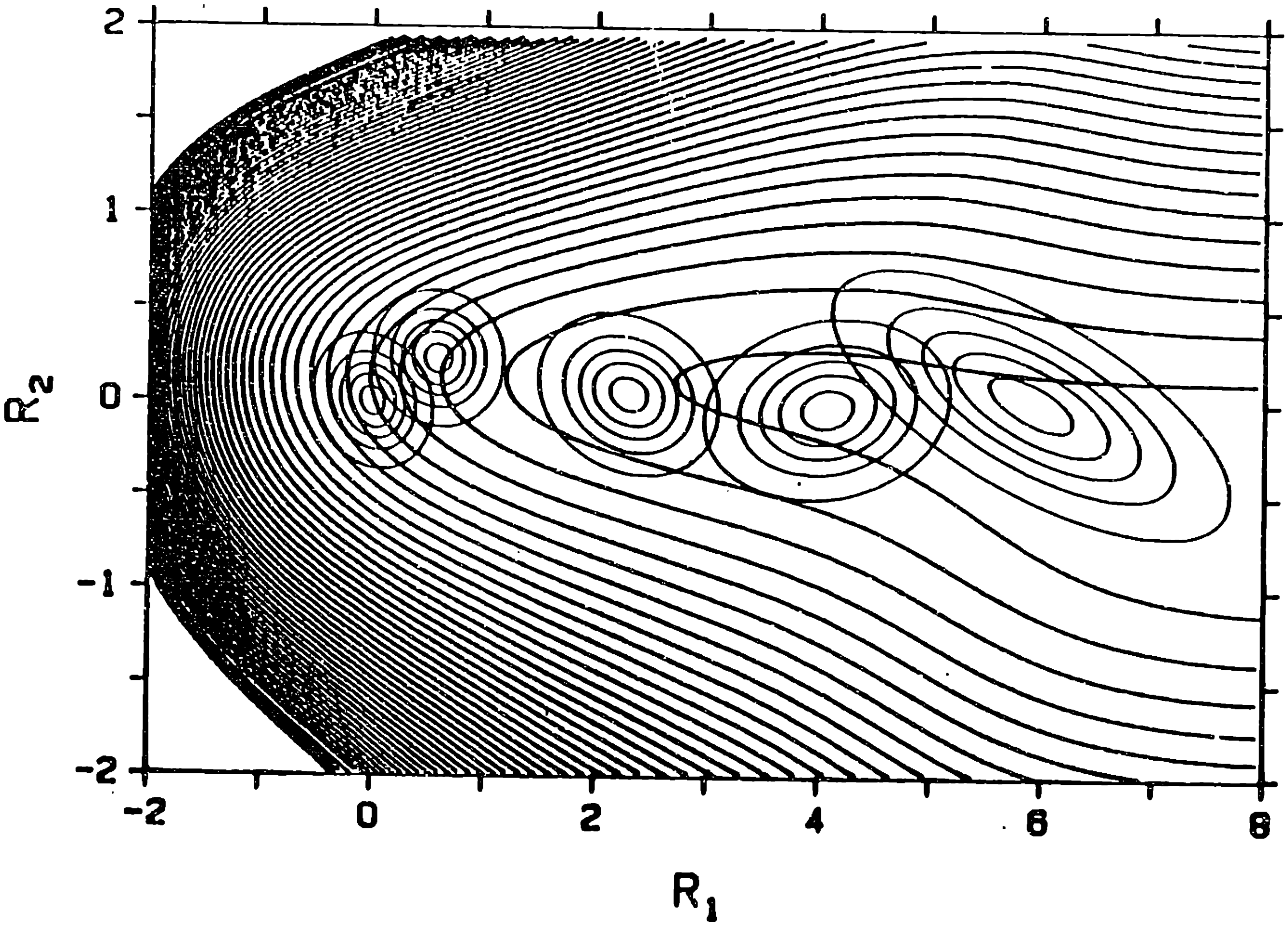

Fig 7-27 - $|\psi|^2$ at various times (~2 femto seconds apart) during the reaction on Ex (D).

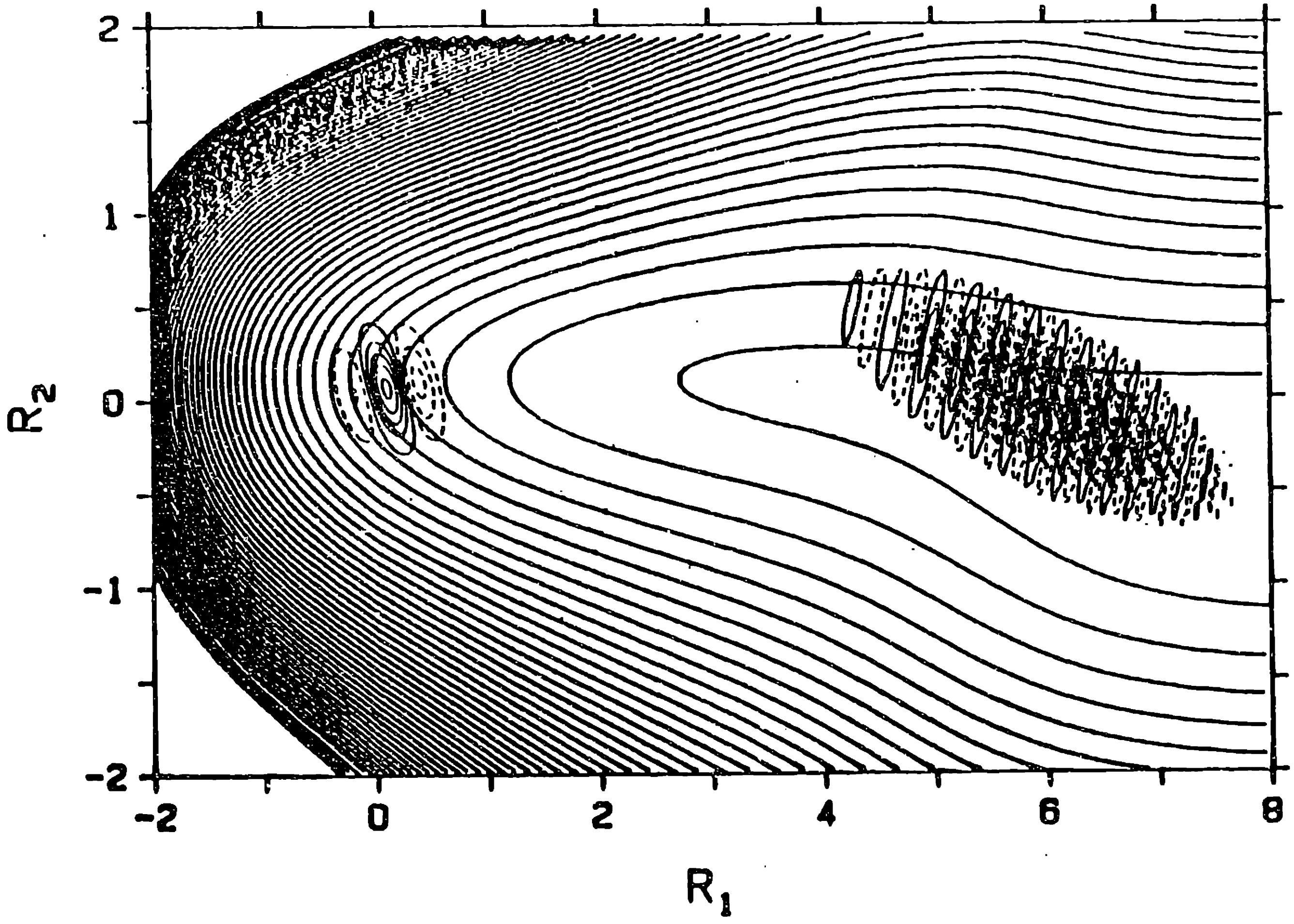

Fig 7-28 -Imψ at 4 and 49 femto seconds.

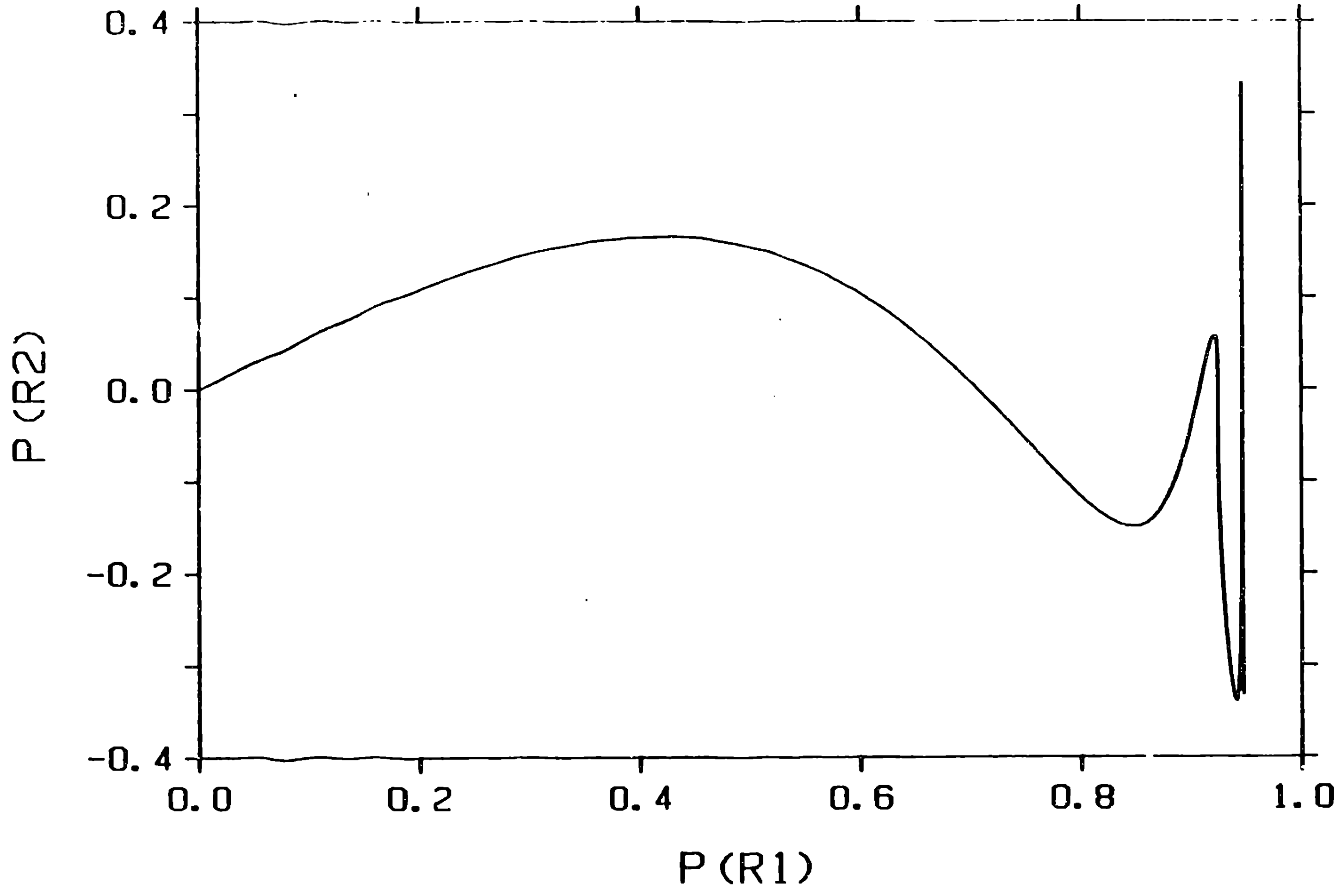

Fig 7-29 - Classical trajectory in momentum space.

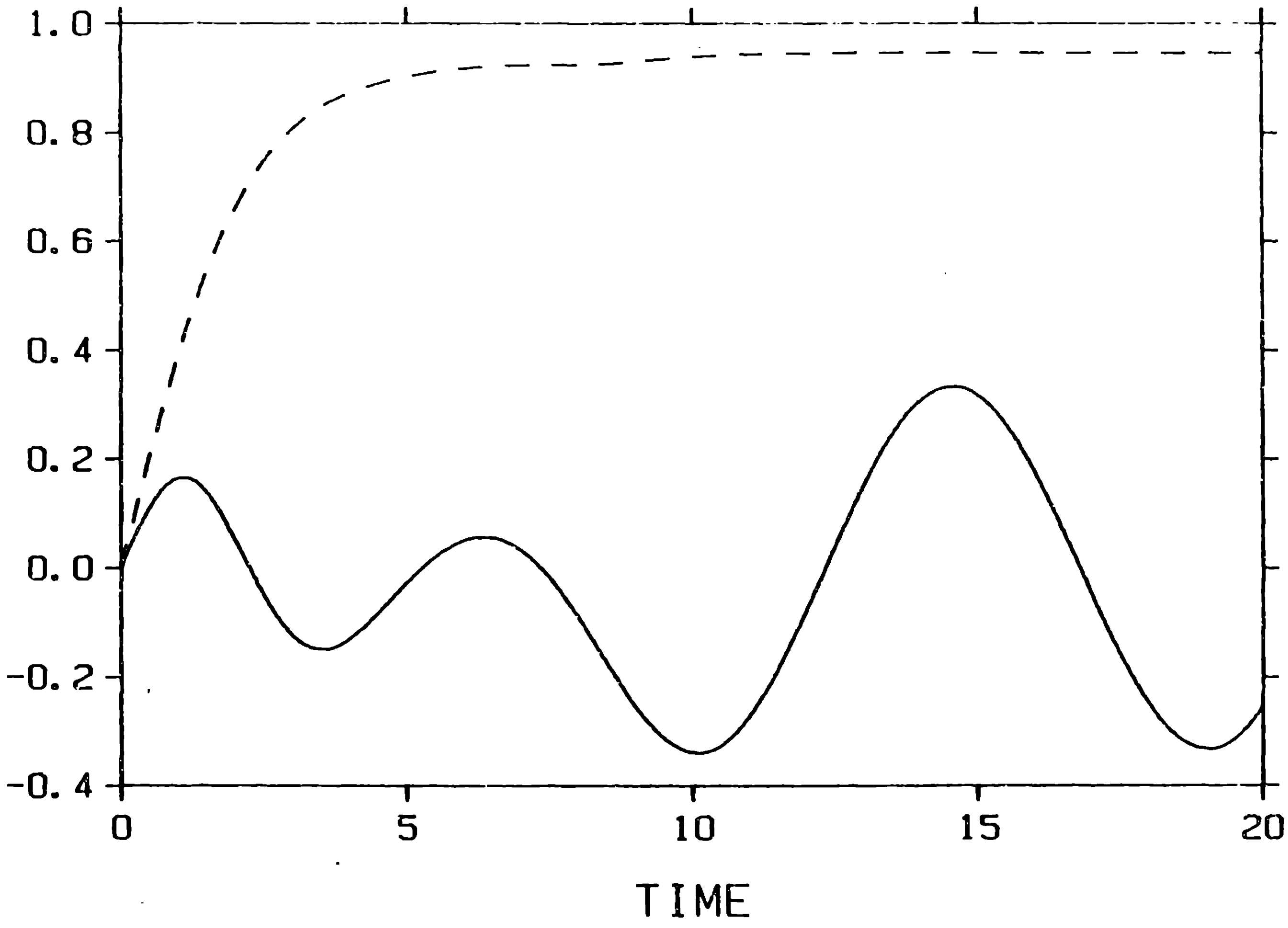

Fig 7-30 - Time evolution of P_{R_1} ---, and P_{R_2} ——.

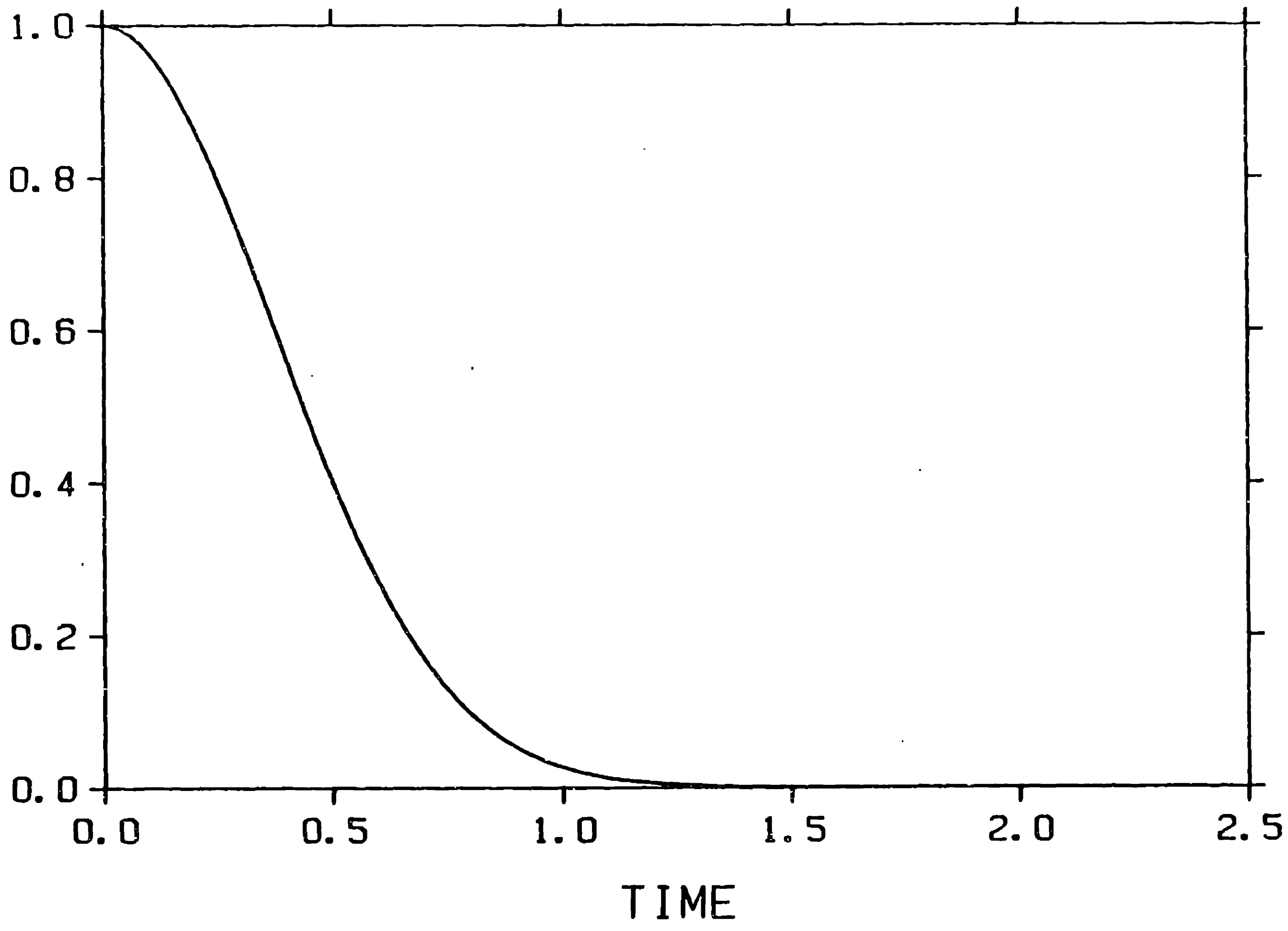

Fig 7-31 - $\langle\phi|\phi(t)\rangle$ for the reaction on Ex (D).

II. The Ground State

To reproduce observed ground state vibrational eigen energies a variational method was used. Following the procedure suggested by Davis[97], gaussian basis functions of the following forms were employed:

$$\text{VII.6} \quad G = \operatorname{Exp}[a_i (q_i^\circ - q)^2 - iP_i q] + cc$$

with $\Delta p \, \Delta q = \hbar$

and $a_i = \frac{\omega_i}{2\hbar}$

These were placed on a grid in phase space .25 apart. The advantage of the gaussian basis set lies in the ease with which matrix elements can be calculated. Unfortunately the functional form that we have used for the potential does not yield closed form analytic expressions for the matrix elements. To alleviate this problem the original surface (G (B)) was refitted by a new functional form given in Appendix F and shown in Figure 7-32. In the new potential (G (C)) each hyperbolic tangent function was fitted by a gaussian function. The new functional form yielded analytic expressions for the matrix elements. Preliminary diagonalization using a small basis set suggested the desirability of a slight change in the Morse part of the potential to produce vibrational energies closer to the observed ones. That final modification is given in Appendix H (surface G(D)). The diagonalization using a large basis set (390 basis function) gave the calculated energies listed in Table 7-1.

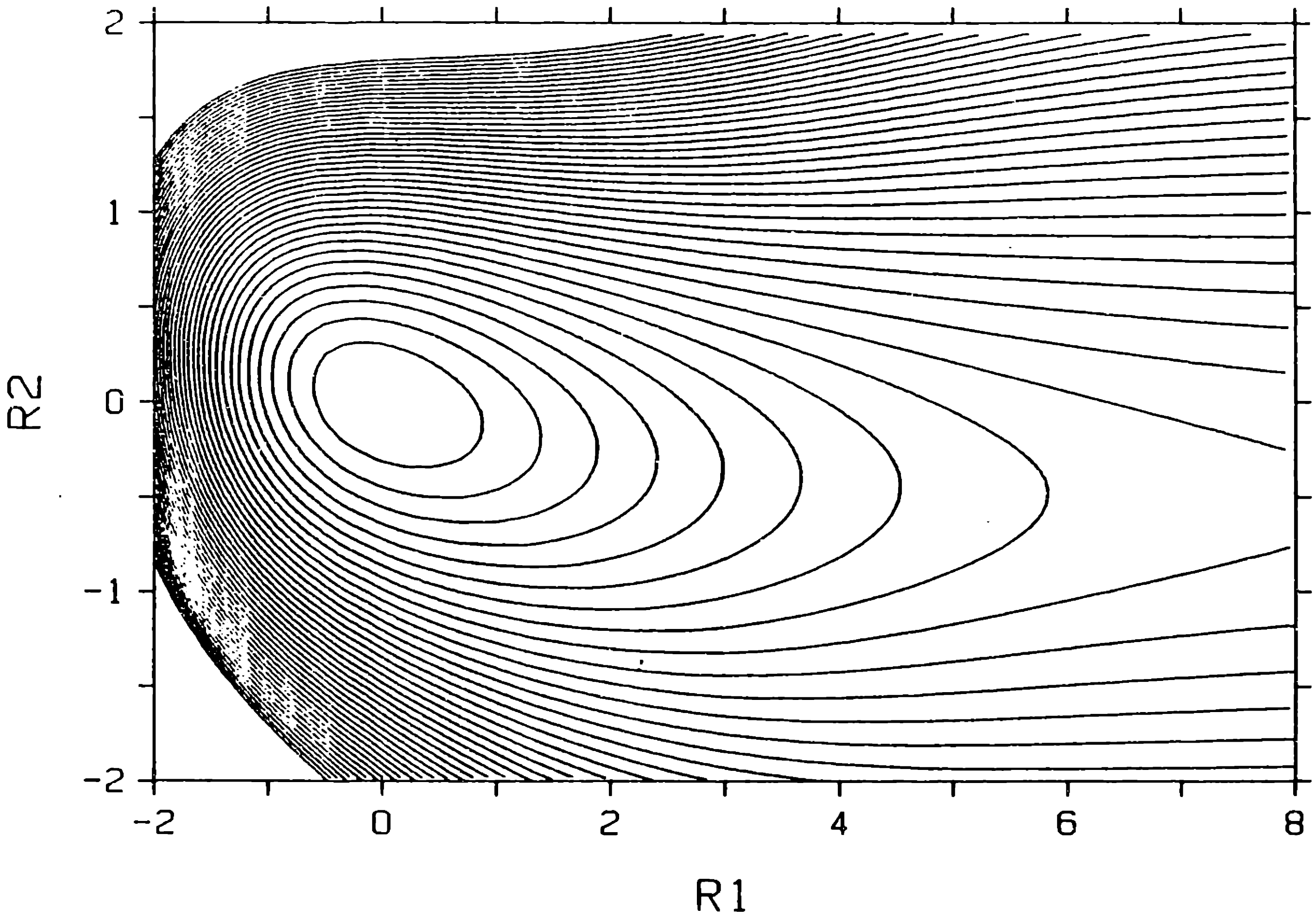

Fig 7-32 - Contour plot for G (C) surface.

Table 7-1

State#	Assignment	Calc. Energy cm^{-1}	Expt. Calc. cm^{-1}
2	3_1	536	-3
3	3_2	1065	-5
4	2_1	1246	8
5	3_3	1588	-9
7	3_4	2104	-12
10	3_5	2614	-20
11	$2_1 3_3$	2815	-1
13	3_6	3117	-23
14	$2_1 3_4$	3324	-18
16	3_7	3614	-24
18	$2_1 3_5$	3828	--
20	3_8	4105	-26
22	$2_1 3_6$	4325	-26
24	3_9	4588	-23
26	$2_1 3_7$	4816	-35
29	3_{10}	5067	-23
31	$2_1 3_8$	5299	-22
34	3_{11}	5538	-22
36	$2_1 3_9$	5777	11
38	3_{12}	6003	-21
42	$2_1 3_{10}$	6247	1
43	3_{13}	6461	-15
47	$2_1 3_{11}$	6712	-10
49	3_{14}	6914	-18
52	$2_1 3_{12}$	7170	-11
55	3_{15}	7361	-14
59	$2_1 3_{13}$	7623	-19
62	3_{16}	7803	-19
66	$2_1 3_{14}$	8060	-20
69	3_{17}	8245	-33
77	3_{18}	8698	-64
85	3_{19}	9176	-116
94	3_{20}	9687	-211
104	3_{21}	10233	-347

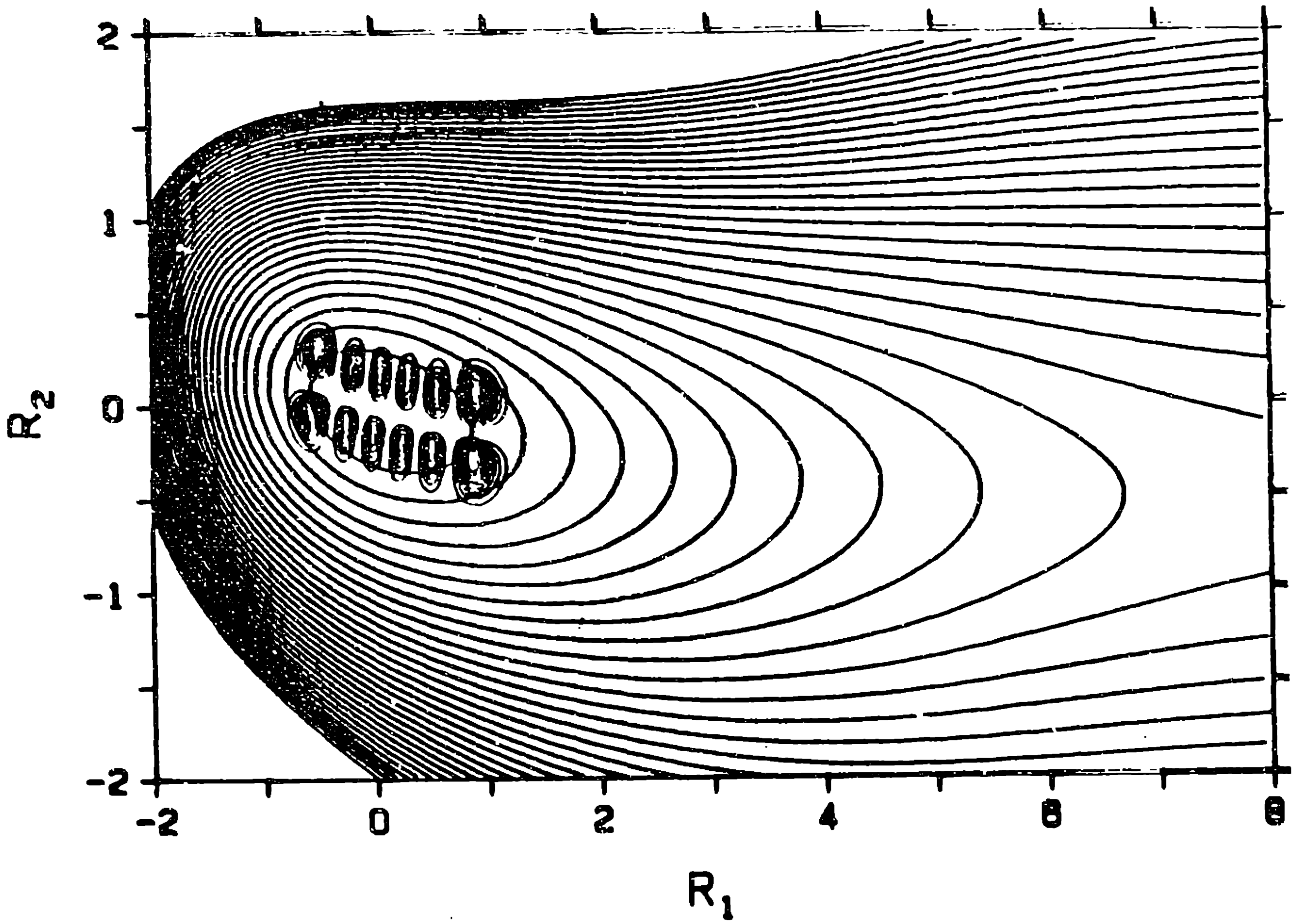

Fig 7-33 - The $2_1\ 3_5$ vibrational wave function

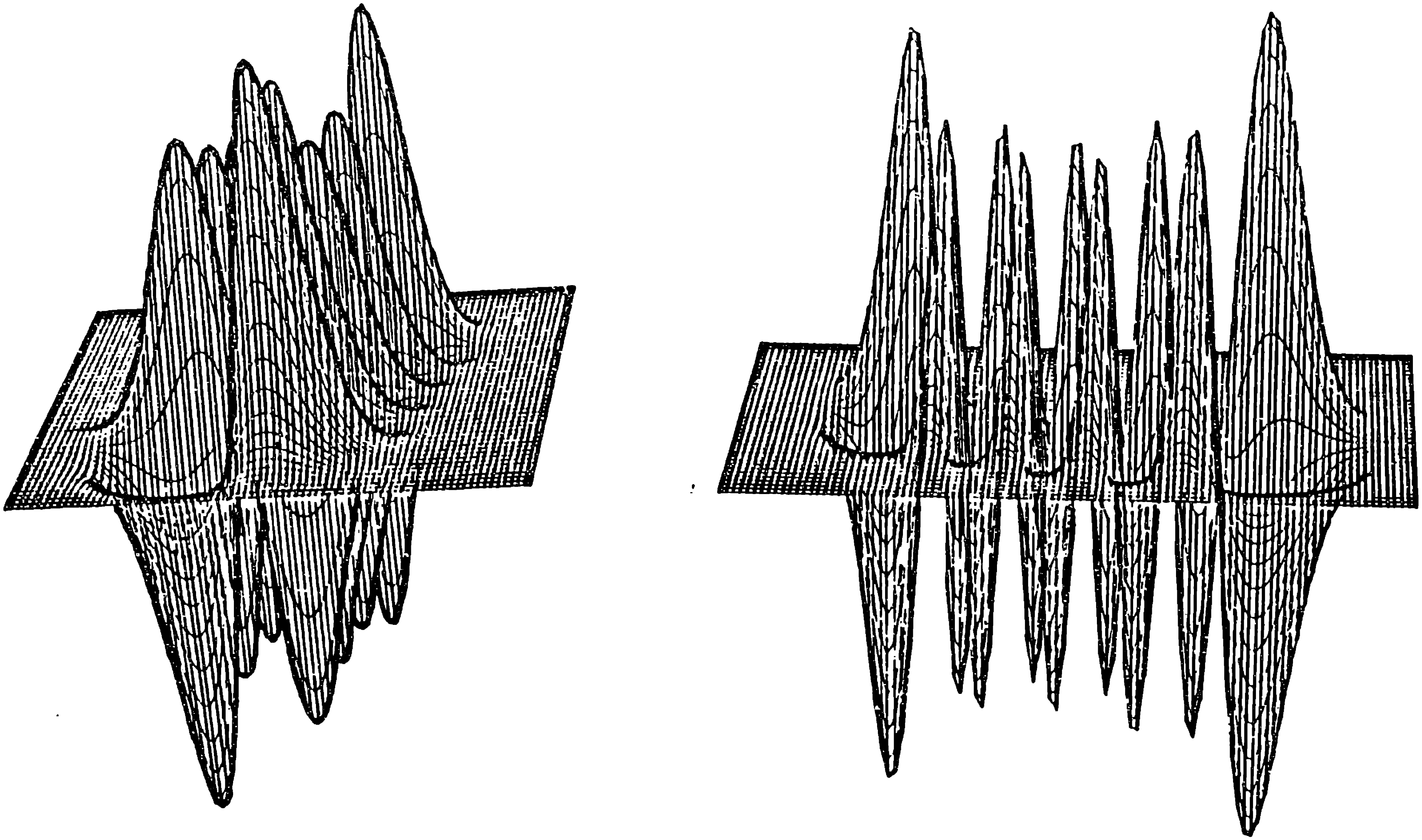

Fig 7-34 - Three dimensional representation of the $2_1 3_8$ state.

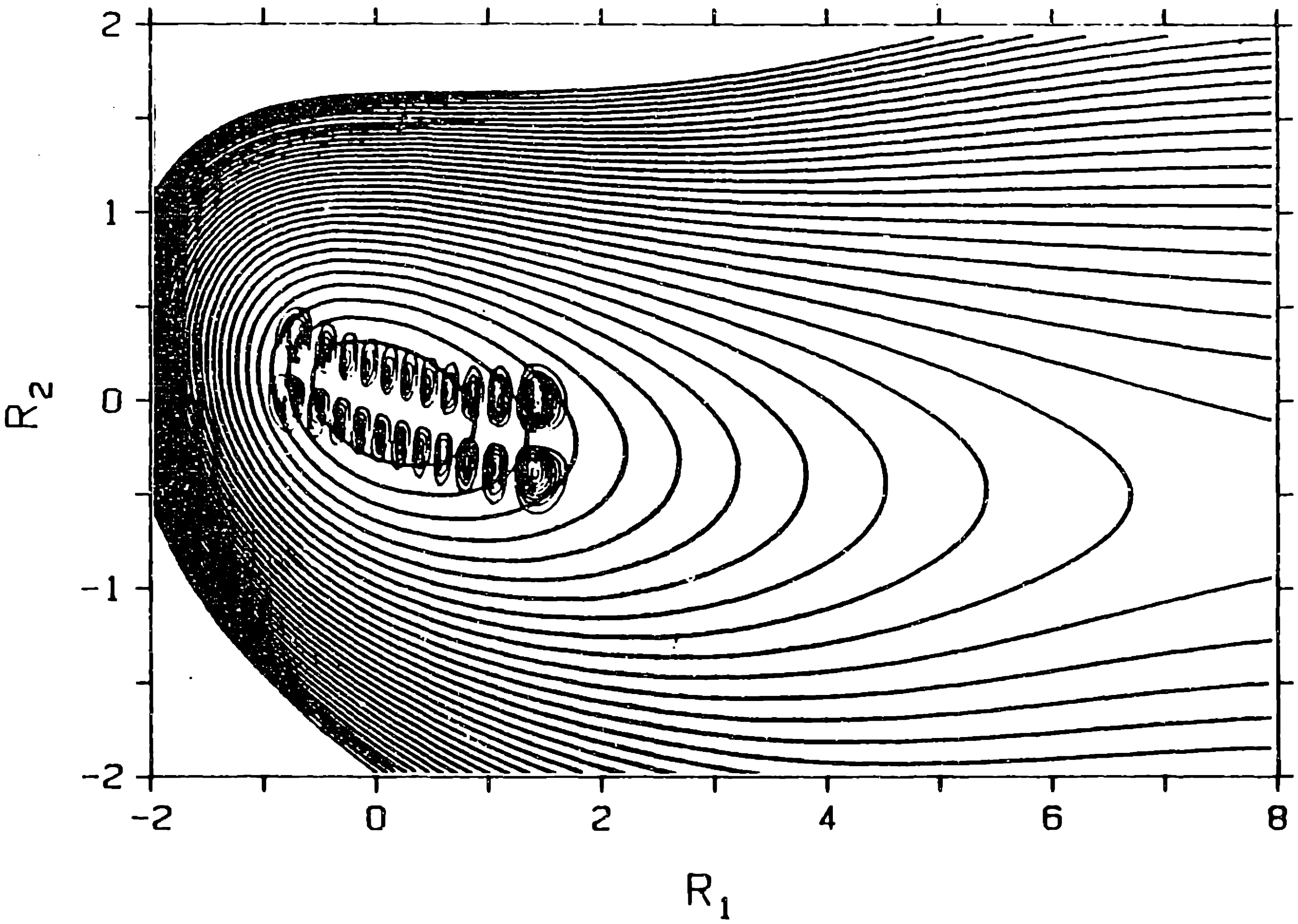

Fig 7-35 - The $2_1\ 3_{10}$ vibrational wave function

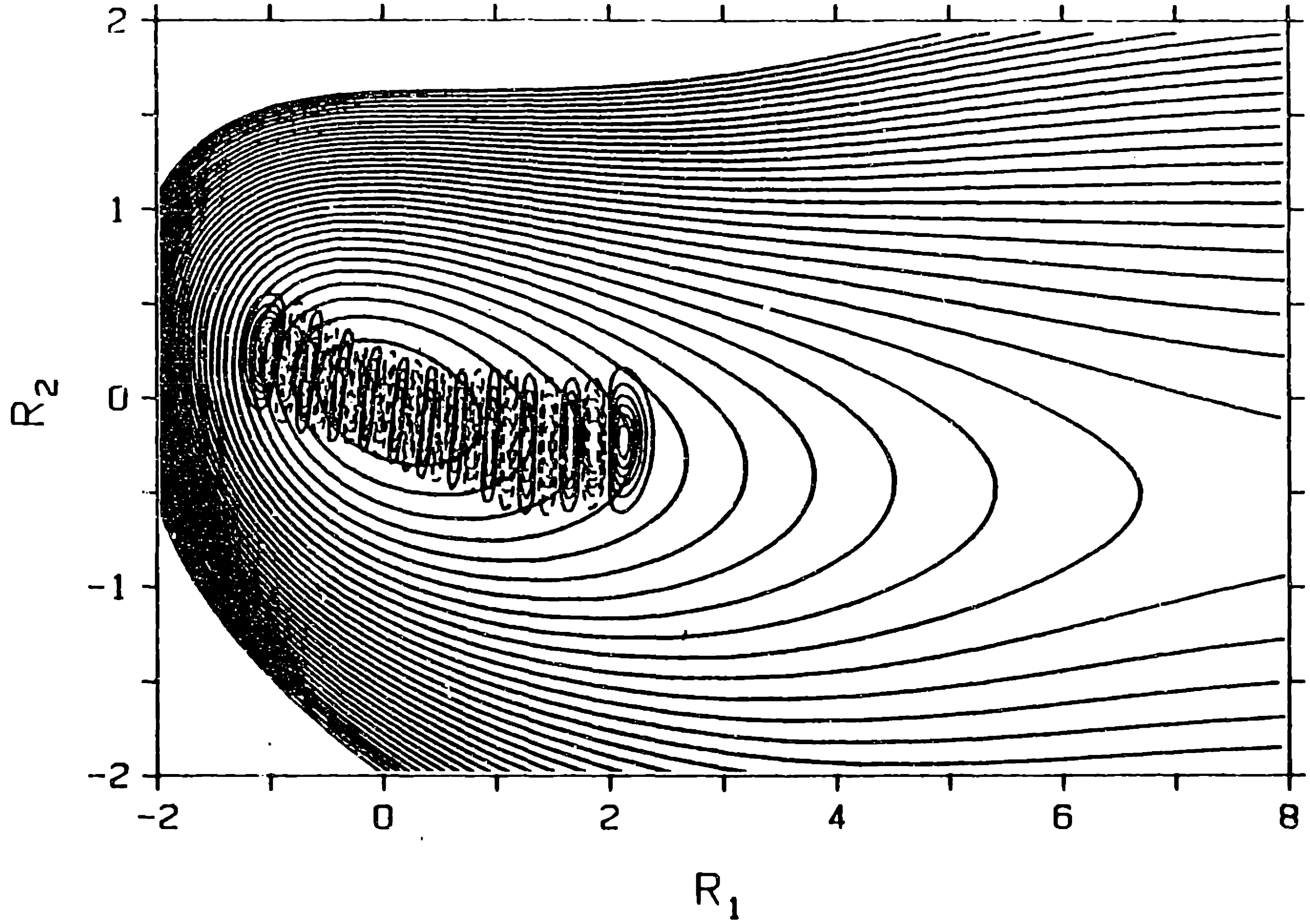

Fig 7-36 - The 3_{20} vibrational wave function.

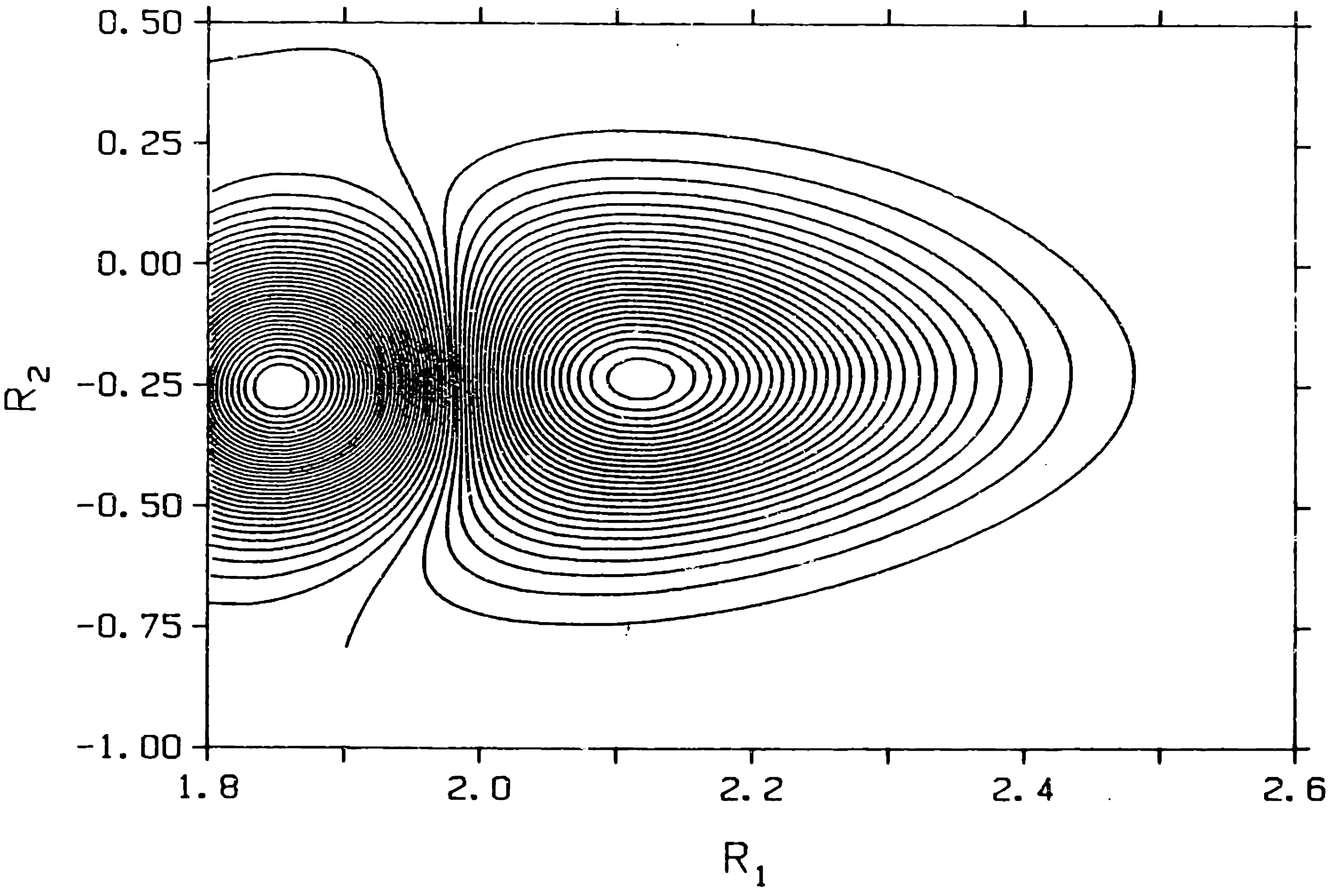

Fig 7-37 - Detail of the 20th node of the 3_{20} vibrational state.

The same calculation was used to obtain vibrational eigenfunctions. Some of these are shown in Figures 7-33 through 7-37. All the wave functions we have examined (up to 10,000 cm^{-1}) show very regular nodal patterns, thus affording easy assignments. The nodal lines in the excited vibrational eigenfunctions appear to define a "natural coordinate system" for describing the vibrational motion in this two-dimensional system. This coordinate system is curvolinear, but seems to define a set of "natural" as opposed to "normal" vibrational modes.

To crudely simulate the photoemission experiment, information from classical photodissociation trajectories on surfaces Ex (C) and Ex (D) was used to determine a set of initial conditions for classical trajectories on the ground state surface. Classical trajectories run on the excited state PES yielded R_1, R_2, P_{R_1}, P_{R_2} for each t. At selected time intervals these upper-state values were transferred to the ground state (simulating vertical transitions). The subsequent classical dynamics are illustrated in Figure 7-38 through 7-47. In general, the trajectories exhibit Lissajous motion with large amplitude in R_1 and smaller amplitude motion in R_2. The general areas covered by these trajectories are strikingly similar to those covered by the wave functions corresponding to the excited vibrational levels observed in the photoemission experiment. We have not yet completed the more complicated calculation indicated by the dynamic theory expression for the Raman amplitudes: half Fourier-transform of the overlap between the moving wave packet and the selected ground-state vibrational wave function. The current results, however, are quite encouraging as to the prospects that this procedure will successfully pick out the actual vibrational states that occur in the emission spectrum.

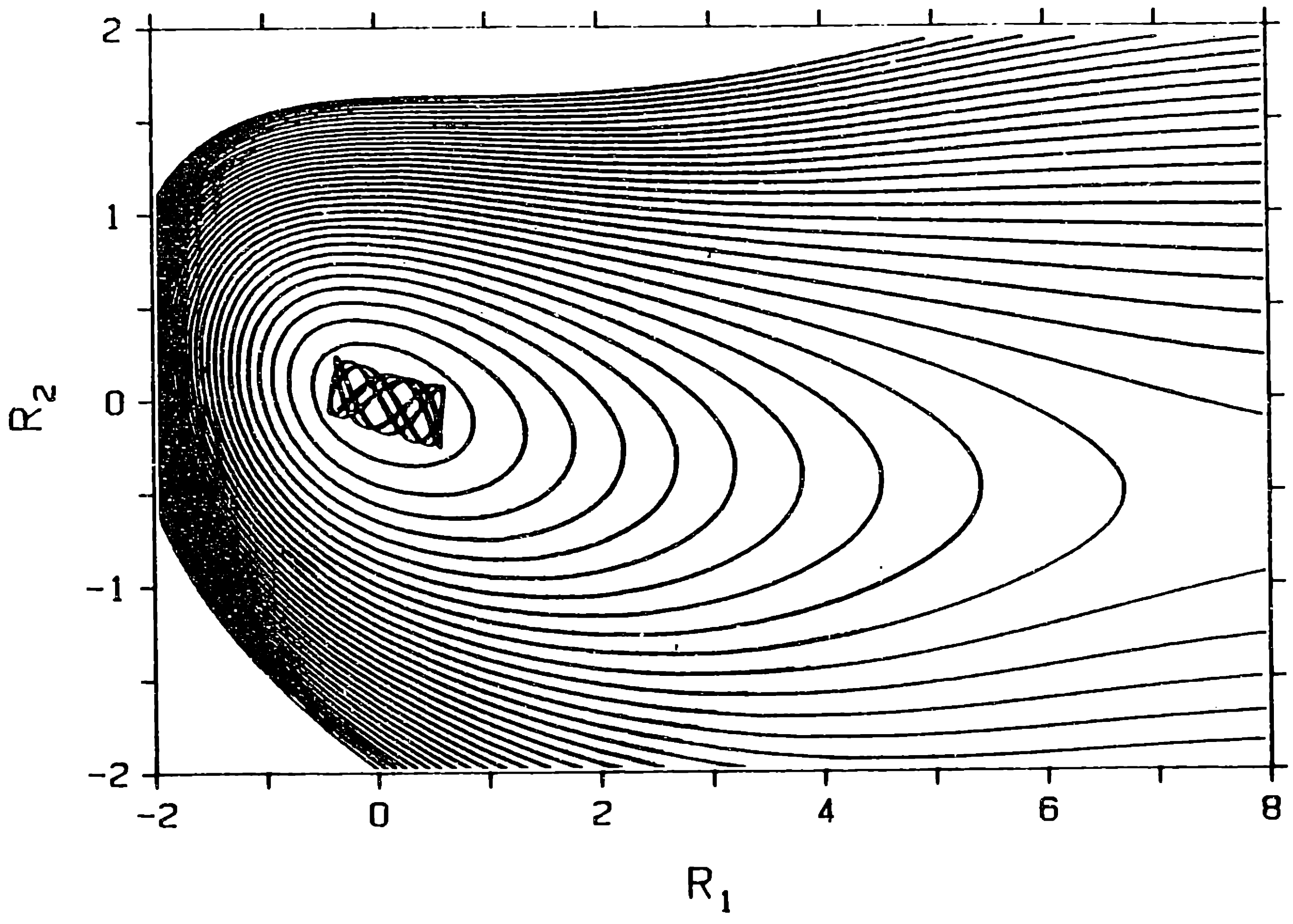

Fig 7-38 - Classical trajectory on G (C). Initial condition: transferral from Ex (C) at t = .754 with $R_1 = .13$, $R_2 = .06$, $P_{R_1} = .34$ $P_{R_2} = .14$.

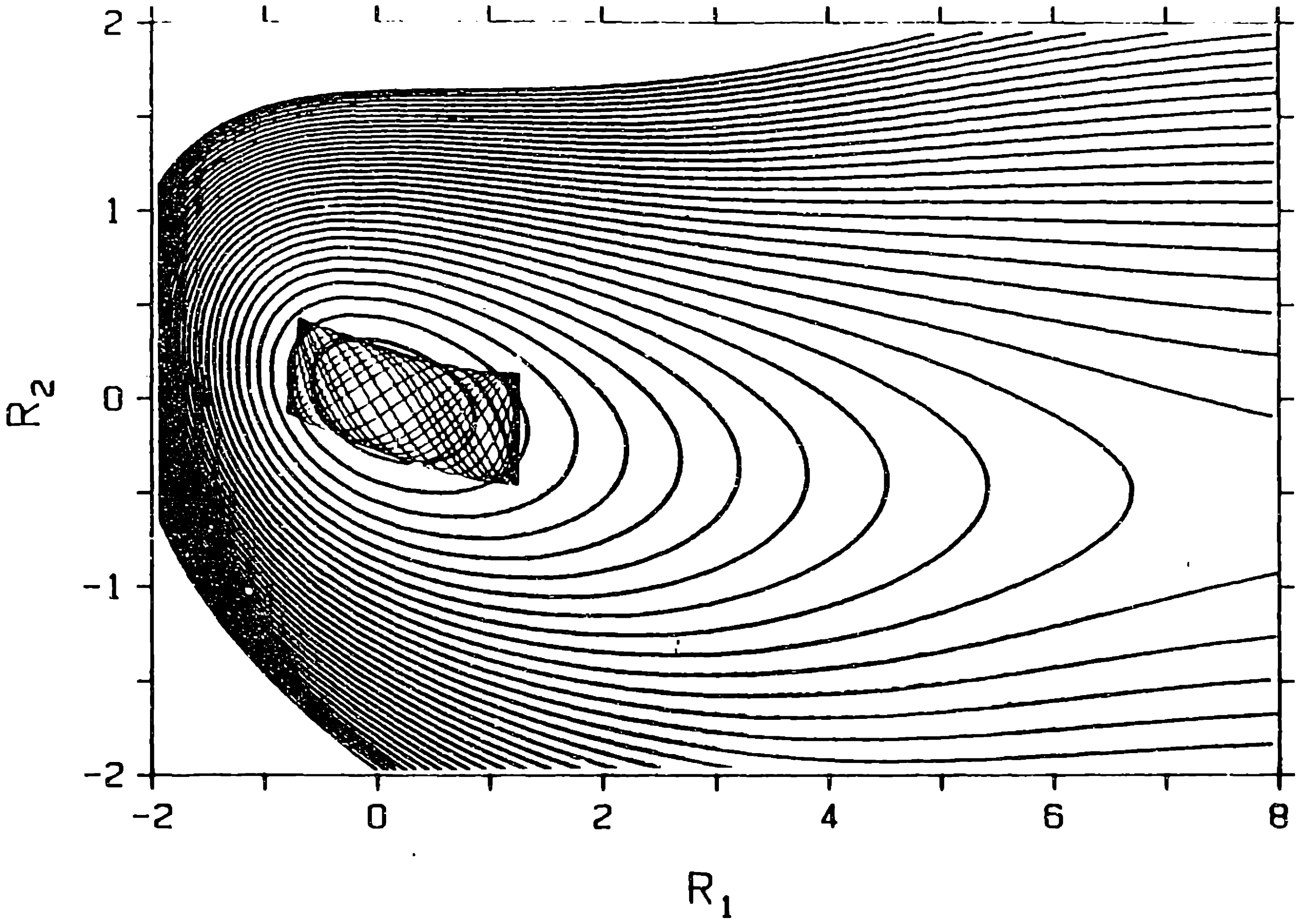

Fig 7-39 - From Ex (C) at t = 1.508 with $R_1 = .48$, $R_2 = .15$ $P_{R_1} = .57$ $P_{R_2} = .07$.

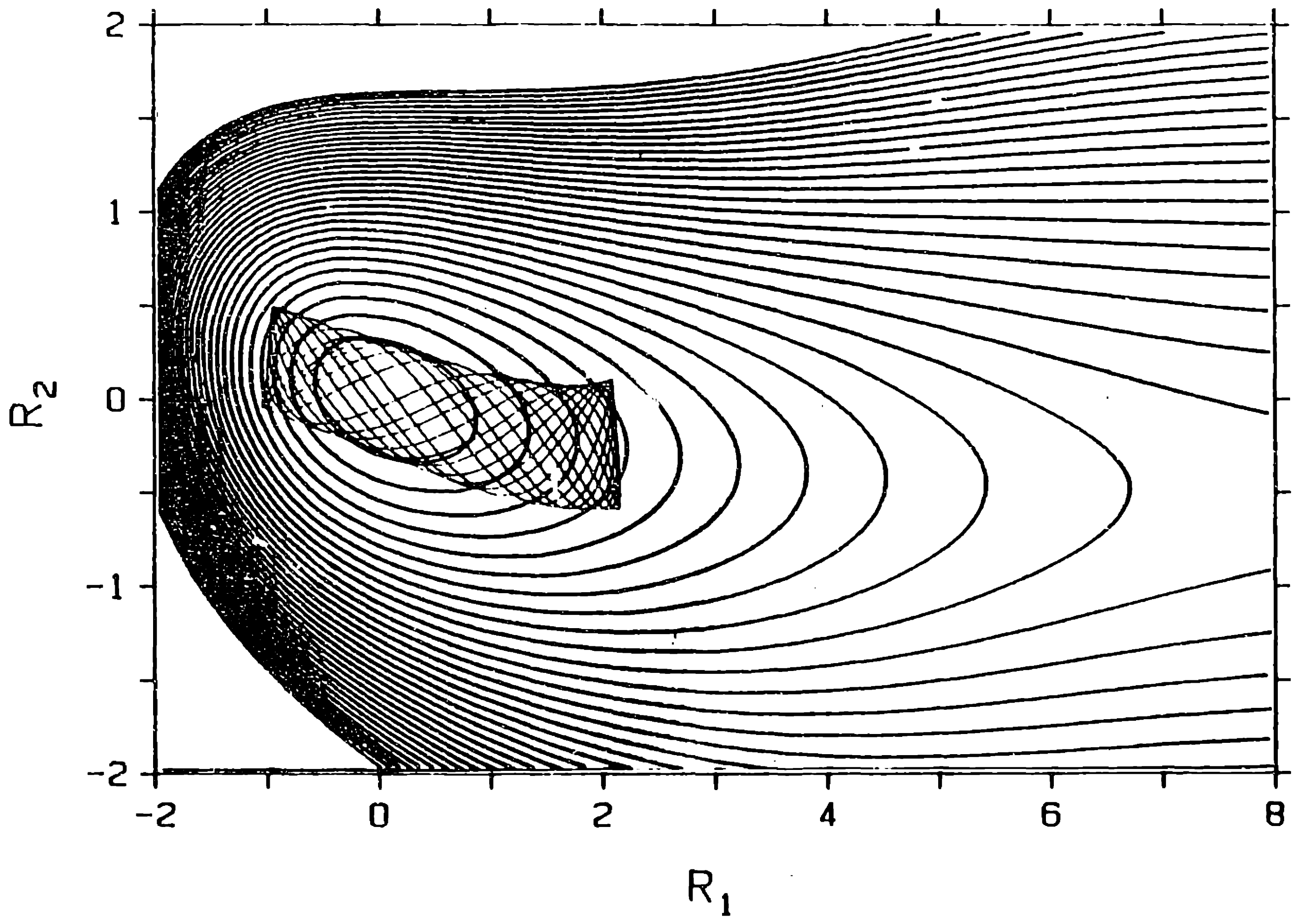

Fig 7-40 - From Ex (C) at t = 2.261 with $R_1 = .97$ $R_2 = .11$ $P_{R_1} = .71$ $P_{R_2} = -.2$.

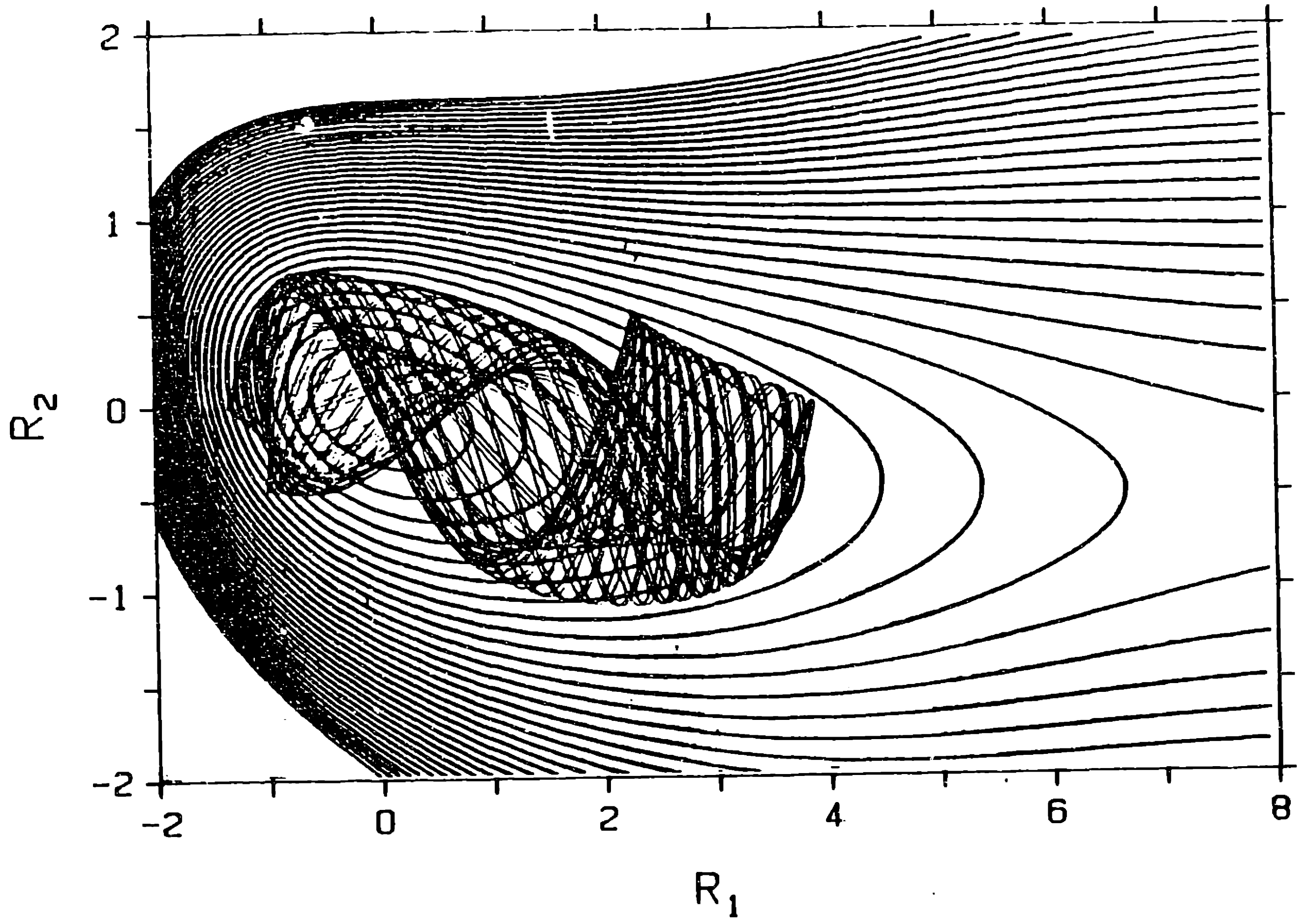

Fig 7-41 - From Ex (C) at t = 3.266 with R_1 = 1.75, R_2 = -.27, P_{R_1} = .84 P_{R_2} = -.52.

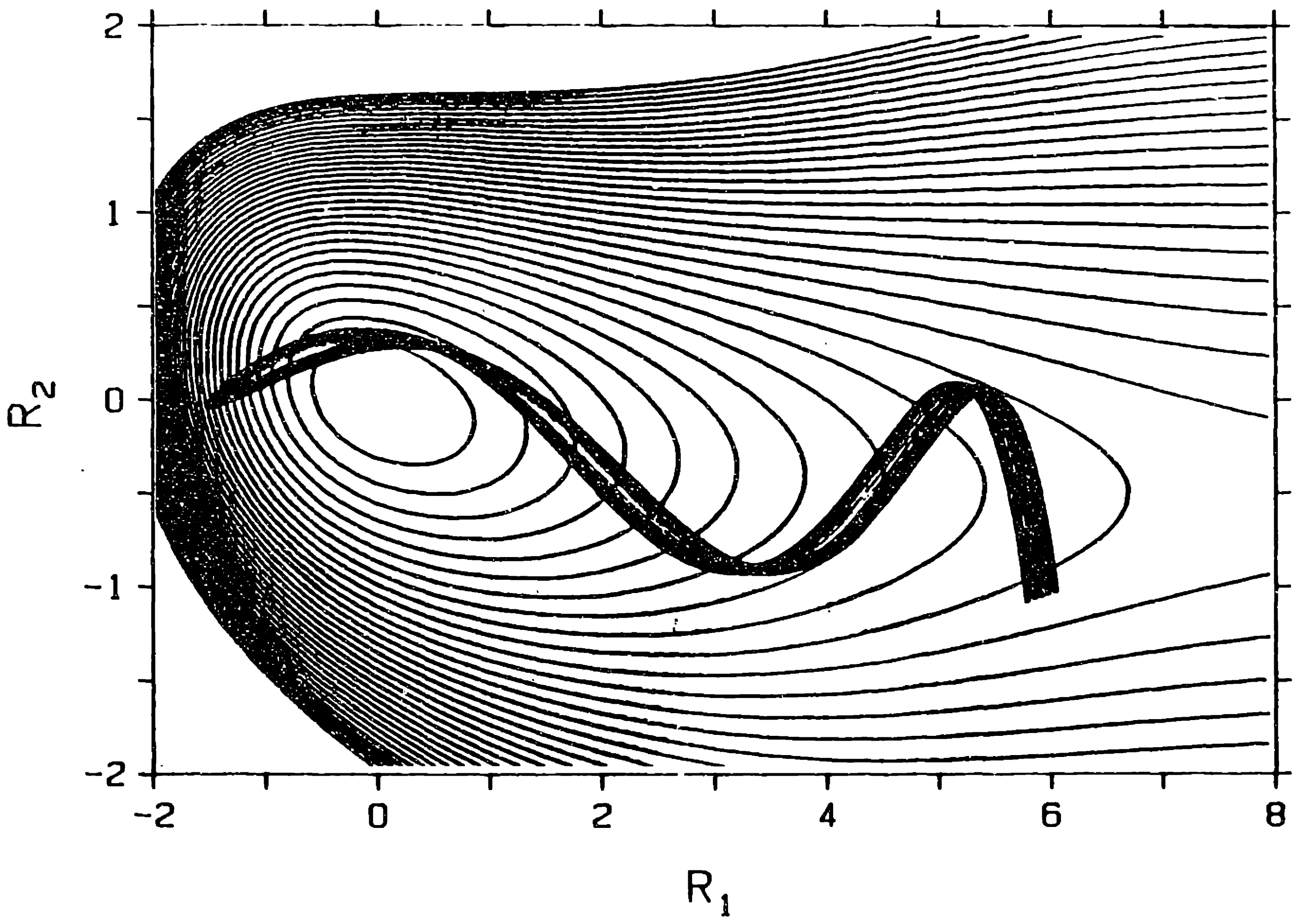

Fig 7-42 - From Ex (C) at t = 4.02 with $R_1 = 2.41$, $R_2 = -.665$ $P_{R_1} = .89$ $P_{R_2} = -.5$.

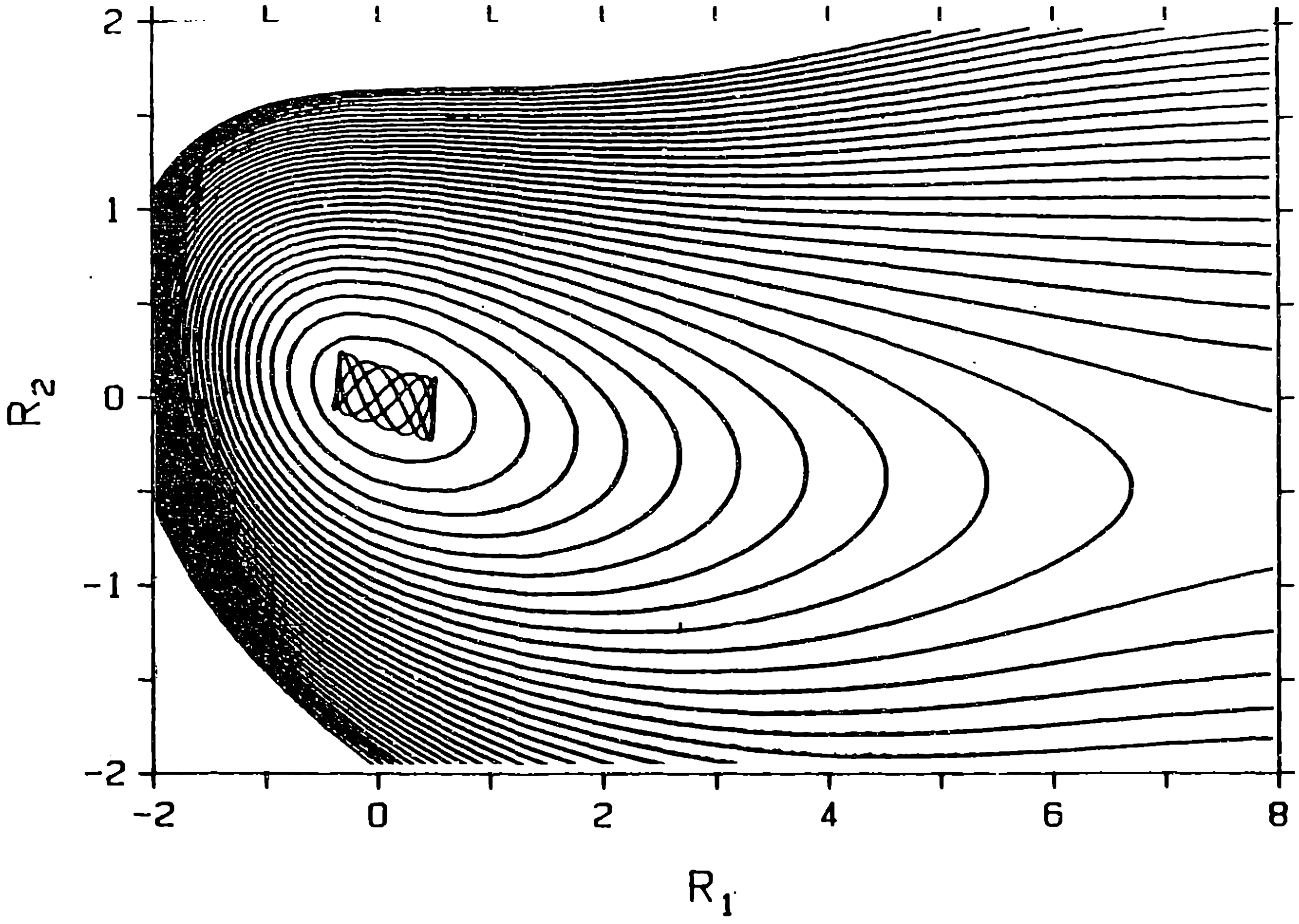

Fig 7-43 - From Ex (D) at $t = .754$ with $R_1 = .11$, $R_2 = .06$ $P_{R_1} = .3$ $P_{R_2} = .15$.

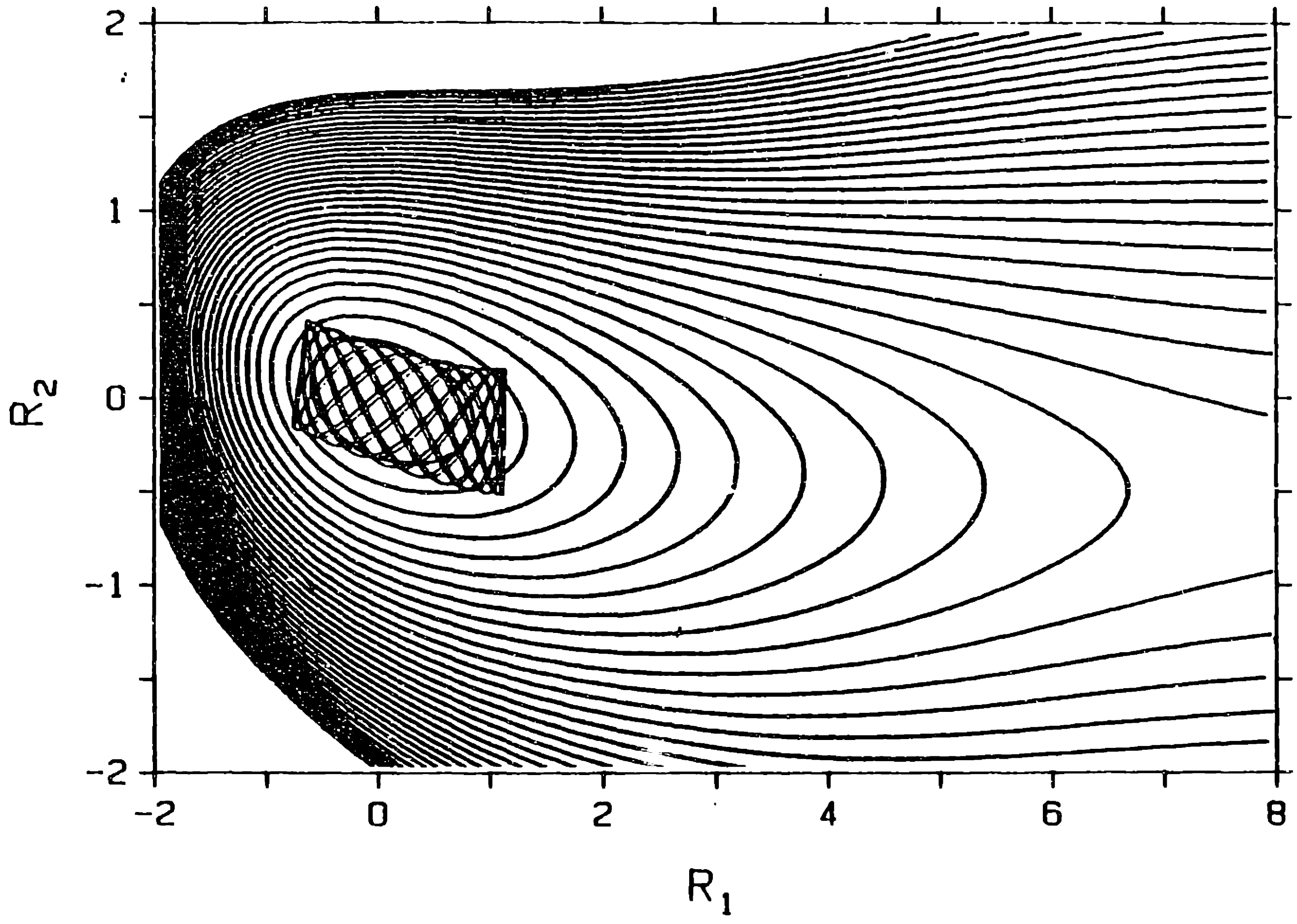

Fig 7-44 - From Ex (D) at t = 1.507 with R_1 = .44, R_2 = .18, P_{R_1} = .54, P_{R_2} = .14.

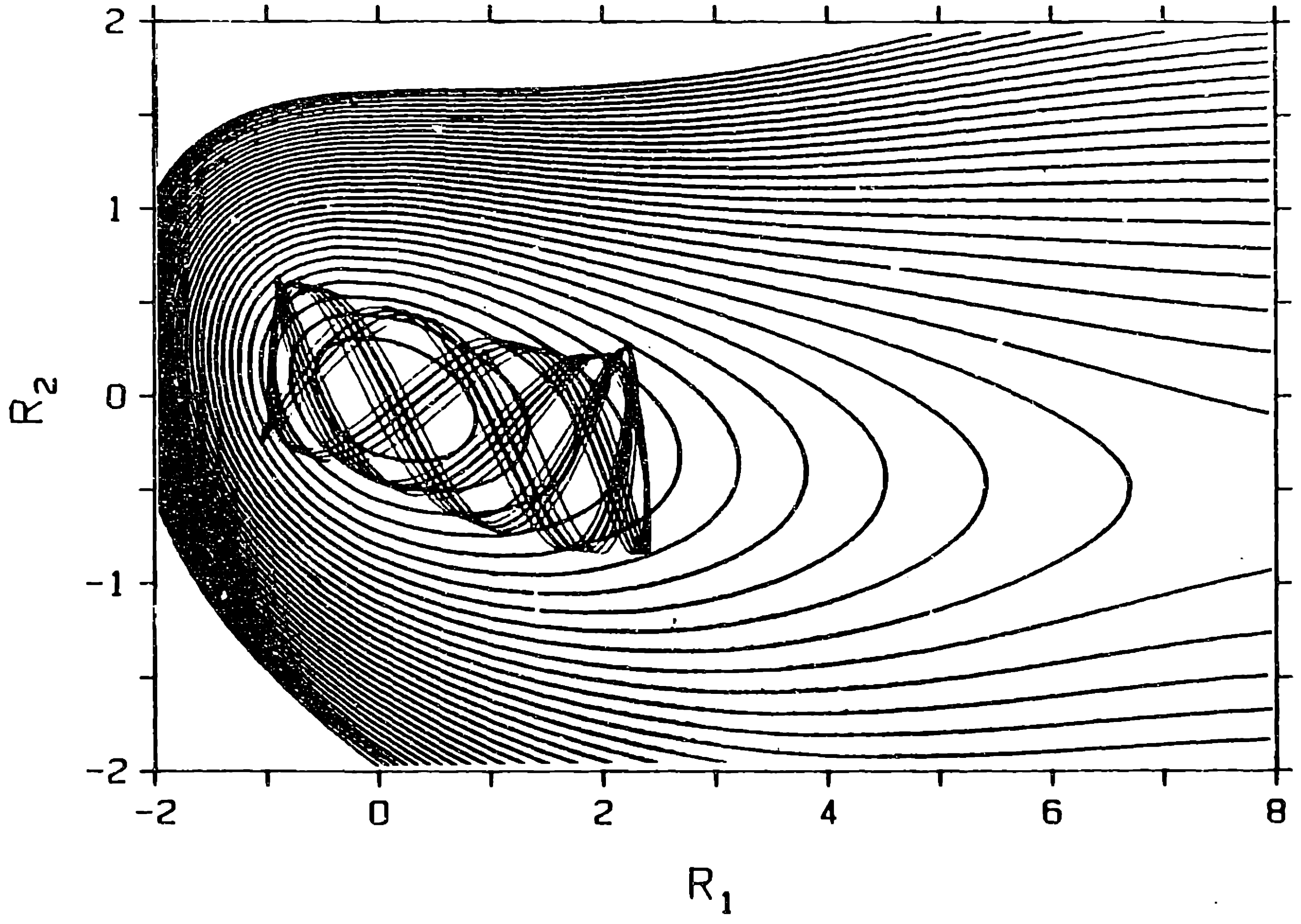

Fig 7-45 - From Ex (D) at t = 2.26 with $R_1 = .92$, $R_2 = .23$ $P_{R_1} = .7$ $P_{R_2} = -.004$.

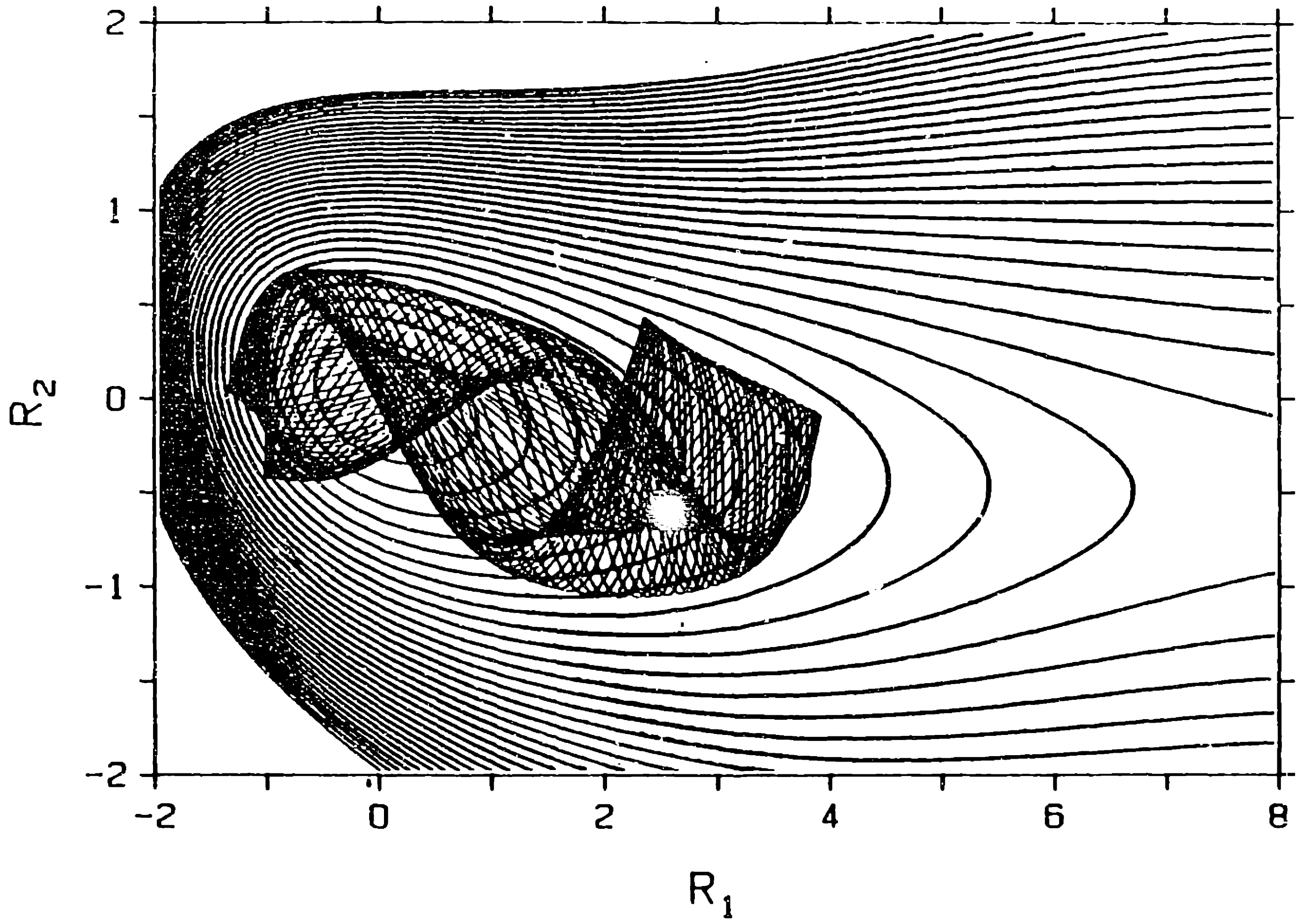

Fig 7-46 - From Ex (D) at $t = 3.367$ with $R_1 = 1.78$, $R_2 = .13$ $P_{R_1} = .84$ $P_{R_2} = -.15$.

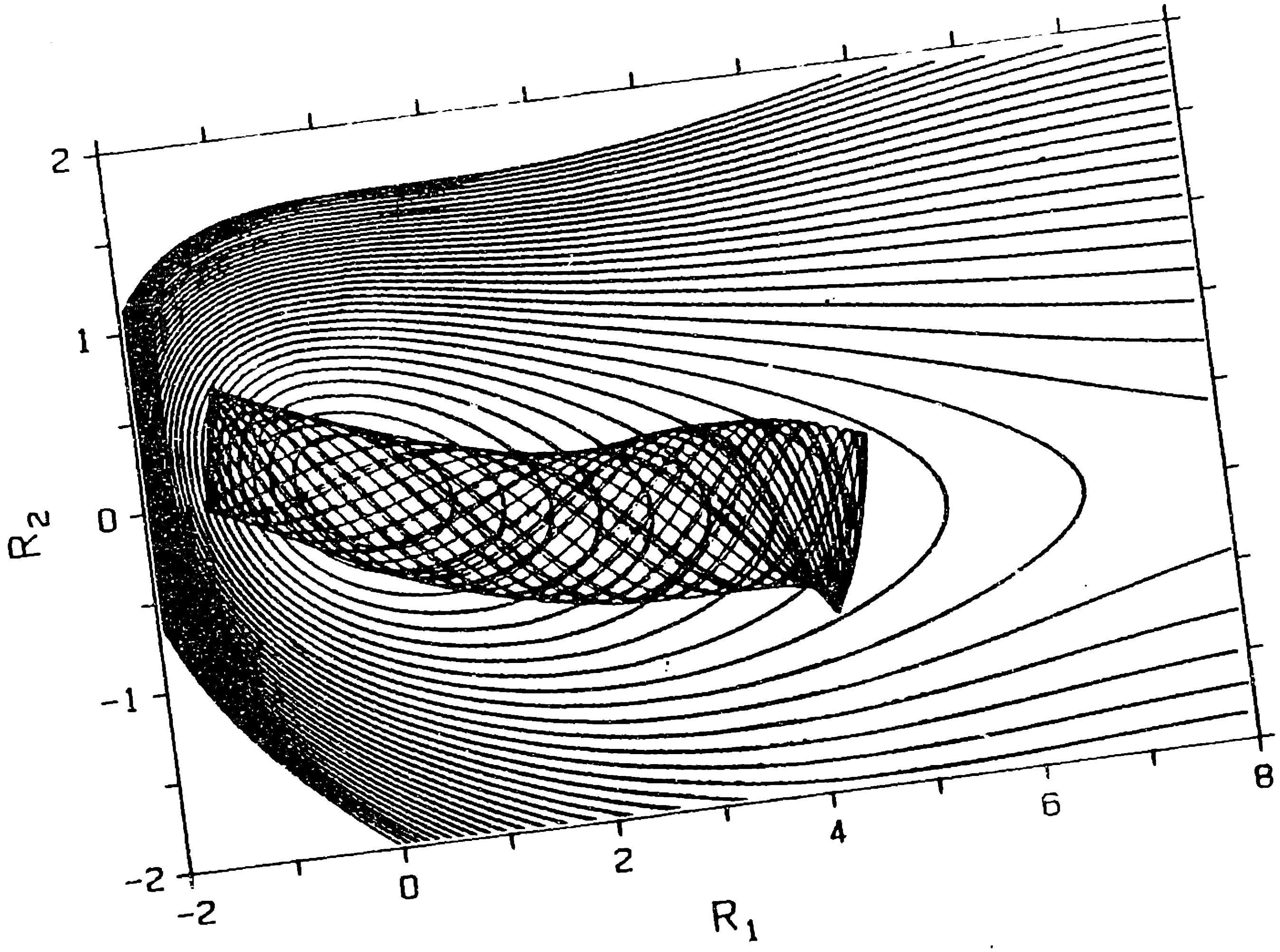

Fig 7-47 - From Ex (D) at t = 4.02 with R_1 = 2.344, R_2 = -.04, P_{R_1} = .87, P_{R_2} = -.13.

CHAPTER 8: CONCLUSION

We have demonstrated that emission spectra from molecules in the process of photodissociation can be a powerful tool in the study of reaction dynamics. These spectra yield on an almost intuitive basis a description of the reaction process. This is especially true when absorption and emission of light is viewed in the time domain.

The same spectra contain very selective information about the ground electronic surface. They provide a means to observe large amplitude vibrational motions in restricted regions of the ground-state PES.

In our studies, methyl iodide was used as a test case since it has a relatively simple dissociation process, which is dominated by forces and essentially confined to two dimensions. In contrast, ozone dissociates by a combination of force-dominated motion and wave packet spreading.

The analysis presented in chapter 7 comprises the preliminary quantitive analysis of the photodissociation reaction and ground-state dynamics of methyl iodide. Our analysis confirms that absorption spectra lack the detail required to generate a complete PES. Because internal state distributions sample the complete history of the reaction, they provide few clues as to the features of specific potential regions. The emission spectrum should enable determination of the surface in a piecewise fashion, starting from the Franck-Condon region and proceeding towards larger internuclear separations. The calculations so far have introduced many simplifying approximations such as a constant transition moment, and a quadratic functional form for the bending coordinate. Further refinements should be added by elimination of these approximations.

Our preliminary studies indicate that the functional form which we have chosen is sufficiently flexible to allow a semi-quantitative fit to all the observations. Translation of the hyperbolic tangent functions for the minimum in R_2 mainly changes the wavelength sensitivity of the internal state distribution. Changing the rate at which this minimum varies with R_2 changes the product vibrational state distribution.

The variational calculation shows that the ground state vibrational eigenfunctions up to 50% of the dissociation limit are very ordered along a set of curvolinear natural vibrational coordinates. This vibrational eigen value calculation is limited (from a practical point of view) by the number of basis functions that can be used; for the higher vibrational levels a semiclassical method would be more applicable.

Finally, the surface which we have not attempted to test is shown in Figure 8-1. This surface is clearly expected to generate interesting dynamics.

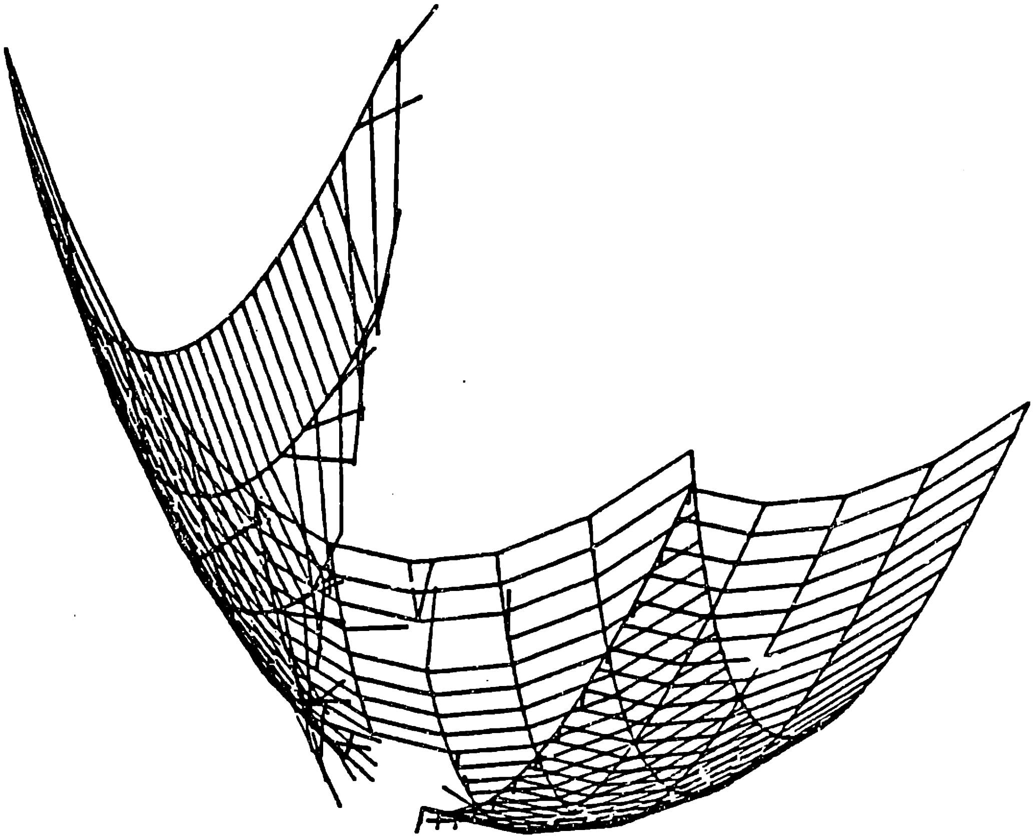

Fig 8-1 -

LIST OF REFERENCES

1. C.N. Hinshelwood, The Kinetics of Chemical Change in Gaseous Systems., Hunsfry Milford, London, (1926)

2. R.B. Bernstein, Chemical Dynamics Via Molecular Beam and Laser Techniques., Oxford University Press, (1982)

3. R.D. Levine and R.B. Bernstein, Molecular Reaction Dynamics., Oxford University Press, (1974)

4. H.W. Cruse, P.J. Dagdigian and R.N. Zare, Far. Dis. Chem. Soc., Molecular Beam Scattering, vol. 53, (1973)

5. L.T. Cowley, D.S. Horne, and J.C. Polanyi, Chem. Phys, Lett. 12, 144, (1971)

6. E.E. Brumberg, A.E. Proctor and R.B. Bernstein, J. Chem. Phys., 63, 3278, (1975)

7. T.E. Gough, R.E. Miller and G. Scoles, Appl. Phys. Lett., 30, 228, (1977)

8. D.R. Herschbach, G.H. Kwei, and J.A. Norris, J. Chem. Phys., 34, 1842, (1961)

9. J.A. Serri, A. Morales, W Moskowitz, D.E. Pritchard, C.H. Becker, and J.L. Kinsey, J. Chem. Phys., 72, 6304, (1980)

10. Y.T. Lee, and Y.R. Shen, Physics Today, 33, 52, (1980)

11. D.H. Maylotte, J.C. Polanyi and K.B. Woodall, J. Chem. Phys., 57, 1547, (1972)

12. J.O. Hirschfelder, C.F. Curtiss and R.B. Bird, Molecular Theory of Gases and Liquids, New York: Wiley, 1954, 1964

13. J.O. Hirschfelder, Int. J. Quantum Chem. Symp., 3, 17 (1969)

14. J.C. Polyani and W.H. Wong, J. Chem. Phys., 51, 1439, (1969)

15. W.R. Green, J. Lukasik, J.R. Willison, M.D. Wright, J.F. Young and S.E. Harris, Phys. Rev. Lett., 42, 970, (1979) and ref. therein

16. Brechnignac, P.H. Cahuzac, and P.E. Toschek, Phys. Rev. A, 21, 1961, (1980)

17. P. Polak-Dingels, J.F. Delpech and J. Weiner, Phys. Rev. Lett., 44, 1663, (1980)

18. P. Arrowsmith, F.E. Bartoszek, S.H.P. Bly, T. Carrington Jr., P.E. Charters and J.C. Polanyi, J. Chem. Phys., 73, 5895, (1980)

19. H.J. Foth, J.C. Polanyi, and H.H. Telle, J. Phys. Chem., 22, 3654, (1982)

20. T.C. Maguire, Philip R. Brooks, and R.F. Curl, Jr., Phys. Rev. Lett., 50, 1918, (1983)

21. P.R. Brooks, R.F. Curl, Jr., and T.C. Maguire, Ber. Bunsenges. Phys. Chem., 86, 401, (1982)

22. S.R. Leone, Adv. Chem. Phys., Dynamics of the Excited State, Vol. L, Ed. K. Lawley, J. Wiley & Son, (1982)

23. M.J. Berry, Chem. Phys. Lett. 27, 73, (1974)

24. M.N.R. Ashfold and J.P. Simons, J. Chem. Soc. Farday Tran. 2, 74, 280 (1978)

25. M.N.R. Ashfold and J.P. Simons, J. Chem. Soc., Faraday Trans. 2, 74, 280, (1978)

26. J.H. Ling and K.R. Wilson, J. Chem. Phys., 63, 101, (1975)

27. R.J. Cody, M.J. Sabety-Dzvonik, and W.M. Jackson, J. Chem. Phys., 66, 2145, (1977)

28. L.C. Lee, J. Chem. Phys., 72, 4334, (1980)

29. K.H. Becker, W. Greth, and D. Kley, Z. Naturforsch, A20, 748, (1965)

30. E.J. Stone, G.M. Lawrence and C.E. Fairchild, J. Chem. Phys., 65, 5083, (1976)

31. R.L. Sundberg and E.J. Heller, Chem. Phys. Lett., 24, 586, (1982)

32. E.J. Heller, R. Sundberg, and D. Tannor, J. Phys. Chem., 86, (1982)

33. E.J. Heller, Accnt. Chem. Res., 14, 368, (1981)

34. E.J. Heller, J. Chem. Phys., 68, 2066, (1978)

35. S.Y. Lee and E.J. Heller, J. Chem. Phys., 71, 477, (1979)

36. L. Eisenbud, Thesis, (1945)

37. E.P. Wigner and L. Eisenbud, Phys. Rev., 72, 29, (1947)

38. F.T. Smith, J. Chem. Phys., 38, 1304, (1963)

39. P. Pechukas, Phys. Rev. Lett., 51, 943, (1983)

40. D.W. Noid, M.L. Koszkowski, and R.A. Marcus, Ann. Rev. Phys, Chem., 32, 267, (1981)

41. The June 10, (1982), issue of the J. of Phys. Chem., Vol. 8, no. 12

42. V. Buch, R.B. Gerber, and M.A. Ratner, J. Chem. Phys., 76, 5397, (1982)

43. E.J. Heller, Farad. Diss., A, 75, 1, (1983)

44. K.K. Lehmann, G.J. Scherer, and W. Klemperer, J. Chem. Phys., 76, 2853, (1982)

45. E.H. Abramson, R.W. Field, D. Imre, K.K. Innes and J.L. Kinsey, J. Chem. Phys., 80, 2298, (1984)

46. PH. Vaccaro, J.L. Kinsey, R.W. Field, and H.-L. Dai, J. Chem. Phys., 78, 3659, (1983)

47. J.B. Hopkins, D.E. Powers, S. Mukamel and R.E. Smalley, J. Chem. Phys., 72, 5049, (1980)

48. D. Imre, A. Sinha, J. Krenos, and J.L. Kinsey, J. Phys. Chem., in print.

49. G. Herzberg, Molecular Spectra and Molecular Structure., Van Nostrand, NY, (1979)

50. A. Gedanken, and M.D. Rowe, Chem. Phys. Lett., 34, 39, (1975)

51. R.S. Muliken, J. Chem. Phys., 8, 382, (1940)

52. J.V.V. Kasper and G.C. Pimentel, Appl. Phys. Lett., 5, 231, (1964)

53. S.J. Riley and K.R. Wilson Disc. Far. Soc., 53, 132, (1972)

54. R.K. Sparks, K. Shobatake, L.R. Carlson, and Y.T. Lee, J. Chem. Phys., 75, 3838, (1981)

55. S.L. Baughcum and S.R. Leone, J. Chem. Phys., 72, 6531, (1980)

56. M.J. Dzvonik, and S.C. Young, Rev. Sci. Inst., 45, 750, (1974)

57. L.E. Brus and V.E. Bondybey, J. Chem. Phys., 65, 71, (1976)

58. Ian J. McNaught, J. Chem. Ed., 59, 879, (1982)

59. C. Yamada, E. Hirota, and K. Kawaguchi, J. Chem. Phys., 75, 5256, (1981)

60. M. Shapiro, and R. Bersohn, J. Chem. Phys., 73, 3310, (1980)

61. S.Y. Lee and E.J. Heller, J. Chem. Phys., 76, 3035, (1982)

62. Raman/IR, Atlas, Eds., B. Schader and W. Weimer, Pub., Verlag Chemic, (1974)

63. J.D. Cox, and G. Pilcher, Thermochemistry of Organic and Organometalic Compounds., Academic, London, (1970)

64. Joshino Tanaka private communication

65. E.C.Y. Inn and yoshino Tanaka, J. Opt. Soc. Am., 43, 870, (1953)

66. E. Vigroux, Ann. Geophys., 25, 70, (1969) and earlier work cited therein

67. J.W. Simons, R.J. Paur, H.A. Webster 3rd, and E.J. Bair, J. Chem. Phys., 59, 1203, (1973)

68. D.H. Katayama, J. Chem. Phys., 71, 815, (1979)

69. J.C.D. Brand, K.J. Cross, and A.R. Hoy, Can. J. Phys., 56, 327, (1978)

70. P.J. Hay, and T.H. Dunning Jr., J. Chem. Phys., 67, 2290, (1977)

71. P.J. Hay, R.T. Pack, R.B. Walker, and E.J. Heller, J. Phys. Chem., 86, 862, (1982)

72. L.E. Fairchild, E.J. Stone and G.M. Lawrence, J. Chem. Phys., 69, 3632, (1978)

73. S.M. Adler-Golden, E.L. Schweitzer, and J.I. Steinfeld, J. Chem. Phys., 76, 2201, (1982)

74. G.K. Mortgat, and P. Warneck, Z. Naturforsch, 30A, 835, (1975)

75. D.L. Philen, R.T. Watson, and D.D. Davis, J. Chem. Phys., 67, 3316, (1977)

76. I Arnold, F.J. Comes and G.K. Moortgat, Chem. Phys., 24, 211, (1977)

77. W. B. DeMone, and O.F. Raper, J. Chem. Phys., 44, 1780, (1966)

78. P.W. Fairchild, and Eduard K.C. Lee, Chem. Phys. Lett., 60, 36, (1978)

79. S.T. Amimoto, A.P. Force, and J.R. Wiesnfeld, Chem. Phys. Lett., 60, 40, (1978)

80. R.K. Sparks, L.R. Carlson, K. Shobatake, M.L. Kowalczyk, and Y.T. Lee, J. Chem. Phys., 72, 1401, (1980)

81. J.J. Valenti, Chem. Phys. Lett., 96, 395, (1983)

82. A. Barbe, C. Secroun, and P. Jouve, J. Mol. Spec., 49, 171, (1974)

83. A. Barbe, C. Secroun, and P. Jouve, J. Mol. Spec., 64, 343, (1977)

84. A. Barbe, C. Secroun, and P. Jouve, and P. Jouve, J. Mol. Spec., 86, 86, (1981)

85. A. Barbe, C. Secroun, and P. Jouve, J. Mol. Spec., 75, 103, (1979)

86. A. Goldman, J.R. Gillis, D.G. Murray, A. Barbe, and C. Secroun, J. Mol. Spec., 96, 279, (1982)

87. A. Barbe, and C. Secroun, J. Mol. Spec., 100, 377, (1983)

88. Private communications

89. M.G. Sheppard, and Robert Walker, J. Chem. Phys., 78, 7191, (1983)

90. H. Selig, and H.H. Clausen, Isr. J. Chem., 6, 499, (1968)

91. E.J. Heller, private communications

92. E.J. Heller, J. Chem. Phys., 68, 3891, (1978) and references cited therein.

93. E.J. Heller, J. Chem. Phys., 62, 1544, (1974)

94. K.C. Kulander, E.J., Heller, J. Chem. Phys., 69, 2439, (1978)

95. R.D. Coalson and M. Karplus, Chem. Phys. Lett., 90, 301, (1982)

96. G.N.A. Van Veen, T. Baller, A.E. de Vries N.J.A. Van Veen Chem. Phys., 87, 405, (1984)

97. M.J. Davis, E.J. Heller, J. Chem. Phys., 71, 3383, (1979)

APPENDIX A

GROUND STATE POTENTIAL ENERGY SURFACE G(A) ab intio FIT

```
     POTENTIAL = 0.5*(2.45*TANH(0.1294*Y-0.2728*X-7.46d-02)+3.05)*
A     (Y-0.499*TANH(0.1
1     294*Y-0.2728*X+4.81333d-02)+2.4d-02)**2+8.51d-01*(1-EXP(-1.725*
2     (0.2728*X-1.55877d-03)))**2-0.5*(0.499*TANH(0.2728*X-4.7368546d
3     -02)+1.809d-02)**2*(3.05-2.45*TANH(0.2728*X+7.536d-02))
```

DERIVATIVES OF THE GROUND POTENTIAL ENERGY SURFACE

```
     dV/dX = -0.33418*SECH(0.1294*Y-0.2728*X-7.46d-02)**2*
A     (Y-0.499*TANH(0.1294*
      0.2728*X+4.81333d-02)+2.4d-02)**2+0.1361272*(2.45*TANH(0.1294
2     *Y-0.2728*X-7.46d-02)+3.05)*SECH(0.1294*Y-0.2728*X+4.81333d-02)
3     **2*(Y-0.499*TANH(0.1294*Y-0.2728*X+4.81333d-02)+2.4d-02)+8.009
4     271600000001d-01*(1-EXP(-1.725*(0.2728*X-1.55877d-03)))*EXP(-1
5     .725*(0.2728*X-1.55877d-03))-0.1361272*SECH(0.2728*X-4.7368546d
6     -02)**2*(0.499*TANH(0.2728*X-4.7368546d-02)+1.809d-02)*(3.05-2.
7     45*TANH(0.2728*X+7.536d-02))+0.33418*(0.499*TANH(0.2728*X-4.736
8     8546d-02)+1.809d-02)**2*SECH(0.2728*X+7.536d-02)**2

     dV/dY = 0.158515*SECH(0.1294*Y-0.2728*X-7.46d-02)**2*
A     (Y-0.499*TANH(0.1294*
1     Y-0.2728*X+4.81333d-02)+2.4d-02)**2+(2.45*TANH(0.1294*Y-0.2728*
2     X-7.46d-02)+3.05)*(1-6.4570600000000001d-02*SECH(0.1294*Y-0.272
3     8*X+4.81333d-02)**2)*(Y-0.499*TANH(0.1294*Y-0.2728*X+4.81333d-0
4     2)+2.4d-02)
```

```
     2   2
   dV/dX =-0.182328608*SECH(0.1294*Y-0.2728*X-7.46d-02)**2*
A   TANH(0.1294*Y-0.2
1   728*X-7.46d-02)*(Y-0.499*TANH(0.1294*Y-0.2728*X+4.81333d-02)+2.
2   4d-02)**2+7.4271000320000001d-02*(2.45*TANH(0.1294*Y-0.2728*X-7
3   .46d-02)+3.05)*SECH(0.1294*Y-0.2728*X+4.81333d-02)**2*TANH(0.12
4   94*Y-0.2728*X+4.81333d-02)*(Y-0.499*TANH(0.1294*Y-0.2728*X+4.81
5   333d-02)+2.4d-02)-0.181963950784*SECH(0.1294*Y-0.2728*X-7.46d-0
6   2)**2*SECH(0.1294*Y-0.2728*X+4.81333d-02)**2*(Y-0.499*TANH(0.12
7   94*Y-0.2728*X+4.81333d-02)+2.4d-02)+1.85306145798d-02*(2.45*TA
8   NH(0.1294*Y-0.2728*X-7.46d-02)+3.05)*SECH(0.1294*Y-0.2728*X+4.8
9   1333d-02)**4-3.7690030295280001d-01*(1-EXP(-1.725*(0.2728*X-1.5
:   5877d-03)))*EXP(-1.725*(0.2728*X-1.55877d-03))+3.769003029528OO
;   01d-01*EXP(-3.45*(0.2728*X-1.55877d-03))-0.182328608*(0.499*TAN
<   H(0.2728*X-4.7368546d-02)+1.809d-02)**2*SECH(0.2728*X+7.536d-02
=   )**2*TANH(0.2728*X+7.536d-02)+7.4271000320000001d-02*SECH(0.272
>   8*X-4.7368546d-02)**2*(0.499*TANH(0.2728*X-4.7368546d-02)+1.809
?   d-02)*TANH(0.2728*X-4.7368546d-02)*(3.05-2.45*TANH(0.2728*X+7.5
@   36d-02))-1.85306145798d-02*SECH(0.2728*X-4.7368546d-02)**4*(3.
1   05-2.45*TANH(0.2728*X+7.536d-02))+0.181963950784*SECH(0.2728*X-
2   4.7368546d-02)**2*(0.499*TANH(0.2728*X-4.7368546d-02)+1.809d-02
3   )*SECH(0.2728*X+7.536d-02)**2


     2   2
   dV/dY = -4.1023682000000001d-02*SECH(0.1294*Y-0.2728*X-
A   7.46d-02)**2*TANH(0
1   .1294*Y-0.2728*X-7.46d-02)*(Y-0.499*TANH(0.1294*Y-0.2728*X+4.81
2   333d-02)+2.4d-02)**2+1.671087128d-02*(2.45*TANH(0.1294*Y-0.2728
3   *X-7.46d-02)+3.05)*SECH(0.1294*Y-0.2728*X+4.81333d-02)**2*TANH(
4   0.1294*Y-0.2728*X+4.81333d-02)*(Y-0.499*TANH(0.1294*Y-0.2728*X+
5   4.81333d-02)+2.4d-02)+0.63406*SECH(0.1294*Y-0.2728*X-7.46d-02)*
6   *2*(1-6.4570600000000001d-02*SECH(0.1294*Y-0.2728*X+4.81333d-02
7   )**2)*(Y-0.499*TANH(0.1294*Y-0.2728*X+4.81333d-02)+2.4d-02)+(2.
8   45*TANH(0.1294*Y-0.2728*X-7.46d-02)+3.05)*(1-6.4570600000000001
9   d-02*SECH(0.1294*Y-0.2728*X+4.81333d-02)**2)**2

     2
   dV/dXdY = 8.6485784000000001d-02*SECH(0.1294*Y-0.2728*X-
A   7.46d-02)**2*TANH(0.
1   1294*Y-0.2728*X-7.46d-02)*(Y-0.499*TANH(0.1294*Y-0.2728*X+4.813
2   33d-02)+2.4d-02)**2-3.5229719360000001d-02*(2.45*TANH(0.1294*Y-
3   0.2728*X-7.46d-02)+3.05)*SECH(0.1294*Y-0.2728*X+4.81333d-02)**2
4   *TANH(0.1294*Y-0.2728*X+4.81333d-02)*(Y-0.499*TANH(0.1294*Y-0.2
5   728*X+4.81333d-02)+2.4d-02)+4.3156406216000001d-02*SECH(0.1294*
6   Y-0.2728*X-7.46d-02)**2*SECH(0.1294*Y-0.2728*X+4.81333d-02)**2*
7   (Y-0.499*TANH(0.1294*Y-0.2728*X+4.81333d-02)+2.4d-02)-0.66836*S
8   ECH(0.1294*Y-0.2728*X-7.46d-02)**2*(1-6.4570600000000001d-02*SE
9   CH(0.1294*Y-0.2728*X+4.81333d-02)**2)*(Y-0.499*TANH(0.1294*Y-0.
:   2728*X+4.81333d-02)+2.4d-02)+0.1361272*(2.45*TANH(0.1294*Y-0.27
;   28*X-7.46d-02)+3.05)*SECH(0.1294*Y-0.2728*X+4.81333d-02)**2*(1-
<   6.4570600000000001d-02*SECH(0.1294*Y-0.2728*X+4.81333d-02)**2)
```

EXCITED STATE POTENTIAL ENERGY SURFACE Ex(A) ab initio FIT

```
   EXCIPOT = 389.9*EXP(-2.9*(.2728*X+2.1404))+.5*(2.925
1   -2.32*TANH(1.11*(.2728*X-.1294*Y+.2146)))*(Y+.024+
2   .499*TANH(1.29*(.2728*X-.1294*Y-.1004)))**2-.5*
3   (2.925-2.32*TANH(1.11*(.2728*X+.2154)))*(.1809+
4   0.499*TANH(1.29*(.2728*X-.09964)))**2+1.2569
```

DERIVATIVES OF THE EXCITED STAE POTENTIAL ENERGY SURFACE

```
   dV/dX=-0.35125728*SECH(1.11*(-0.1294*Y
a   +0.2728*X+0.2146))**2*(Y+0.499*TAN
1   H(1.29*(-0.1294*Y+0.2728*X-0.1004))+2.4d-02)**2+0.175604088*SEC
2   H(1.29*(-0.1294*Y+0.2728*X-0.1004))**2*(2.925-2.32*TANH(1.11*(-
3   0.1294*Y+0.2728*X+0.2146)))*(Y+0.499*TANH(1.29*(-0.1294*Y+0.272
4   8*X-0.1004))+2.4d-02)-308.457688*EXP(-2.9*(0.2728*X+2.1404))-0.
5   175604088*SECH(1.29*(0.2728*X-9.9639999999999999d-02))**2*(0.49
6   9*TANH(1.29*(0.2728*X-9.9639999999999999d-02))+0.1809)*(2.925-2
7   .32*TANH(1.11*(0.2728*X+0.2154)))+0.35125728*(0.499*TANH(1.29*(
8   0.2728*X-9.9639999999999999d-02))+0.1809)**2*SECH(1.11*(0.2728*
9   X+0.2154))**2

   dV/dY=0.16661544*SECH(1.11*
a   (-0.1294*Y+0.2728*X+0.2146))**2*(Y+0.499*TANH
1   (1.29*(-0.1294*Y+0.2728*X-0.1004))+2.4d-02)**2+(1-8.32960740000
2   00001d-02*SECH(1.29*(-0.1294*Y+0.2728*X-0.1004))**2)*(2.925-2.3
3   2*TANH(1.11*(-0.1294*Y+0.2728*X+0.2146)))*(Y+0.499*TANH(1.29*(-
4   0.1294*Y+0.2728*X-0.1004))+2.4d-02)

    2   2
   dV/dX=0.2127270288848*SECH(1.11*
a   (-0.1294*Y+0.2728*X+0.2146))**2*TANH(1.
1   11*(-0.1294*Y+0.2728*X+0.2146))*(Y+0.499*TANH(1.29*(-0.1294*Y+0
2   .2728*X-0.1004))+2.4d-02)**2-0.123594371632512*SECH(1.29*(-0.12
3   94*Y+0.2728*X-0.1004))**2*TANH(1.29*(-0.1294*Y+0.2728*X-0.1004)
4   )*(2.925-2.32*TANH(1.11*(-0.1294*Y+0.2728*X+0.2146)))*(Y+0.499*
5   TANH(1.29*(-0.1294*Y+0.2728*X-0.1004))+2.4d-02)-0.2467288572310
6   426*SECH(1.29*(-0.1294*Y+0.2728*X-0.1004))**2*SECH(1.11*(-0.129
7   4*Y+0.2728*X+0.2146))**2*(Y+0.499*TANH(1.29*(-0.1294*Y+0.2728*X
8   -0.1004))+2.4d-02)+3.083679572231174 5d-02*SECH(1.29*(-0.1294*Y+
9   0.2728*X-0.1004))**4*(2.925-2.32*TANH(1.11*(-0.1294*Y+0.2728*X+
:   0.2146)))+244.02704613056*EXP(-2.9*(0.2728*X+2.1404))-0.2127270
;   2888448*(0.499*TANH(1.29*(0.2728*X-9.9639999999999999d-02))+0.1
<   809)**2*SECH(1.11*(0.2728*X+0.2154))**2*TANH(1.11*(0.2728*X+0.2
=   154))+0.123594371632512*SECH(1.29*(0.2728*X-9.9639999999999999d
>   -02))**2*(0.499*TANH(1.29*(0.2728*X-9.9639999999999999d-02))+0.
?   1809)*TANH(1.29*(0.2728*X-9.9639999999999999d-02))*(2.925-2.32*
@   TANH(1.11*(0.2728*X+0.2154)))-3.0836795722311745d-02*SECH(1.29*
1   (0.2728*X-9.9639999999999999d-02))**4*(2.925-2.32*TANH(1.11*(0.
2   2728*X+0.2154)))+0.2467288572310426*SECH(1.29*(0.2728*X-9.96399
3   99999999999d-02))**2*(0.499*TANH(1.29*(0.2728*X-9.9639999999999
4   999d-02))+0.1809)*SECH(1.11*(0.2728*X+0.2154))**2
```

```
    2   2
   dV/dY=4.786328421792000 1d-02*SECH
a   (1.11*(-0.1294*Y+0.2728*X+0.2146))**2*T
1   ANH(1.11*(-0.1294*Y+0.2728*X+0.2146))*(Y+0.499*TANH(1.29*(-0.12
2   94*Y+0.2728*X-0.1004))+2.4d-02)**2-2.780856089704800 1d-02*SECH(
3   1.29*(-0.1294*Y+0.2728*X-0.1004))**2*TANH(1.29*(-0.1294*Y+0.272
4   8*X-0.1004))*(2.925-2.32*TANH(1.11*(-0.1294*Y+0.2728*X+0.2146))
5   )*(Y+0.499*TANH(1.29*(-0.1294*Y+0.2728*X-0.1004))+2.4d-02)+0.66
6   646176*(1-8.3296074000000001d-02*SECH(1.29*(-0.1294*Y+0.2728*X-
7   0.1004))**2)*SECH(1.11*(-0.1294*Y+0.2728*X+0.2146))**2*(Y+0.499
8   *TANH(1.29*(-0.1294*Y+0.2728*X-0.1004))+2.4d-02)+(1-8.329607400
9   0000001d-02*SECH(1.29*(-0.1294*Y+0.2728*X-0.1004))**2)**2*(2.92
:   5-2.32*TANH(1.11*(-0.1294*Y+0.2728*X+0.2146)))

    2
   dV/dXdY=-0.10090497631104*SECH(1.11
a   *(-0.1294*Y+0.2728*X+0.2146))**2*TANH(1
1   .11*(-0.1294*Y+0.2728*X+0.2146))*(Y+0.499*TANH(1.29*(-0.1294*Y+
2   0.2728*X-0.1004))+2.4d-02)**2+5.862577598697600 2d-02*SECH(1.29*
3   (-0.1294*Y+0.2728*X-0.1004))**2*TANH(1.29*(-0.1294*Y+0.2728*X-0
4   .1004))*(2.925-2.32*TANH(1.11*(-0.1294*Y+0.2728*X+0.2146)))*(Y+
5   0.499*TANH(1.29*(-0.1294*Y+0.2728*X-0.1004))+2.4d-02)+5.8516704
6   775837442d-02*SECH(1.29*(-0.1294*Y+0.2728*X-0.1004))**2*SECH(1.
7   11*(-0.1294*Y+0.2728*X+0.2146))**2*(Y+0.499*TANH(1.29*(-0.1294*
8   Y+0.2728*X-0.1004))+2.4d-02)-0.70251456*(1-8.3296074000000001d-
9   02*SECH(1.29*(-0.1294*Y+0.2728*X-0.1004))**2)*SECH(1.11*(-0.129
:   4*Y+0.2728*X+0.2146))**2*(Y+0.499*TANH(1.29*(-0.1294*Y+0.2728*X
;   -0.1004))+2.4d-02)+0.175604088*SECH(1.29*(-0.1294*Y+0.2728*X-0.
<   1004))**2*(1-8.3296074000000001d-02*SECH(1.29*(-0.1294*Y+0.2728
=   *X-0.1004))**2)*(2.925-2.32*TANH(1.11*(-0.1294*Y+0.2728*X+0.214
>   6)))
```

APPENDIX B

GROUND STATE POTENTIAL ENERGY SURFACE G(B)

```
   POTENTIAL = 0.41*(2.45*TANH(0.1294*Y-0.2728*
A   X-7.46d-02)+3.05)*(Y-0.499*TANH(0.
1   1294*Y-0.2728*X+4.81333d-02)+2.4d-02)**2+1*(1-EXP(-1.702*(0
2   .2728*X-1.07151d-03)))**2-0.41*(0.499*TANH(0.2728*X-4.7368546d-
3   02)+1.809d-02)**2*(3.05-2.45*TANH(0.2728*X+7.536d-02))
```

DERIVATIVES OF THE GROUND STATE POTENTIAL ENERGY SURFACE

```
   dV/dX = -0.2740276*SECH(0.1294*Y-0.2728*
A   X-7.46d-02)**2*(Y-0.499*TANH(0.129
1   4*Y-0.2728*X+4.81333d-02)+2.4d-02)**2+0.111624304*(2.45*TANH(0.
2   1294*Y-0.2728*X-7.46d-02)+3.05)*SECH(0.1294*Y-0.2728*X+4.81333d
3   -02)**2*(Y-0.499*TANH(0.1294*Y-0.2728*X+4.81333d-02)+2.4d-02)+0
4   .9286112*(1-EXP(-1.702*(0.2728*X-1.07151d-03)))*EXP(-1.702*(
5   0.2728*X-1.07151d-03))-0.111624304*SECH(0.2728*X-4.7368546d-02)
6   **2*(0.499*TANH(0.2728*X-4.7368546d-02)+1.809d-02)*(3.05-2.45*T
7   ANH(0.2728*X+7.536d-02))+0.2740276*(0.499*TANH(0.2728*X-4.73685
8   46d-02)+1.809d-02)**2*SECH(0.2728*X+7.536d-02)**2

   dV/dY = 0.1299823*SECH(0.1294*Y-0.2728*
A   X-7.46d-02)**2*(Y-0.499*TANH(0.1294
1   *Y-0.2728*X+4.81333d-02)+2.4d-02)**2+0.82*(2.45*TANH(0.1294*Y-0
2   .2728*X-7.46d-02)+3.05)*(1-6.4570600000000001d-02*SECH(0.1294*Y
3   -0.2728*X+4.81333d-02)**2)*(Y-0.499*TANH(0.1294*Y-0.2728*X+4.81
4   333d-02)+2.4d-02)
```

```
    2   2
   dV/dX = -0.14950945856*SECH(0.1294*Y-
@   0.2728*X-7.46d-02)**2*TANH(0.1294*Y-0
1   .2728*X-7.46d-02)*(Y-0.499*TANH(0.1294*Y-0.2728*X+4.81333d-02)+
2   2.4d-02)**2+6.09022202624d-02*(2.45*TANH(0.1294*Y-0.2728*X-7.46
3   d-02)+3.05)*SECH(0.1294*Y-0.2728*X+4.81333d-02)**2*TANH(0.1294*
4   Y-0.2728*X+4.81333d-02)*(Y-0.499*TANH(0.1294*Y-0.2728*X+4.81333
5   d-02)+2.4d-02)-0.14921043964288*SECH(0.1294*Y-0.2728*X-7.46d-02
6   )**2*SECH(0.1294*Y-0.2728*X+4.81333d-02)**2*(Y-0.499*TANH(0.129
7   4*Y-0.2728*X+4.81333d-02)+2.4d-02)+1.51951039554688d-02*(2.45*T
8   ANH(0.1294*Y-0.2728*X-7.46d-02)+3.05)*SECH(0.1294*Y-0.2728*X+4.
9   81333d-02)**4-0.43115938038272*(1-EXP(-1.702*(0.2728*X-1.07151d
:   -03)))*EXP(-1.702*(0.2728*X-1.07151d-03))+0.43115938038272*EXP(
;   -3.404*(0.2728*X-1.07151d-03))-0.14950945856*(0.499*TANH(0.2728
<   *X-4.7368546d-02)+1.809d-02)**2*SECH(0.2728*X+7.536d-02)**2*TAN
=   H(0.2728*X+7.536d-02)+6.09022202624d-02*SECH(0.2728*X-4.7368546
>   d-02)**2*(0.499*TANH(0.2728*X-4.7368546d-02)+1.809d-02)*TANH(0.
?   2728*X-4.7368546d-02)*(3.05-2.45*TANH(0.2728*X+7.536d-02))-1.51
@   951039554688d-02*SECH(0.2728*X-4.7368546d-02)**4*(3.05-2.45*TAN
1   H(0.2728*X+7.536d-02))+0.14921043964288*SECH(0.2728*X-4.7368546
2   d-02)**2*(0.499*TANH(0.2728*X-4.7368546d-02)+1.809d-02)*SECH(0.
3   2728*X+7.536d-02)**2

    2   2
   dV/dY = -3.3639419240000001d-02*
@   SECH(0.1294*Y-0.2728*X-7.46d-02)**2*TANH(0
1   .1294*Y-0.2728*X-7.46d-02)*(Y-0.499*TANH(0.1294*Y-0.2728*X+4.81
2   333d-02)+2.4d-02)**2+1.37029144496d-02*(2.45*TANH(0.1294*Y-0.27
3   28*X-7.46d-02)+3.05)*SECH(0.1294*Y-0.2728*X+4.81333d-02)**2*TAN
4   H(0.1294*Y-0.2728*X+4.81333d-02)*(Y-0.499*TANH(0.1294*Y-0.2728*
5   X+4.81333d-02)+2.4d-02)+0.5199292*SECH(0.1294*Y-0.2728*X-7.46d-
6   02)**2*(1-6.4570600000000001d-02*SECH(0.1294*Y-0.2728*X+4.81333
7   d-02)**2)*(Y-0.499*TANH(0.1294*Y-0.2728*X+4.81333d-02)+2.4d-02)
8   +0.82*(2.45*TANH(0.1294*Y-0.2728*X-7.46d-02)+3.05)*(1-6.4570600
9   000000001d-02*SECH(0.1294*Y-0.2728*X+4.81333d-02)**2)**2

    2
   dV/dXdY=7.091834288d-02*
@   SECH(0.1294*Y-0.2728*X-7.46d-02)**2*TANH(0.1294*Y-
1   0.2728*X-7.46d-02)*(Y-0.499*TANH(0.1294*Y-0.2728*X+4.81333d-02)
2   +2.4d-02)**2-2.8888369875200001d-02*(2.45*TANH(0.1294*Y-0.2728*
3   X-7.46d-02)+3.05)*SECH(0.1294*Y-0.2728*X+4.81333d-02)**2*TANH(0
4   .1294*Y-0.2728*X+4.81333d-02)*(Y-0.499*TANH(0.1294*Y-0.2728*X+4
5   .81333d-02)+2.4d-02)+3.5388253097120001d-02*SECH(0.1294*Y-0.272
6   8*X-7.46d-02)**2*SECH(0.1294*Y-0.2728*X+4.81333d-02)**2*(Y-0.49
7   9*TANH(0.1294*Y-0.2728*X+4.81333d-02)+2.4d-02)-0.5480552*SECH(0
8   .1294*Y-0.2728*X-7.46d-02)**2*(1-6.4570600000000001d-02*SECH(0.
9   1294*Y-0.2728*X+4.81333d-02)**2)*(Y-0.499*TANH(0.1294*Y-0.2728*
:   X+4.81333d-02)+2.4d-02)+0.111624304*(2.45*TANH(0.1294*Y-0.2728*
;   X-7.46d-02)+3.05)*SECH(0.1294*Y-0.2728*X+4.81333d-02)**2*(1-6.4
<   570600000000001d-02*SECH(0.1294*Y-0.2728*X+4.81333d-02)**2)
```

APPENDIX C

EXCITED STATE POTENTIAL ENERGY SURFACE Ex(B)

```
   EXCIPOT=0.41*(2.925-2.32*TANH(1.11*(-0.1294*
A   Y+0.2728*X+0.2146)))*(Y+0.499*
1   TANH(1.29*(-0.1294*Y+0.2728*X-.1004))+2.4d-02)**2+965.7*EX
2   P(-3.5964*(0.2728*X+2.1404))-0.41*(0.499*TANH(1.29*(0.2728*X-.0
3   9964))+.01809)**2*(2.925-2.32*TANH(1.11*(0.2728*X+0.21384)))+
4   1.3469
```

DERIVATIVES OF THE EXCITED STATE POTENTIAL ENERGY SURFACE

```
   dV/dX = -0.2880309696*SECH(1.11*
A   (-0.1294*Y+0.2728*X+0.2146))**2*(Y+0.499*TANH
1   (1.29*(-0.1294*Y+0.2728*X-.1004))+2.4d-02)**2+0.143995352
2   16*SECH(1.29*(-0.1294*Y+0.2728*X-.1004))**2*(2.925-2.32*TANH
3   (1.11*(-0.1294*Y+0.2728*X+0.2146)))*(Y+0.499*TANH(1.29*(-0.1294
4   *Y+0.2728*X-.1004))+2.4d-02)-947.45*EXP(-3.5964*(0.272
5   8*X+2.1404))-0.14399535216*SECH(1.29*(0.2728*X-.09964))**2*(
6   0.499*TANH(1.29*(0.2728*X-.09964))+.01809)*(2.925-2.32*TANH(
7   1.11*(0.2728*X+0.21384)))+0.2880309696*(0.499*TANH(1.29*(0.2728
8   *X-.09964))+.01809)**2*SECH(1.11*(0.2728*X+0.21384))**2

   dV/dY = 0.1366246608*SECH(1.11*(-0.1294*Y+
A   0.2728*X+0.2146))**2*(Y+0.499*TA
1   NH(1.29*(-0.1294*Y+0.2728*X-.1004))+2.4d-02)**2+0.82*(1-8.32
2   9607400000001d-02*SECH(1.29*(-0.1294*Y+0.2728*X-.1004))**2)
3   *(2.925-2.32*TANH(1.11*(-0.1294*Y+0.2728*X+0.2146)))*(Y+0.499*T
4   ANH(1.29*(-0.1294*Y+0.2728*X-.1004))+2.4d-02)
```

```
     2   2
    dV/dX = 0.1744361636852736*SECH(1.11*
A    (-0.1294*Y+0.2728*X+0.2146))**2*TANH(
1    1.11*(-0.1294*Y+0.2728*X+0.2146))*(Y+0.499*TANH(1.29*(-0.1294*Y
2    +0.2728*X-.1004))+2.4d-02)**2-0.1013473847386598*SECH(1.29*(
3    -0.1294*Y+0.2728*X-.1004))**2*TANH(1.29*(-0.1294*Y+0.2728*X-
4    .1004))*(2.925-2.32*TANH(1.11*(-0.1294*Y+0.2728*X+0.2146)))*
5    (Y+0.499*TANH(1.29*(-0.1294*Y+0.2728*X-.1004))+2.4d-02)-0.20
6    23176629294549*SECH(1.29*(-0.1294*Y+0.2728*X-.1004))**2*SECH
7    (1.11*(-0.1294*Y+0.2728*X+0.2146))**2*(Y+0.499*TANH(1.29*(-0.12
8    94*Y+0.2728*X-.1004))+2.4d-02)+2.5286172492295631d-02*SECH(1
9    .29*(-0.1294*Y+0.2728*X-.1004))**4*(2.925-2.32*TANH(1.11*(-0
:    .1294*Y+0.2728*X+0.2146)))+929.54*EXP(-3.5964*(0.2728
;    *X+2.1404))-0.1744361636852736*(0.499*TANH(1.29*(0.2728*X-.0996
<    4))+.01809)**2*SECH(1.11*(0.2728*X+0.21384))**2*TANH(1.11*(0
=    .2728*X+0.21384))+0.1013473847386598*SECH(1.29*(0.2728*X-.09964
>    ))**2*(0.499*TANH(1.29*(0.2728*X-.09964))+.01809)*TANH(1.
?    29*(0.2728*X-.09964))*(2.925-2.32*TANH(1.11*(0.2728*X+0.2138
@    4)))-2.5286172492295631d-02*SECH(1.29*(0.2728*X-.09964))**4*
1    (2.925-2.32*TANH(1.11*(0.2728*X+0.21384)))+0.2023176629294549*S
2    ECH(1.29*(0.2728*X-.09964))**2*(0.499*TANH(1.29*(0.2728*X-.099
3    64))+.01809)*SECH(1.11*(0.2728*X+0.21384))**2

     2   2
    dV/dY = 3.9247893058694402d-02*SECH
A    (1.11*(-0.1294*Y+0.2728*X+0.2146))**2*T
1    ANH(1.11*(-0.1294*Y+0.2728*X+0.2146))*(Y+0.499*TANH(1.29*(-0.12
2    94*Y+0.2728*X-.1004))+2.4d-02)**2-2.280301993557936d-02*SECH
3    (1.29*(-0.1294*Y+0.2728*X-.1004))**2*TANH(1.29*(-0.1294*Y+0.
4    2728*X-.1004))*(2.925-2.32*TANH(1.11*(-0.1294*Y+0.2728*X+0.2
5    146)))*(Y+0.499*TANH(1.29*(-0.1294*Y+0.2728*X-.1004))+2.4d-0
6    2)+0.5464986432*(1-8.329607400000001d-02*SECH(1.29*(-0.1294*Y+
7    0.2728*X-.1004))**2)*SECH(1.11*(-0.1294*Y+0.2728*X+0.2146))*
8    *2*(Y+0.499*TANH(1.29*(-0.1294*Y+0.2728*X-.1004))+2.4d-02)+0
9    .82*(1-8.329607400000001d-02*SECH(1.29*(-0.1294*Y+0.2728*X-.10
:    04))**2)**2*(2.925-2.32*TANH(1.11*(-0.1294*Y+0.2728*X+0.2146
;    )))

     2
    dV/dXdY = -8.2742080575052801d-02*
A    SECH(1.11*(-0.1294*Y+0.2728*X+0.2146))**2*
1    TANH(1.11*(-0.1294*Y+0.2728*X+0.2146))*(Y+0.499*TANH(1.29*(-0.1
2    294*Y+0.2728*X-.1004))+2.4d-02)**2+4.8073136309320322d-02*SE
3    CH(1.29*(-0.1294*Y+0.2728*X-.1004))**2*TANH(1.29*(-0.1294*Y+
4    0.2728*X-.1004))*(2.925-2.32*TANH(1.11*(-0.1294*Y+0.2728*X+0
5    .2146)))*(Y+0.499*TANH(1.29*(-0.1294*Y+0.2728*X-.1004))+2.4d
6    -02)+4.7983697916186703d-02*SECH(1.29*(-0.1294*Y+0.2728*X-.1004
7    ))**2*SECH(1.11*(-0.1294*Y+0.2728*X+0.2146))**2*(Y+0.499*TAN
8    H(1.29*(-0.1294*Y+0.2728*X-.1004))+2.4d-02)-0.5760619392*(1-
9    8.329607400000001d-02*SECH(1.29*(-0.1294*Y+0.2728*X-.1004))
:    **2)*SECH(1.11*(-0.1294*Y+0.2728*X+0.2146))**2*(Y+0.499*TANH(1.
;    29*(-0.1294*Y+0.2728*X-.1004))+2.4d-02)+0.14399535216*SECH(1
<    .29*(-0.1294*Y+0.2728*X-.1004))**2*(1-8.329607400000001d-02
=    *SECH(1.29*(-0.1294*Y+0.2728*X-.1004))**2)*(2.925-2.32*TANH(
>    1.11*(-0.1294*Y+0.2728*X+0.2146)))
```

APPENDIX D

EXCITED STATE POTENTIAL ENERGY SURFACE Ex(C)
(C(1)=2.5 C(2)=-.1304)

```
   EXCIPOT=.41*(2.925-2.32*TANH(1.11*(-0.1294*Y
1   +0.2728*X+0.1246)))*(Y+0.499*TANH(C(1)*(-0.1294*Y
2   +0.2728*X+C(2)))+0.024)**2+950*EXP(-3.664*
3   (0.2728*X+2.1404))-0.41*(0.499*TANH(C(1)*(0.2728*
4   X+C(2)+.00086))+0.1809)**2*(2.925-2.32*TANH(1.11*
5   (0.2728*X+0.21384)))+1.3949
```

DERIVATIVES OF THE EXCITED STATE POTENTIAL ENERGY SURFACE

```
   dV/dX = -0.2880309696*SECH(1.11*
A   (-0.1294*Y+0.2728*X+0.1246))**2*(Y+0.499*T
1   ANH(C(1)*(-0.1294*Y+0.2728*X+C(2)))+2.4d-02)**2+0.111624304*C(1
2   )*(2.925-2.32*TANH(1.11*(-0.1294*Y+0.2728*X+0.1246)))*SECH(C(1)
3   *(-0.1294*Y+0.2728*X+C(2)))**2*(Y+0.499*TANH(C(1)*(-0.1294*Y+0.
4   2728*X+C(2)))+2.4d-02)-950.25*EXP(-3.664*(0.2728*X+2.1404
5   ))+0.2880309696*SECH(1.11*(0.2728*X+0.21384))**2*(0.499*TANH(C(
6   1)*(0.2728*X+C(2)+8.600000000000001d-04))+0.1809)**2-0.1116243
7   04*C(1)*(2.925-2.32*TANH(1.11*(0.2728*X+0.21384)))*SECH(C(1)*(0
8   .2728*X+C(2)+8.600000000000001d-04))**2*(0.499*TANH(C(1)*(0.27
9   28*X+C(2)+8.600000000000001d-04))+0.1809)
```

```
   dV/dY = 0.1366246608*SECH(1.11*
A   (-0.1294*Y+0.2728*X+0.1246))**2*(Y+0.499*TA
1   NH(C(1)*(-0.1294*Y+0.2728*X+C(2)))+2.4d-02)**2+0.82*(2.925-2.32
2   *TANH(1.11*(-0.1294*Y+0.2728*X+0.1246)))*(1-6.457060000000001d
3   -02*C(1)*SECH(C(1)*(-0.1294*Y+0.2728*X+C(2)))**2)*(Y+0.499*TANH
4   (C(1)*(-0.1294*Y+0.2728*X+C(2)))+2.4d-02)
```

```
    2   2
   dV/dX = 0.1744361636852736*SECH
A   (1.11*(-0.1294*Y+0.2728*X+0.1246))**2*TANH(
1   1.11*(-0.1294*Y+0.2728*X+0.1246))*(Y+0.499*TANH(C(1)*(-0.1294*Y
2   +0.2728*X+C(2)))+2.4d-02)**2-6.0902202624d-02*C(1)**2*(2.925-2
3   .32*TANH(1.11*(-0.1294*Y+0.2728*X+0.1246)))*SECH(C(1)*(-0.1294*
4   Y+0.2728*X+C(2)))**2*TANH(C(1)*(-0.1294*Y+0.2728*X+C(2)))*(Y+0.
5   499*TANH(C(1)*(-0.1294*Y+0.2728*X+C(2)))+2.4d-02)-0.15683539761
6   97325*C(1)*SECH(1.11*(-0.1294*Y+0.2728*X+0.1246))**2*SECH(C(1)*
7   (-0.1294*Y+0.2728*X+C(2)))**2*(Y+0.499*TANH(C(1)*(-0.1294*Y+0.2
8   728*X+C(2)))+2.4d-02)+1.51951039554688d-02*C(1)**2*(2.925-2.32*
9   TANH(1.11*(-0.1294*Y+0.2728*X+0.1246)))*SECH(C(1)*(-0.1294*Y+0.
:   2728*X+C(2)))**4+949.8*EXP(-3.664*(0.2728*X+2.1404)
;   )+6.0902202624d-02*C(1)**2*(2.925-2.32*TANH(1.11*(0.2728*X+0.2
<   1384)))*SECH(C(1)*(0.2728*X+C(2)+8.6000000000000001d-04))**2*(0
=   .499*TANH(C(1)*(0.2728*X+C(2)+8.6000000000000001d-04))+0.1809)*
>   TANH(C(1)*(0.2728*X+C(2)+8.6000000000000001d-04))-0.17443616368
?   52736*SECH(1.11*(0.2728*X+0.21384))**2*TANH(1.11*(0.2728*X+0.21
@   384))*(0.499*TANH(C(1)*(0.2728*X+C(2)+8.6000000000000001d-04))+
1   0.1809)**2+0.1568353976197325*C(1)*SECH(1.11*(0.2728*X+0.21384)
2   )**2*SECH(C(1)*(0.2728*X+C(2)+8.6000000000000001d-04))**2*(0.49
3   9*TANH(C(1)*(0.2728*X+C(2)+8.6000000000000001d-04))+0.1809)-1.5
4   1951039554688d-02*C(1)**2*
A   (2.925-2.32*TANH(1.11*(0.2728*X+.21384)))*
5   SECH(C(1)*(0.2728*X+C(2)+8.6000000000000001d-04))**4

    2   2
   dV/dY = 3.9247893058694402d-02*
A   SECH(1.11*(-0.1294*Y+0.2728*X+0.1246))**2*T
1   ANH(1.11*(-0.1294*Y+0.2728*X+0.1246))*(Y+0.499*TANH(C(1)*(-0.12
2   94*Y+0.2728*X+C(2)))+2.4d-02)**2-1.37029144496d-02*C(1)**2*(2.9
3   25-2.32*TANH(1.11*(-0.1294*Y+0.2728*X+0.1246)))*SECH(C(1)*(-0.1
4   294*Y+0.2728*X+C(2)))**2*TANH(C(1)*(-0.1294*Y+0.2728*X+C(2)))*(
5   Y+0.499*TANH(C(1)*(-0.1294*Y+0.2728*X+C(2)))+2.4d-02)+0.5464986
6   432*SECH(1.11*(-0.1294*Y+0.2728*X+0.1246))**2*(1-6.457060000000
7   0001d-02*C(1)*SECH(C(1)*(-0.1294*Y+0.2728*X+C(2)))**2)*(Y+0.499
8   *TANH(C(1)*(-0.1294*Y+0.2728*X+C(2)))+2.4d-02)+0.82*(2.925-2.32
9   *TANH(1.11*(-0.1294*Y+0.2728*X+0.1246)))*(1-6.4570600000000001d
:   -02*C(1)*SECH(C(1)*(-0.1294*Y+0.2728*X+C(2)))**2)**2

    2
   dV/dXdY=-8.2742080575052801d-02*
A   SECH(1.11*(-0.1294*Y+0.2728*X+0.1246))**2*
1   TANH(1.11*(-0.1294*Y+0.2728*X+0.1246))*(Y+0.499*TANH(C(1)*(-0.1
2   294*Y+0.2728*X+C(2)))+2.4d-02)**2+2.8888369875200001d-02*C(1)**
3   2*(2.925-2.32*TANH(1.11*(-0.1294*Y+0.2728*X+0.1246)))*SECH(C(1)
4   *(-0.1294*Y+0.2728*X+C(2)))**2*TANH(C(1)*(-0.1294*Y+0.2728*X+C(
5   2)))*(Y+0.499*TANH(C(1)*(-0.1294*Y+0.2728*X+C(2)))+2.4d-02)-0.5
6   760619392*SECH(1.11*(-0.1294*Y+0.2728*X+0.1246))**2*(1-6.457060
7   0000000001d-02*C(1)*SECH(C(1)*(-0.1294*Y+0.2728*X+C(2)))**2)*(Y
8   +0.499*TANH(C(1)*(-0.1294*Y+0.2728*X+C(2)))+2.4d-02)+3.71966650
9   51307522d-02*C(1)*SECH(1.11*(-0.1294*Y+0.2728*X+0.1246))**2*SEC
:   H(C(1)*(-0.1294*Y+0.2728*X+C(2)))**2*(Y+0.499*TANH(C(1)*(-0.129
;   4*Y+0.2728*X+C(2)))+2.4d-02)+0.111624304*C(1)*(2.925-2.32*TANH(
<   1.11*(-0.1294*Y+0.2728*X+0.1246)))*SECH(C(1)*(-0.1294*Y+0.2728*
=   X+C(2)))**2*(1-6.4570600000000001d-02*C(1)*SECH(C(1)*(-0.1294*Y
>   +0.2728*X+C(2)))**2)
```

APPENDIX E

EXCITED STATE POTENTIAL ENERGY SURFACE Ex(D)
(C(1)=2.5 C(2)=-1.5)

```
    EXCIPOT=.41*(2.925-2.32*TANH(1.11*(-0.1294*Y
1    +0.2728*X+0.1246)))*(Y+0.3192*TANH(C(1)*(-0.1294*Y
2    +0.2728*X+C(2)))+.2038)**2+.42734*EXP(-3.5771*
3    (0.2728*X))-0.41*(0.3192*TANH(C(1)*(0.2728*
4    X+C(2)+.00086))+0.2194)**2*(2.925-2.32*TANH(1.11*
5    (0.2728*X+0.21384)))+1.3526
```

DERIVATIVES OF THE EXCITED STATE POTENTIAL ENERGY SURFACE

```
    dV/dX = -0.2880309696*SECH
A    (1.11*(-0.1294*Y+0.2728*X+0.1246))**2*(Y+0.3192*
1    TANH(C(1)*(-0.1294*Y+0.2728*X+C(2)))+0.2038)**2+7.14037632d-02*
2    C(1)*(2.925-2.32*TANH(1.11*(-0.1294*Y+0.2728*X+0.1246)))*SECH(C
3    (1)*(-0.1294*Y+0.2728*X+C(2)))**2*(Y+0.3192*TANH(C(1)*(-0.1294*
4    Y+0.2728*X+C(2)))+0.2038)-0.417*EXP(-0.9758*X)+0.28
5    80309696*SECH(1.11*(0.2728*X+0.21384))**2*(0.3192*TANH(C(1)*(0.
6    2728*X+C(2)+.00086))+0.2194}**2
A    -7.14037632d-02*C(1)*(2.925-2.32*TAN
7    H(1.11*(0.2728*X+0.21384)))*SECH(C(1)*
A    (0.2728*X+C(2)+.00086))**2*(0
8    .3192*TANH(C(1)*(0.2728*X+C(2)+.00086))+0.2194)

    dV/dY = 0.1366246608*SECH(1.11*
A    (-0.1294*Y+0.2728*X+0.1246))**2*(Y+0.3192*T
1    ANH(C(1)*(-0.1294*Y+0.2728*X+C(2)))+0.2038)**2+0.82*(2.925-2.32
2    *TANH(1.11*(-0.1294*Y+0.2728*X+0.1246)))*(1-4.130448d-02*C(1)*S
3    ECH(C(1)*(-0.1294*Y+0.2728*X+C(2)))**2)*(Y+0.3192*TANH(C(1)*(-0
4    .1294*Y+0.2728*X+C(2)))+0.2038)
```

```
    2   2
   dV/dX = 0.1744361636852736*
A   SECH(1.11*(-0.1294*Y+0.2728*X+0.1246))**2*TANH(
1   1.11*(-0.1294*Y+0.2728*X+0.1246))*(Y+0.3192*TANH(C(1)*(-0.1294*
2   Y+0.2728*X+C(2)))+0.2038)**2-3.895789320192d-02*C(1)**2*(2.925-
3   2.32*TANH(1.11*(-0.1294*Y+0.2728*X+0.1246)))*SECH(C(1)*(-0.1294
4   *Y+0.2728*X+C(2)))**2*TANH(C(1)*(-0.1294*Y+0.2728*X+C(2)))*(Y+0
5   .3192*TANH(C(1)*(-0.1294*Y+0.2728*X+C(2)))+0.2038)-0.1003243665
6   735844*C(1)*SECH(1.11*(-0.1294*Y+0.2728*X+0.1246))**2*SECH(C(1)
7   *(-0.1294*Y+0.2728*X+C(2)))**2*(Y+0.3192*TANH(C(1)*(-0.1294*Y+0
8   .2728*X+C(2)))+0.2038)+6.2176797550264318d-03*C(1)**2*(2.925-2.
9   32*TANH(1.11*(-0.1294*Y+0.2728*X+0.1246)))*SECH(C(1)*(-0.1294*Y
:   +0.2728*X+C(2)))**4+0.40692*EXP(-0.97583*X)+3.895
;   789320192d-02*C(1)**2*(2.925-2.32*TANH(1.11*(0.2728*X+0.21384))
<   )*SECH(C(1)*(0.2728*X+C(2)+.00086))**2
A   *(0.3192*TANH(C(1)*(0.2728*X+
=   C(2)+.00086))+0.2194)*
A   TANH(C(1)*(0.2728*X+C(2)+.00086))-0.1744361636852
>   736*SECH(1.11*(0.2728*X+0.21384))**2*TANH(1.11*(0.2728*X+0.2138
?   4))*(0.3192*TANH(C(1)*
A   (0.2728*X+C(2)+.00086))+0.2194)**2+0.10032436
@   65735844*C(1)*SECH(1.11*(0.2728*X+0.21384))**2*SECH(C(1)*(0.272
1   8*X+C(2)+.00086))**2*
A   (0.3192*TANH(C(1)*(0.2728*X+C(2)+.00086))+0.2194)-
2   6.2176797550264318d-03*C(1)**2*(2.925-2.32*TANH(1.11*(0.2728*X+
3   0.21384)))*SECH(C(1)*(0.2728*X+C(2)+.00086))**4

    2   2
   dV/dY = 3.9247893058694402d-02*
A   SECH(1.11*(-0.1294*Y+0.2728*X+0.1246))**2*T
1   ANH(1.11*(-0.1294*Y+0.2728*X+0.1246))*(Y+0.3192*TANH(C(1)*(-0.1
2   294*Y+0.2728*X+C(2)))+0.2038)**2-8.7654715276800003d-03*C(1)**2
3   *(2.925-2.32*TANH(1.11*(-0.1294*Y+0.2728*X+0.1246)))*SECH(C(1)*
4   (-0.1294*Y+0.2728*X+C(2)))**2*TANH(C(1)*(-0.1294*Y+0.2728*X+C(2
5   )))*(Y+0.3192*TANH(C(1)*(-0.1294*Y+0.2728*X+C(2)))+0.2038)+0.54
6   64986432*SECH(1.11*(-0.1294*Y+0.2728*X+0.1246))**2*(1-4.130448d
7   -02*C(1)*SECH(C(1)*(-0.1294*Y+0.2728*X+C(2)))**2)*(Y+0.3192*TAN
8   H(C(1)*(-0.1294*Y+0.2728*X+C(2)))+0.2038)+0.32*(2.925-2.32*TANH
9   (1.11*(-0.1294*Y+0.2728*X+0.1246)))*(1-4.130448d-02*C(1)*SECH(C
:   (1)*(-0.1294*Y+0.2728*X+C(2)))**2)**2

   dV/dXdY = -8.2742080575052801d-02*
A   SECH(1.11*(-0.1294*Y+0.2728*X+0.1246))**2*
1   TANH(1.11*(-0.1294*Y+0.2728*X+0.1246))*(Y+0.499*TANH(C(1)*(-0.1
2   294*Y+0.2728*X+C(2)))+2.4d-02)**2+2.8888369875200001d-02*C(1)**
3   2*(2.925-2.32*TANH(1.11*(-0.1294*Y+0.2728*X+0.1246)))*SECH(C(1)
4   *(-0.1294*Y+0.2728*X+C(2)))**2*TANH(C(1)*(-0.1294*Y+0.2728*X+C(
5   2)))*(Y+0.499*TANH(C(1)*(-0.1294*Y+0.2728*X+C(2)))+2.4d-02)-0.5
6   760619392*SECH(1.11*(-0.1294*Y+0.2728*X+0.1246))**2*(1-6.457060
7   000000001d-02*C(1)*SECH(C(1)*(-0.1294*Y+0.2728*X+C(2)))**2)*(Y
8   +0.499*TANH(C(1)*(-0.1294*Y+0.2728*X+C(2)))+2.4d-02)+3.71966650
9   51307522d-02*C(1)*SECH(1.11*(-0.1294*Y+0.2728*X+0.1246))**2*SEC
:   H(C(1)*(-0.1294*Y+0.2728*X+C(2)))**2*(Y+0.499*TANH(C(1)*(-0.129
;   4*Y+0.2728*X+C(2)))+2.4d-02)+0.111624304*C(1)*(2.925-2.32*TANH(
<   1.11*(-0.1294*Y+0.2728*X+0.1246)))*SECH(C(1)*(-0.1294*Y+0.2728*
=   X+C(2)))**2*(1-6.4570600000000001d-02*C(1)*SECH(C(1)*(-0.1294*Y
>   +0.2728*X+C(2)))**2)
```

APPENDIX F

GROUND STATE POTENTIAL ENERGY SURFACE G(C)

```
   POTENTIAL = 0.41*(2.45*(2.048487*
A   EXP(-0.3700034*(0.1294*Y-0.2728*X-1.472666)**
1   2)-1.0)+3.05)*(-0.499*(1.901363*EXP(-0.3931171*(0.1294*Y-0.2728
2   *X-1.2381)**2)-1.0)+Y+2.4d-02)**2+(1-EXP(-1.702*(0.2728*X-1.071
3   51d-03)))**2-0.41*(0.499*(2.019078*EXP(-0.170973*(0.2728*X-2.01
4   7065)**2)-1.0)+1.809d-02)**2*(3.05-2.45*(2.023055*EXP(-0.149470
5   5*(0.2728*X-1.985729)**2)-1.0))
```

DERIVATIVES OF THE GROUND POTENTIAL ENERGY SURFACE

```
   dV/dX = 0.4153968795439264*(0.1294*Y-0.2728*X-1.472666)
A   *EXP(-0.3700034*(0.
1   1294*Y-0.2728*X-1.472666)**2)*(-0.499*(1.901363*EXP(-0.3931171*
2   (0.1294*Y-0.2728*X-1.2381)**2)-1.0)+Y+2.4d-02)**2-0.16686902693
3   46141*(0.1294*Y-0.2728*X-1.2381)*(2.45*(2.048487*EXP(-0.3700034
4   *(0.1294*Y-0.2728*X-1.472666)**2)-1.0)+3.05)*EXP(-0.3931171*(0.
5   1294*Y-0.2728*X-1.2381)**2)*(-0.499*(1.901363*EXP(-0.3931171*(0
6   .1294*Y-0.2728*X-1.2381)**2)-1.0)+Y+2.4d-02)+0.9286112*(1-EXP(-
7   1.702*(0.2728*X-1.07151d-03)))*EXP(-1.702*(0.2728*X-1.07151d-03
8   ))+7.7067165931796031d-02*(0.2728*X-2.017065)*EXP(-0.170973*(0.
9   2728*X-2.017065)**2)*(0.499*(2.019078*EXP(-0.170973*(0.2728*X-2
:   .017065)**2)-1.0)+1.809d-02)*(3.05-2.45*(2.023055*EXP(-0.149470
;   5*(0.2728*X-1.985729)**2)-1.0))-0.1657247909876092*(0.2728*X-1.
<   985729)*(0.499*(2.019078*EXP(-0.170973*(0.2728*X-2.017065)**2)-
=   1.0)+1.809d-02)**2*EXP(-0.1494705*(0.2728*X-1.985729)**2)

   dV/dY=0.82*(2.45*(2.048487*EXP(-0.3700034*
A   (0.1294*Y-0.2728*X-1.472666)**
1   2)-1.0)+3.05)*(9.652766292351705 1d-02*(0.1294*Y-0.2728*X-1.2381
2   )*EXP(-0.3931171*(0.1294*Y-0.2728*X-1.2381)**2)+1)*(-0.499*(1.9
3   01363*EXP(-0.3931171*(0.1294*Y-0.2728*X-1.2381)**2)-1.0)+Y+2.4d
4   -02)-0.1970394289332261*(0.1294*Y-0.2728*X-1.472666)*EXP(-0.370
5   0034*(0.1294*Y-0.2728*X-1.472666)**2)*(-0.499*(1.901363*EXP(-0.
6   3931171*(0.1294*Y-0.2728*X-1.2381)**2)-1.0)+Y+2.4d-02)**2
```

```
      2   2
    dV/dX = 8.3857769445118949D-02*
A    (0.1294*Y-0.2728*X-1.472666)**2*EXP(-0.3700
1    034*(0.1294*Y-0.2728*X-1.472666)**2)*(-0.499*(1.901363*EXP(-0.3
2    931171*(0.1294*Y-0.2728*X-1.2381)**2)-1.0)+Y+2.4D-02)**2-0.1133
3    202687395831*EXP(-0.3700034*(0.1294*Y-0.2728*X-1.472666)**2)*(-
4    0.499*(1.901363*EXP(-0.3931171*(0.1294*Y-0.2728*X-1.2381)**2)-1
5    .0)+Y+2.4D-02)**2-3.5790851472623798D-02*(0.1294*Y-0.2728*X-1.2
6    381)**2*(2.45*(2.048487*EXP(-0.3700034*(0.1294*Y-0.2728*X-1.472
7    666)**2)-1.0)+3.05)*EXP(-0.3931171*(0.1294*Y-0.2728*X-1.2381)**
8    2)*(-0.499*(1.901363*EXP(-0.3931171*(0.1294*Y-0.2728*X-1.2381)*
9    *2)-1.0)+Y+2.4D-02)+4.5521870547762739D-02*(2.45*(2.048487*EXP(
:    -0.3700034*(0.1294*Y-0.2728*X-1.472666)**2)-1.0)+3.05)*EXP(-0.3
;    931171*(0.1294*Y-0.2728*X-1.2381)**2)*(-0.499*(1.901363*EXP(-0.
<    3931171*(0.1294*Y-0.2728*X-1.2381)**2)-1.0)+Y+2.4D-02)-0.338131
=    0882008299*(0.1294*Y-0.2728*X-1.472666)*(0.1294*Y-0.2728*X-1.23
>    81)*EXP(-0.3931171*(0.1294*Y-0.2728*X-1.2381)**2-0.3700034*(0.1
?    294*Y-0.2728*X-1.472666)**2)*(-0.499*(1.901363*EXP(-0.3931171*(
@    0.1294*Y-0.2728*X-1.2381)**2)-1.0)+Y+2.4D-02)+3.395764896354265
1    9D-02*(0.1294*Y-0.2728*X-1.2381)**2*(2.45*(2.048487*EXP(-0.3700
2    034*(0.1294*Y-0.2728*X-1.472666)**2)-1.0)+3.05)*EXP(-0.7862342*
3    (0.1294*Y-0.2728*X-1.2381)**2)-0.43115938038272*(1-EXP(-1.702*(
4    0.2728*X-1.07151D-03)))*EXP(-1.702*(0.2728*X-1.07151D-03))+0.43
5    115938038272*EXP(-3.404*(0.2728*X-1.07151D-03))-7.189046328403
5    589D-03*(0.2728*X-2.017065)**2*EXP(-0.170973*(0.2728*X-2.017065
7    )**2)*(0.499*(2.019078*EXP(-0.170973*(0.2728*X-2.017065)**2)-1.
8    0)+1.809D-02)*(3.05-2.45*(2.023055*EXP(-0.1494705*(0.2728*X-1.9
9    85729)**2)-1.0))+2.1023922866193957D-02*EXP(-0.170973*(0.2728*X
:    -2.017065)**2)*(0.499*(2.019078*EXP(-0.170973*(0.2728*X-2.01706
;    5)**2)-1.0)+1.809D-02)*(3.05-2.45*(2.023055*EXP(-0.1494705*(0.2
<    728*X-1.985729)**2)-1.0))-7.2431073960475 4D-03*(0.2728*X-2.0170
=    65)**2*EXP(-0.341946*(0.2728*X-2.017065)**2)*(3.05-2.45*(2.0230
>    55*EXP(-0.1494705*(0.2728*X-1.985729)**2)-1.0))+1.351503979778 8
?    616D-02*(0.2728*X-1.985729)**2*(0.499*(2.019078*EXP(-0.170973*(
@    0.2728*X-2.017065)**2)-1.0)+1.809D-02)**2*EXP(-0.1494705*(0.272
1    8*X-1.985729)**2)-4.5209722981 4198D-02*(0.499*(2.019078*EXP(-0.
2    170973*(0.2728*X-2.017065)**2)-1.0)+1.809D-02)**2*EXP(-0.149470
3    5*(0.2728*X-1.985729)**2)+6.2302146175874617D-02*(0.2728*X-2.01
4    7065)*(0.2728*X-1.985729)*(0.499*(2.019078*EXP(-0.170973*(0.272
5    8*X-2.017065)**2)-1.0)+1.809D-02)*EXP(-0.1494705*(0.2728*X-1.98
6    5729)**2-0.170973*(0.2728*X-2.017065)**2)
```

```
       2   2
     dV/dY = 1.8867880935864307D-02*
A     (0.1294*Y-0.2728*X-1.472666)**2*EXP(-0.3700
1     034*(0.1294*Y-0.2728*X-1.472666)**2)*(-0.499*(1.901363*EXP(-0.3
2     931171*(0.1294*Y-0.2728*X-1.2381)**2)-1.0)+Y+2.4D-02)**2-2.5496
3     902103959459D-02*EXP(-0.3700034*(0.1294*Y-0.2728*X-1.472666)**2
4     )*(-0.499*(1.901363*EXP(-0.3931171*(0.1294*Y-0.2728*X-1.2381)**
5     2)-1.0)+Y+2.4D-02)**2+0.82*(2.45*(2.048487*EXP(-0.3700034*(0.12
6     94*Y-0.2728*X-1.472666)**2)-1.0)+3.05)*(1.2490679582303107D-02*
7     EXP(-0.3931171*(0.1294*Y-0.2728*X-1.2381)**2)-9.820599468848417
8     1D-03*(0.1294*Y-0.2728*X-1.2381)**2*EXP(-0.3931171*(0.1294*Y-0.
9     2728*X-1.2381)**2))*(-0.499*(1.901363*EXP(-0.3931171*(0.1294*Y-
:     0.2728*X-1.2381)**2)-1.0)+Y+2.4D-02)-0.7881577157329044*(0.1294
;     *Y-0.2728*X-1.472666)*EXP(-0.3700034*(0.1294*Y-0.2728*X-1.47266
<     6)**2)*(9.6527662923517051D-02*(0.1294*Y-0.2728*X-1.2381)*EXP(-
=     0.3931171*(0.1294*Y-0.2728*X-1.2381)**2)+1)*(-0.499*(1.901363*
>     EXP(-0.3931171*
A     (0.1294*Y-0.2728*X-1.2381)**2)-1.0)+Y+2.4D-02)+0.
?     82*(2.45*(2.048487*EXP(-0.3700034*(0.1294*Y-0.2728*X-1.472666)*
@     *2)-1.0)+3.05)*(9.6527662923517051D-02*(0.1294*Y-0.2728*X-1.238
1     1)*EXP(-0.3931171*(0.1294*Y-0.2728*X-1.2381)**2)+1)**2

       2
     dV/dXdY = -3.977710911363047D-02*
A     (0.1294*Y-0.2728*X-1.472666)**2*EXP(-0.3700
1     034*(0.1294*Y-0.2728*X-1.472666)**2)*(-0.499*(1.901363*EXP(-0.3
2     931171*(0.1294*Y-0.2728*X-1.2381)**2)-1.0)+Y+2.4D-02)**2+5.3752
3     356212984083D-02*EXP(-0.3700034*(0.1294*Y-0.2728*X-1.472666)**2
4     )*(-0.499*(1.901363*EXP(-0.3931171*(0.1294*Y-0.2728*X-1.2381)**
5     2)-1.0)+Y+2.4D-02)**2+0.82*(2.45*(2.048487*EXP(-0.3700034*(0.12
6     94*Y-0.2728*X-1.472666)**2)-1.0)+3.05)*(2.0703705835408409D-02*
7     (0.1294*Y-0.2728*X-1.2381)**2*EXP(-0.3931171*(0.1294*Y-0.2728*X
8     -1.2381)**2)-2.6332746445535452D-02*EXP(-0.3931171*(0.1294*Y-0.
9     2728*X-1.2381)**2))*(-0.499*(1.901363*EXP(-0.3931171*(0.1294*Y-
:     0.2728*X-1.2381)**2)-1.0)+Y+2.4D-02)+0.8307937590878529*(0.1294
;     *Y-0.2728*X-1.472666)*EXP(-0.3700034*(0.1294*Y-0.2728*X-1.47266
<     6)**2)*(9.6527662923517051D-02*(0.1294*Y-0.2728*X-1.2381)*EXP(-
=     0.3931171*(0.1294*Y-0.2728*X-1.2381)**2)+1)*(-0.499*(1.901363*
>     EXP(-0.3931171*
A     (0.1294*Y-0.2728*X-1.2381)**2)-1.0)+Y+2.4D-02)+8.
?     0194579936193895D-02*(0.1294*Y-0.2728*X-1.472666)*(0.1294*Y-0.2
@     728*X-1.2381)*EXP(-0.3931171*(0.1294*Y-0.2728*X-1.2381)**2-0.37
1     00034*(0.1294*Y-0.2728*X-1.472666)**2)*(-0.499*(1.901363*EXP(-0
2     .3931171*(0.1294*Y-0.2728*X-1.2381)**2)-1.0)+Y+2.4D-02)-0.16686
3     90269346141*(0.1294*Y-0.2728*X-1.2381)*(2.45*(2.048487*EXP(-0.3
4     700034*(0.1294*Y-0.2728*X-1.472666)**2)-1.0)+3.05)*EXP(-0.39311
5     71*(0.1294*Y-0.2728*X-1.2381)**2)*(9.6527662923517051D-02*(0.12
6     94*Y-0.2728*X-1.2381)*EXP(-0.3931171*(0.1294*Y-0.2728*X-1.2381)
7     **2)+1)
```

APPENDIX H

GROUND STATE POTENTIAL ENERGY SURFACE G(D)

```
   POTENTIAL = 0.41*(2.45*(2.048487*
A   EXP(-0.3700034*(0.1294*Y-0.2728*X-1.472666)**
1   2)-1.0)+3.05)*(-0.499*(1.901363*EXP(-0.3931171*(0.1294*Y-0.2728
2   *X-1.2381)**2)-1.0)+Y+2.4d-02)**2+1.5*(1-EXP(-1.55*(0.2728*X-1.
3   07d-03)))**2-0.41*(0.499*(2.019078*EXP(-0.170973*(0.2728*X-2.01
4   7065)**2)-1.0)+1.809d-02)**2*(3.05-2.45*(2.023055*EXP(-0.149470
5   5*(0.2728*X-1.985729)**2)-1.0))
```